



ADVERTIMENT. L'accés als continguts d'aquesta tesi queda condicionat a l'acceptació de les condicions d'ús establertes per la següent llicència Creative Commons:  <https://creativecommons.org/licenses/?lang=ca>

ADVERTENCIA. El acceso a los contenidos de esta tesis queda condicionado a la aceptación de las condiciones de uso establecidas por la siguiente licencia Creative Commons:  <https://creativecommons.org/licenses/?lang=es>

WARNING. The access to the contents of this doctoral thesis it is limited to the acceptance of the use conditions set by the following Creative Commons license:  <https://creativecommons.org/licenses/?lang=en>



Computational modeling of hybrid materials for applications in photonics and catalysis

Dídac Armand Fenoll Silvestre

Supervised by:

Dr. Mariona Sodupe

Dr. Xavier Solans Monfort

A thesis submitted in fulfillment of the requirements for the degree of Doctor in Philosophy

Department of Chemistry

Physical Chemistry Unit

-2023-

UAB

Universitat Autònoma de Barcelona

Memòria presentada per aspirar al **Grau de Doctor en Química**
per Dídac Armand Fenoll Silvestre.

Donen el seu vist-i-plau,

Dra. Mariona Sodupe
Departament de Química
Facultat de Ciències
Universitat Autònoma de Barcelona

Dr. Xavier Solans-Monfort
Departament de Química
Facultat de Ciències
Universitat Autònoma de Barcelona

Bellaterra, 2023

To my family, friends and teachers

Abstract.

To the many health, environmental and energy generation concerns being faced at the beginning of the XXI Century, an equal amount of solutions are being searched for throughout the plentiful room at the bottom. This much is clear from theoretical and applied research into nanomaterials. In this Thesis, DFT simulations are used to characterize a wide range of nanomaterials, broadly divided into two categories: semiconductor materials for imaging applications, and metal catalysts for heterogeneous hydrogen evolution.

Herein presented is a comparative description of the electronic structure of (MX) binary metal chalcogenide (MX = CdSe, CdS, ZnSe and ZnS), from bulk and surfaces to quantum dots. It has been shown that deleterious defects on slab surfaces and quantum dots can be reduced through ligand- and inorganic shell-passivation. The highly toxic CdSe was first characterized on its own, followed by the other three materials. Different (CdSe)@(MX) core-shell quantum models were simulated, for which different frontier orbital behaviors are seen in the ligand-coordinated core-shell models depending on the shell material.

The computational material screening for hydrogen evolution electrocatalysts is firstly centered on the metal-only Pt(111) and Ru(100), modeled both as pristine and defective surfaces. Results show that Pt(111) activity remains high regardless, while that of defective Ru(100) slabs is enhanced on reconstructed binding sites. Finally, recently synthesized core-shell RuO₂@Ru nanoparticles with high HER activity have been modeled as periodic, surface slab models. The RuO₂ core is proposed to induce important structural and oxidation states changes on the Ru shell which benefit the HER onset.

The need for *hybrid materials* with unique, highly tunable properties is made abundantly clear and lies at the heart of this Thesis.

Contents

1	Introduction.	11
1.1	Hybrid nanomaterials.	13
1.2	Semiconductor nanoparticles.	14
1.2.1	Passivated, core-only quantum dots.	15
1.2.2	Core-shell quantum dots.	17
1.2.3	<i>In silico</i> characterization of quantum dots.	20
1.3	Water electrolysis as a green energy source.	24
1.3.1	Heterogeneous hydrogen evolution reaction.	26
1.3.2	<i>In silico</i> water splitting electrocatalysis.	29
1.4	Research objectives.	32
2	Theoretical background	33
2.1	Fundamentals of Computational Chemistry.	33
2.1.1	The Schrödinger equation: formalism and approximations.	35
2.1.2	The Born-Oppenheimer approximation.	37
2.1.3	The variation principle.	39
2.1.4	Spin-orbitals and basis sets.	39
2.1.5	The Hartree-Fock method.	42
2.2	Density functional theory.	43
2.2.1	Fundamentals of density functional theory.	43

2.2.2	Exchange-correlation functionals. Semi-empirical corrections.	46
2.2.3	Time-dependent Density Functional Theory.	49
2.3	Potential energy surface.	51
2.4	Thermal effects and thermochemistry.	52
2.5	Periodic boundary conditions in crystalline systems.	55
2.5.1	Direct and reciprocal space.	55
2.5.2	The Born-von Karman conditions. The Bloch theorem.	57
2.5.3	Plane waves.	59
2.6	Solvation methods.	61
2.7	Ab initio molecular dynamics (AIMD)	62
3	Core-only CdSe structures.	65
3.1	Introduction	65
3.2	Computational details.	68
3.3	Results and discussion.	73
3.3.1	<i>In silico</i> characterization of core-only systems.	73
3.3.2	Method calibration.	74
3.3.3	Low surface coverage ligand adsorption.	75
3.3.4	Full surface coverage ligand adsorption.	80
3.3.5	Surface and ligand-mediated deprotonation of Lewis acids on CdSe ZB(110).	83
3.3.6	Optical properties of CdSe materials.	85
3.4	Conclusions.	90
4	Core-Shell Quantum Dots	93
4.1	Introduction.	93
4.2	Computational Details.	99
4.3	Results and discussion.	102
4.3.1	Pristine bulk materials.	102
4.3.2	CdSe-ZnSe solid solutions. Vegard's law.	104
4.3.3	Pristine extended surface materials.	107
4.3.4	Passivated extended surface materials.	109

4.4	Core-only and core-shell quantum dots.	114
4.4.1	Core-only quantum dots: effects of size, shape and material composition. . .	115
4.4.2	Core-shell $(\text{CdSe})_6@(\text{MX})_{27}$ quantum dots.	121
4.5	Conclusions.	126
5	Metal electrocatalysts for hydrogen evolution.	129
5.1	Introduction.	130
5.1.1	Selected elements of electrochemistry.	132
5.2	<i>In silico</i> HER on metal surfaces.	133
5.3	Computational details.	137
5.4	Results and discussion	140
5.4.1	Hydrogen evolution on pristine Pt(111) and Ru(100) facets.	140
5.4.2	Hydrogen evolution on defective metal surfaces.	142
5.5	Conclusions.	151
6	Hybrid materials for hydrogen evolution.	153
6.1	Introduction.	153
6.1.1	Summary of experimental results.	154
6.2	Computational details.	157
6.3	Results and discussion.	158
6.3.1	Hydrogen adsorption energies on $\text{RuO}_2@(\text{Ru})$ surface slabs.	158
6.4	Conclusions.	163
7	General conclusions	165

Introduction.

There is no shortage of promising solutions to the many environmental, energy and health-related issues raised this far into the XXI Century. Multidisciplinary research efforts become essential as the urgency of these pressing matters increases, oftentimes struggling against political inaction and vested economic interests. Chief among these challenges is climate change and the on-going energy crisis [1]. In their 2022 report, the International Energy Agency states that CO₂ energy-linked emissions have risen to 36.6 Gt/year coinciding with the significant global economy rebound from the COVID-19 pandemic: the enforcement of the Stated Policies by September 2022 is expect to halt emissions at 37 Gt/year, with a progressive decline to 32 Gt/year by 2050. In this scenario, global temperatures are expected to still rise by 2.5°C by 2100. The more ambitious Net Zero Emissions Scenario could lower it to 1.5°C, but would in turn require a three-fold increase in the current investment in clean energy and infrastructure by 2023 and the active involvement of developing economies. Circumstantially, future roadmaps must now account for the on-going Russian invasion of Ukraine and its impact on the already-fragile energy stock. Ideally, all projected surges in demand and supply bottlenecks should be met with green energy policies that also align with the climate objectives.

The impact of climate change goes beyond the catastrophic alteration of weather patterns: resource exhaustion and pollution are inflicting irreversible damage across the biosphere, endangering wildlife and humans alike. The need for research into biomedicine and biological remediation has recently been made all the more clear by the COVID-19 pandemic. In this regard, nanotechnol-

ogy has offered a multidisciplinary approach from its early development, with vast applications in catalysis, energy storage, biological remediation and biomedicine, to name a few. Venturing into material science, advances in nanoscience and nanofabrication are intrinsically linked to Physics, Chemistry, Biology and Engineering. Many different "nanomaterials" have been developed encompassing a wide compositional spectrum, each providing new or enhanced properties which are already part of the current state-of-the-art (see Figure 1.1).

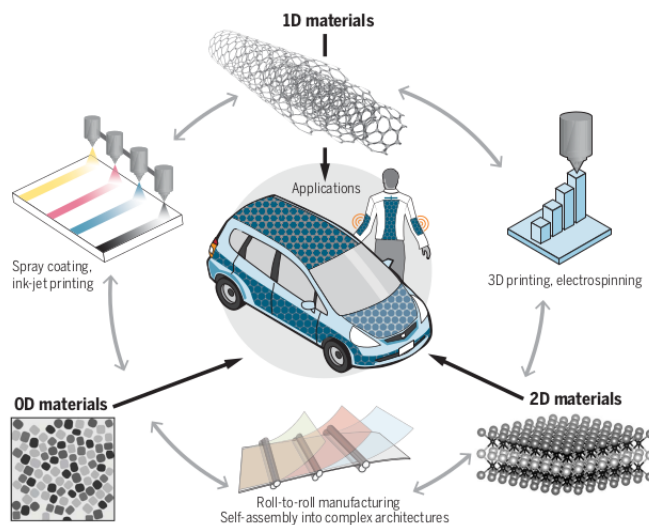


Figure 1.1. *Nanomaterials have already been used in highly flexible and resilient electronic devices which provide high power and energy densities [2].*

Owing to exotic quantum phenomena taking place at the microscopic scale, nanomaterials exhibit unique physical and chemical properties, including enhanced mechanical features, higher photonic yields or higher catalytic activities compared to their bulk counterparts [3, 4]. Due to their wide compositional and morphological variety, different classification criteria have been developed to characterize them. A standard criterion is dimensionality, that is, the number of non-nanometric (conventionally, above 100 nm) directions in a nanomaterial¹ (Figure 1.2) [5].

¹Their properties also depend on their aspect ratio, a measure of the confined dimension with respect to the non-confined directions.

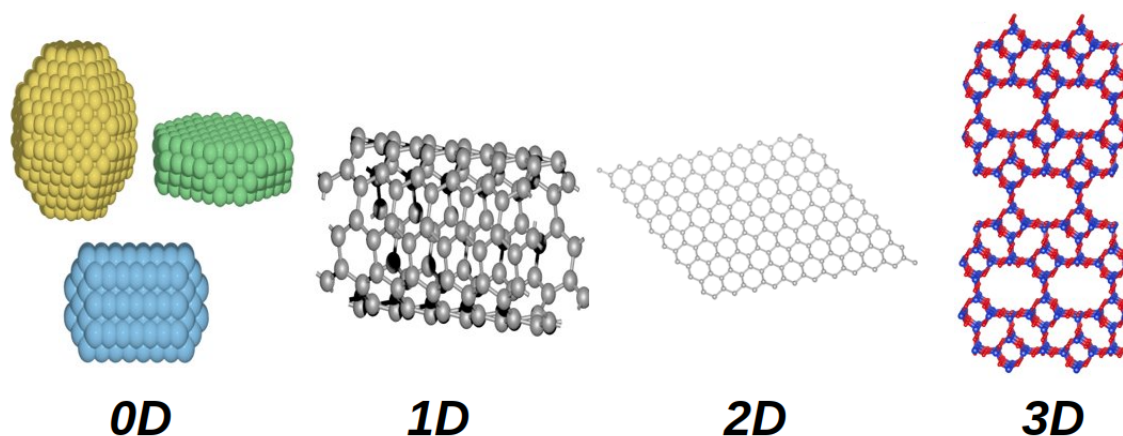


Figure 1.2. Archetypal nanomaterials with different dimensionalities.

Exhibiting the lowest dimensionality, zero-dimensional (0D) nanomaterials are completely nanometric. Many 0D morphologies have been characterized, including spheroidal nanoparticles, nanocrowns, nanorods or nanoplatelets, to name a few. One-dimensional nanomaterials (1D) are nanometric in all but one direction, with carbon nanotubes being the paradigmatic example. Only one direction is nanometric in 2D nanomaterials, surfaces which may also be comprised by more than one layer (*e.g.* monolayer graphene or few-layered MoS₂). Finally, three-dimensional (3D) nanomaterials present an extended, macroscopic structure but contain nanoscale structures (*e.g.* hierarchical architectures with interconnected 3D networks [6]).

The term "hybrid nanomaterial" has been coined to broadly encompass the rich and ever-increasing variety of nanomaterials, as they seldom involve only one material [7]. Although a general review of hybrid materials is presented in Section 1.1, it should be noted that this Thesis discusses specific types of hybrid nanomaterial: metal chalcogenide surfaces and quantum dots capped with organic ligand molecules², core-shell quantum dots and metal-metal oxide surfaces.

1.1 Hybrid nanomaterials.

While the term "hybrid material" already suggests the presence of more than one component, more specific criteria have been devised to accurately distinguish them. The nature of the interactions present in a system provides a particularly useful criterion, inasmuch as they determine its over-

²The terms "ligand molecule", "passivating ligand" and "capping ligand" are herein used interchangeably.

all morphology, properties and potential range of applications [7]. Such is the rationale behind the Class A / Class B criterion hereby presented. In Class A hybrid materials, lowly-covalent or non-covalent interactions are the most abundant, mostly corresponding to hydrogen bonding, electrostatic forces, $\pi - \pi$ and van der Waals interactions. Conversely, Class B materials exhibit strong covalent, ionic or metallic bonds which frequently result in well-defined networks. In the simplest cases, single-composition nanomaterials are surrounded by ligand molecules which can alter their catalytic or electro-optical performance (Class A). In more complex nanomaterials, two or more solid-state materials are in atomistic contact through strong covalent or metallic interactions, thus constituting examples of Class B hybrid materials³. Ultimately, their properties also depend on the hybrid nanomaterial's morphology and on the type of interface between materials. It should be noted that, due to their distinct chemical nature, Class A and Class B materials involve vastly different synthetic routes [7].

In this Thesis, hybrid materials of both Class A (core-only semiconductor nanoparticles with ligand coordination) and Class B (core-shell semiconductor nanoparticles and metal - metal oxide materials for hydrogen evolution) are considered. For the sake of discussion, concise state-of-the-art reviews of each material are presented in Section 1.2 and Section 1.3. Each Section ends with a brief reflection on how this Thesis is expected to contribute to the topic at hand (*Advancing Research*).

1.2 Semiconductor nanoparticles.

Regardless of their exact composition, zero-dimensional nanomaterials are broadly categorized as "nanoparticles". Pertinent to this work, "quantum dot" more strictly refers to a nanoparticle of a semiconductor material⁴. Single-component quantum dots are herein referred to as "core-only", while "core-shell" is used when the quantum dot contains more than one semiconductor nanomaterial. For ease of discussion, both "core-only" and "core-shell" are henceforth also applied in the context of extended surfaces with an analogous meaning.

³As per most synthetic processes, the exposed surfaces of nanomaterials commonly present ligands.

⁴Some authors employ the term "semiconductor nanocrystal" interchangeably.

1.2.1 Passivated, core-only quantum dots.

Materials. Chief among semiconductor nanoparticles are those consisting of binary metal chalcogenides, namely those involving group XII and group XVI elements: cadmium and zinc selenides, sulphides and telurides stand out in the literature. Specifically, cadmium selenide (CdSe) has garnered significant attention [8–10]. CdSe has two main polymorphs: wurtzite and zincblende. The former is stable under laboratory conditions, while the latter is metastable. Additionally, a high-pressure, rock salt polymorph for bulk CdSe has also been reported [11, 12]. Colloidal nanoparticle synthesis (Figure 1.3) has found widespread use owing to its relative simplicity, requiring readily available precursors and ligands [13–15].

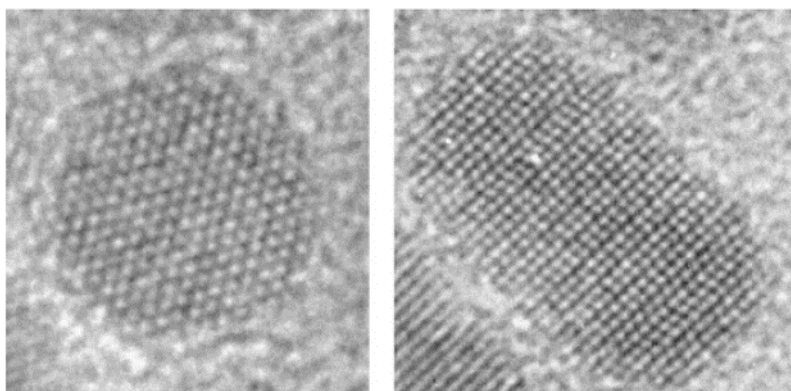


Figure 1.3. Transmission electron micrographs of a single CdSe quantum dot: top view (left) and side view (right) with respect to its rotation axis [15].

Hazardous cadmium precursors, such as $(\text{CH}_3)_2\text{Cd}$ [15, 16], have been replaced by safer and cheaper precursors [14], although the high toxicity of Cd remains problematic [17]. Despite their highly tunable band gap energies, photostability and narrow emission spectra [18], use of Cd-containing quantum dots in *in vivo* cell monitoring requires prior biocompatible functionalization [19, 20]. Attempts at preparing biocompatible quantum dots are expected to either replace Cd by another material, or to generate a sufficiently thick biocompatible shell that can prevent Cd leeching without compromising its optical properties.

Chemical insight. Novel photonic properties of quantum dots are a result of quantum confinement: in essence, exciton generation becomes size-dependent when the size of the quantum dot is below the bulk Bohr exciton radius [21–23]. The smaller the nanoparticle, the closer its

band structure resembles the discrete electronic structure of a molecule (a concomitant blue shift of the optical adsorption and emission is observed as the nanoparticle shrinks [21]). There are other factors controlling the effective optical gap and exciton relaxation mechanisms in quantum dots. Significantly, the presence of structural defects has been suggested to favor non-radiative exciton decay mechanisms (resulting in a decrease of photoluminescence quantum yields) and the appearance of both hole and electron trap states in the band gap region [21, 23–26]. In the case of extended defects, surface reconstruction and interlayer relaxation are mechanisms through which surface energy may be reduced [5, 25]. Another frequent cause for the appearance of charge carrier traps is the presence of under-coordinated surface atoms [26]. Trap states may be removed or "passivated" with a large band gap semiconductor overcoating (*i.e.* core-shell quantum dots), provided sufficient crystallographic compatibility exists [26]. The potential for ligand-mediated surface passivation has been the subject of extended research [23, 24, 27] and still drives current research [10]. Since ligands are ubiquitous in quantum dot fabrication and applications, understanding their influence (or lack thereof) on the electronic structure is essential, particularly in the case of core-shell quantum dots, in which core-shell effects are not trivially distinguishable from ligand-surface interactions. Apart from their role in surface functionalization, ligands are necessary as part of the post-synthetic treatment required to prevent nanoparticle aggregation (the so-called Ostwald ripening) and ensure adequately monodisperse samples. A vast range of ligands have been used in quantum dots synthesis: stearic acid, trioctylphosphine (TOP) [27, 28], trioctylphosphine oxide (TOPO) [27, 29], hexadecylamine (HDA), thioglycolid acid [23] or octylphosphonic acid (OPA) [30] are frequently employed. Nitrogen-containing ligands include amines, which despite providing high quantum yields are easily dissociated from the surface [30].

Applications. Semiconductor nanoparticles have found widespread use in all manner of catalytic, electrooptical and bioimaging applications owing to their excellent quantum yields and stability; as such, they have been subject to extensive experimental [31–33] and computational [9, 10, 34–36] research in the last decades. Quantum dots have been employed in state of the art applications in electronics, lasing and photonic devices [23, 27, 36] and biological imaging [20], with a myriad of synthetic methods [5, 15, 16, 25] allowing for significant control to be exerted on the composition, size, morphology and surface chemistry of nanoparticles [30].

Advancing research. Crucial insight into the nature and extent of ligand passivation can be

gained through theoretical calculations, provided a sufficiently large sample of ligand functionalities is considered. Properly understanding passivation in core-only CdSe surface slab models is a necessary step towards exploring ligand effects on other core-only MX quantum dots and, ultimately, on the more complex core-shell systems (namely, MX=CdS, ZnSe and ZnS).

1.2.2 Core-shell quantum dots.

Materials. Highly precise synthesis methods for core-shell quantum dots have been known for decades, with fabrication processes only growing in complexity ever since. In general terms, core-shell structures can either be zero-dimensional particles (spherical or otherwise, including hollow nanoparticles) or one-dimensional structures (*e.g.* nanorods) [37]. Based on their chemical composition, core-shell nanoparticles can simply be divided into four groups: a) inorganic@inorganic, b) inorganic@organic, c) organic@inorganic and d) organic@organic⁵ [38]. Precise synthetic procedures were developed decades ago, as Bawendi and coworkers [21] synthesized a series of highly luminescent core-shell CdSe@ZnS quantum dots with core sizes ranging from 23 to 55 Å. More recently, two-component ZnS@CdS@ZnS and CdS@CdSe@CdS core-shell structures multilayered quantum dots have also been fabricated, two-component systems in which a low band gap material is surrounded by a larger band gap one [38]. A myriad of surface functionalization options are available, for instance, that of CdSe@CdTe quantum dots covered with glycoprotein inhibitors [39]. Inorganic coatings include metal oxides, as in composites of tin or niobium oxide on CdS, or metals in a colloidal Pd@CdS nanocomposite [37].

Chemical insight. Overcoating core-only quantum dots with higher band gap inorganic semiconductors has been known to enhance photoluminescence, an effect attributed to the passivation of nonradiative recombination sites [21]. Importantly, great control over the optical properties of the quantum dot can be exerted both by carefully selecting the material and by tuning shell thickness [24]. The core-shell interaction is known to introduce a greater degree of "band engineering", that is, control over the band structure. Conversely, the presence of significant defects, such as those caused by excessive strain at the interface, are known to negatively impact the optical properties of hybrid nanoparticles [21]. Interfacial strain is commonly characterized by means of lattice mismatch, a measure of how different the lattice parameters of two crystallographically similar

⁵Conventionally, in A@B type core-shell structures, A is the core and B is the shell.

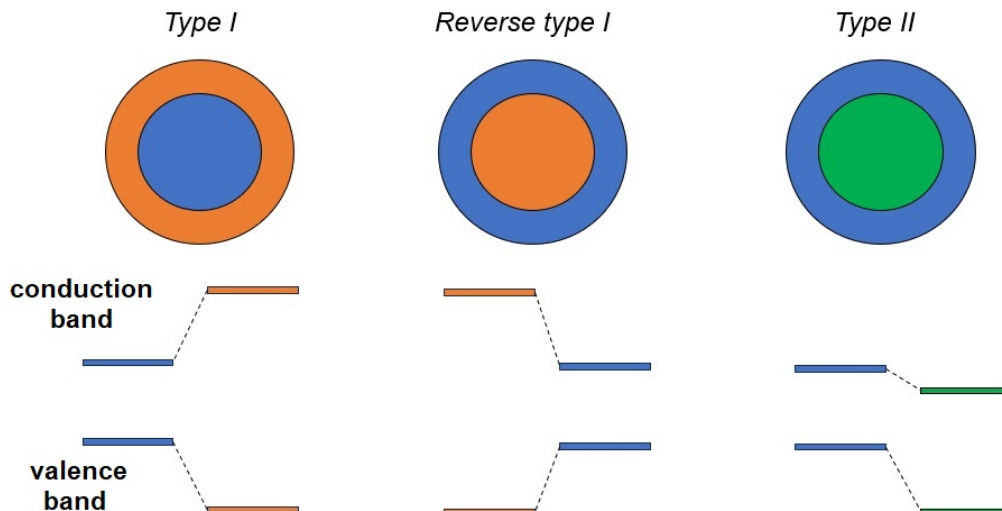
materials are: excessive mismatch hinders epitaxial growth, favoring the appearance of trap states that activate non-radiative decay mechanisms [21, 24, 29]. Strain induced by ZnSe shell growth (7 % lattice mismatch) reportedly introduces thickness-proportional defects when grown on CdSe quantum dots, reducing the photoluminescence quantum yield [40]. Grünwald *et al.* [11] have proposed a practical limit to the lattice mismatch of 11%, although as much as a 12% mismatch has been reported for ZnS-coated CdSe quantum dots [29]). Indeed, incoherent growth of the ZnS shell in CdSe@ZnS core-shell quantum dots was ascribed to the structural relaxation caused by dislocations and low-angle grain boundaries arising from mismatch [21]. CdSe-CdS core-shells have a lower lattice mismatch (ca. 4.2%), but are sensitive to oxidation and exhibit a lower photoluminescence quantum yield [41].

Charge separation of excitons can be achieved through core-shell nanofabrication by confining the electron (or hole) to either the core or the shell [41, 42]. Alternatively, both can be confined in the same region to create a bright and stable fluorophore [43]. The confinement regime changes depending on whether the wide band gap semiconductor is used as the shell or as the core, resulting in three different types of core-shell structures (see Scheme 1.1) [38]:

- **Type-I.** The wide-band gap corresponds to the shell, as in CdSe@CdS, CdSe@ZnS or CdTe@CdS.
- **Reverse Type-I.** The wide-band gap corresponds to the core, as in CdS@CdSe or ZnS@CdSe.
- **Type-II.** The core's conduction and valence bands are either above or below those of the shell, as in CdTe@CdSe (CdSe@CdTe), ZnTe@CdS or PbTe@CdTe (most Te-containing quantum dots can be fabricated into Type-II core-shells).

In Type-I core-shells, hole and electron are both delocalized throughout the core since the valence and conduction bands are constrained by the shell's band gap. The opposite occurs in reverse Type-I core-shells, where the charge carriers are confined within the shell. Conversely, in Type-II core-shells, each region has only one of the carriers. Type-II charge separation could be conveniently used to hinder exciton recombination and enhance photovoltaic and photoconductive devices [44]. Exciton decay times are shorter in Type-I and reverse Type-I core-shells and are thus less suitable than the Type-II ones for photovoltaic applications [38].

Applications. In broad terms, core-shell structures are highly versatile materials with en-



Scheme 1.1. Core-shell quantum dot types (Type I, reverse Type I and Type II) and of the relative positions of their conduction band minima and valence band maxima.

hanced physical and chemical properties compared to their individual components, ranging from improved stability to enhanced catalytic activity [37]. The promising applications of core-shell nanoparticles have been attributed to four factors: a) high photocatalytic activities stemming from their individual components, b) significant electronic structure tunability, c) suppression of nanoparticle aggregation, and d) they are commonly reusable and highly stable [37]. Composites of sufficiently monodisperse core-shell quantum dots may compete with polymeric LEDs, both in wavelength tunability and overall stability [27], with thick-core CdS@ZnS quantum dots being used as stable, 20W LEDs for hydrogen evolution [37]. White light-emitting diodes have been fabricated by placing a high band gap semiconductor between two shells of the same lower band gap material, as in ZnS@CdS@ZnS or in CdS@CdSe@CdS [38]. Among other photonic devices, CdS@SnO₂ quantum dots exhibit enhanced light harvesting capabilities and facilitate charge separation [37]. Recyclable, magnetic microspheres of Fe₃O₄@Zn_xCd_{1-x}S constitute an interesting example of Class B hybrid material [38].

As suggested above, core-shell structures can have more interesting bioimaging applications owing to their increased biocompatibility [37]. For instance, since CdTe is less toxic than CdSe, CdSe@CdTe biofluorescent probes loaded with 5-Fu and P-gp glycoprotein inhibitors (anti-cancer drugs) have promising *in vivo* applications [39]. Different combinations of quantum dots (including

CdSe@CdZnS or CdSe@CdS) have been bound to mice antibodies, obtaining stable nanoparticle-antibody conjugates with low dispersity and high quantum yields [19].

Advancing research. *In vivo* bioimaging would greatly benefit from fully understanding the effect of shell composition and morphology once grown on otherwise toxic cores (*e.g.* CdSe). Promising shell candidates include other group XII - group XVI binary metal chalcogenides, namely: CdS, ZnSe and ZnS. Their higher biocompatibility and similar optical performance has attracted significant attention.

1.2.3 *In silico* characterization of quantum dots.

Theoretical calculations on metal chalcogenide, core-only quantum dots have commonly been devoted to the analysis of surface passivation with organic capping ligands and its effect on the optical properties (band gap and/or absorption spectrum) and the radiative/non-radiative relaxation processes [9, 35, 45]. Throughout the years increasingly larger nanoparticle models have been employed, with experimentally relevant large models requiring sizeable computational resources. Striving for a realistic representation of any system requires taking into consideration as many physical and chemical experimental factors as possible within the restraints of computational feasibility. That is, a compromise between computational resources and sufficiently accurate simulations is always necessary. In order to control said balance, it is essential to understand two basic constituents of theoretical calculations: the *model* and the *method*.

Model. The *scale* of the model is defined by the number particles it contains, be it electrons, atoms, or molecules. While molecular and cluster-like systems commonly involve tens to hundreds of atoms, the systems involved in biological and solid-state reactions may contain thousands of atoms. Experimental evidence may be used to detect non-essential components of the system, which can be simplified (*e.g.* shortening of alkyl chains when changes in dispersion are expected to be mostly inconsequential) or neglected. In this sense, the extent to which any model is a realistic representation of a nanomaterial depends on how accurately experimental evidence is incorporated. Intuitively, a model should account for the system's chemical make-up and structure in terms of its *dimensionality* and its *scale*. In this context, dimensionality concerns how a system may either be discrete or continuous. Discrete systems involve a set number of particles (*e.g.* a CdSe quantum dot model with full ligand coverage), whereas a continuous system contains a virtually

infinite number of them (*e.g.* an extended CdSe surface and all of its adsorbed ligand molecules). Discrete systems are frequently represented with finite models (clusters), while periodic models are a natural choice for continuous systems. Bulk and surface slab models fall in the latter category, consisting of discrete unit cells which can generate the entire system through symmetry-conserving translations. Still, there remains the possibility of representing continuous systems as finite models or vice versa. The (infinite) surface of a catalyst may be replaced by a small cluster provided it properly reproduces the chemical details of the active site. Conversely, periodic surface slabs may be used to separately explore the different facets of nanoparticles: by doing so, edge tip effects are effectively neglected, which may negatively impact model accuracy if the target nanoparticle is small or highly faceted.

Whether cluster-like or slab, the models employed are usually stoichiometric: it is an easily enforced condition during modelization, and the calculation of certain properties is easier than in non-stoichiometric models. For example, specific surface energies in stoichiometric slabs are readily estimated from their potential energies, whereas a more complex treatment involving chemical potentials is required in non-stoichiometric systems. Stoichiometry aside, slab and cluster models can also exhibit polarity (often caused by the termination of their facets) and require a more nuanced treatment [46]. Case in point, the (110) facet of zinc blende CdSe is stoichiometric and non-polar, whereas the also stoichiometric but polar (100) facet can be Se- or Cd-terminated (*i.e.* two different models should be considered). Exploration of low-energy facets is crucial to the understanding of their ligand chemistry. It is no less crucial than selecting a representative set of ligand functionalities based on experimental reports. Detailed models should also account for different ligand surface concentrations as a means to characterize steric and cooperative effects. All in all, a wide range of models have been successfully employed throughout the last twenty years with varying degrees of complexity (Figure 1.4).

Small and large cluster models can be generated either by being cut from their bulk structures [10] or constructed on the grounds of the Wulff theorem [47, 48]. Similarly, surface slab models can be constructed with different unit cell sizes, allowing for different ligand surface concentrations to be represented. In a straightforward approach to core-shell modeling, the internal/external atoms may be directly replaced in a preexisting core-only model; however, this strategy may result in

poor models if lattice mismatch is not accounted for beforehand. Lattice mismatch is reduced in composition gradient core-shells, in which buffer layers with intermediate compositions are placed between the core and the shell.

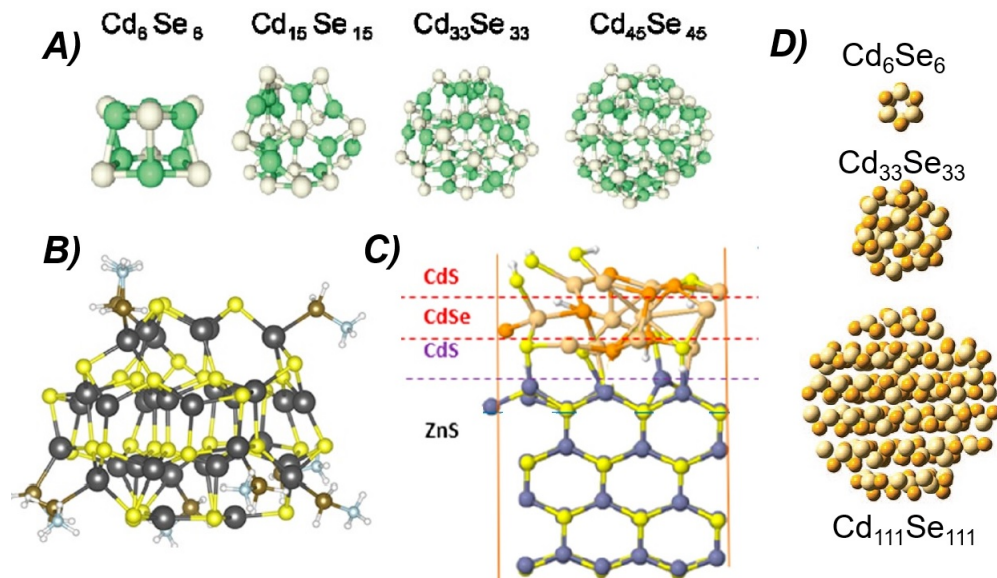


Figure 1.4. Representative models used in theoretical calculations of CdSe structures, including a) differently-sized, unpassivated quantum dots [8], MePH₂-capped (CdSe)₃₃ quantum dots [10], c) layered ZnS@CdS@CdSe@CdS surface slabs and d) alternative morphologies of pristine CdSe quantum dots with different sizes [49].

Method. Detailed accounts on Computational Chemistry and the methods employed in this work are presented in Chapter 2. For now, suffice it to say that each method is broadly characterized by its accuracy and its scaling, which are strongly interdependent. Method accuracy mostly depends on how precisely quantum mechanical effects in the system are factored in the calculation, loosely referred to as "level of theory". For instance, in Density Functional Theory (DFT), incremental addition of higher derivatives of the electron density is said raise level of theory of each successive method, but it is not the only contributing factor to accuracy. Furthermore, at any given level of theory, the accuracy can be increased by improving the system's description. For example, increasing the number of basis functions used per electron should enhance accuracy in orbital-based methods, with certain caveats (*e.g.* basis set superposition error).

Each computational method has a specific scaling, that is, an approximate measure of the computational resources needed to run a successful simulation. The cost of electronic structure calculations

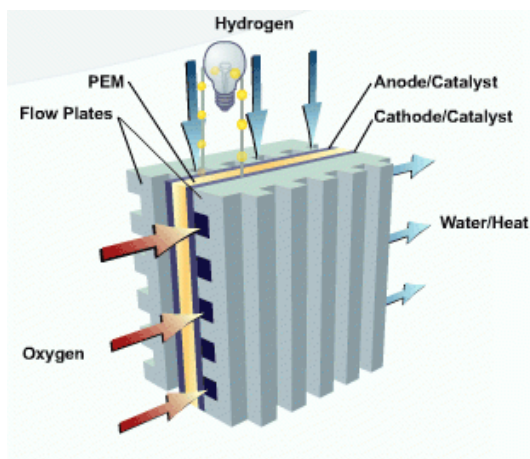
increases with the number of electrons in the system (N), commonly expressed in terms of the number of basis functions (atomic orbital-based algorithms) or the electron kinetic energy cut-off (plane wave algorithms) employed. For instance, DFT methods are said to scale as N^3 , while the electron-count scaling for wave function methods is over three orders in magnitude higher (*e.g.* from N^6 up to N^8 , depending on the specific formalism). Scaling is a pervasive concern in systems with high particle counts, but it is also present in smaller models whenever high levels of theory are needed. Meanwhile, in dynamic simulations, accuracy also relies on ensuring sufficient thermalization and sampling times are achieved, two factors which are absent in static calculations. In any case, adequate method choice relies heavily on proper initial calibration against available experimental data and an exhaustive review of prior computational research.

State of the art. *In silico* research on quantum dots has followed different approaches throughout the years, including *ab initio* thermochemical analysis [10, 50], molecular dynamics [10] and phase transformation characterization [11]. From the early small cluster systems [8], increasingly larger models [10, 50] are being used in high level of theory calculations, although computational demands remain significant if ligand coverage is considered explicitly [10]. CdSe@ZnS and ZnS@CdSe core-shell nanowires have been computationally studied in order to assess their relative stability and quantum confinement effects [51]. In predicting properties of excited states or band gap energies in semiconductors, method-dependent limitations to DFT simulations can lead to significant deviations from experimental data [52–54]. Nonetheless, DFT is commonly employed for electronic structure calculations involving quantum dots, from core-only CdSe systems [8, 10, 55] to core-shell models [41], as well as phonon-charge carrier interactions in CdSe and PbSe quantum dots [56]. Still, there exist cautionary reports against its use in highly correlated electronic states, for instance, in exciton-exciton interactions [55].

Advancing research. A systematic approach to the analysis of surface slab and nanoparticle models involving ligand molecules should reveal the effect on their electronic structure. Considering a large variety of ligand functionalities and the inclusion of solvent and thermal effects should provide additional insight.

1.3 Water electrolysis as a green energy source.

Clean H_2 generation through water electrolysis is hailed as one of the most promising solutions to sustainable energy generation [1, 48, 57–61]. First and foremost, both its raw source (water) and its by-products (H_2 and O_2) are renewable and non-hazardous [62]. Its coupling to renewable energy sources has been envisioned as a solution to shortages and intermittence, having already attracted noteworthy research [57, 60, 61, 63–67]. Indeed, the energy density of H_2 ($140 \text{ MJ}\cdot\text{kg}^{-1}$) greatly surpasses the capabilities of liquid fuels (ca. $50 \text{ MJ}\cdot\text{kg}^{-1}$) [68]. As part of the broader "hydrogen economy" [58], hydrogen is a necessary reagent in key chemical processes, including hydrocarbon hydrogenation and ammonia synthesis, as well as a reducing agent in metallurgy [62]. Coming back to energy generation, fuel cells (Scheme 1.2) are paradigmatic examples. Succinctly, fuel cells generate electricity and residual heat as part of the charge transfer involved in the electrochemical splitting of a reaction fuel and O_2 [69].



Scheme 1.2. Schematic representation of a fuel cell, in which a polymeric proton-electron membrane acts as an electrolyte. Adapted from [70]

In proton exchange membrane fuel cells employing H_2 , protons flow from the anode to the cathode across a solid polymer membrane (internal circuit), while electrons from the anode to the cathode through an external circuit [69]. Owing to their individual low voltage output (roughly 1.1 eV), cell stacking is necessary; hundreds of fuel cells may be combined in series, ultimately impacting its transportation [69, 70]. Importantly, low temperature fuels cells (70-90 °C range) require costly Pt catalysts to enhance the reaction rate and highly-pure H_2 [69].

Overall, use of the hydrogen evolution reaction still remains marginal, with most H_2 being obtained from coal steam gasification and methane reforming [62]. Large scale application of the electrochemical splitting of water suffers from the costly noble metal reagents needed to enhance its kinetics, particularly, platinum [63, 71]. The low Earth crust abundance of platinum is a major concern indeed. Virtually all platinum is extracted in South Africa (reported to hold roughly 80% of all the Pt in the crust in 2008 [72]) and Russia, with only two plants in the U.S. that provide less than 7% of world supply. In 2020, up to 166.000 kg of platinum were mined world-wide according to the 2022 report forwarded by the U.S. Department of Energy. As one of the "platinum group metal" catalysts (which also include palladium, ruthenium, rhodium and iridium), platinum demand will increase in response to zero carbon emission policies (catalytic converters are the main market for platinum consumption). Meeting the ever-increasing Pt requires generous research investment: potential solutions imply developing more efficient Pt fuel cells, improving the existing recycling procedures or finding an Earth-abundant alternative [72].

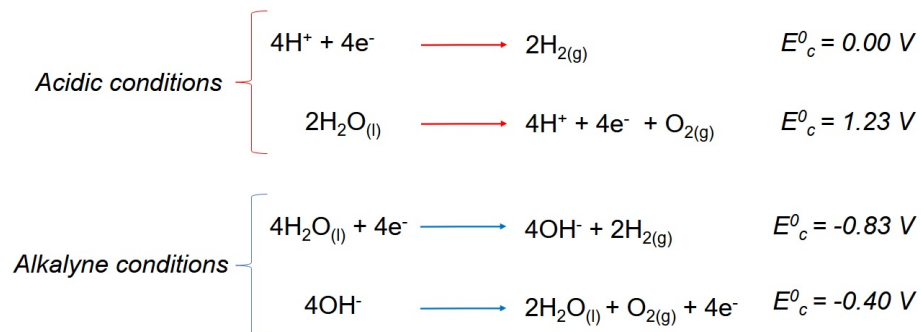
In this Thesis, two distinct approaches to this problem are discussed (other feasible strategies notwithstanding): a) synthesizing new electrocatalysts with lower overpotentials or b) lowering the noble metal content of the already known ones. Either approach should result in a significant decrease in scaling costs, and they are not mutually exclusive. Approach a) would lower the energy required to sustain the water electrolysis process, while approach b) would reduce the cost of already-known electrocatalysts. Both require an in-depth experimental and computational understanding of the catalyst-water interface [71, 73, 74]. These general principles concern both homogeneous and heterogeneous electrocatalyst design, and can be extended to other important reactions such as ammonia and CO_2 formation [65]. Nevertheless, the present work centers around heterogeneous electrocatalysts for the hydrogen evolution reaction, the main chemical aspects of which are promptly presented.

Chemical insight. Water electrolysis is an endergonic reaction ($\Delta G_r^0 = +237.2 \text{ kJ}\cdot\text{mol}^{-1}$) with a deceptively simple global redox reaction:



Water electrolysis has been subject to extensive electrochemical research in order to fully elu-

cidate the most probable mechanisms for its constituent half-reactions and create highly active catalysts [1, 63, 75, 76]. In the common two-electrode approach, water is oxidized into O_2 at the anode through oxygen evolution reaction (OER) and reduced to H_2 at the cathode through the hydrogen evolution reaction (HER) (3,7). Conceptually, separating both half-reactions facilitates their study and eventual catalyst design for the overall process. These half-reactions are known to be different in acidic and alkaline media, as shown in Scheme 1.3:



Scheme 1.3. Water splitting half-reactions in acid and alkaline conditions, and the corresponding standard reduction potentials against the standard hydrogen electrode.

Where E_c^0 is the standard reduction potential of the half-reaction against the standard hydrogen electrode⁶. Water electrolysis is greatly hindered by the sluggish kinetics of the OER and the costly precious metals used as anodes (*e.g.* Ru and Ir) and cathodes (*e.g.* Pt and Ru) in acidic media. The HER can also be the source of unwanted overpotentials, although its proposed mechanisms (see Section 5.1.1) are less complex than those of OER (the oxygen evolution reaction will not be discussed further).

Advancing research. A novel heterogeneous HER electrocatalyst, consisting of hybrid core-shell $RuO_2@Ru$ core-shell nanoparticles supported on carbon nanotubes, has been recently synthesized by Dr. Xavier Sala and coworkers (Autonomous University of Barcelona). Theoretical calculations should provide crucial insight into its atomistic structure and enhanced activity.

1.3.1 Heterogeneous hydrogen evolution reaction.

Materials. Although research into economical alternatives to costly noble metals has surged in recent years, the yet unparalleled HER activity of platinum [1, 58, 75] still drives forward significant

⁶The first reaction is, in fact, the reference reaction for said electrode, for which $E_c^0=0$ by convention.

research. For example, Pt(111) has been used to study the influence of pH on the H binding energies and its ultimate impact on the sluggish kinetics of the HER in alkaline media [58]. Despite the privileged position of the Pt(111) facet on both experimental and theoretical volcano plots (see Figure 1.5) [60, 64], its activity can be enhanced further through Mo and Fe doping [77] or defect inclusion and surface functionalization with organic molecules [60]. Koper and coworkers [60] have covered Pt(111) with increasingly-defective graphene overlayers, and shown that HER activity is enhanced precisely around said defects. The effect of non-pristine coordination numbers in Pt(111) has also been studied by Calle-Vallejo and coworkers [78]. Ruthenium, a similarly scarce metal, provides adequate HER activities: crystalline *fcc* Ru has shown promising HER activity [79]) and many high-performance nanoscale electrocatalysts have been synthesized, including *fcc* Ru nanotubes and *hcp* Ru nanocrystals [59].

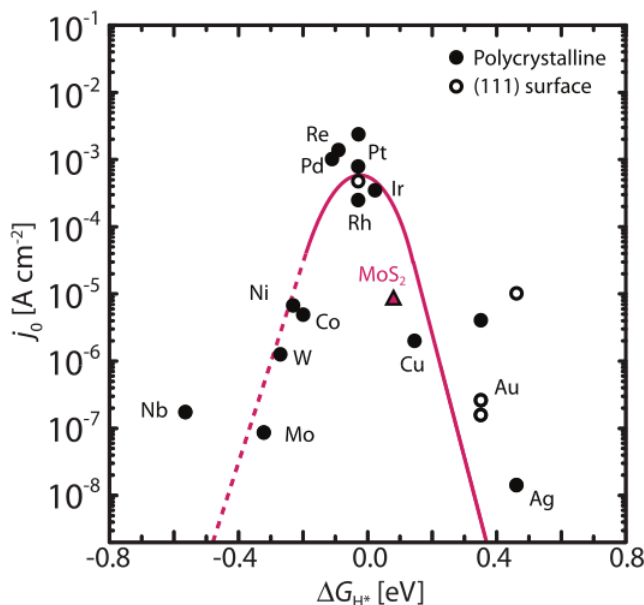


Figure 1.5. Hydrogen evolution reaction volcano plot for different metals and MoS_2 , in which HER activity (in terms of the exchange current density) is plotted against the hydrogen adsorption Gibbs free energy. Extracted from [1].

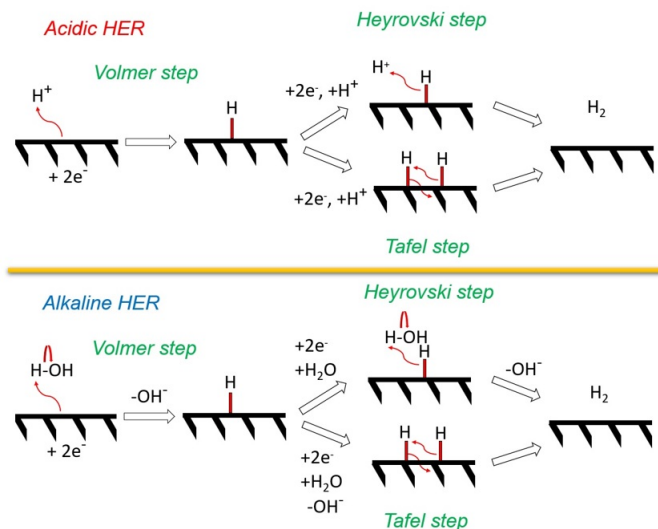
Otherwise prohibitive up-scaling costs may be reduced by lowering the noble metal content loaded on the electrocatalysts, for instance, through replacement or alloying with less costly, Earth-abundant transition metals [58, 76]. These non-precious metals (*e.g.* Co, Ni, Mo, Fe) and their derivatives have attracted significant attention [80].

Apart from metals, the photochemical induction of the HER has been carried out using different types of light-harvesting semiconductors. These include costly and toxic compounds such as CdSe [81], CdS and Ag_3PO_4 [66], the more conventional TiO_2 and ZnO [61] or few-layered transition metals, such as MoS_2 [80]. Significantly, a quantitative relation between quantum confinement in CdSe quantum dots and their activity in water electrolysis has been characterized by Osterloh and coworkers [81], proving that said activity can be tuned by changing the nanoparticles' size (specifically, smaller nanoparticles lead to faster kinetics).

Nanoparticles are highly versatile candidates for electrocatalysis, both for water reduction and oxidation [82–84]. Owing to their high surface-to-volume ratios, high surface areas are obtained even if the noble metal ratio is reduced. In order to prevent aggregation (*e.g.* Ostwald ripening), nanoparticles must be properly dispersed on the electrode [71], a process that also facilitates charge transfer with the electrocatalyst [83, 85]. In the case of ruthenium-based nanoparticles, this has been achieved by supporting them on carbon nanotubes, resulting in highly HER active electrocatalysts [86–88]. The need for nanoparticle downsizing and dispersion has been recurrently brought up in the literature [71, 89]: inasmuch as only surface atoms are active sites, the majority of the noble metal loaded on the nanoparticle is inactive. In this regard, single-atom catalysts (SAC) consist of one-atom clusters supported on solid substrates, constituting a clear example of noble metal downsizing to achieve maximum efficiency [62]. Atomic layer deposition has been employed in the fabrication of a N-doped, graphene-supported platinum SAC that greatly surpasses the activity of nanoparticle-based Pt electrocatalysts (by a factor of 37) while also exhibiting high stability [89]. Although not all substrates provide the necessary electrolytic conditions or enable adequate SAC-electrode charge transfer, doped graphene has found widespread use [80, 89].

Chemical insight. Mechanistically, the hydrogen evolution reaction in acidic conditions involves a surface-mediated, two-electron transfer with one intermediate species plausibly taking place through the two potential pathways shown in Scheme 1.4 [1, 90].

In acidic media, the initial hydrogen adsorption (Volmer step) takes place on an available surface site involving a fast two-electron transfer from the electrode to a solvated proton; in basic media, the Volmer step corresponds to HO-H dissociation reaction [77], also involving a two-electron transfer from the surface. It is followed by the evolution of H_2 either through the Heyrovski or the Tafel desorption steps [1]. In the acidic Heyrovski step, the adsorbed hydrogen binds to another solvated



Scheme 1.4. *Hydrogen evolution reaction mechanisms in acidic and alkaline media, as proposed in [1].*

proton, thus being released from the surface as H_2 . Conversely, in the alkaline Heyrovski step the adsorbed H^* reacts with a neutral water molecule, producing OH^- and H_2 . Meanwhile, the Tafel step involves an electron transfer between adsorbed hydrogen atoms, resulting in the evolution of H_2 . Preference for either step appears to be mostly condition and material-dependent, even varying across different facets of the same metal [75, 91]. In the case of Pt, experimental and computational evidence suggest the Tafel step is rate-determining on Pt(110), while the Heyrovski step is rate-determining on Pt(100) and polycrystalline Pt. It is unclear which step is favoured on the ubiquitous Pt(111) surface⁷.

1.3.2 *In silico* water splitting electrocatalysis.

As an intuitive application of the Sabatier principle, Norskov and coworkers have proposed that the kinetics of the HER are largely controlled by the hydrogen adsorption free energy [63]. If hydrogen binds too weakly to the surface, the positive entropic term dominates and the reaction becomes endergonic (the Volmer step becomes rate-determining). Conversely, if the binding is exceedingly strong, H_2 evolution is hindered and either desorption mechanism (Heyrovski/Tafel steps) is rate-determining. Norskov [63] has proposed the use of ΔG_H as a descriptor for HER activity, so that catalysts for which $\Delta G_H \approx 0$ should provide the highest activities. This much is true for Pt, as

⁷In any case, its HER activation energy is known to be roughly 0.2 eV [75]

shown by its privileged position on the volcano plot in Figure 1.5 with respect to other transition metals.

Models. Although the nature of the catalyst influences the choice between continuous or cluster models (for heterogeneous and homogeneous catalysts, respectively), in both instances the best model ultimately depends on the finer details of the water-catalyst interface, extended defects or the morphology. In heterogeneous catalysis, surface slab models are a natural choice for extended catalyst surfaces, but are also commonly used to reproduce specific facets of nanoparticles. Doing so can significantly decrease the computational cost of the simulation, albeit forgoing the edges of the facets or introducing width-dependent effects absent in the more realistic nanoparticle models. Models striving for realism should also factor in the effect of surface coverage at the catalyst-water interface. While nanoparticles and large surface slabs have many metal binding sites, full monolayer coverage is seldom considered, with many contributions only dealing with single-molecule adsorption on small surface unit cells. On a general note, inclusion of explicit water solvation or non-coordinated hydrogen atoms as an electrical double layer provides a more realistic description of the system [75].

Method. Density functional theory is the *de facto* level of theory for *in silico* water electrolysis. Theoretical calculations have been carried out either with periodic [1, 48, 74, 92] or non-periodic algorithms [67]. The PBE functional has found widespread use in heterogeneous electrocatalysis, being employed mainly for ligand adsorption energies and density of states determination [1, 48, 74, 92, 93]. Plane-wave algorithms are the straightforward choice for extended surfaces, whereas the molecular orbital-based approach is more common for cluster-like catalysts (see Chapter 2 for a detailed discussion on Computational Chemistry methods). Either strategy can be employed to calculate adsorption energies and to probe the electronic structure, be it through density of state analysis (for plane-wave calculations) or from its molecular orbitals (orbital-based calculations) [67]. The hydrogen adsorption energy (E_H) has been widely used as a material screening descriptor in solid-state HER catalysis based on theoretical and experimental results by Norskov and coworkers [63]. In practice, hydrogen adsorption energies change depending on the binding site considered (*e.g.* octahedral, tetrahedral or top) and the presence/absence of other adsorbed hydrogen atoms. To this end, Calle-Vallejo and coworkers [94] have devised a complementary screening method, the generalized coordination numbers. These screening methods are discussed in greater detail in

Chapter 5. As mentioned above, single-atom adsorptions are frequently used to infer the catalyst's HER activity.

State of the art. Extensive research involving pristine and defective Pt and Ru surface slabs has been carried out using DFT and periodic models [64, 65, 78, 95] as well as nanoparticle models [96]. Single-Pt clusters models developed by Cai and Anderson were used to assess the strength of Pt-H bonds [91]. The Volmer and Heyrovski steps were also studied using periodic calculations with SAC models (M= Co, Ni, Fe, Pd, Re, Mo, Ti, W, Ta) supported on N-doped graphene [80]. While experimental measurements can provide support to proposed mechanisms, unknown elementary steps may remain concealed if only global reaction rates are considered [75, 91]. In this regard, an in-depth understanding of surface chemistry and atomic-scale properties through computational simulations is crucial to the characterization of HER electrocatalysts [48, 74, 75, 97]. Owing to its status as the "golden standard", a fair share of computational reports are centered on heterogeneous platinum facets Pt(111) [78] or Pt(110) [75]. Fewer examples are reported for Ru, although its high HER activity has more recently been recognized.

Advancing research. Theoretical calculations are expected to provide complementary insight to the newly synthesized HER electrocatalysts, using the different computational screening descriptors.

1.4 Research objectives.

Computational Chemistry provides valuable atomistic insight into the structural, chemical and photonic-electronic properties of hybrid nanomaterials. The general objectives of this Thesis consist on the characterization of core-only and core-shell, metal chalcogenide semiconductor nanoparticles for imaging applications, and of metal and metal-metal oxide hybrid surfaces for the hydrogen evolution reaction. *In silico* water electrolysis is a well-established active research topic in the BioNanoCat research group [48, 74, 92], with quantum dot modelization being a more recent undertaking [47].

The present research objectives are promptly detailed:

- Structural and electronic characterization of core-only and core-shell quantum dots.
 - Ligand, thermal and solvent effects on pristine CdSe surfaces and core-only (CdSe)₃₃.
 - Size and ligand effects in (MX)_n core-only quantum dots, where MX=CdSe, CdS, ZnSe, ZnS and $n = 6, 33, 60, 68, 105, 133$.
 - Case study of passivation and solvent effects in core-shell (CdSe)₆@(MX)₂₇ quantum dots, where MX= CdS, ZnSe, ZnS.
- Computational screening of heterogeneous electrocatalysts for the hydrogen evolution reaction.
 - Pristine and defective Pt(111) and Ru(100) surfaces for hydrogen evolution.
 - Surface amorphization and charge transfer in RuO₂@Ru core-shell surfaces.

Theoretical background

Computational Chemistry is firmly built on the grounds of Quantum Mechanics, thus it is adequate to dedicate the present Chapter to a comprehensive overview of its foundations and derived methods. Details on the computational methods employed herein focus most of the discussion. The present heuristic approach to Quantum Mechanics better suits the Thesis’s scope, while more rigorous accounts on Computational Chemistry methods can be found here [98] and [99].

2.1 Fundamentals of Computational Chemistry.

In Dirac’s notation, the symbol $|\Phi\rangle$ represents an entire physical quantum state; this mathematical entity, known as “ket”, corresponds to N-dimensional vector of an N-dimensional Hilbert complex vector space. Each Hilbert space has a corresponding dual space, in which the dual vector of $|\Phi\rangle$ is $\langle\Phi|$, the ”bra”, which is also its conjugate transpose, $\langle\Phi| = |\Phi\rangle^*$. The inner product or overlap between any ket-bra pair is conventionally defined as followed:

$$\langle\Psi_j|\Psi_i\rangle = \int_{\Omega} |\Psi_j\rangle^* |\Psi_i\rangle d\tau = \delta_{ij} \quad (2.1)$$

Where δ_{ij} is Dirac’s delta. There exists a bijective correspondence between the ket and the quantum state it represents, and as such, the former contains the system’s complete information. Physical information may be obtained using operators; more specifically, certain physical magnitudes or observables have a corresponding linear self-adjoint operator which can be diagonalized.

Let \hat{O} be an arbitrary operator such that:

$$\hat{O} |\Psi_i\rangle = \lambda_i |\Psi_i\rangle \quad (2.2)$$

Where $|\Psi_i\rangle$ is an eigenvector, and λ_i is the corresponding eigenvalue. Such operators are known as “Hermitian”: by virtue of the spectral theorem, they are always diagonalizable and all their eigenvalues are real numbers. The complete set of an operator’s eigenvalues, which depends on the physics of the problem under consideration, constitutes its spectrum. Being diagonalizable, it is always possible to obtain a corresponding set of eigenvectors¹ for the operator, $\{|\Psi_i\rangle\}$, which in turn constitutes a complete, orthonormal basis of the Hilbert space. That is, any other state $|\Phi_i\rangle$ may be written as a linear combination of $\{|\Psi_i\rangle\}$. Whether a given state $|\Psi\rangle$ is an eigenstate of operator \hat{O} or not, its expectation value for that operator is defined as follows:

$$\langle \hat{O} \rangle_{|\Psi\rangle} = \langle \Psi | \hat{O} | \Psi \rangle = \int_{\Omega} |\Psi\rangle^* \hat{O} |\Psi\rangle d\tau = \lambda_i \in \mathbb{R} \quad (2.3)$$

Chief among quantum operators is the total energy operator or Hamiltonian, \hat{H} , which is such that:

$$\hat{H} |\Psi_i\rangle = E_i |\Psi_i\rangle \quad (2.4)$$

Where E_i is the energy of state $|\Psi_i\rangle$. In physical terms, the eigenstates of the Hamiltonian correspond to the allowed energy state of the system. As discussed above, any quantum state $|\Phi_i\rangle$ may be written in the basis of eigenstates of the Hamiltonian, provided the appropriate normalization constant is introduced:

$$|\Phi\rangle = N(c_1 |\Psi_1\rangle + \dots + c_n |\Psi_n\rangle) \quad (2.5)$$

Where the coefficients $c_i \in [0, 1]$ weigh the contribution of the i -th eigenstate to the linear combination of $|\Phi\rangle$, and N is the so-called normalization constant. Unless $|\Phi_i\rangle$ is an eigenstate itself, the Hamiltonian’s expectation value is not so readily apparent:

¹Interchangeably, eigenstate.

$$E_{|\Phi\rangle} = \langle \Phi | \hat{H} | \Phi \rangle = N^2 (c_1 \langle \Psi_1 | + \dots + c_n \langle \Psi_n |) \hat{H} (c_1 | \Psi_1 \rangle + \dots + c_n | \Psi_n \rangle) \quad (2.6)$$

Owing to the orthonormalization condition, the only non-zero terms are $\langle \Psi_i | \hat{H} | \Psi_i \rangle = E_i$, so that the system's total energy is:

$$E_{|\Phi\rangle} = N^2 (c_1^2 E_1 + \dots + c_n^2 E_n) \quad (2.7)$$

While determining the allowed energy levels of a quantum system is useful in and of itself, the Hamiltonian operator is also instrumental to describing the system's dynamics by virtue of the Schrödinger equation.

2.1.1 The Schrödinger equation: formalism and approximations.

Mathematical expressions for the Hamiltonian operator must account for any physical and chemical factors contributing to the system's energy, some of which may also be time dependent. The time evolution of a given quantum state $|\Phi(t)\rangle$ is governed by the time-dependent Schrödinger equation:

$$i\hbar \frac{d}{dt} |\Phi(t)\rangle = \hat{H} |\Phi(t)\rangle \quad (2.8)$$

Relativistic corrections may be included (Dirac's equation) to account for experimentally known phenomena which do not arise naturally from the non-relativistic Schrödinger equation (e.g. electron spin, spin-orbit coupling or the lanthanide contraction). Time-dependence and relativistic effects certainly provide more accurate descriptions of quantum systems, albeit at an increased mathematical complexity. When studying already complex systems, a precise description of relativistic effects may be neglected or simplified for time and resource economy's sake. For example, electron spin may be added *ad hoc* to the non-relativistic formalism. Similarly, time dependence may be forgone by focusing instead on its non-relativistic stationary solutions if the system is not expected to undergo any time-dependent perturbations. Stationary states are solutions to the corresponding time-independent Schrödinger equation,

$$\hat{H} |\Psi_i\rangle = E_i |\Psi_i\rangle \quad (2.9)$$

Where state $|\Psi_i\rangle$ is the i -th eigenvector of the Hamiltonian operator, and E_i is the energy of the i -th state. Further discussion of the time-dependent formalism is deferred to Section 2.2.3.

The physical and chemical characteristics of a quantum system determine the expression of the non-relativistic, time-independent Hamiltonian operator. Both for its simplicity and physical relevance, the hydrogen atom is employed as a starting model for more complex systems. It should include all the contributions to the system's total energy, thus:

$$\hat{H} = \hat{T}_e + \hat{T}_n + \hat{V}_{ne} \quad (2.10)$$

Where \hat{T}_e and \hat{T}_n are the kinetic energy operators of the electron (e) and the nucleus (n), and \hat{V}_{ne} is the electron-nucleus potential energy operator. The corresponding reduced (unitless) Hamiltonian may be explicitly written as follows:

$$\hat{H} = -\frac{1}{2}\nabla_e^2 - \frac{1}{2}\nabla_n^2 - \frac{1}{r_e - r_n} \quad (2.11)$$

The kinetic energy operators result in readily solvable one-electron integrals, while the potential energy operator implies a two-particle integral which can be solved analytically. The Hamiltonian may be further simplified by working with the proton-electron center of mass and the corresponding reduced mass. In any case, diagonalization of the non-relativistic, hydrogen atom Hamiltonian results in a complete basis set of eigenstates (atomic orbitals) fully characterized by three different, interdependent quantum numbers (n, l, m_l) . Each set of valid quantum numbers describes an atomic orbital with quantized energy (only determined by n , hence degenerate), angular momentum (determined by l) and the z component of the angular momenta (determined by l and m_l). The electron, which may occupy any atomic orbital provided it has the allowed energy, is additionally described by its spin state. As a fermion with $S = \frac{1}{2}$, the electron is characterized by a two-valued spin quantum number, $m_S = \pm\frac{1}{2}$, which is introduced *ad hoc*.

In polyelectronic atoms and molecules, the Hamiltonian operator must account for a many-body interactions, for which no analytical solutions are available. Certain effects (e.g. relativistic effects, energy-level splitting) that could be safely ignored in the one-electron hydrogen atom become relevant, more so in heavy atoms. In order to solve the time-independent Schrödinger equation in many-body systems, it is necessary to simplify the Hamiltonian using a different approximations.

The most commonly applied procedures include, but are not limited to, the already-mentioned non-relativistic formalism, the Born-Oppenheimer approximation, and the use of one electron spin-orbitals in Slater determinants. While these approximations limit the accuracy of the solutions, the variational theorem provides a systematic means to iteratively improve their accuracy within the limits of the approximations used.

2.1.2 The Born-Oppenheimer approximation.

In polyelectronic atoms, as well as in molecules, each electron is interacting with at least two other particles. Inasmuch as only chemical reactions are being considered, the nucleus, regardless of how many nucleons are present, may be approximated as a point charge and treated as a rigid body. For the specific case of molecules,

$$\hat{H} = \hat{T}_e + \hat{T}_n + \hat{V}_{ee} + \hat{V}_{en} + \hat{V}_{nn} \quad (2.12)$$

Where the kinetic energy operators account for all the present electrons (\hat{T}_e) and nuclei (\hat{T}_n), and the potential energy operators account for all pair-wise interactions: electron-electron (\hat{V}_{ee}), electron-nucleus (\hat{V}_{en}) and nucleus-nucleus (\hat{V}_{nn}). In reduced units, the many-body Hamiltonian may be written in terms of positions vectors:

$$\hat{H} = - \sum_i \frac{1}{2} \nabla_i^2 - \sum_k \frac{1}{2} \nabla_k^2 - \sum_i \sum_k \frac{1}{r_{ik}} + \sum_{i < j} \frac{1}{r_{ij}} + \sum_{k < l} \frac{Z_k Z_l}{r_{kl}} \quad (2.13)$$

Where indices i and j run over the electrons, and k and l run over the nuclei. The nuclear mass is significantly larger than that of any number of electrons the atom may have, since $m_p \approx 1000m_e$. The Born-Oppenheimer approximation suggests that the electronic and nucleic dynamics can be decoupled, so that the previous Hamiltonian may be written as the sum of an electronic Hamiltonian (\hat{H}_e) and a nuclear Hamiltonian (\hat{H}_n). Furthermore, it is proposed the nuclear motion is slow enough for the electrons to perceive the nuclei as quasi-static positive charges i.e. as if the nuclei were at fixed positions. The electronic and nuclear Hamiltonians are thus:

$$\hat{H}_e = - \sum_i \frac{1}{2} \nabla_i^2 + \sum_{i < j} \frac{1}{r_{ij}} - \sum_i \frac{1}{R_{ik}} \quad \hat{H}_n = - \sum_i \frac{1}{2} \nabla_k^2 + \hat{V}_{nn} \quad (2.14)$$

Where R_{ik} runs over all electrons for fixed nuclei. As per the linearity of the Hamiltonian operator, the Schrödinger equation may be rewritten as follows:

$$(\hat{H}_n + \hat{H}_e) |\Psi\rangle = \hat{H}_n |\Psi\rangle + \hat{H}_e |\Psi\rangle = (E_n + E_{el}) |\Psi\rangle \quad (2.15)$$

The total quantum state $|\Psi\rangle$ can be written as the product of a nuclear state and an electronic state:

$$|\Psi\rangle = |\Psi_n\rangle |\Psi_e\rangle \quad (2.16)$$

Combining this product with equation 2.15, it is clear that allowed nuclear and electronic states are therefore the eigenvectors of the nuclear and electronic Hamiltonians, respectively. Once decoupled, the dynamics of the electrons may be treated almost-separately from those of the nuclei. Modern electronic structure methods employ the Born-Oppenheimer approximation to, firstly, solve the electronic Schrödinger equation for different sets of fixed nuclear coordinates.

$$(\hat{H}_e + V(R)) |\Psi_e\rangle (r; R_n) = E_{el} |\Psi_e\rangle (r; R_n) \quad (2.17)$$

Where $V(R)$ is the nuclear-nuclear repulsion energy, which is a constant for each nuclear configuration. By repeating the process for all possible nuclear positions, a potential energy surface is generated (see Section 2.3 for an in-depth discussion), which allows for the nuclear Schrödinger equation to be solved:

$$(\hat{T}_n + E_{el}) |\Psi_n\rangle (R) = E |\Psi_n\rangle (R) \quad (2.18)$$

Where the total system energy E now includes the kinetic energy of the nuclei. The importance of the Born-Oppenheimer approximation cannot be understated. Not only is it a very mild, almost-always justified approximation, but it is also the standpoint for the potential energy surface and useful derived notions, such as those of equilibrium and transition state geometries.

2.1.3 The variation principle.

Succinctly, the variational principle provides an upper bound to the expectation value of the Hamiltonian when its eigenstates are unknown. Let $|\Psi_0\rangle$ be the ground state eigenvector of the Hamiltonian \hat{H} whose expectation value is the true ground state energy E_0 . Let $|\Psi_\lambda\rangle$ be a different eigenvector, a trial function, with one or more variable parameters, and expectation value E_λ . The variational principle states that:

$$E_0 = \langle \Psi_0 | \hat{H} | \Psi_0 \rangle \leq E_\lambda = \langle \Psi_\lambda | \hat{H} | \Psi_\lambda \rangle \quad (2.19)$$

That is, the Hamiltonian expectation value for the trial state is an upper-bound to the expectation value of the real Hamiltonian ground state eigenvector. By introducing adjustable parameters in the trial state, iteratively better trial states may be found through energy minimization; it should be noted that absolute convergence of the successive trial eigenvectors to the real one is not guaranteed. The variational principle is essential in *ab initio* computational methods, that is, those that require an iterative approach to solving the Schrödinger equation.

2.1.4 Spin-orbitals and basis sets.

As an *ansatz*, let each electron in the polyelectronic system be described by one-electron wave functions analogous to those of the electron in the hydrogen atom, that is, consisting of a product of a spatial function, $|\phi\rangle$, and a two-valued spin function, $|\alpha\rangle$ or $|\beta\rangle$. The resulting state is referred to as spin-orbital:

$$|\chi\rangle = |\psi\rangle |\alpha\rangle \quad |\chi\rangle = |\psi\rangle |\beta\rangle \quad (2.20)$$

The fact that a system of N electrons must have N spin-orbitals warrants further explanation. Firstly, since electrons are indistinguishable particles, all spin-orbitals must be allowed to describe any electron. Moreover, on the grounds of the antisymmetry principle, the total state of the electrons (fermions) cannot be a mere direct product of the spin-orbitals: the total wave function must be anti-symmetric with respect to the exchange of any two electrons. As a corollary to the antisymmetry principle, the Pauli exclusion principle postulates that two electrons sharing the same spatial function necessarily have antisymmetric spin states.

Mathematically, these conditions are fulfilled when the spin-orbitals are arranged in a Slater determinant:

$$|\Psi\rangle = \frac{1}{\sqrt{N!}} \begin{vmatrix} |\chi_1(1)\rangle & \dots & |\chi_N(1)\rangle \\ \vdots & \ddots & \vdots \\ |\chi_1(N)\rangle & \dots & |\chi_N(N)\rangle \end{vmatrix}$$

Which is also duly normalized. For Slater determinants to be useful, an actual expression for the spatial factor of the spin-orbitals is required. As suggested by the previous *ansatz*, linear combinations of hydrogenoid atomic orbitals are an adequate initial guess. Historically, the resulting linear combinations of atomic orbitals (LCAO) are referred to as molecular orbitals (MO), constituting the so-called LCAO-MO approach. Provided the complete Hamiltonian is known, the Slater determinant of spin-orbitals built in the LCAO-MO approach can be systematically improved using the variational principle. In practice, the LCAO-MO approach is computationally costly if the actual hydrogenoid eigenstates are used, so linear combinations of Gaussian-type functions are used instead.

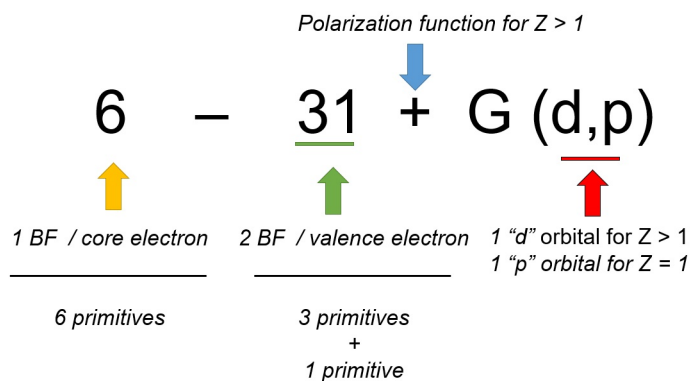
A given collection of functions (Gaussian or otherwise) employed to generate the LCAO-MO is known as a "basis set". Different basis sets assign a specific number of parameterized basis functions to the electrons. Expressing each molecular orbital as an infinite series of basis functions would provide their most exact description at a given level of theory. Such an infinite series, known as a complete basis set, is commonly out of practical reach. Therefore, finite basis sets must be employed instead, with their degree of completeness and actual mathematical structure largely determining simulation accuracy.

In broad terms, current electronic structure methods employ one of two possible approaches: the already-discussed atom-localized spin-orbitals, and plane waves (Section 2.5.3). The former approach describes molecular orbitals as finite basis functions, which in turn are linear combinations of Gaussian functions known as "primitives":

$$p(r, \theta, \phi) \propto Y_{(l,m)}(\theta, \phi) r^{(2n-2-l)} e^{-\zeta r^2} \quad (2.21)$$

Their straightforward computational integration and their atomistic accuracy makes these func-

tions a natural choice for, but not restricted to, molecular systems. A wide range of basis sets have been developed, ranging from the well-known Pople basis (Scheme 2.1) to the more recent Karlsruhe-type and correlation-consistent basis sets, which allow for high level of theory calculations at lower computational costs.



Scheme 2.1. Schematic description of the 6-31+G (d, p) Pople basis set (BF: basis functions).

Different approaches to improving the precision-to-cost ratio have been developed. Split-valence basis sets account for the higher chemical relevance of valence electrons with respect to the more chemically inert core electrons, by assigning the former more than one basis function. For instance, valence double- ζ basis sets assign two basis functions to valence electrons, each comprised of a specific number of Gaussian functions; valence triple- ζ basis sets employ three basis functions, and so on. Furthermore, the often inadequate description of the orbitals' characteristics provided by Gaussian functions can be improved by rigging basis functions with polarization (better bond description) and diffusion functions (better description of regions far from the nuclei). In the example shown in Scheme 2.1, corresponding to one of the Pople basis sets hereby used, the above-discussed characteristics are duly noted. Similar notation conventions are followed for the Karlsruhe basis sets, which have also been used in our research. For example, def2-TZVPD corresponds to the Karlsruhe split-valence, triple- ζ with polarization and diffusion functions basis set.

Split-valence basis sets are conceptually linked to the frozen core approximation, in which core electrons are considered to be mostly chemically inert. Their explicit inclusion in simulations may be replaced by a pseudopotential, a potential field parametrized through large set of coefficients generated from high level of theory calculations (and, oftentimes, semi-empirical corrections) which include significant chemical and physical properties which do impact the valence electrons.

Pseudopotentials are often used in conjunction with basis sets as well as with plane waves. In doing so, the computational cost of the simulations is greatly reduced, particularly in those involving second and third row transition metals, as the ones used in this Thesis. Plane wave-based algorithms, which are extensively used in this work, are discussed at length further below.

2.1.5 The Hartree-Fock method.

The iterative resolution of the electronic Schrödinger equation with one single Slater determinant is known as the Hartree-Fock method. As an alternative to the non-solvable two-electron integrals, the Hartree-Fock method develops into a pseudo-eigenvalue problem concerning the interaction of each individual electron with the mean, self-consistent field generated by the other electrons. Conveniently, Slater determinants naturally include the electrons' tendency to avoid electrons in their same spin-state and its effect on the system's total energy (Fock exchange). Conversely, as electrons are considered not to interact with each other directly, the Hartree-Fock method does not account for the favorable interaction between antiparallel spin electrons. Even if an infinite basis set were used (E_{limit}^{HF}), a certain fraction of the system's real energy (E_{real}) would not be accounted for by the Hartree-Fock method. This correlation energy (E_{corr}) is conventionally defined as follows:

$$E_{corr} = E_{real} - E_{limit}^{HF} \quad (2.22)$$

As tiny a fraction as it may be, the correlation energy is crucial to all but the most basic of chemical simulations, and thus more advanced methods strive to accurately calculate it. The Hartree-Fock method will not be described further, as it has not found any direct use in this Thesis. Broadly speaking, two types of methods stem from the original Hartree-Fock formalism: wave function-based methods and electron density methods. The former, often referred to as post-Hartree-Fock methods, attempt to recover the correlation energy by expanding the wavefunction into more than one Slater determinant in order to include excited electronic configurations. Examples of post-Hartree-Fock methods include configuration interaction, Möller-Plesset or coupled-cluster; no post-Hartree-Fock methods have been employed in the present Thesis.

The methods which have been used are instead based on electron density descriptions, more specifically, on the Density Functional Theory.

2.2 Density functional theory.

Accounting for electron correlation is as important as it is complex. Density functional theory is an alternative to post-Hartree-Fock methods in which the 3N-coordinate wave function description is dropped in favor of a three-dimensional electronic density distribution in space. Intuitively, the electron density function must account for the N electrons responsible. Electron density ($\rho(\vec{r})$) is thus defined as:

$$\rho(\vec{r}) = N \cdot \int \Psi(r_1, \dots, r_N) \Psi^*(r_1, \dots, r_N) d\sigma_1 \dots d\sigma_N dr_1 \dots dr_N \quad (2.23)$$

Where the wave function is integrated across all the electrons' positions (r_i) and spin states (σ_i). Furthermore, ρ must be differentiable at any point in $\mathbb{R}^{\#}$, so that a continuous potential energy function can be described. Having defined the electronic density of an N-electron system, we now examine the theoretical foundations of DFT.

2.2.1 Fundamentals of density functional theory.

Density functional theory is built on the two Hohenberg-Kohn theorems. Let ρ be a valid ground-state electron density generated by a system of N electrons.

Theorem 1 (1st Hohenberg-Kohn theorem) *There exists an exact, unique functional relation between the expectation value of any observable and the ground-state of a non-degenerate system.*

Theorem 2 (2nd Hohenberg-Kohn theorem) *Any given trial electron density expression may be variationally optimized towards the real electron density, provided the exact energy functional $E[\rho]$ is known.*

The first Hohenberg-Kohn theorem is one of existence, while the second theorem is only truly constructive if the energy functional is known. For now, let $E^{HK}[\rho]$ represent the exact Hohenberg-Kohn energy functional. By virtue of variational principle underlying the second Hohenberg-Kohn theorem,

$$E^{HK}[\rho_{real}] = E_0 \leq E^{HK}[\rho_{trial}] \quad (2.24)$$

That is, provided the exact energy functional is known, the exact ground state energy E_0 may be calculated by variationally minimizing the energy of a trial electronic density. Our immediate concern is finding an expression for the energy functional. Energy minimization over all wave functions that integrate to the desired electron density results in the following expression:

$$\min_{\Psi \rightarrow \rho} \langle \Psi | \hat{H} | \Psi \rangle = \min_{\Psi \rightarrow \rho} \langle \Psi | \hat{T} + \hat{V}_{ee} | \Psi \rangle + \min_{\Psi \rightarrow \rho} \int V_{ext}(\vec{r}) \rho(\vec{r}) d^3r \quad (2.25)$$

Where $V_{ext}(\vec{r})$ is the external Coulomb interaction between the electrons and the nuclei, as previously defined. The first term in the equation above is now redefined as the universal density functional:

$$F[\rho] = \min_{\Psi \rightarrow \rho} \langle \Psi | \hat{T} + \hat{V}_{ee} | \Psi \rangle \quad (2.26)$$

The exact expression of universal energy functional remains unknown, but many approximate functionals have been proposed. A general *ansatz* for the electronic energy functional is the following:

$$E[\rho] = T_e[\rho] + V_{ee}[\rho] + V_{ne}[\rho] \quad (2.27)$$

While potential energy density functionals are known, no expression is known for the electron kinetic energy functional. Consequently, in Kohn-Sham theory, molecular orbitals are reintroduced to recover Slater determinants of spin-orbitals, for which a functional relation to electron kinetic energy is known, $T_S[\rho]$. The real N-electron system may be conceptually replaced by a N-electron system of non-interacting particles if and only if the occupied spin-orbitals (now referred to as Kohn-Sham orbitals) reproduce the real electron density:

$$\rho = \sum_{i=1}^{occ} |\chi_i|^2 \quad (2.28)$$

Trivially, the energy functional above can be written as follows:

$$E[\rho] = T_e[\rho] + T_S[\rho] - T_S[\rho] + J[\rho] - J[\rho] + V_{ee}[\rho] + V_{ne}[\rho] \quad (2.29)$$

Where $J[\rho]$ is the Coulomb electron-electron energy functional, also present in the Hartree-Fock method. Several terms above may be conveniently gathered in the so-called exchange-correlation functional:

$$E_{xc}[\rho] = T_e[\rho] - T_S[\rho] - J[\rho] + V_{ee}[\rho] \quad (2.30)$$

Which contains the differences between the real and non-interacting kinetic energy and potential energy functionals. The resulting energy functional is:

$$E[\rho] = T_S[\rho] + J[\rho] + V_{ne}[\rho] + E_{xc}[\rho] \quad (2.31)$$

Where expressions for all the terms are known except for the exchange-correlation functional, which requires modelling and, loosely speaking, characterizes each DFT method.

In any case, trial Kohn-Sham orbitals are refined by iteratively solving the one-electron Kohn-Sham equations:

$$\hat{h}_{ks} |\chi_i\rangle = \epsilon_i |\chi_i\rangle \quad (2.32)$$

Where the Kohn-Sham Hamiltonian, \hat{h}_{ks} , is written as follows:

$$\hat{h}_{ks} = -\frac{1}{2}\nabla^2 - \sum_i^N \frac{Z}{r_{1i}} + \int \frac{\rho(r_j)}{r_{ij}} d^3r_j + V_{xc} \quad (2.33)$$

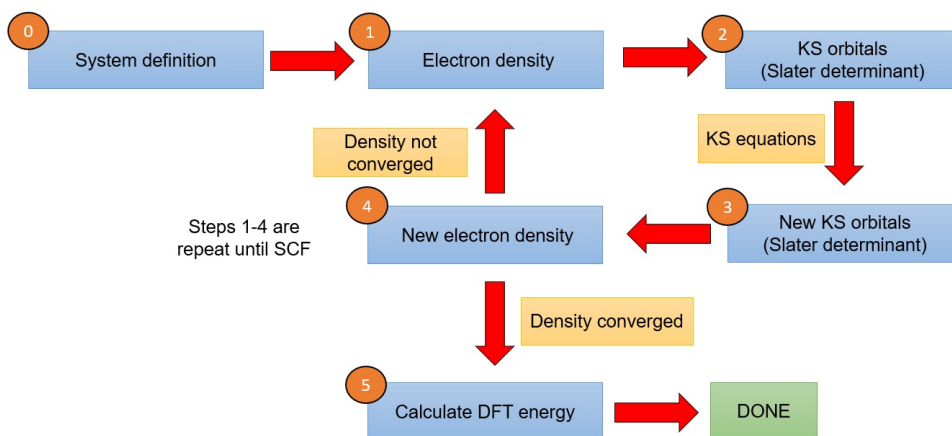
Significantly, whichever its exact expression may be (see Section 2.2.2), the exchange-correlation potential V_{xc} corresponds to the interaction between a given electron and the total electron density, so that:

$$V_{xc}(r) = \frac{\delta E_{xc}[\rho]}{\delta \rho(r)} \quad (2.34)$$

If the system under consideration is suspected to have non-zero magnetic moment (*i.e.* open shell systems), the Kohn-Sham equations must be modified to accommodate for the presence of unpaired electrons. If the total electronic density is taken to be the sum of each spin state, $\rho =$

$\rho_{up} + \rho_{down}$, then only the exchange-correlation potential explicitly depends on the spin-state. The Kohn-Sham equations must be solved twice in spin-polarized systems, which results in a two-fold increase in computational time. The extent of spin-polarization in a system is assessed by means of the magnetization density ($\mu(r)$) descriptor, which is simply $\mu(r) = \rho_{up}(r) - \rho_{down}(r)$.

A flow diagram for the generally involved steps in DFT simulations is shown in Scheme 2.2:

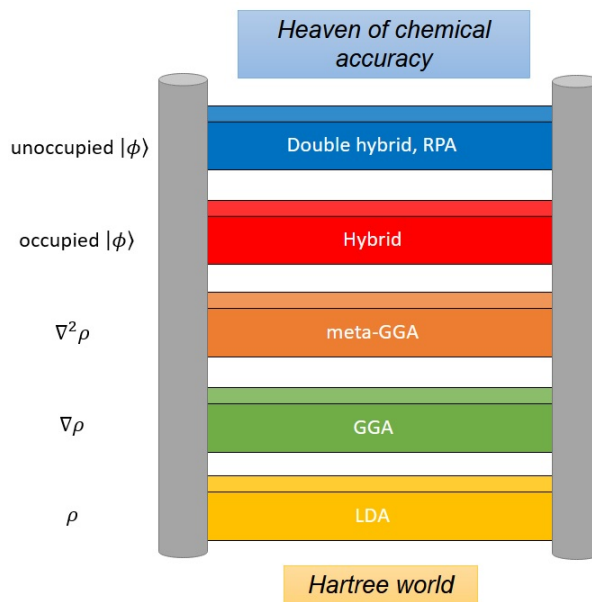


Scheme 2.2. Flow diagram of density functional theory calculations.

That is, a system-specific electronic density is used to generate a Slater determinant of density-consistent Kohn-Sham orbitals. By solving Equation 2.32, a new Slater determinant is obtained, from which another electron density profile is derived. Additional iterations are ran until a user-defined convergence criterion is met, at which point the Kohn-Sham orbitals and the electron density are said to be self-consistent.

2.2.2 Exchange-correlation functionals. Semi-empirical corrections.

There is no unique approach to improving the accuracy of the exchange-correlation functional, so benchmarking requires either experimental data or post-Hartree-Fock results. In designing a functional, the physical characteristics of electron density are necessarily considered. In broad terms, exchange-correlation functionals are characterized by their account of the electron density and its derivatives. Herein $\rho = \rho_{up} + \rho_{down}$ is the total electron density and $\nabla^2 \rho$ is trivially connected to the kinetic energy of the occupied, non-local Kohn-Sham orbitals. As proposed by Perdew and Schmidt, increasingly more comprehensive functionals are equated to metaphorical rungs in Jacob's ladder [100], shown in Scheme 2.3.



Scheme 2.3. *Jacob’s ladder of exchange-correlation functionals. Adapted from [100].*

As more rungs are included in the final functional, better descriptions of the exchange-correlation functional are expected. The lowest rung, closest to the “Hartree world”, corresponds to the local spin density approximation (LSDA), in which only the electron density (ρ) is explicitly included. The LSDA methods are adequate for systems with slowly varying electron densities, such as metals, but perform poorly otherwise. The generalized gradient approximation (GGA) method includes the gradient of the electron density ($\nabla\rho$) to the functional, better describing finer changes in the electron density, thus moving one rung upwards. Nevertheless, GGA methods still offer a highly local description of the electron density, which negatively impacts the representation of delocalized phenomena. For instance, dispersion interactions are not accounted for owing to the large distances implied. Likewise, the electron-delocalization induced by exciton formation in semiconductors is ill-described by uncorrected GGA methods, which then systematically underestimate band gap energies. Relevant to this Thesis, the Perdew-Burke-Ernzerhof (PBE) GGA functional has found extensive use in solid-state simulation. Alternatively, meta-GGA functionals go one rung further in Jacob’s ladder by incorporating a kinetic energy operator, which in turn includes the Laplacian of the electron density ($\nabla^2\rho$).

Rigging GGA functionals with energy contributions from Fock exchange integrals, ranging from 20 % to 50 % (based on calibration), reportedly improves simulation accuracy by introducing

non-locality ad hoc. Examples of these so-called hybrid functionals include B3LYP (20 % Fock exchange) and PBE0 (25% Fock exchange). The highest rung corresponds to double hybrid and random-phase approximation methods, which provide superior precision at higher computational costs.

Most DFT functionals provide an inadequate description of van der Waals interactions, as these rely on long-range electron correlation. Dispersion is commonly introduced through the Grimme dispersion formalism (also known as DFT-Dn), a semi-empirical atom pair-wise correction with the following general expression:

$$E_{DFT-D} = E_{DFT} + E_{disp} \quad (2.35)$$

Where E_{disp} is an additive, semi-empirical correction to the as-obtained DFT energy. Due to their accuracy and minimal computational cost, the semi-empirical corrections proposed by Grimme have found widespread use. Grimme's D2 correction general formula is shown below:

$$E_{disp} = S_6 \sum_{i=1}^{N-1} \sum_{j=i+1}^N \frac{C_6^{ij}}{R_6^{ij}} f_{damp}(R_{ij}) \quad (2.36)$$

In a system of N atoms, Grimme's dispersion implies the pairwise averaged isotropic n-th order dispersion coefficient, C_6^{ij} , and the internuclear distance R_6^{ij} ; both are readily available from experimental data and first principles computation. Dispersion coefficients are obtained from *ab initio* atomic ionization potentials (I_P) and static dipole polarizabilities (α):

$$C_6 = \alpha \frac{N \cdot I_P}{20} \quad (2.37)$$

Intuitively, the R^{-6} scaling reliably reproduces long-range attractive dispersion interactions. Conversely, repulsion must be tuned through the functional-dependent a global scaling parameter, S_6 . The damping function, $f_{damp}(R_{ij})$, is also used to avoid spurious short-range behavior of the correction, both by avoiding short R_{ij} singularities and by removing the double-counting occurring at intermediate distance. One such damping function may be written is the following:

$$f_{damp}(R_{ij}) = \frac{1}{1 + \exp\left[\frac{-d \cdot R_{ij}}{(R_{r-1})}\right]} \quad (2.38)$$

Where R_r is the sum of the atoms' van der Waals radii. The actual expression of the damping function is assumed to greatly influence the overall quality of the correction.

Both LSDA and GGA functionals are known to inadequately describe the strong correlation between d and f electrons. The DFT+U method (or Hubbard's correction) element-wise, angular momentum-specific penalty to the total energy expression that enhances on-site occupancy (\hat{n}^σ). In its simplest approach (Dudarev formalism), DFT+U applies the following rotationally invariant, occupancy matrix-dependent ($\alpha(\hat{n}^\sigma)$) correction to total energy:

$$E_{DFT+U} = E_{DFT} + \frac{(U - J)}{2} \cdot \alpha(\hat{n}^\sigma) \quad (2.39)$$

Where the effective on-site Coulomb (U) and exchange (J) parameters are user-defined based on constrained-DFT calculations or through method calibration; under the Dudarev formalism, either value may be set to zero as only their difference is relevant.

2.2.3 Time-dependent Density Functional Theory.

Under an external, time-dependent potential $V_{ext}(\vec{r}, t)$ the electronic density of a system varies with time in response. The Runge-Gross theorem establishes a bijective relation between $V_{ext}(\vec{r}, t)$ and the one-electron density $\rho(\vec{r}, t)$. Time-Dependent Density Functional Theory (TD-DFT) builds on this theorem to calculate the expectation values of the observables of interest. The electron density may be expressed as an $n - th$ order Taylor polynomial around $t = 0$. In linear response theory, the expansion is cut at first order. Note that $\rho(\vec{r}, 0)$ corresponds to the ground state of the electron density corresponding to time independent DFT, $\rho_{GS}(\vec{r})$. We may conveniently write:

$$\rho_1(\vec{r}) = \left. \frac{\delta \rho(\vec{r}, t)}{\delta t} \right|_{t=0} \quad (2.40)$$

In conclusion, the linear approximation to the electron density for $t \rightarrow 0$ is:

$$\rho(\vec{r}, t) \approx \rho_{GS}(\vec{r}) + \rho_1(\vec{r}) \quad (2.41)$$

The excitation energies are calculated using the density-density response function, $\chi(\vec{r}, \vec{r}', \omega)$,

where ω is the frequency of the external perturbation:

$$\chi(\vec{r}, \vec{r}', \omega) = \sum_I \left(\frac{\langle \Psi_0 | \hat{\rho}(\vec{r}) | \Psi_I \rangle \langle \Psi_I | \hat{\rho}(\vec{r}') | \Psi_0 \rangle}{\omega - \Omega_I + i0^+} - \frac{\langle \Psi_0 | \hat{\rho}(\vec{r}) | \Psi_I \rangle \langle \Psi_I | \hat{\rho}(\vec{r}') | \Psi_0 \rangle}{\omega + \Omega_I + i0^+} \right) \quad (2.42)$$

The density operator, $\hat{\rho} = \sum_{i=1}^N (\delta(\hat{r} - \hat{r}'))$, acts upon all the excited states, $|\Psi_I\rangle$, which are then overlapped with the ground-state eigenvector $|\Psi_0\rangle$. The excitation energies coincide with the poles in the response function, ω . Similarly to time independent DFT, $\chi(\vec{r}, \vec{r}', \omega)$ is split to describe a Kohn-Sham system (non-interacting particles) and an electron-correlated one. The latter is described by an exchange-correlation kernel, f_{xc} :

$$f_{xc}[\rho_{GS}(rt, r't')] = \left. \frac{\delta V_{xc}[\rho](\vec{r}, t)}{\delta \rho(\vec{r}', t')} \right|_{\rho=\rho_{GS}} \quad (2.43)$$

Common kernels include adiabatic versions of time-independent DFT functionals: A-LSDA, A-GGA or hybrid functionals such as A-B3LYP. Further development leads to an eigenvalue problem (the Casida equations) regarding single-electron transitions of the ground-state Kohn-Sham system,

$$\begin{bmatrix} [A & B] \\ [B^* & A^*] \end{bmatrix} - \Omega_I \begin{bmatrix} 1 & 0 \\ 0 & -1 \end{bmatrix} \begin{bmatrix} X_I \\ Y_I \end{bmatrix} = \begin{bmatrix} 0 \\ 0 \end{bmatrix}$$

Where the kernel-corrected transitions between the Kohn-Sham orbitals are included in the electron Hessians A and B, X_I and Y_I are the transition vectors, eigenvectors of the Kohn-Sham time-dependent density matrix with eigenvalues Ω_I . Physical meaning may be attributed to the transition vectors if understood as orbitals, and not merely as mathematical entities. TD-DFT scales similarly to configuration interaction singles, yielding better results. Adiabatic performance is similar to standard DFT: A-LDA and A-GGA functionals underestimate vertical singlet excitation energies. Hybrid functionals with intermediate Fock exchange, namely B3LYP and PBE0, provide accurate results and are commonly used with TD-DFT, as they provide good estimates of the transition dipoles.

2.3 Potential energy surface.

By virtue of electron-nuclei kinetic decoupling enforced by the Born-Oppenheimer approximation, the electronic Schrödinger equation is solved at different fixed nuclear positions. For each nuclear configuration of the N atoms in a molecule, that many different electronic energy eigenvalues are obtained, resulting in a $3N-1$ hypersurface when mapped to each other. The potential energy surface (PES) contains all the relevant features of the system's dynamics in terms of its nuclear arrangements, thus providing crucial structural information and chemical reactivity; an arbitrary, elementary PES profile is shown in Figure 2.1.

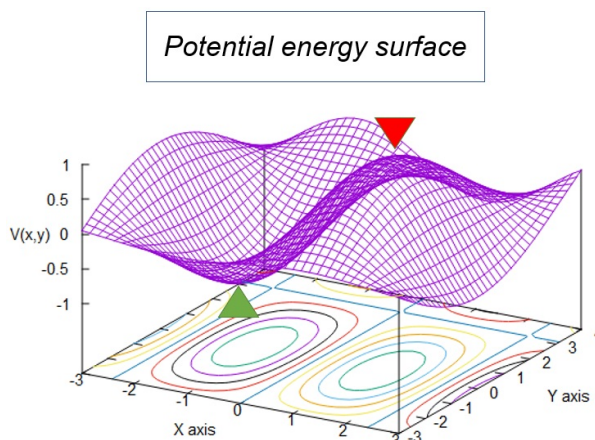


Figure 2.1. *Generic PES with a two-dimensional reaction coordinate. The green triangle marks a minimum and the red one, a transition state (first order saddle point).*

Although an exhaustive PES exploration may be computationally intensive, the most chemically relevant points correspond to its different stationary points, which are more easily evaluated. The exact nature of the stationary points is determined from the eigenvalues of the Hessian, that is, the matrix containing the surface energy second derivatives with respect to the nuclear coordinates. The stationary points on the PES are then characterized by the diagonalization of the Hessian, thus providing a conveniently systematic framework to study the system's dynamics. For a molecule with N atoms, Hessian diagonalization results in $3N-6$ eigenvectors ($3N-5$ for linear molecules) known as normal modes, each corresponding to distinct vibrational modes. Their corresponding eigenvalues or "frequencies" may either be negative (imaginary frequencies) or positive (real frequencies). Stationary points, and in turn nuclear arrangements, may be easily characterized through the sign

of their frequencies. Succinctly, two different stationary points are of interest: minima and first order saddle points. Regarding non-linear molecules, minima on the PES have $3N-6$ positive frequencies. First order saddle points have one imaginary frequency, which mathematically indicates a maximum in the one direction that connects any two relative minima. This first order saddle point geometry is known as “transition state”, and its importance is paramount to the reaction kinetics of the minima it connects. In chemical terms, relative minima correspond to the ground state geometries of molecules (reactants, products or reaction intermediates); as suggested by its “relative” status, a PES may indeed have an absolute minimum, however, its actual determination is complex. In the simplified PES shown in Figure 2.1, two stationary points are easily spotted: a green arrow points at a relative minimum, which could correspond to a minimum energy geometry; meanwhile, a red arrow points at a saddle point, a transition state structure lying between two minimum energy structures.

While thermal effects invariably induce changes in bond lengths and angles, low energy geometries are expected to better represent the average ground state structures of molecules. Minimum energy geometries may be found employing different optimization algorithms, which commonly involve both electronic and ionic relaxation steps. Conceptually, the steepest descent optimization algorithm employs a straightforward approach. In each iteration, the PES gradient is calculated, and the opposite vector (which indicates the steepest descent direction) is used to change the structure. Due to its convergence becoming troublesome near the minimum energy configuration, the conjugate gradient algorithm was developed. In essence, the current gradient and that of the prior step are combined to perform the search; convergence is therefore improved, yet more storage is required. Both methods are built on the Hellman-Feynman theorem, which states that at the minimum energy atomic configuration the forces acting on the atoms become vanishingly small; in practice, varyingly strict computational restrictions are implemented, so that forces below the $0.01-0.05 \text{ eV}/\text{\AA}$ range are considered to be null.

2.4 Thermal effects and thermochemistry.

Quantum mechanics provides atomistic insight into a wide range of physical and chemical processes, but its already complex formalism becomes insurmountable when considering a large number of

molecules. Conversely, thermodynamics target large quantities of particles and thus offer macroscopical insight into the same processes, while also lending themselves to different experimental measurements.

When measured, thermodynamic magnitudes are expected to reflect an average behavior of the particles contained in the system. For instance, some molecules will have higher kinetic energies than others, but the system's measured temperature does not explicitly reflect these differences. Once thermodynamic equilibrium is reached, a time average of the fluctuation on certain microscopic properties (e.g. kinetic energy) of every particle in the system should properly reproduce the observed macroscopic behavior. Yet these time averages should encompass an arbitrarily large time interval for the averages to be significant. While semi-classical computational methods may provide large simulation time intervals, their computational cost may be too high for practical purposes; such is all the more true for the expensive *ab initio* methods. Fortunately, there is an alternative to time averages by virtue of the ergodic hypothesis, which states that infinite-time averages in a system are equivalent to an instantaneous average across an infinite number of copies of the system. That is, thermodynamic properties may be extracted from the microscopical configuration of a system by employing ensembles.

An ensemble, in broad terms, corresponds to an arbitrarily large number of copies of the system of interest in which only certain macroscopic properties are allowed to change. An ensemble is described by a partition function, through which statistical mechanics connects the microscopic (quantum) behavior of particles to their macroscopic properties. Depending on which properties are kept fixed across the images of the system, different types of ensembles are possible. In the so-called canonical or NVT-ensemble, three macroscopical properties are fixed: the number of particles (N) and the system's volume (V) and temperature (T). Other properties, such as total energy (E) or pressure (P) are expected to change from one image to the other. In the canonical ensemble, the partition function is:

$$Q(N, V, T) = \sum_{i=1}^N \exp\left[-\frac{E_i(N, V)}{k_B T}\right] \quad (2.44)$$

The otherwise discrete energy levels of single particles are thus replaced by energy states, with energy E_i , involving all the particles contained in the system. In order to find a suitable expression

for the partition function the ideal gas approximation is frequently assumed, that is, the system is said to behave like an ensemble of non-interacting particles. As such, the total partition function may be written in terms of the energies of the individual particles:

$$Q(N, V, T) = \frac{1}{N!} \sum_{i=1}^N \exp\left[-\frac{(\epsilon_1(V) + \dots + \epsilon_n(V))_i}{k_B T}\right] = \frac{[q(V, T)]^N}{N!} \quad (2.45)$$

Where the $1/N!$ factor derives from the indistinguishable nature of the particles, ϵ_i is the total, individual particle energy and q is the so-called *molecular* partition function. It is then assumed that the molecular energy may be expressed as a sum of translational, electronic, rotational and vibrational terms:

$$\epsilon = \epsilon_{trans} + \epsilon_{trans} + \epsilon_{trans} + \epsilon_{elec} + \epsilon_{rot} + \epsilon_{vib} \quad (2.46)$$

Under this assumption, the molecular partition function is factored as as follows:

$$q(V, T) = q_{trans}(V, T) \cdot q_{rot}(T) \cdot q_{vib}(T) \cdot q_{elec}(T) \quad (2.47)$$

Each partition function in Equation 2.47 must be in turn computed by applying different approximations *e.g.* the energy levels of the particle-in-a-cubic-box are employed for the translational component. Forgoing additional demonstrations, once the partition functional has been computed, there exists a direct relation between the partition function and the system's Helmholtz energy (A):

$$A = -k_B T \cdot \ln(Q) \quad (2.48)$$

Through numerous other thermodynamic relations, additional relations between the partition function and other, more frequently employed state functions may be derived:

$$U = k_B T^2 \cdot \left. \frac{\delta \ln(Q)}{\delta T} \right|_{(N, V)}, \quad S = k_B \cdot \ln(Q) + k_B T \cdot \left. \frac{\delta \ln(Q)}{\delta T} \right|_{(N, V)} \quad (2.49)$$

Most relevant to thermochemistry is the Gibbs free energy, which can also be written in terms

of the partition function using its relation to enthalpy and entropy:

$$U = H + P \cdot V, \quad G = H - T \cdot S \quad (2.50)$$

Electronic calculations are required in two instances. On the one hand, for the electronic energy levels for the vibrational partition function. On the other, vibrational energy can only be calculated if the corresponding Hessian has been diagonalized, that is, if the vibrational frequency for each normal mode is known; it should correspond to the lowest-energy molecular geometry i.e. a minimum on the PES. For even in the absence of thermal energy (absolute zero), there is constant, vibrational zero-point energy (E_{ZPE}) contribution to the system's total energy. For non-linear molecules:

$$E_{ZPE} = \sum_{i=1}^{3N-6} \frac{\hbar \cdot \omega_i}{2} \quad (2.51)$$

Where ω_i is the angular frequency of normal mode i . The zero-point energy must be considered if accurate thermochemical results are desired, as its contribution is significant even at room temperature. The internal energy U_0 of a molecule is the sum of E_{ZPE} and the electronic energy at its minimum-energy stationary point on the potential energy surface.

2.5 Periodic boundary conditions in crystalline systems.

Owing to the sheer number of atoms (or ions) present, first principles modelling of crystalline solids requires the enforcement of unit cell symmetry and periodic boundary conditions. To that end, we first introduce the concept dual space of \mathbb{R}^3 , or reciprocal space, on which discussion on the essential Born-von Karman periodic conditions and the Bloch theorem rest.

2.5.1 Direct and reciprocal space.

Any crystal lattice may be completely described by symmetry-conserving translations (isometries) of its unit cell in \mathbb{R}^3 and the symmetry operations concerning the crystal's motif (i.e. the atomic or ionic arrangement in the unit cell). The unit cell is characterized by three orthogonal vectors $B = \{\vec{a}, \vec{b}, \vec{c}\}$, which form a base B in \mathbb{R}^3 . In this context, the usual Euclidean \mathbb{R}^3 vector space

is known as direct space. The vectors' respective moduli (a,b,c) , and the angles formed (α, β, γ) are collectively referred to as lattice parameters. Depending on their values, a unit cell belongs to one of seven possible crystal systems, which can be broken down to 14 different Bravais lattices. Meanwhile there are 32 crystallographic points groups, each compatible with the 14 Bravais lattices. Therefore 230 crystallographic space groups exist, to which any possible unit cell can be ascribed, up to the values of the lattice parameters. In its connection to group theory, space groups conveniently factor in all the allowed symmetry operations. Any point in the crystal lattice can be described employing a position vector \vec{R} , which out of convenience may be written in the base of lattice vectors as follows:

$$\vec{R} = x \cdot \vec{a} + y \cdot \vec{b} + z \cdot \vec{c} \quad x, y, z \in \mathbb{R} \quad (2.52)$$

Isometries of the unit cell can be generalized with the following translation vector:

$$\vec{T} = u \cdot \vec{a} + v \cdot \vec{b} + w \cdot \vec{c} \quad (2.53)$$

Where $u, v, w \in \mathbb{Z}$ are the coordinates of the translation vector in the base B , and thus serve as a means to translate any point in the unit cell to any other point of the real space lattice.

Let \mathbb{R}^* be the dual space of \mathbb{R}^3 , or reciprocal space. That is, \mathbb{R}^* corresponds to the vector space of linear forms of \mathbb{R}^3 . As a three-dimensional space, any linear form $f \in \mathbb{R}^*$ can be written in a base of three vectors, hereby referred to as the dual base. A convenient and constructive relation between any base in \mathbb{R}^3 and its corresponding dual base in \mathbb{R}^* is deduced from their algebraic structure. Let $\vec{a}_1, \vec{a}_2, \vec{a}_3$ be an orthogonal base of \mathbb{R}^3 , then the vectors of its dual base $\vec{a}_1^*, \vec{a}_2^*, \vec{a}_3^*$ are such that:

$$\vec{a}_i^* \cdot \vec{a}_j = \delta_{ij} \quad (2.54)$$

That is, vector \vec{a}_1^* is parallel to \vec{a}_1^* (with unitary norm) and orthogonal to vectors \vec{a}_2, \vec{a}_3 and so forth. Thus, any vector in the reciprocal space can be written as the cross-product of the other two vectors in direct space. For instance,

$$\vec{a}_1^* = \frac{\vec{a}_2 \times \vec{a}_3}{|\vec{a}_1 \cdot (\vec{b} \times \vec{c})|} \quad (2.55)$$

Most conveniently, we may select the three lattice vectors as a base of \mathbb{R}^3 to obtain the vectors of the reciprocal unit cell $[\vec{a}_1^*, \vec{a}_2^*, \vec{a}_3^*]$. It should be noted that, by choosing this base, the denominator in Equation 2.55 corresponds to unit cell's volume:

$$V = |\vec{a} \cdot (\vec{b} \times \vec{c})| \quad (2.56)$$

The three reciprocal lattice vectors span a reciprocal unit cell. The lattice unit cell in direct space is not unique, neither in its size nor its construction. The first Wigner-Seitz cell is a primitive cell in real space (i.e. contains one lattice point) defined as the loci closer to the contained lattice point than to any other lattice point. The corresponding reciprocal lattice cell, known as the first Brillouin zone, is instrumental to the Bloch theorem. While successive Brillouin zones can be constructed, the first Brillouin zone contains all the crystallographic information required to study wave function propagation in the crystal lattice. There exists a useful relation between \mathbb{R}^3 and its reciprocal space:

$$h \cdot x + k \cdot y + l \cdot z = 0 \quad (2.57)$$

Thus any crystallographic plane in real space can be symbolized as (hkl) , its Miller indices. It should be noted that parallel planes in \mathbb{R}^3 have proportional Miller indices; the irreducible indices are most frequently employed. Miller indices are commonly used to reference specific surfaces in faceted systems (e.g. nanoparticles).

2.5.2 The Born-von Karman conditions. The Bloch theorem.

Assume the periodicity of a crystal lattice is such that the entire lattice can be represented as a cubic array of $N = N_1 \cdot N_2 \cdot N_3$, with side a , as schematically represented in Scheme 2.4. Let $\psi(\vec{r})$ be the wave function corresponding to the state limited to the unit cell. The Born – von Karman periodic boundary conditions are such that the following equality holds:

$$\psi_{i,k}(\vec{r} + N_j \cdot a) = \psi_{i,k}(\vec{r}) \quad (2.58)$$

Electrons in a crystal lattice propagate under a periodic potential energy profile, which itself depends on the lattice's periodicity. As discussed above, a crystal lattice's unit cell includes its

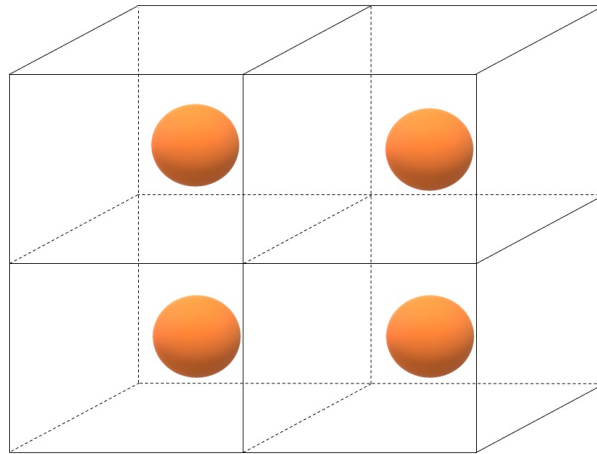
motif and symmetry operations, and as such the potential energy scalar field must also reproduce that of the entire crystal lattice. Should the electronic wave function in the unit cell be determined, and under the Born-von Karman boundary conditions, the electron wave function at any point in the lattice can be written as follows by virtue of the Bloch theorem:

$$\psi_{i,k}(\vec{r} + \vec{R}) = \psi_{i,k}(\vec{r}) \cdot \exp(i \cdot \vec{k} \cdot \vec{T}) \quad (2.59)$$

Where \vec{k} is a vector contained within the first Brillouin zone and \vec{T} is the translation vector corresponding to $\vec{r} + \vec{T}$. That is, the wave function can be propagated by means of its symmetry, as implicitly included in the lattice's reciprocal space description. The fineness with which \vec{k} divides the first Brillouin zone, which ideally should be infinitesimal, must be finite for practical purposes. In general, \vec{k} has the following expression in the reciprocal lattice base:

$$\vec{k} = \frac{n_1}{N_1} \cdot \vec{a}^* + \frac{n_2}{N_2} \cdot \vec{b}^* + \frac{n_3}{N_3} \cdot \vec{c}^* \quad (2.60)$$

Larger values of N provide increasingly better descriptions of the first Brillouin zone, but in practical terms imply greater computational resources. The fineness is symbolized by three indices $[K_1 K_2 K_3]$, often referred to as k-points or k-point mesh.



Scheme 2.4. *Periodic images of spheroid in a cubic lattice, akin to the nanoparticle simulation environments employed in this Thesis.)*

The Bloch theorem centers the problem on solving the Schrödinger equation in the unit cell, which can be solved employing the already-discussed methods. Importantly, the real space cell

volume must be taken into consideration when time-intensive simulations are carried out: denser k-point meshes provide more accurate descriptions of the system at an increased computational cost. In this aspect, the inverse relation between the real cell volume and its reciprocal cell volume, as deduced from Equation 2.56 is of great use. Larger real cells will have correspondingly smaller first Brillouin zones, for which coarser k-point meshes can be employed whilst not significantly affecting the simulation's precision.

2.5.3 Plane waves.

The Bloch theorem provides a natural approach to the description of periodic electronic structures by means of plane waves. Let $u(\vec{r})$ be a potential energy function correctly describing the symmetry and periodicity of the system's unit cell, and as such, invariant to translations through the crystal lattice:

$$u(\vec{r} + \vec{T}) = u(\vec{r}) \quad (2.61)$$

In a similar fashion to free electrons, which are represented as plane waves with wave vector \vec{k} , let each electron i affected by this potential be described as follows:

$$\psi_{(i,k)}(\vec{r}) = u(\vec{r}) \cdot \exp(i \cdot \vec{k} \cdot \vec{r}) \quad (2.62)$$

Where each electron's wave vector is restricted to the first Brillouin zone. Since $u(\vec{r})$ is a periodic function, it may be expanded as a Fourier series:

$$u_i = \sum_G c_{i,G} \cdot \exp(i \cdot \vec{G} \cdot \vec{r}) \quad (2.63)$$

Where \vec{G} stands for each reciprocal lattice vector, such that $\vec{G} \cdot \vec{r} = 2 \cdot \pi \cdot m, m \in \mathbf{Z}$, and $c_{(i,G)}$ are the plane wave expansion coefficients. Thus the electronic wave function can be represented as a linear combination of the so-called Bloch functions:

$$\psi_{(i,k)}(\vec{r}) = \sum_G c_{i,k+G} \cdot \exp(i \cdot (\vec{k} + \vec{G}) \cdot \vec{r}) \quad (2.64)$$

As an infinite sum, it must be truncated to have any computational use. The absolute value of the electron's kinetic energy, which correspond to the coefficients of the Bloch functions, is used as a cut-off criterion (E_{cut}):

$$E_{cut} = \frac{\hbar^2}{2m} \|\vec{k} + \vec{G}\| \quad (2.65)$$

Setting an upper-bound to the moduli of the reciprocal lattice vectors used in the plane wave expansion results in a finite basis set. For instance, the electronic wave function in cubic unit cell with $a = 15\text{\AA}$ has 20.000 plane waves for $E_{cut} = 200eV$. Plane wave basis sets are indeed larger than Gaussian-type basis sets with similar accuracy. Finite Gaussian-type orbital basis sets incur in the basis set superposition error, which arises when atoms borrow basis functions from other atoms, resulting in an unphysical stabilization that introduces a bias in the energy minimization process. Concerning both intra- and intermolecular overlap, the use of larger basis sets is not guaranteed to prevent the spurious overlap and specific methods have been developed to prevent it. By abandoning the orbital basis set description, basis set superposition errors are absent in plane-wave methods. Plane wave basis sets adequately describe delocalized, slowly varying electron densities, such as those exhibited by metallic systems. Furthermore, a strong tendency to localize electron density around the nucleus implies one-electron phenomena (e.g. exciton formation in semiconductors) are ill-described, whilst also requiring additional plane waves to obtain proper descriptions. All in all, plane wave basis sets are frequently used in conjunction with semi-empirical pseudopotentials, which smear the nuclear charge by modelling the core-electrons, and in some instances may also implicitly include relativistic corrections. While pseudopotentials are typically modelled from isolated atoms, they are used in many different simulation environments as they commonly exhibit remarkable versatility.

The full-potential linearized augmented plane wave method offers a high enough accuracy to be considered for benchmarking other DFT methods employed in solid state simulations. It is significantly more computationally intensive than the less accurate pseudopotentials, which lead Blöchl to develop the project augmented wave (PAW) method as a compromise. Succinctly, the PAW wave function incorporates a valence term (as a plane wave series) for which grid-evaluated core contributions have been determined. Core region contributions are defined as the electron density

difference of the all-electron atomic orbitals and that of nodeless, pseudo-atomic orbitals. The thus-generated wave function adaptability results in valence orbital nodes being adequately represented. Furthermore, the PAW method ensures the core and valence electron wave functions are orthogonal to each other.

2.6 Solvation methods.

In the absence of explicit solvation, the simulations employed in this Thesis consider every system to be *in vacuo*. Despite reducing the overall cost of the calculations, *in vacuo* simulations are not fully representative of their experimental counterparts, which in our case imply both aqueous and organic media. Solvation methods can be broadly categorized as explicit, implicit or a combination of both. Explicit solvation implies including however many solvent molecules in the simulations to adequately reproduce the real system; this procedure commonly implies hundreds, if not thousands, of molecules, which decidedly increases the simulation’s computational cost. Heavily solvated solutes may have hundreds or thousands of solvent molecules, which restricts the use of computationally demanding first principles methods. Implicit or continuum solvation methods model solvents as a linear, homogenous, polarizable dielectric with permittivity ϵ . The solute is placed in an equally shaped hole in the dielectric, at the cost of a cavitation energy ($\Delta G_{cav} > 0$). Within the hole, the solute is stabilized by the solvent through dispersion ($\Delta G_{disp} < 0$) and electrostatic interactions ($\Delta G_{elec} < 0$), as the dielectric itself is polarized. The solvation Gibbs free energy is then:

$$\Delta G_{solv} = \Delta G_{cav} + \Delta G_{disp} + \Delta G_{elec} \quad (2.66)$$

Solute-solvent dispersion and the cavitation energy are commonly considered linearly proportional to the total solvent accessible surface (SAS) area,

$$\Delta G_{cav} + \Delta G_{disp} = \alpha \cdot SAS + \beta \quad (2.67)$$

Different approaches to describing the electrostatic interaction are known, each having its own reportedly adequate uses. Implicit solvation results presented in this Thesis make use of the Poisson equation, a partial, second order differential equation relating the charge distribution in a medium

and the corresponding electrostatic potential:

$$\nabla^2 \phi(\vec{r}) = -\frac{\rho(\vec{r})}{\epsilon} \quad (2.68)$$

The Poisson equation sets the ground for the well-known Debye-Hückel theory of dilute electrolyte solutions.

An intermediate approach to solvation can be followed if solvent effects are expected to be properly represented by the innermost solvent coordination spheres. Explicit solvation may then be restricted to significantly fewer solvent molecules; additional implicit solvation should provide a more realistic description of the contribution of the outermost solvent molecules at a lower computational cost.

2.7 Ab initio molecular dynamics (AIMD)

While the dynamical evolution of a system is governed by the time-dependent Schrödinger equation, time evolution in chemical systems is analyzed semi-classically by means of molecular dynamics (MD). In molecular dynamics, Newtonian mechanics dictate the particle trajectories under the influence of an *interaction potential*. An (ideal) infinite molecular dynamics simulation of a chemical system corresponds to the exploration of its entire phase space (full set of microstates), from which macroscopic properties are obtained by virtue of the ergodic hypothesis. Said interaction potential may be described by a force field (a defined set of semi-empirical equations and parameters) or generated from electronic structure methods as needed. In the latter approach, known as *ab initio* molecular dynamics (AIMD), particle motion follows Newton's second law:

$$m \frac{d^2}{dt^2} R = -\nabla U(R(t)) \quad (2.69)$$

That is, the force acting on the particles is proportional to the gradient of the ground-state potential energy surface. Inasmuch as the PES is calculated on-the-fly from electronic structure simulations, AIMD is more versatile than the more case-sensitive, force-field based molecular dynamics.

As an alternative to the Newtonian equations of motion, the Lagrange equations of motion

can be employed (the Lagrangian is defined as the difference between the kinetic and potential energies):

$$\frac{d}{dt} \left(\frac{\delta L}{\delta \dot{r}_i} \right) = \frac{dL}{dr_i} \quad (2.70)$$

Time evolution may be described using any equivalent equation of motion, but in any case, a suitable timestep (δt) must be selected (time line discretization). Large timesteps will lower the runtime of the simulation but may result in short timescale phenomena being overlooked. In general, the shortest timescale event is chosen as a timestep: a common reference is the stretching of bonds with hydrogen, for which a timestep of 0.5-1 fs is advised. Once initialized, the potential energy is calculated at each step to update the forces acting on the particles, from which their velocities and positions are updated; these serve as a starting point for the next step of the simulation. Numerous integration algorithms exist, each having specific energy convergence criteria, accuracy, reversibility and overall efficiency. Since these algorithms imply numerical integration, errors are invariably introduced and should be carefully considered.

In general terms, molecular dynamics methods are designed to either work in, or out of, thermal equilibrium conditions. This discussion is limited to MD under thermal equilibrium. Importantly, total energy is the sum of the kinetic and potential energy of all the particles in the system, so that in the absence of time-dependent fluctuations, it corresponds to the classical Hamiltonian:

$$E_{tot} = \sum_{i=1}^N \frac{1}{2} \cdot m_i \cdot v_i^2 + V(r_i) \quad (2.71)$$

Particles are considered to be non-interacting so as to introduce the ideal gas phase approximation, with added benefit of introducing the Maxwell-Boltzmann statistics. By doing so, it is possible to randomize a complete set of initial velocities to initiate a given algorithm. Furthermore, a useful relation between the average kinetic energy of N particles restricted by C constraints and the temperature of the system is obtained:

$$\langle T \rangle = \frac{1}{2} N \cdot k_B \cdot T \cdot (3 - C) \quad (2.72)$$

Since MD is mostly concerned with the average values of magnitudes, the averages of the kinetic

energy and the potential energy are conveniently related by the virial theorem:

$$2\langle T \rangle = \langle V \rangle \quad (2.73)$$

MD methods may employ different ensembles depending on each system's specifications. For instance, in NVE-MD the number of particles (N), volume (V) and total energy (E) remain constant throughout the simulation. Regardless of which ensemble is employed, it is clear that time averages of any given magnitude $\langle X \rangle$ (e.g. atomic positions) are eventually calculated as ensemble-averages (M):

$$\langle X \rangle = \lim_{t \rightarrow +} \frac{1}{t} \int_{t_0}^{t_0+t} X(\tau) d\tau = \lim_{M \rightarrow +} \frac{1}{M} \int_{t_0}^{t_0+t} X(\tau) d\tau \quad (2.74)$$

Conveniently, the so-obtained ensemble averages include thermodynamical and dynamical properties, such as transport coefficients. In NVT or NPT ensembles velocities and positions must be specified at each timestep. Therefore temperature is expected to randomly change from one step to the next one, an undesirable effect that requires velocity scaling to recover the selected temperature. Alternatively, in thermostatic methods the system is coupled to an infinite reservoir of thermal energy, a so-called heat bath (with coupling parameter τ), which provides additional control over temperature fluctuations:

$$\frac{dT}{dt} = \tau \cdot (T_{target} - T_{instant}) \quad (2.75)$$

A frequently used method, and the one employed in our MD simulations, is known as the Nosé-Hoover thermostat, in which the heat bath is more directly coupled to the system by introducing a specific fictitious coordinate which evolves alongside the system's dynamics.

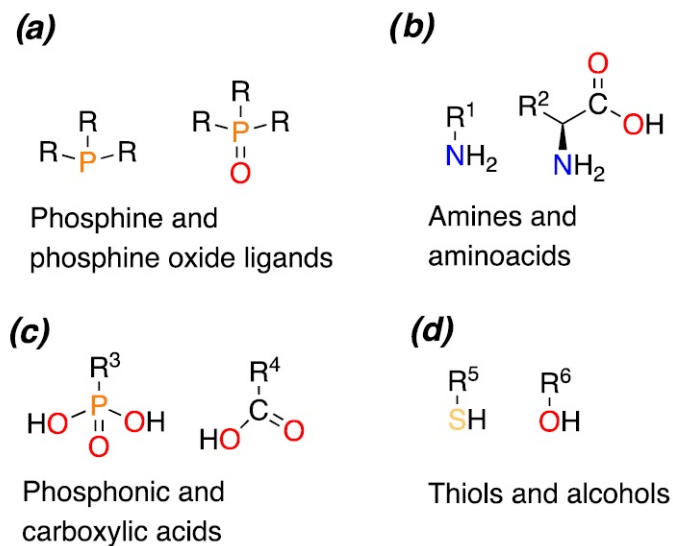
Core-only CdSe structures.

Nanomaterials based on cadmium selenide are crucial in photonics, catalysis, and biomedicine due to their highly-tunable optical properties. In this Chapter, DFT simulations are used to explore ligand adsorption and its effect on the electronic properties of the (110) surface of zinc blende and wurtzite CdSe, as well as on a $(\text{CdSe})_{33}$ quantum dot model. Results show that adsorption energies depend on ligand surface coverage and strike a balance between chemical affinity, ligand-surface and ligand-ligand dispersive interactions. Minor structural reorganization occurs upon slab formation, while in the quantum dot Cd···Cd distances become shorter and the Se-Cd-Se angles, smaller. Consequently, mid gap states are formed which strongly influence the absorption optical spectra of nonpassivated $(\text{CdSe})_{33}$. Indeed, structural reconstruction is apparent for the quantum dot nanoparticle, which significantly increases its HOMO-LUMO gap upon passivation. Solvent effects increase the band gap energies, as the absorption maxima are blue-shifted by roughly 20 nm due to the presence of ligands, thereby reducing the band gap difference between passivated and unpassivated quantum dots.

3.1 Introduction

Semiconductor low-dimensional materials (*e.g.* quantum dots, two-dimensional single- or few-layered sheets) exhibit different electro-optical properties with respect to their bulk counterparts [3, 4]. These have already been exploited in photonic devices in catalysis and in biological applications [101–112]. Behind these noble properties lie the enhancement of quantum mechanical

effects through spatial confinement and the increase in the surface-to-volume ratio [4, 113]. The composition, morphology and surface chemistry of the nanomaterial determine its potential applications, which may be further tailored through various synthetic and post-synthetic methods [31, 114–117]; in this regard, low-dimensional CdSe structures have garnered special attention [32, 118–120]. Wurtzite and zinc blende are the most frequently studied CdSe polymorphs. Nanofabrication involving either polymorph requires great control over their growth and surface chemistry to adequately tune their chemical and electro-optical properties [118–123]. In this regard, despite the control over the optical properties that can be exerted through detailed control of the size, shape and structure of the nanoparticle, quantum dot surface chemistry has emerged as an additional strategy to tune material properties [4, 33, 115, 124]. Most of the surface atoms are undercoordinated, which influences their electronic states and can result in the appearance of charge carrier traps and electronic states in the band gap that ultimately impact the optical properties, oftentimes in an undesirable manner. In this context, surface passivation appears as a suitable strategy [33]. Passivation can be achieved either by the presence of capping ligands [34, 125–127] or by adding a shell of another semiconductor material with a larger band gap, thus containing the photoprocess in the core [128–132]. A wide range of ligands has been used for surface passivation including, but not limited to, the following groups (Scheme 3.1): a) phosphines and phosphine oxide ligands (*e.g.* trioctylphosphine and trioctylphosphine oxide); b) amines and amino-acids (*e.g.* dodecylamine); c) phosphonic and carboxylic acids (*e.g.* octylphosphonic, oleic, stearic and 3-mercaptopropionic acids); and d) alcohols and thiols (*e.g.* decanethiol). The nature of the capping ligand is important, as it can modify the emission wavelength and enhance (or quench) photoluminescence [103, 113, 115]. Understanding capping ligand interactions and their influence on adsorption energies and the electronic structure of the surface is essential to the development of new materials with enhanced optical properties; consequently, many experimental [34, 124, 126, 133–136] and computational contributions ([8, 10, 30, 45, 50, 55, 56, 137–146] have been reported in the literature.



Scheme 3.1. Four main types of capping ligands employed in the passivation of the herein discussed CdSe structures.

Both surface slab [33, 147–150] and nanoparticle models [8, 9, 30, 45, 50, 55, 56, 137–140, 142, 143, 145, 146, 151–155] have already been used in prior contributions. Periodic slab models have been employed in the characterization of ligand adsorption on specific facets, albeit at the cost of forgoing finer details present in the structure of the nanoparticle [33, 147–150]. Regarding the modeling with clusters and nanoparticles, significant effort has been centered on models with up to 30 CdSe units, with (CdSe)₁₃ being the most frequently used [30, 135, 137, 138, 151–154, 156–161] owing to its significant stability, in accordance to mass spectrometry experiments [162]. Recently, larger nanoparticle models have been employed which allowed representing more realistically-sized quantum dots as well as increasing the number of ligand molecules explicitly considered in the calculations [8–10, 56, 136, 139, 140, 144, 145].

The appearance of traps states at the edges of the band gap region appears to be related to surface defects due to incomplete passivation [8, 141, 143]. Consequently, most of the calculations with small nanoparticle models agree with the fact that capping ligand adsorption alters the band gap [55, 152, 156, 158–160], thus leading to shifts in the emission wavelength when compared to ligand-free models. Meanwhile, calculations performed with larger models have resulted in some controversy: while there is a consensus that both anionic and neutral ligands modify the band gap of large, non-stoichiometric nanoparticles [45, 143], the role of neutral ligands in stoichiometric

nanoparticle models is less pronounced [9, 55, 138, 140]. In this context, an article published during the development of this Thesis has shown thermal effects to be crucial in properly identifying the band gap blue-shift upon ligand adsorption [10]. Finally, the presence of ligands influences the localization of the frontier orbitals [33], and it can increase material luminescence in two ways: firstly, it decreases the rate constant of non-radiative decay, and secondly, the presence of electronic states delocalized both on the material surface and the ligands enables new mechanisms for radiative decay from the excited state [153].

To the best of our knowledge, previous contributions to the *in silico* low-dimensional CdSe characterization have not included, simultaneously, a broad scope in ligand variety for both surface and nanoparticle models and the analysis of thermal and solvent effects. The hereby presented results are expected to shed light on the influence of ligand passivation and surface reconstruction on the appearance of trap states on the band structure of the CdSe surfaces and quantum dot model.

3.2 Computational details.

All calculations were carried out with the VASP code [163, 164], which performs three-dimensional periodic calculations using a plane wave-based basis sets. Regardless of the dimensionality of the model, simulations involve periodicity in the three directions. For periodic surface slabs and quantum dots, the lattice parameters used guarantee a distance between the outermost atoms of the images of, at least, 10 Å in the non-periodic directions. For ligand adsorption on slabs, parameter c is set to 30 Å or 40 Å depending on the length of the alkyl chain of the ligand. Additionally, the (CdSe)₃₃ quantum dot and the corresponding capped models are placed in a 35 Å cubic box.

Low dimensional CdSe and ligand models. Ligand adsorption on low-dimensional CdSe structures and its effect on the band gap were simulated on surface slabs and a finite (CdSe)₃₃ quantum dot model, presented in Figure 3.1.

Regarding the slab models, two different low energy surfaces were considered: stoichiometric (110) zinc blende (ZB) and stoichiometric (110) wurtzite (WZ) slabs, both non-polar. Layer-wise surface energy convergence was used to select optimal slab thickness. Facets were represented by (3x3) and (2x2) supercells of ZB(110) and WZ(110) surfaces, respectively, whenever lateral

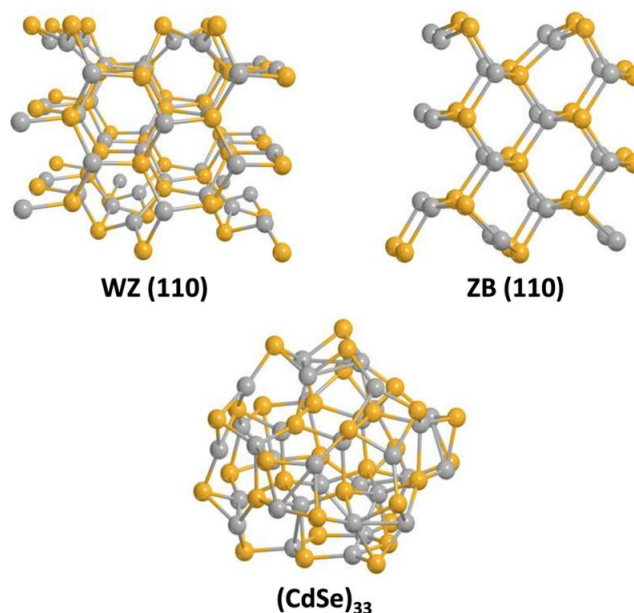
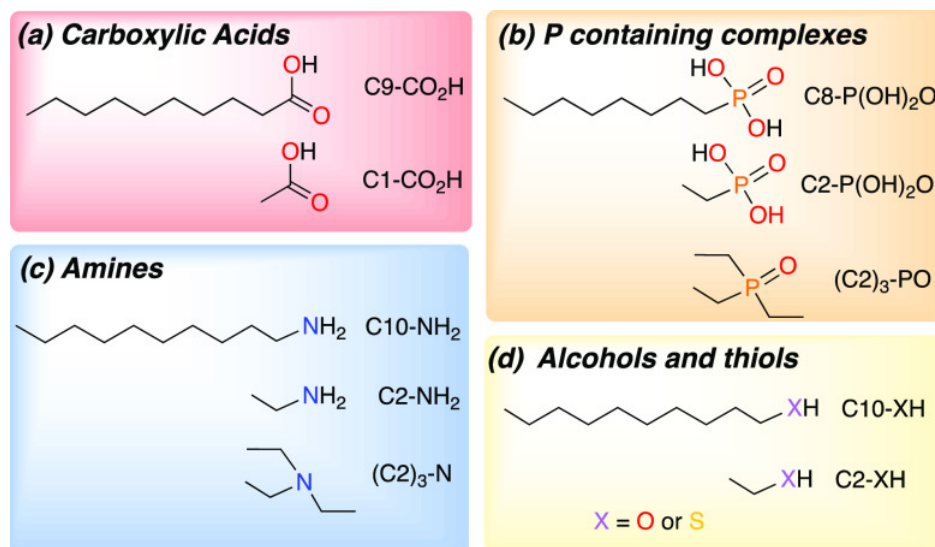


Figure 3.1. Optimized structures of the (110) wurtzite and zinc blende surface slabs and the $(\text{CdSe})_{33}$ nanoparticle model. In gray, cadmium atoms; in orange, selenium atoms.

interactions between ligands across periodic images were undesired. Conversely, smaller surface unit cells were employed to simulate higher ligand surface concentrations: (1x1) and (2x2) for ZB(110), and (1x1) for WZ(110). Moreover, the importance of ligand coverage on the adsorption energy and the band gap structure was analyzed on the smallest (110) ZB and (110) WZ (1x1) surfaces. The nanoparticle model (Figure 3.1) was constructed from a spherical cut on bulk, crystalline wurtzite as detailed in prior works [8–10, 50, 56, 138, 140, 146]. This model includes 33 CdSe units, corresponding to one of the clusters identified by mass spectrometry [162]. Moreover, the nanoparticle model has 27 surface Cd centers *i.e.* it presents 27 surface vacancies, each being initially saturated with one capping ligand in the full-coverage nanoparticle calculations. During structure optimizations, all atoms were allowed to relax both on the slab and nanoparticle models; cell parameters were kept fixed in all cases.

The effect of ligand structure was analyzed by considering four groups of ligands, shown in Scheme 3.2: a) carboxylic acids, b) phosphine oxides and phosphonic acids, c) amines, and d) alcohols and thiols. For each group, small-large pairs of ligands were considered. For the small models, the alkyl chain is $\text{CH}_3\text{-CH}_2\text{-}$ (C2), whereas the larger counterparts have $\text{CH}_3\text{-(CH}_2\text{)}_9\text{-}$ (C10) instead, with few exceptions. Additionally, in the case of amines and the phosphonic acids, the bulkier triethyl

amine and triethylphosphine oxide ligands were included to analyze how steric effects may influence ligand surface coverage.



Scheme 3.2. Summary of the capping ligands employed in the ligand adsorption simulations hereby presented.

Level of theory. Geometry optimizations were carried out at DFT level using the GGA-type Perdew-Burke-Erzerhof (PBE) exchange-correlation functional [165] with Grimme's D2 correction [166], as implemented in VASP 5.4; PBE-D2 has been shown to provide better estimates for cell parameters than PBE-D3 in prior solid-state reports [74, 92]. Since all results include Grimme's correction, the "D2" tag is promptly dropped for ease of discussion. Spin-polarized calculations were performed for bulk and pristine surfaces to successfully confirm the absence of magnetization; all the results reported hereafter are based on non-spin-polarized calculations. The atomic ionic cores were represented with projected augmented wave (PAW) pseudo-potentials [167, 168], and the valence electrons were represented with a plane wave basis set with a 500 eV cutoff (a value that ensures accuracy in a cost-efficient manner). For each system, different Monkhorst-Pack [169] reciprocal space k -point grids were employed depending on cell dimensions in order to optimize the cost-to-accuracy ratio of the simulations. The nanoparticle model was computed at the Γ point due to its non-periodic nature. For the ZB (110) slab, 2x2x1 and 8x8x1 k -point meshes were employed for ZB(3x3) and ZB(1x1) cells, respectively. For the wurtzite (110) facet, 2x2x1 and 4x4x1 meshes were used for WZ(2x2) and WZ(1x1), respectively, owing to their larger unit cell parameters. Bader

charge analysis [170, 171] was performed to analyze charge transfer between ligands and the CdSe materials.

Since GGA functionals are prone to underestimate semiconductor band gaps, two main strategies have been proposed to overcome this limitation: a) use of hybrid functionals and b) the inclusion of Hubbard’s correction (DFT-U). In the case of CdSe, the hybrid PBE0 functional has been shown to provide adequate results [137, 151], while other authors have successfully applied Hubbard’s correction [172] under the Dudarev scheme [173]. Consequently, the optical properties of the CdSe-based materials have been analyzed at three different levels of theory: PBE, PBE-U and PBE0. Firstly, the band gap of bulk zinc blende CdSe is used to calibrate the U_{eff} , concluding that a value of 14 eV on the Cd d orbitals provides a sufficiently accurate estimate on an already-optimized structure at PBE level. This is because, as shown in Figure 3.2, ion and cell optimization for large U values on Cd d orbitals leads to an unphysical cell compression and a non-linear increase in band gap energy. Thus, PBE+U should be preemptively applied only to already optimized structures. Band gap dependence on the Monkhorst-Pack mesh density also warranted an examination: 32x32x32 and 32x32x1 meshes lead to sufficient band gap convergence with respect to the 1st Brillouin zone representation. Unfortunately, such dense k -point meshes are impractical for hybrid functionals, as they lead to significantly lengthy computation times. The PBE, PBE+U, PBE0 and best estimated value band gap energies of the optimized models are presented in Table 3.1.

Table 3.1. *Band gap energies (in eV) for bulk zinc blende and wurtzite, ZB(110) and WZ(110) pristine surfaces, and (CdSe)₃₃ nanoparticle model computed at PBE, PBE+U and PBE0 level. BEV stands for best estimated value.*

Model	PBE	PBE-U	PBE0	BEV
WZ bulk	0.78	1.65	3.09	2.24
ZB bulk	0.66	1.56	2.49	2.08
WZ(110)	1.34	2.01	3.28	2.79
ZB(110)	1.21	1.92	2.99	2.66
(CdSe) ₃₃	1.61	1.76	3.08	3.06

As expected, PBE values are systematically lower than PBE0 and PBE-U values. However,

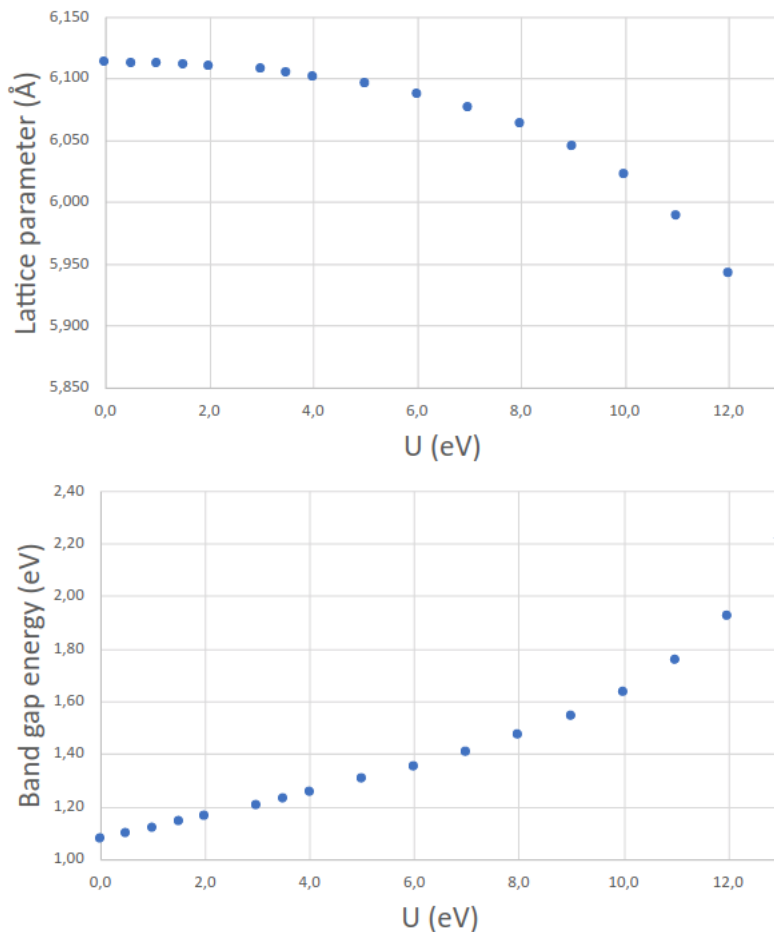


Figure 3.2. Bulk zinc blende CdSe lattice parameter (top) and band gap energy (bottom) from PBE+U optimizations with increasing U values on Cd d orbitals with an $8 \times 8 \times 8$ k-point mesh. Significant, non-physical cell compression is observed for values above 10-11 eV, for which the band gap energies more closely match the experimental value. PBE+U has only been used in single-point calculations on already optimized structures.

while the difference between PBE and PBE0 with the same number of k -points is constant (1.42-1.47 eV) regardless of the material considered, the difference between PBE and PBE-U decreases significantly at lower dimensionalities. Moreover, experimental data for $(\text{CdSe})_{33}$ suggest that its band gap should be around 3.0 eV [162], a value not well reproduced by PBE-U. The large U_{eff} value also shifts the orbitals contributing to the valence and conduction bands, namely, by increasing the contribution of the Cd 4d orbitals to the conduction band. These results suggest that PBE-U may not be suitable to analyze the electronic structure of the CdSe nanoparticles, and should be avoided in similar systems. In conclusion, the best estimate band gap values (BEV) are

obtained by adding the mean difference between PBE and PBE0 at the same number of *k*-points (1.45 eV) to the PBE band gap energies obtained with a denser *k*-point mesh.

Thermal effects on the full coverage nanoparticles models [(CdSe)₃₃-L₂₇] (L = capping ligand) were taken into account by performing NVT *ab initio* molecular dynamics, setting a Nosé-Hoover thermostat to 300K [174, 175]. An optimized structure for each type of capping ligand was taken as the initial structure in a 0.5 ps equilibration simulation. Once thermalization ensued, 1 ps (1000 steps) of AIMD were used for clusterization. Clusterization was performed with the algorithm provided in UCSF Chimera [176] by considering the Cd center distribution. Representative structures resulting from the clusterization were used to analyze the thermal effects on full coverage nanoparticle optical properties. Additionally, the effect of solvent on the band gap was analyzed by implicit inclusion with VASPSOL [177]. Water solvation is considered as the limit case, while calculations with toluene and acetonitrile were ran to confirm that the effects observed with water can be further tuned by changing solvent polarity. Finally, to further analyze the optical properties of the passivated and unpassivated (CdSe)₃₃ nanoparticles, TD-DFT calculations were performed at PBE0 level of theory (as implemented in the Gaussian 16 package [178]) on structures obtained during the AIMD simulation. Atoms were represented with def2-SVP [179, 180] basis sets and the corresponding pseudopotentials [181]. Water solvation effects were included with the CPCM continuum model [182, 183]. Absorption spectra are obtained by considering three representative structures of the AIMD simulation: i) the structure with the lowest band gap energy; ii) the structure with the largest band gap energy; and iii) the structure with the closest band gap energy to the weighted average value. In each case, the first 10 excited singlet states were considered, with the intensity being computed based on the oscillator strength and the number of structures contributing to the specific cluster.

3.3 Results and discussion.

3.3.1 *In silico* characterization of core-only systems.

Characterization results of the core-only CdSe bulk, surface and nanoparticle models are structured as follows. Firstly, the pristine structures of bulk zinc blende and wurtzite, the corresponding stoichiometric, non-polar (110) surfaces and the (CdSe)₃₃ models are explored. Additional surfaces

were initially considered, such as the non-polar (431) facet, but have been dropped as their specific surfaces energies are higher than that of the (110) facets. The two distinct Cd- and Se-terminations of the polar and non-stoichiometric (111) and (001) facets, were similarly shown to be higher in specific surface energy. The intrinsic ligand-material interactions and the adsorption energies on the surfaces at low ligand coverage conditions are then presented, followed by an equivalent characterization at high-coverage conditions on the surfaces and on $(\text{CdSe})_{33}$ aimed at elucidating cooperative and competitive effects. Lastly, ligand-induced band gap shifts are considered in the full-coverage scenario for the surface slabs and the $(\text{CdSe})_{33}$ nanoparticle. Regarding the latter model, results from *in vacuo* static calculations are followed by those in which thermal effects and implicit solvation have been included.

3.3.2 Method calibration.

The structural properties of bulk zinc blende and wurtzite CdSe, the largest optimized, pristine (110) zinc blende and (110) wurtzite surfaces (ZB(3x3) and WZ(2x2), respectively) and the $(\text{CdSe})_{33}$ nanoparticle model are examined first. The main structural parameters and the Cd-Se and Cd \cdots Cd distances of the optimized structures (see Figure 3.1) are presented in Table 3.2 (bulk ZB and WZ X-ray results are added in parenthesis for additional reference).

Table 3.2. *PBE-D2 cell parameters and Cd-Se distances (in Å) for zinc blende and wurtzite and the (110) main crystallographic facet of each polymorph (X-ray values are added in parenthesis). ^a Surface atoms, ^b Internal atoms. ^c Average values.*

Model	Cell parameters	d(Cd-Se)	d(Cd-Cd)
WZ	a,b =4.394 (4.299) c=7.171 (7.010)	2.648	4.322
ZB	a=6.022 (6.017)	2.647	4.323
WZ(110)	a=14.095 b=14.935	2.590 ^a /2.660 ^b	3.818 ^c
ZB(110)	a=8.623 b=12.195	2.612 ^a /2.657 ^b	3.712 ^c
$(\text{CdSe})_{33}$	-	2.677 ^a /2.667 ^b	3.16/3.42

Cell parameters at PBE-D2 level are close to experimentally determined values for both poly-

morphs, the largest deviation being of 0.16 Å for the c parameter in wurtzite. Computed Cd-Se and Cd ··· Cd distances in bulk ZB and WZ are in good agreement with experimental values reported in Table 3.2. Overall, this indicates that the methodology used is accurate enough for structural characterization. The Cd-Se distances in the surface models are similar to those in the bulk, with significant differences observed only for the outermost surface atoms: this leads to shorter Cd ··· Cd distances in the 3.7 - 3.8 Å range. Conversely, large reorganization is observed on the nanoparticle model, particularly at the surface, where several Cd ··· Cd interactions with substantially shorter distances are reported (Table 3.2). Additional characterization is provided through Bader charge analysis, presented in Table 3.3. Bader charge analysis provides similar results for both bulk ZB and WZ CdSe. Charges are not homogeneously distributed in the slab models¹, as the outermost Se and Cd atoms present lower charge separation (-0.66 for both polymorphs) than the innermost centers, whose values are closer to those in the bulk materials (-0.71 and -0.72 for bulk ZB and WZ, respectively). Consistently, Se atoms are Lewis bases and Cd atoms are Lewis acids, and as such, ligands preferentially bind to surface Cd sites.

Table 3.3. *Bader charges for bulk wurtzite and zincblende, and surface WZ(110) and ZB(110) systems. For the surface slab models, separate values for core and external atoms are presented.*

	WZ	Q_{Bader}	ZB	Q_{Bader}
Bulk	Se	-0.71	Se	-0.71
	Cd	+0.71	Cd	+0.71
Surface	Se_{surf}	-0.66	Se_{surf}	-0.66
	Se_{core}	-0.72	Se_{core}	-0.71
	Cd_{surf}	+0.69	Cd_{surf}	+0.68
	Cd_{core}	+0.71	Cd_{core}	+0.70

3.3.3 Low surface coverage ligand adsorption.

Firstly, the intrinsic interaction between the ligand and the surface was evaluated by considering the spacious ZB(3x3) and WZ(2x2) surface models to avoid lateral ligand interactions. Overall, two ligand-surface orientations were considered: perpendicular and parallel. Perpendicular adsorption of capping ligands occurs mainly by interaction of the basic heteroatom of the ligand with Cd surface atoms, with alkyl chains being perpendicular to the surface. In a parallel adsorption, the

¹Non-zero net Bader charges result from numerical approximation.

capping ligand alkyl is parallel to the surfaces and interacts with it through dispersion forces. While perpendicular adsorption could be explored for all the ligands selected, parallel orientation was only plausible for the larger unit cells. The Cd-capping ligand distances and the adsorption energies of ZB(3x3) and WZ(2x2) (perpendicular adsorption) are presented in Table 3.4. Figure 3.3 shows the optimized structure for the perpendicular adsorptions of the shorter ligand of each type.

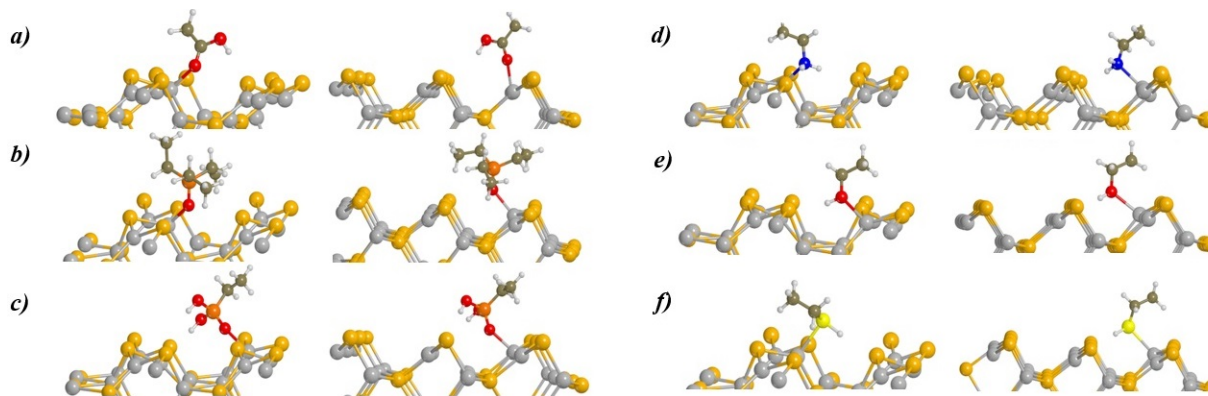


Figure 3.3. Low-coverage ligands adsorbed on WZ(2x2) (slabs on the left) and ZB(3x3) (slabs on the right) including a) acetic acid, b) ethylphosphonic acid, c) trimethylphosphine oxide, d) ethylamine, e) ethanol and f) ethanethiol.

Perpendicular adsorption takes place similarly for the different ligands. Ligands adsorb through the coordination of the heteroatom (X) to Cd, with Cd \cdots X distances varying between 2.287 Å and 2.769 Å. According to Bader charge analysis of the capping ligands, reported in Table 3.5, the interaction is electrostatic with negligible charge transfer. Nevertheless, the alkyl chain is in all cases slightly tilted due to dispersive interactions between the alkyl chain and the surface. A comparison between the different kinds of ligands shows that, for both surfaces, the shortest Cd \cdots X distances correspond to the phosphonic acid and phosphine oxide species, whereas the largest distances are obtained in the case of thiols. Furthermore, R-SH and R-OH ligands can additionally form hydrogen bond contacts with the surface selenium atoms. However, the H \cdots Se distances vary from 2.297 Å to 2.992 Å, showing that hydrogen bonding between the ligands and the surface is weak (the possibility of proton transfer between ligands and the surface is explored in Section 3.3.5).

Table 3.4. Ligand adsorption energies (in $\text{kJ}\cdot\text{mol}^{-1}$) and Cd-X distances on ZB(110) and WZ (110), for the low- and high-coverage scenarios. X stands for the ligand's heteroatom. ^a Most stable configuration, ^b unit cell is too small to accommodate the ligand.

type	ligand	low coverage				high coverage			
		ZB(3x3)	WZ(2x2)	ZB(1x1)	WZ(1x1) ^a				
		d(Cd-X)	ΔE	d(Cd-X)	ΔE	d(Cd-X)	ΔE	d(Cd-X)	ΔE
$R - \text{CO}_2\text{H}$	$\text{C9} - \text{CO}_2\text{H}$	2.415	-83.2	2.446	-63.2	2.415	-113.5	2.524/2.472	-99.7
	$\text{C1} - \text{CO}_2\text{H}$	2.400	-81.1	2.417	-70.1	2.425	-79.2	2.432/2.427	-73.1
$R - \text{P}(\text{X})_2\text{O}$	$\text{C8} - \text{P}(\text{OH})_2\text{O}$	2.287	-111.7	2.309	-97.7	2.301	-106.6	2.574/2.610	144.4
	$\text{C2} - \text{P}(\text{OH})_2\text{O}$	2.292	-125.9	2.330	-94.4	2.501	-85.2	2.396/2.524	-129.3
	$(\text{C2})_3 - \text{PO}$	2.297	-130.2	2.305	-123.1	--- ^b	--- ^b	--- ^b	--- ^b
$R - \text{NX}_2$	$\text{C10} - \text{NH}_2$	2.353	-112.7	2.380	-99.6	2.427	-141.3	2.397/2.403	-134.7
	$\text{C2} - \text{NH}_2$	2.363	-117.3	2.364	-107.0	2.386	-111.0	2.395/2.389	-105.2
	$(\text{C2})_3 - \text{N}$	2.550	-49.6	4.177	-54.1	--- ^b	--- ^b	--- ^b	--- ^b
$R - \text{OH}$	$\text{H} - \text{OH}$	2.447	-62.7	2.485	-61.3	2.499	-66.2	2.474/2.489	-58.6
	$\text{C10} - \text{OH}$	2.397	-80.2	2.412	-65.3	2.631	-109.3	2.463/2.477	-114.0
	$\text{C2} - \text{OH}$	2.405	-83.0	2.428	-74.4	2.486	-81.1	2.464/2.473	-75.7
$R - \text{SH}$	$\text{C10} - \text{SH}$	2.730	-76.0	2.745	-65.0	2.815	-112.6	2.851/2.790	-100.5
	$\text{C2} - \text{SH}$	2.722	-73.0	2.769	-66.1	2.813	-85.7	2.811/2.800	-75.3

Table 3.5. *Ligand Bader charges of C2-NH₂, C2-COOH, C2-OH and C2-SH after the adsorption on ZB(1x1) and WZ(1x1).*

Ligand	ZB (110)	WZ (110)
C2-NH ₂	0.09	0.08
C2-COOH	-0.05	-0.03
C2-OH	0.00	0.00
C2-SH	0.06	0.05

Perpendicular mode adsorption energies range between -130.2 and -61.3 kJ·mol⁻¹, with the exception of (C2)₃N, which presents lower adsorption energies (in absolute value) due to the absence of a direct N ··· Cd interaction. Comparison between the computed values allows for establishing three trends. First, the adsorption energy of the short and long analogous ligands differs at most by 13.0 kJ·mol⁻¹, in most cases being between 1.3 and 6.6 kJ·mol⁻¹. This suggests that lateral interactions are negligible and therefore no dispersion interactions between alkyl chains exist in these large supercells. Second, the strongest adsorption energies are computed for the phosphonic acid, phosphine oxide and primary amine ligands, while the weakest are associated with carboxylic acids, alcohols and thiols. The specific order for the short models is (C2)₃-PO > (C2)-P(OH)₂O ~ (C2)-NH₂ > (C1)-COOH ~ (C2)-SH, in agreement with the proton affinity trends of the different ligands presented in Table 3.6, which may also be classified in these two groups.

Table 3.6. *PBE0/6-311+G(d) proton affinities (in kJ·mol⁻¹) of the selected ligands.*

Ligand	(C2) ₃ -PO	C2-NH ₂	(C2)-P(OH) ₂ O	C2-SH	C2-OH	H-OH
	937.7	913.8	849.0	785.0	772.1	689.2

Third, the adsorption energies on the ZB surface are systematically higher than those computed on the WZ slab by about 5.8 - 30.2 kJ·mol⁻¹, with most values falling in the 10.9 - 15.1 kJ·mol⁻¹ range. These higher adsorption energies for ZB are attributed to larger surface-ligand dispersive interactions due to surface morphology. As shown in Table 3.7, adsorption energies without Grimme's dispersion corrections (ΔE_{PBE}) are similar for both surfaces, while the dispersion contribution to the adsorption energy (ΔE_{PBE-D2}) is 11.1 - 25.0 kJ·mol⁻¹ larger in ZB and that in WZ. Parallel mode adsorption energies of the ligands presented in Figure 3.4 range between -142.6 and -87.7

$\text{kJ}\cdot\text{mol}^{-1}$ (see Table 3.8). They are systematically higher than the corresponding perpendicular adsorptions.

Table 3.7. *Effect of the D2 dispersion correction on the low coverage ligand absorption of acetic acid, ethylamine and ethanethiol on WZ(110) and ZB(110) (in $\text{kJ}\cdot\text{mol}^{-1}$).*

	Ligand	ΔE_{PBE-D2}	ΔE_{PBE}	ΔE
WZ(2x2)	C10 – COOH	-63.2	-25.0	-38.2
	C10 – NH ₂	-99.6	-68.3	-31.3
	C10 – SH	-66.0	-34.8	-31.2
ZB(3x3)	C10 – COOH	-83.2	-31.4	-51.8
	C10 – NH ₂	-112.7	-56.4	-56.3
	C10 – SH	-76.1	-33.2	-42.3

Table 3.8. *Adsorption energies (in $\text{kJ}\cdot\text{mol}^{-1}$) and Cd-X distances (in Å) of different ZB(3x3) ligand parallel conformations.*

Ligand	ΔE	d(Cd-X)
C10-COOH	-104.6	2.435
C10-NH ₂	-142.6	2.422
C10-SH	-111.8	2.833
C8-P(OH) ₂ O	-87.7	2.628
C10-OH	-113.6	2.546

The parallel adsorption mode presents systematically larger Cd \cdots X distances, approximately by 0.02 Å, although increases above 0.1 Å are reported for C10-SH (from 2.730 to 2.833 Å) and for C10-OH (from 2.397 to 2.546 Å), as per Tables 3.4 and 3.8. The alkyl chain and the surfaces distances are around 3-4 Å, which indicates dispersive interactions between the alkyl chain and the surface. The alkyl chain-surface dispersion is enhanced at the cost of weakening the local Cd \cdots X interaction, although the alkyl chain-surface dispersion interactions more than compensates for it. In this context, results suggest that at low coverages ligands will mainly adopt a conformation that maximizes the interaction between the alkyl chain and the surface, regardless of the functional

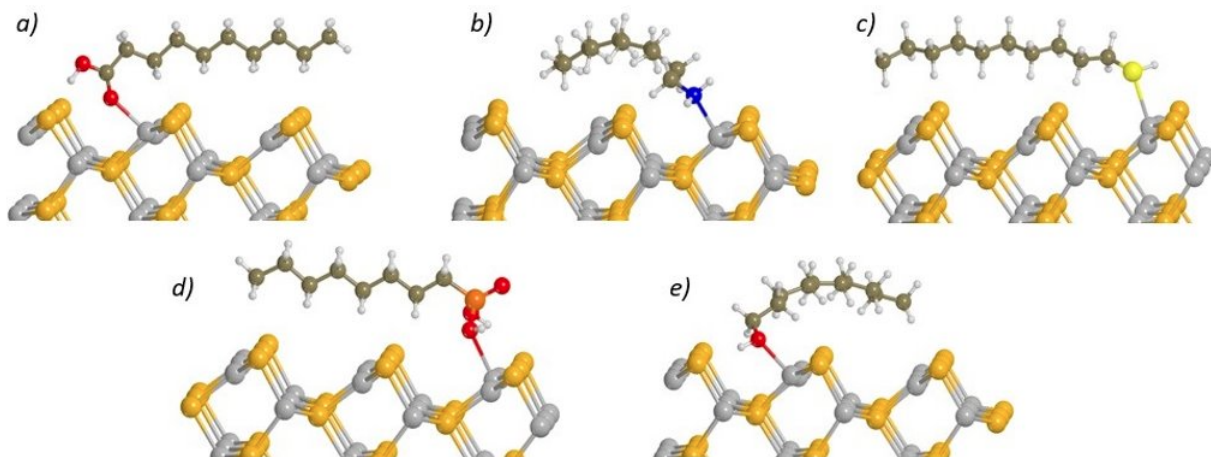


Figure 3.4. Representative structures of the different parallel ligand adsorptions on $ZB(3 \times 3)$ of a) decanoic acid, b) decylamine, c) decanethiol, d) octylphosphonic acid, e) decanol.

group.

3.3.4 Full surface coverage ligand adsorption.

The full ligand coverage, defined as the adsorption of one ligand molecule per surface Cd, is addressed with the same ligands considered for the low coverage scenario. This is the model that best represents the experimental conditions and better reproduces ligand-ligand lateral interactions. Only the perpendicular mode of adsorption was considered. The $(C2)_3PO$ and $(C2)_3N$ ligands have been excluded from said calculations as they are too large to fit inside the $ZB(1 \times 1)$ unit cell. This outlines that these two ligands and their associated families (phosphine oxides and tertiary amines) are not suitable for saturating all cadmium vacant sites. The $Cd \cdots X$ distance in the full coverage is akin to that of the low coverage, albeit slightly larger in general. The $Cd \cdots X$ distance trends are equivalent to those observed for the isolated systems, that is, $(C2)-P(OH)_2O < (C2)-NH_2 < (C1)-COOH < (C2)-OH < (C2)-SH$. This suggests that the ligand - surface interaction is similar to that in the low-coverage simulation with minimum competitive effects. As a consequence, the adsorption energies can again be divided into the same two groups as in the low-coverage scenario: those of phosphonic acid and amine ligands, which are systematically adsorbed more strongly for a fixed alkyl chain length, and those of carboxylic acids, alcohols, and thiols. The adsorption energies at full coverage (see Table 3.4) for the smallest C2 models on ZB are in general close to those of

the low coverage (the largest deviations being around ± 10 kJ·mol⁻¹). In contrast, the adsorption energy for the largest models is systematically larger than the value for the low coverage by about 30 kJ·mol⁻¹ (in the range of 28.6 - 36.6 kJ·mol⁻¹). Since the Cd \cdots X distances do not vary significantly, this stems from the dispersive stabilizing ligand-ligand interactions, which are particularly important in the large models. Calculations involving several thiols with increasing alkyl chains show that the ligand-ligand stabilizing interaction increases by about 5.2 kJ·mol⁻¹ per CH₂ unit (see Figure 3.5), and becomes linear for 1-pentanethiol and longer alkylthiols.

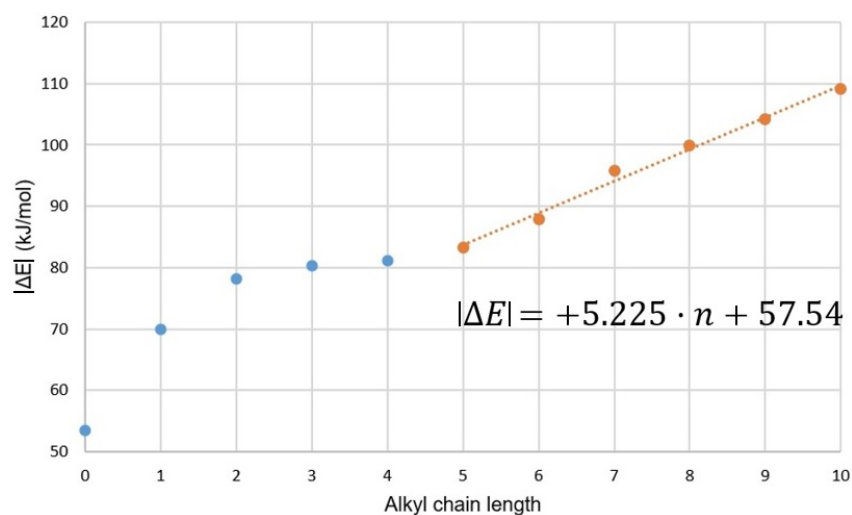


Figure 3.5. Adsorption energies for linear alkylthiols from $n=1$ to $n=10$ on ZB(1x1) and the linear regression for $n \geq 5$.

In the case of WZ (110), the presence of two ligands per unit cell gives rise to a larger configurational variability. That is, for thiols, alcohols, and amines, two different adsorption modes have been identified: one in which the two ligands interact with cadmium atoms, and another one where one ligand is directly adsorbed on the surface, while the other is hydrogen-bonded to the former (Figure 3.6 A,B). Meanwhile, for carboxylic and phosphonic acids, there are five potential different coordination modes depending on whether the adsorption of each ligand takes place through the =O group or the OH one, and the number of ligands directly adsorbed (1 or 2). However, some of these possibilities are not stable and during the optimization evolve to one of the other conformations (Figure 3.6C). In all cases, the most stable configuration is that for which the two ligands interact with the surface. For the acids, the preferred adsorption mode is through the =O

group by at least $5.5 \text{ kJ}\cdot\text{mol}^{-1}$ per ligand. Still, the configuration where one ligand is desorbed and hydrogen bonded with the other ligand has an adsorption energy per ligand that is only between 3.1 and $17.4 \text{ kJ}\cdot\text{mol}^{-1}$ lower in absolute value. All calculated energies are presented in Table 3.9. Finally, as for ZB, adsorption energies for the long alkyl chain ligands are systematically larger by $35 - 50 \text{ kJ}\cdot\text{mol}^{-1}$ due to ligand - ligand interactions. This increase is larger than in ZB due to a shorter surface $\text{Cd} \cdots \text{Cd}$ distance in WZ, which favors lateral dispersive interactions. As a result, adsorption energies on ZB and WZ at full coverage become more similar.

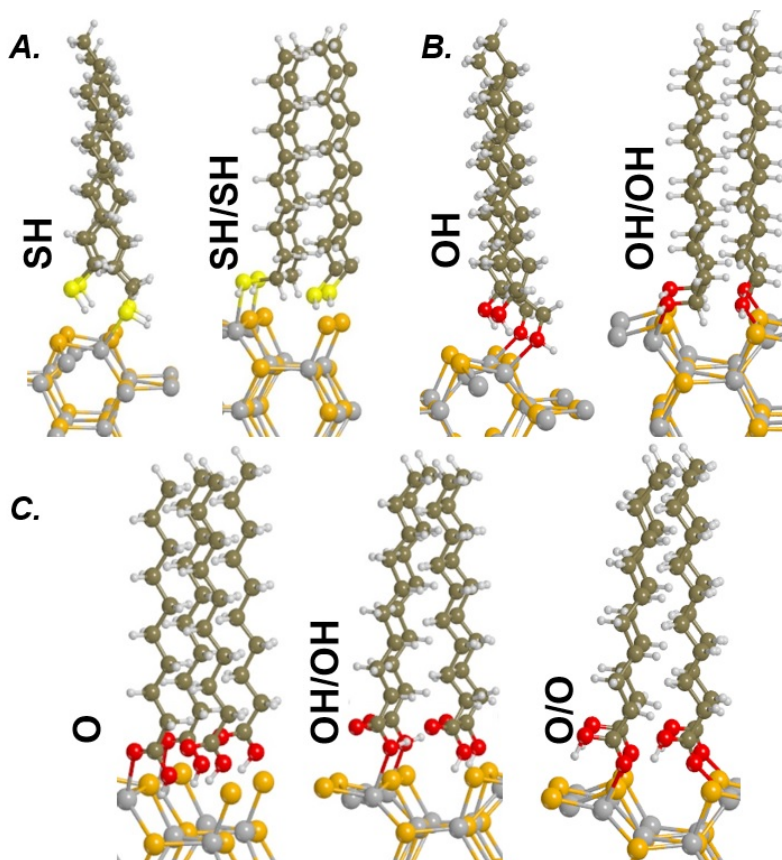


Figure 3.6. Representative structures of the different conformations from full coverage ligands on $WZ(1\times 1)$: a) decanethiol, b) decanol and c) decanoic acid. Different configurations have been explored.

Table 3.9. Adsorption energies (in $\text{kJ}\cdot\text{mol}^{-1}$) of the different WZ(1x1)-ligand (X) conformations explored, some of which are shown in Figure 3.6. Two-ligand adsorptions are indicated by a slash.

Type	Ligand	X/X	XH/XH	XH/X	X	XH
R-CO ₂ H	C9-CO ₂ H	-99.7	-	-83.7	-83.9	-90.8
	C1-CO ₂ H	-73.1	-	-	-	-
R-P(O) ₂ O	C8-P(OH) ₂ O	-143.7	-144.4	-	-	-
	C2P(OH) ₂ O	-129.3	-123.8	-	-	-126.2
R-NH ₂	C10-NH ₂	-	-134.7	-	-	-117.3
	C2-NH ₂	-	-105.2	-	-	-
R-OH	H-OH	-	-58.1	-	-	-
	C10-OH	-	-114.0	-	-	-102.3
	C2-OH	-	-75.7	-	-	-58.4
R-SH	C10-SH	-	-100.5	-	-	-85.1
	C2-SH	-	-75.3	-	-	-

3.3.5 Surface and ligand-mediated deprotonation of Lewis acids on CdSe ZB(110).

Ligand proton transfer on ZB(2x2) has been studied using acetic acid, water and ethanethiol, but also with benzoic acid (HB) to include further variety. As a starting geometry, one H^+ is placed on top of an outermost Se atom, whilst the conjugated base is set close to an outermost Cd. This approach is consistent with the electrodonating (electrowithdrawing) nature of Se (Cd) in CdSe, as inferred from Bader charge analysis shown in Table 3.3. Gas-phase surface-mediated deprotonation is not expected to occur unless the surface is sufficiently basic to stabilize the highly-labile H^+ . All species reported are unstable with respect to deprotonation. Optimization of H^+ / Ac^- and H^+ / OH^- inevitably lead back to the molecular form in ZB(2x2). Although H_2O remains deprotonated in ZB(3x3) provided both ions are far enough from each other, it exhibits a positive relative energy with respect to the molecular form. The optimized structure of H^+ / EtS^- suggests that proton transfer back to the thiolate is significantly less hindered ($+93.3 \text{ kJ}\cdot\text{mol}^{-1}$), with a relative energy difference of $+81.6 \text{ kJ}\cdot\text{mol}^{-1}$ between the deprotonated and molecular forms. The significant instability of the deprotonated forms reinforces the idea that ZB(110) is only weakly basic.

Two benzoic acid molecules (and their deprotonated equivalents) were placed on ZB(2x2) with two starting relative orientations of their phenyl groups: π -stacked and T-shaped. The π -stacking

HB dimer ($-151.4 \text{ kJ}\cdot\text{mol}^{-1}$) binds to the surface with less than twice the binding energy reported for one benzoic acid ligand ($-77.4 \text{ kJ}\cdot\text{mol}^{-1}$), suggesting that the dimerization energy does not fully compensate for the steric hindrance. Interestingly, T-shaped H^+B^- -HB (see Figure 3.7) has a significant negative binding energy ($-52.7 \text{ kJ}\cdot\text{mol}^{-1}$), whereas deprotonation of a single benzoic acid ligand on ZB(2x2) is energetically unfavorable ($+3.7 \text{ kJ}\cdot\text{mol}^{-1}$). Since the shared H^+ in Figure 3.7 is closer to one of the carboxylate groups (1.08 \AA) than the other (1.39 \AA), it is easy to identify which species remains in the molecular form. Meanwhile, the other proton remains adsorbed on a surface Se (1.48 \AA) far from its initial monomer. Cooperative ligand effects are proposed to enhance surface basicity by electrostatically stabilizing H^+ , as inferred from the $\text{C}=\text{O}-\text{H}\cdots\text{O}=\text{C}$ intermolecular bond scheme discussed above. The deprotonated T-shaped dimer is stabilized by the formation of a strong hydrogen bond, as the relative energy between the molecular and deprotonated forms decreases with respect to the single-ligand adsorption of HB (down to $+93.3 \text{ kJ}\cdot\text{mol}^{-1}$ from $111.3 \text{ kJ}\cdot\text{mol}^{-1}$).

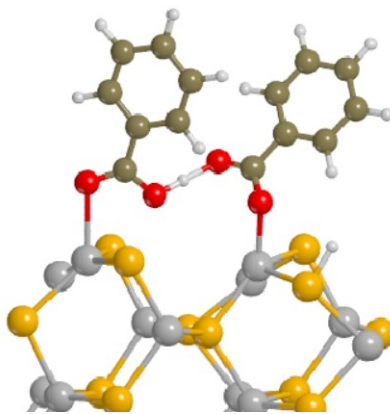


Figure 3.7. *Optimized structure of the deprotonated T-shaped benzoic acid dimer on ZB(2x2).*

Overall, ZB (110) has been shown to be insufficiently basic to stabilize the deprotonated forms of the analyzed ligands. Nonetheless, ligand-mediated deprotonation has been shown to be somewhat favorable for the benzoic acid dimer, despite the negative impact of high steric crowding. Further research into surface basicity should also consider wurtzite surfaces, whose larger unit cells would also allow for more ligands to be explicitly introduced.

3.3.6 Optical properties of CdSe materials.

Before delving into the surface and nanoparticle models, the electronic structure of bulk wurtzite and zinc blende CdSe is analyzed in greater detail. The projected density of states (pDOS) of bulk wurtzite and bulk zinc blende, shown in Figure 3.8. are probed for their exact element and orbital-wise contributions.

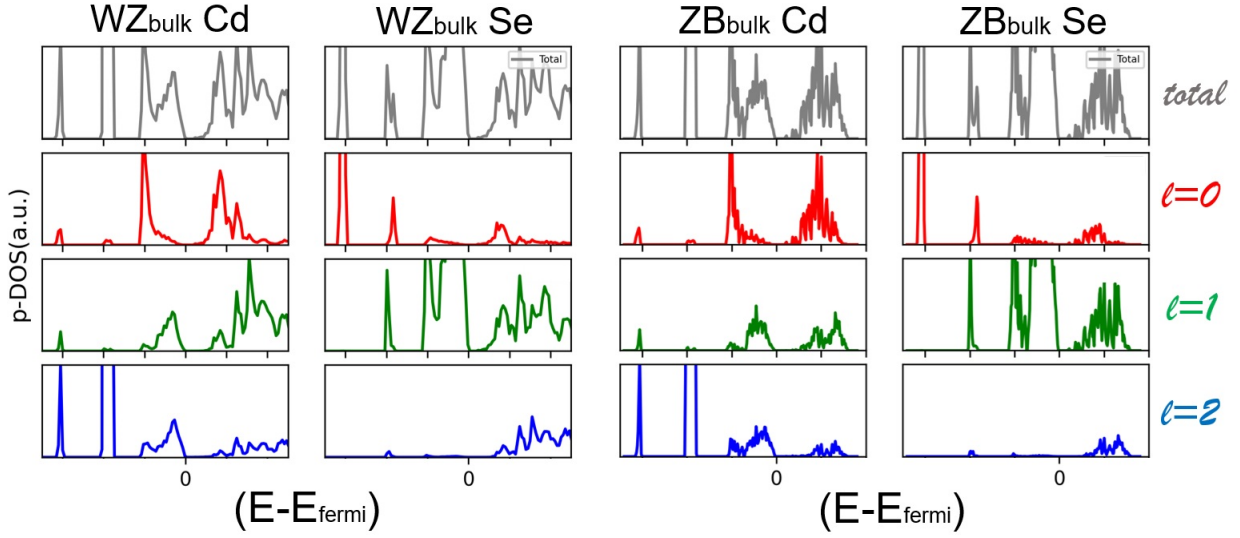


Figure 3.8. Projected density of states of bulk WZ and ZB CdSe, separated into their element and angular momentum-wise ($l = 0, 1, 2$) components.

All bands in bulk wurtzite CdSe have significant contributions from Cd atoms, as seen in Figure 3.8 (left): its d orbitals make up most of the internal bands, in which s and p orbitals have a minor presence. A more even Cd contribution to the valence band is observed, suggesting it is the result of Cd 4d, Cd 5s and Cd 5p orbital mixing. Likewise the conduction band is composed of unoccupied Cd 6s, Cd 6p and, to a lesser extent, Cd 5d. Regarding Se in wurtzite, it greatly contributes to the formation of the valence band through occupied p orbitals, while their unoccupied counterparts also feature extensively in the conduction band. Contribution from Se s orbitals concerns internal bands and the lower edge of the valence and conduction bands, while Se d orbitals are present throughout the conduction band. The Cd pDOS in zincblende (Figure 3.8, right) reveals once more large contributions to the bands at the internal energy levels, likely from core 3d electrons. Overall, contributions from Cd s and p orbitals are similar to those seen in wurtzite CdSe. As for Se, the low energy peaks exhibit contribution from Se core s electrons. The presence of Se p electrons in

both the valence and conduction bands is also analogous to that reported for Se in wurtzite. The effect of ligand passivation on the electronic structure of the surface and nanoparticle models hereby employed has been assessed from the changes in their band gap energies. The band gap energies of pristine ZB(110) and WZ(110), the pristine $(\text{CdSe})_{33}$ nanoparticle as well as their passivated counterparts with the short ligands are presented in Table 3.10, in gas phase and under implicit solvation. The pDOS of the bulk and surface pristine materials (Figure 3.9 a→d), of pristine $(\text{CdSe})_{33}$ (Figure 3.9 e) and $(\text{CdSe})_{33}$ -27C2-SH (Figure 3.9 f) are promptly discussed.

Table 3.10. *Best estimate value band gap energies (in eV) for CdSe pristine and passivated slab and nanoparticle models in gas phase (gp) and implicit water, acetonitrile and toluene solvation.*
^a BEV bulk zinc blende and wurtzite energies are 2.24 and 2.08, respectively.

	ZB(110)		WZ(110)		$(\text{CdSe})_{33}$		acetonitrile	toluene
	gp	water	gp	water	gp	water		
pristine ^a	2.66	2.67	2.79	2.84	3.06	3.43	3.40	3.17
C2-COOH	2.64	2.60	2.81	2.77	3.25	3.49	3.46	3.31
C2-NH ₂	2.65	2.58	2.82	2.76	3.44	3.51	3.50	3.47
C2-OH	2.56	2.55	2.83	2.83	3.30	3.43	3.41	3.33
C2-SH	2.70	2.65	2.83	2.79	3.42	3.49	3.48	3.43

The estimated band gap energies of the pristine models vary between 2.08 and 3.06 eV depending on the model and the polymorph considered. The band gap energy for bulk ZB is 0.12 eV smaller than that of the WZ polymorph [123, 184–186]. This is in agreement with the lower band gap experimentally determined for ZB, although both absolute band gaps are 0.3-0.4 eV higher than those obtained from experiments. The band gap energies of the slab models and the $(\text{CdSe})_{33}$ nanoparticle are higher than those of the bulk structure, which is consistent with a decrease in the dimensionality of the system. The pDOS indicates that the valence band for all materials is mainly formed by Se 4p orbitals, while the conduction band has contributions of both Cd 5s and Se 4p orbitals. Due to the different dimensionalities of the systems, the conduction and valence band edge states appear at different energies for each system. However, when referenced to the Fermi level, the pDOS of bulk and surface models are comparable and none of them present mid-gap states

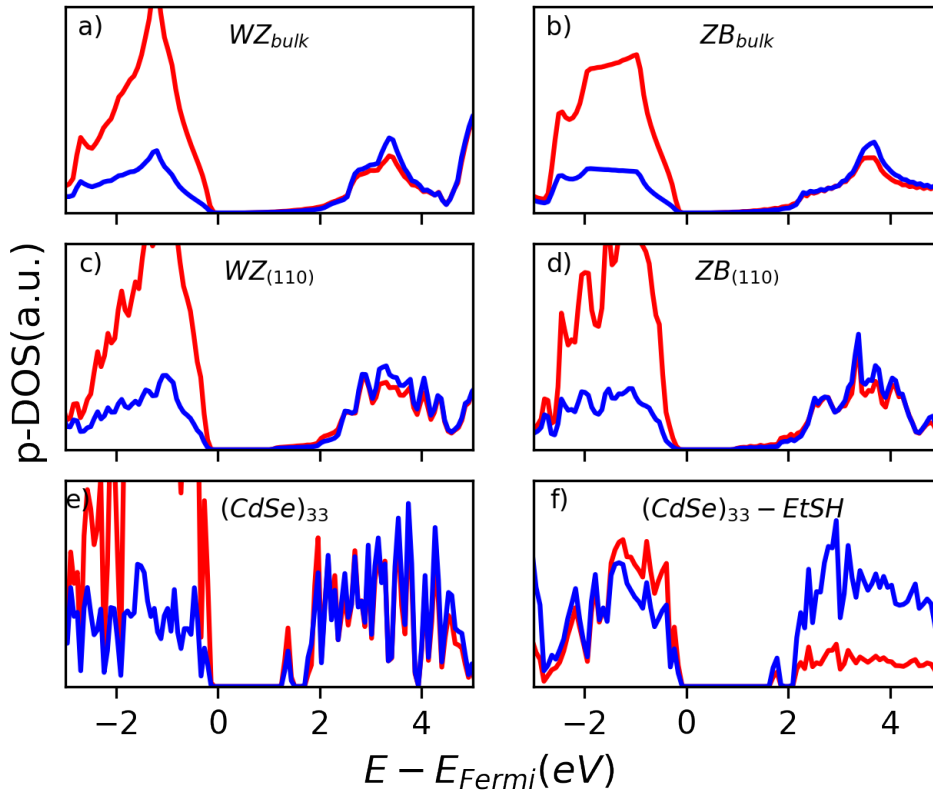


Figure 3.9. Projected density of states of bulk (a) wurtzite (b) zinc blende, the main (110) (c) wurtzite and (d) zinc blende surfaces, (e) the $(\text{CdSe})_{33}$ model and (f) the $(\text{CdSe})_{33}$ nanoparticle with 27 ethanethiol ligands adsorbed on its surface. Cd in blue, Se in red.

(Figure 3.9 a→d). Conversely, the pDOS of the nanoparticle models (Figure 3.9 e) are significantly different and are characterized by the presence of mid-gap states. Said presence is attributed to nanoparticle reconstruction, which results in shorter Cd \cdots Cd distances and smaller Se-Cd-Se angles.

Adsorption of capping ligands and both ZB and WZ surface models does not significantly alter the band gap, with almost all differences being with 0.04 eV. This is linked to a lowly reorganization of the surface Cd \cdots Cd distances. Meanwhile, adsorption on the nanoparticle induces an increase in the band gap of at least 0.2 eV. The band gap blue-shift is related to the displacement of the mid-gap states to higher values with respect to the Fermi level due to the interaction between the nanoparticle and the capping ligands (Figure 3.9 e-f). Particularly, the computed value for

(CdSe)₃₃-(C2-NH₂)₂₇ is 3.44 eV, in reasonable agreement with the reported adsorption spectrum of this cluster with decylamine in toluene ($\lambda=415$ nm) [162]. The band gap obtained from calculations correctly accounts for the differences between the materials hereby studied, yet it is 0.4 eV higher than that of the experiments as already seen in the case of bulk materials. Remarkably, TD-DFT calculations (see Table 3.11) at PBE0/def2-SVP level of theory suggest that the experimental and computational discrepancy does not arise from the selected functional but from the fact that the band gap is being analyzed instead of the optical transitions.

Table 3.11. PBE0/def2-SVP HOMO, LUMO and HOMO-LUMO gap energies (E_{H-L}), excitation energies (TD) and corresponding wavelength (λ) computed on the PBE optimized structures at TD-DFT level.

	HOMO (Ha)	LUMO (Ha)	E_{H-L} (eV)	TD (eV)	λ (nm)
Gas phase					
(CdSe) ₃₃	-0.24230	-0.12483	3.20	2.72	456
(CdSe) ₃₃ -C2-NH ₂	-0.16647	-0.043626	3.34	2.82	439
(CdSe) ₃₃ -C2-OH	-0.20796	-0.07823	3.53	3.03	410
(CdSe) ₃₃ -C2-SH	-0.20364	-0.06930	3.66	3.14	395
Water					
(CdSe) ₃₃	-0.20179	-0.06560	3.71	3.16	392
(CdSe) ₃₃ -C2-NH ₂	-0.18234	-0.04108	3.84	3.40	374
(CdSe) ₃₃ -C2-OH	-0.19448	-0.05143	3.89	3.34	371
(CdSe) ₃₃ -C2-SH	-0.19196	-0.04726	3.94	3.39	366
Toluene					
(CdSe) ₃₃	-0.2250	-0.09769	3.46	2.95	420
(CdSe) ₃₃ -C2-NH ₂	-0.17858	-0.04463	3.64	3.10	391
(CdSe) ₃₃ -C2-OH	-0.20479	-0.06880	3.70	3.17	391
(CdSe) ₃₃ -C2-SH	-0.20128	-0.06219	3.78	3.25	381
Acetonitrile					
(CdSe) ₃₃	-	-	-	-	-
(CdSe) ₃₃ -C2-NH ₂	-0.18239	-0.04140	3.84	3.30	375
(CdSe) ₃₃ -C2-OH	-0.19521	-0.05245	3.88	3.37	368
(CdSe) ₃₃ -C2-SH	-0.19264	-0.04818	3.93	3.38	367

The inclusion of solvent effects at the gas-phase-optimized structures using an implicit continuum model has little influence on the band gap of pristine and passivated surfaces (± 0.06 eV). On the one hand, the computed band gaps with and without surface passivation are very similar and suggest that in the absence of surface reconstruction, neither solvation nor ligand passivation tunes

the band gap. On the other hand, solvent effects have a large influence on the band gap of the pristine nanoparticle, which increases to 3.43 eV in water solution (3.06 eV in the gas phase). The presence of ligands passivating $(\text{CdSe})_{33}$ diminishes the influence of the solvent regardless of the nature of the ligand, and thus, the band gap of the passivated nanoparticles only increases by about 0.1-0.2 eV. Overall, the band gaps of the non-passivated and passivated nanoparticles become very similar in water. Similar trends are found when considering less polar solvents, namely, acetonitrile and toluene, although the effect is less pronounced.

Finally, since the results obtained from static calculations show that the band gap of the nanoparticle is very sensitive to solvation as well as to its structure, subtle changes associated with thermal effects may influence the band gap and the role of capping ligands. To evaluate these thermal effects, *ab initio* molecular dynamics calculations have been performed for five nanoparticle models: pristine $(\text{CdSe})_{33}$, $(\text{CdSe})_{33}\text{-(C2-COOH)}_{27}$, $(\text{CdSe})_{33}\text{-(C2-NH}_2\text{)}_{27}$, $(\text{CdSe})_{33}\text{-(C2-OH)}_{27}$ and $(\text{CdSe})_{33}\text{-(C2-SH)}_{27}$. For each trajectory, clusterization based on the cadmium centers has been performed and the band gap energies of each cluster's representative structure has been computed (with and without solvation). Next, three of the representative structures were selected having the lowest, highest and average band gap energy. The adsorption spectra of these three systems has been computed considering 10 excited states, presented in Figure 3.10.

The band gap energy values as well as the adsorption wavelengths are sensitive to the structure of the nanoparticle, with deviations as large as 0.5 eV (120 nm) in agreement with other reports [10]. The bandwidth of the adsorption spectra decreases once solvation is introduced. Furthermore, the weighted band gaps are smaller than those of the static calculations due to the changes in the HOMO and LUMO energies associated with the general increase of bond distances. Interestingly, the inclusion of thermal effects does not change the observed trends in the static calculations, as evidenced by the following observations. Firstly, even though the difference between the pristine and passivated nanoparticles is smaller than the static calculations, there is an increase in the gas phase band gap energy upon adsorption of the 27 capping ligands. Secondly, the solvent increases the weighted band gap of the pristine nanoparticle significantly but barely modifies that of the passivated models. Overall, the maximum wavelength of the absorption spectra of the solvated pristine nanoparticle is blue-shifted by 80 nm when compared to the *in vacuo* values, while a difference of 20 nm is reported between their relative absorption maxima under solvation.

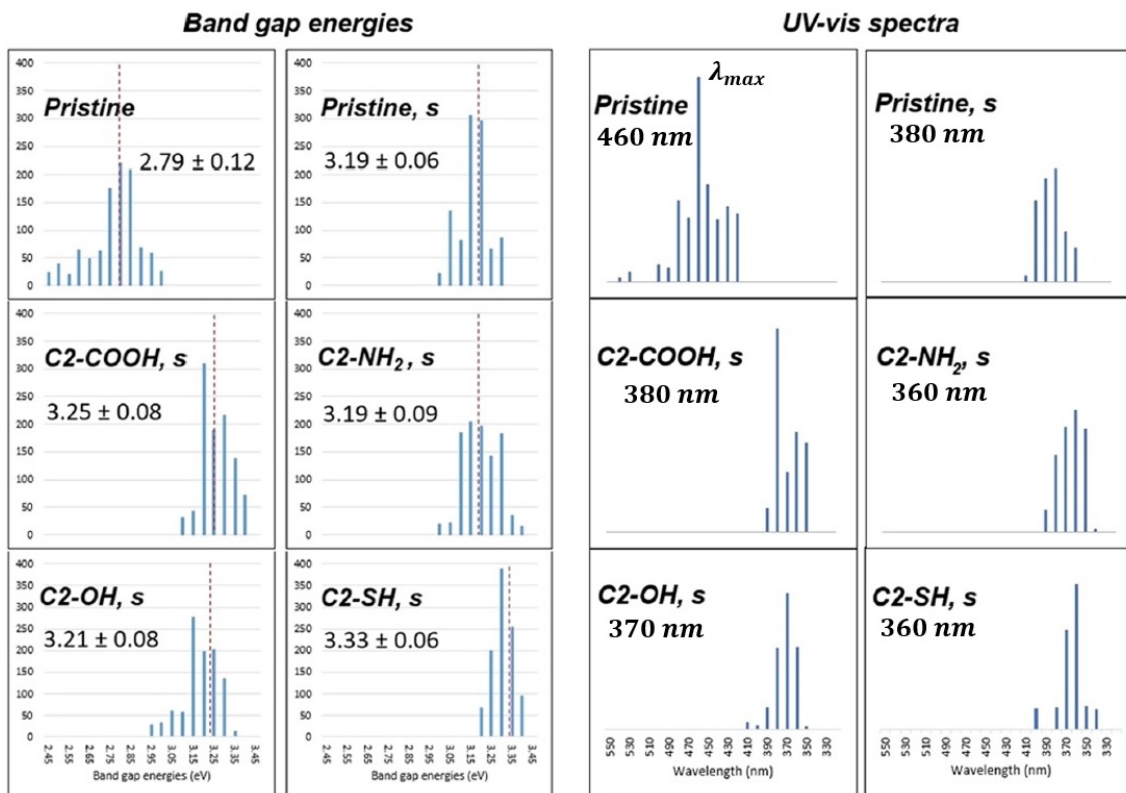


Figure 3.10. Weighted band gap and UV-vis spectra of the representative AIMD structures of pristine $(\text{CdSe})_{33}$ (with - s - and without solvation) and the fully covered nanoparticle models with 27 acetic acid, ethylamine, ethanol and ethanethiol capping ligands.

3.4 Conclusions.

Cadmium selenide nanoparticles are among the most promising quantum dots in photonics, catalysis and bioimaging. Surface passivation by means of capping ligand adsorption is essential for tuning the quantum dot's optical properties, and atomistic insight into how ligands alter their properties is key to the design of new, enhanced quantum dots. The herein presented computational results provide a broad, comprehensive insight into ligand passivation of CdSe nanomaterials through a combination of static and AIMD simulations, involving bulk, surface and nanoparticle models as well as up to five types of experimentally relevant ligands. Ligand adsorption is mainly electrostatic, with virtually no charge transfer from the ligand to the surface. At low coverages, ligand adsorption energies on ZB are computed to be higher than those on WZ by roughly $10\text{-}15 \text{ kJ}\cdot\text{mol}^{-1}$ owing to the larger surface-ligand dispersive interactions. Moreover, for both polymorphs, phosphine oxide,

phosphonic acids and amines adsorb more strongly than carboxylic acids, alcohols and thiols; this correlates adequately with their proton affinities, further supporting the electrostatic nature of the interaction.

Full ligand coverage does not alter the trends reported for low ligand coverages. However, the steric hindrance of phosphine oxides and tertiary amines weakens their adsorption on the undercoordinated surface Cd sites. Furthermore, the adsorption difference between ZB and WZ decreases due to larger ligand-ligand dispersive interactions in the latter. Dispersive ligand-ligand interactions are important mainly for large ligands; their contribution has been estimated to be about $5.2 \text{ kJ}\cdot\text{mol}^{-1}$ per CH_2 unit.

Regarding the optical properties of pristine materials (bulk, surfaces and the nanoparticle), it has been shown that reducing model dimensionality raises the band gap energy. However, the density of states of $(\text{CdSe})_{33}$ presents mid-gap states that decrease the overall HOMO-LUMO energy difference. These mid-gap states arise from the nanoparticle's reconstruction, which leads to shorter $\text{Cd} \cdots \text{Cd}$ distances and smaller Se-Cd-Se angles. Ligand passivation on both ZB and WZ surfaces is not connected to important surface reconstruction, thus, their band gap is similar to that of the bare surfaces. In contrast, ligand adsorption on $(\text{CdSe})_{33}$ induces significant structural reconstruction related to a general increase in the $\text{Cd} \cdots \text{Cd}$ distances. Therefore, mid-gap states are shifted to higher energies: the HOMO-LUMO gap is thus raised, so that the maximum of the adsorption spectrum is blue-shifted upon passivation.

Relevant conclusions can be drawn from the combination of slab and nanoparticle models. In the slab models, the rigid and crystalline unsaturated cadmium atoms are essentially not affected neither by the adsorption of organic ligands nor the solvent effects. Meanwhile, centers located in more flexible environments (*i.e.* the $(\text{CdSe})_{33}$ nanoparticle) are more sensitive to the presence of both the capping ligands and the solvent, although the effects do not depend on the nature of the ligand. This imposes limitations on the tuning of optical properties through ligand passivation. Passivation through core-shell materials are proposed to be a more suitable strategy, as explored in-depth in the following Chapter.

Core-Shell Quantum Dots

After extensively characterizing CdSe-only systems in Chapter 3, our attention is turned to hybrid systems containing more than one type of metal chalcogenide, with three additional materials being considered: CdS, ZnSe and ZnS. Firstly, the validity of Vegard's law for bulk solid solutions is tested on Zn-doped CdSe. Zinc blende CdSe, CdS, ZnSe and ZnS (110) surfaces are explored next. The optical properties of differently sized quantum dots are then determined for the four metal chalcogenides, with and without alkylthiol passivation. Ligand passivation of core-only quantum dots is shown to consistently raise their band gap and HOMO-LUMO gap energies without significantly altering the density of states and frontier orbitals, respectively. Afterwards, the $(MX)_{33}$ quantum dot is made into a $(CdSe)_7(MX)_{27}$ core-shell structure, whose pristine and passivated electronic structure is herein reported. Analysis of frontier orbitals suggests that Type I, reverse Type I or Type II can be obtained depending on the material employed. The model's reduced size prevents an analysis of how core-to-shell ratios influence the frontier orbitals. Overall, results show that the addition of ligand passivation is essential to a comprehensive *in silico* characterization of core-only and core-shell quantum dots.

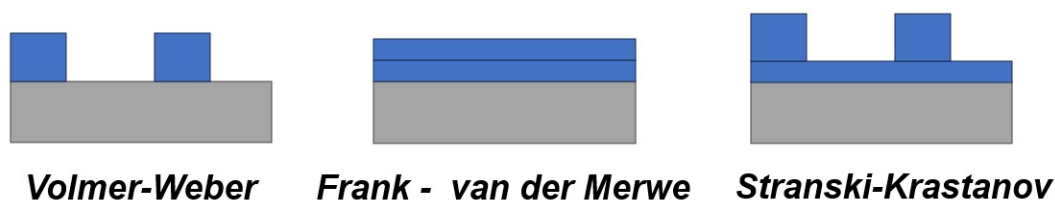
4.1 Introduction.

Early reports on the systematic synthesis of quantum dots already recognized their unique optoelectronic properties [13, 21], which now have become central to state of the art applications in imaging [39], catalysis [187, 188] and electronics [189, 190]. Owing to the quantum confinement of

the excitons generated therein, quantum dots exhibit size-tunable band gap energies, photoluminescence, electroluminescence and cathodoluminescence [17]. Conventionally, the term "quantum dot" is applied to semiconductor nanoparticles with radii in the order of Bohr's exciton radius [35]. The possibility of inducing carrier multiplication (*i.e.* the generation of more than one exciton per absorbed photon), in addition to their already remarkable molar absorption and photostability, makes them ideal materials for photovoltaic devices [190]. Quantum dots have been an active topic of research for the last 30 years, even warranting the 2023 Noble Award in Chemistry to Bawendi, Brus and Ekimov. Despite substantial advances in nanofabrication, colloidal synthesis still finds widespread use as it is reliable and cost-effective [13, 15, 35]. Yet not simple, as already in their early reports Bawendi and coworkers linked effective quantum dot fabrication to careful control over quantum dot growth, particularly by rational use of capping ligands [13]. Ligands were shown to narrow quantum dot size distribution by slowing aggregation kinetics of the Ostwald ripening and to induce an electronic passivation effect, both resulting in higher quantum yields and narrow emission lines [13, 17]. Surface defects were soon identified as a source of carrier trap states deleterious to the optical activity of quantum dots [13, 35]. In the following years, experimental and computational reports [8–10, 191] have shed more light on quantum dot surface passivation, yet precise control of surface passivation remains an active challenge [190].

Core-shell growth and passivation. Ligand functionalization and inorganic shell passivation are two commonly employed, non-mutually exclusive strategies to ensure adequate passivation of said defects. Ligands are invariably present on the surface of quantum dots as a result of the synthetic process, and may be replaced through post-synthetic treatments. For instance, substitution of ligands commonly employed in synthesis (*e.g.* trioctyl phosphine oxide) for more polar-terminated ligands increases water solubility without decreasing photoluminescence [17]. In contrast, fabrication of core-shell quantum dots (as opposed to "core-only") requires carefully controlled epitaxial growth conditions: only materials with similar crystal structures can generate a defect-free interface between the core and the shell. Even then, substantial differences in their lattice parameters (commonly measured in terms of *lattice mismatch*) can also result in interfacial strain and subsequent trap state appearance [21, 24, 29, 192]. Furthermore, faceted cores can also reduce the uniformity of the growing shell, resulting in rough surfaces and non-homogeneous thicknesses [192]. Three

commonly cited growth mechanisms are the Volmer-Weber mode (island growth), the Frank-van der Merwe mode (layer-by-layer) and the Stranski-Krastanov mode (layer-by-layer up to a critical point, followed by island growth). These mechanisms are schematically shown in Scheme 4.1. Which growth mechanism is followed depends on the materials involved, their lattice mismatch or the elastic properties of the core-substrate, and can potentially change during synthesis [192]. On a thermodynamical basis, small cores and thin shells of materials with similar lattice parameters result in the most uniform core-shell quantum dots [192].



Scheme 4.1. Selected surface growth mechanisms, where the blue layers/islands represent new material epitaxially grown on the substrates (gray).

Passivation may serve an additional purpose when biocompatibility concerns arise, particularly for *in vivo* imaging applications. Such is the case of Cd-based quantum dots, whose usage is severely limited by cadmium's cytotoxicity [193]. As a naturally occurring pollutant, cadmium is a strongly carcinogenic agent with a long bioaccumulation period (25-30 years) and an ever-increasing presence linked to industrialization [193]. It is suggested that Cd-induced oxidative stress can damage the mitochondria in liver and kidney cells, while DNA mutations can derive into several epigenetic illnesses [193]. This is especially concerning for cadmium selenide (CdSe) quantum dots, which are otherwise excellent candidates for imaging applications. Although Cd leaching is the main health hazard, Se is not completely innocuous, as excess intake can produce life-threatening selenosis [194]. Naturally, Cd is less likely to leech if its used as the core, leaving open the search for a biocompatible shell which does not negatively impact the catalytic or optoelectronic performance of the core-shell quantum dot¹. In hydrogen evolution photocatalysis, ZnO has found use as a shell to CdS cores owing to its non-toxicity and adequate conductivity [188]. Early, successful *in vivo* applications include the chimeric fusion of proteins to CdSe@ZnS [17] or use of CdSe@CdTe core-shell quantum dots as near-infrared probes for lymph nodes in animals [195]. Highly monodisperse CdSe@CdZnS

¹Regarding notation, MX@NY refers to core of MX and a shell of NY.

and CdSe@CdS quantum dots have been conjugated with mice antibodies without reducing their quantum yields [19], while CdS@CdTe biofluorescent probes capped with glycoprotein inhibitors are promising anti-cancer drugs [39].

Electrooptical properties. In terms of exciton generation and recombination, rational core-shell nanofabrication allows for either charge carrier to be confined in the core, in the shell or delocalized throughout [41–43]. The electronic structure of a core-shell quantum dot² is determined by its composition, with the final alignment between core and shell energy levels depending significantly on the offset of the valence and conduction bands of the shell and the core [189]. As already discussed in Chapter 1 (see Scheme 1.1), at least three types of core-shell quantum dots can be distinguished from charge carrier spatial distributions. In turn, these depend of where the wide band gap material is placed [38, 189]:

- **Type-I.** The shell is the wide-band gap material (*e.g.* CdSe@CdS, CdSe@ZnS or CdTe@CdS).
- **Reverse Type-I.** The core is the wide-band gap material (*e.g.* in CdS@CdSe or ZnS@CdSe).
- **Type-II.** The shell’s conduction and valence bands are either above or below those of the core (*e.g.* in CdTe@CdSe (CdSe@CdTe), ZnTe@CdS or PbTe@CdTe).

In Type-I core-shells, the exciton is confined in the core since as the valence and conduction bands are constrained by the shell’s band gap. Confinement of the exciton within the core can enhance photoluminescence by reducing its interaction with the surrounding medium to a minimum [187]. Owing to their low lattice mismatch, CdSe@CdS quantum dots undergo adequate epitaxial growth and stand amongst the most promising Type I core-shell [189]. In contrast to Type I materials, the charge carriers are confined within the shell in reverse Type-I core-shells. It should be noted that a certain degree of delocalization is possible in Type-I core-shell quantum dots, with differences in delocalization appearing for holes and electrons [187]. Lastly, each domain has one of the charge carriers in Type-II core-shell quantum dots, although the wave function is seldom fully localized [190]. Such is the case of PbX@CdX (X=S,Se) quasi-Type II core-shell quantum dots: while their frontier, occupied orbitals are confined to the core, the orbitals above the LUMO

²As a reminder, the herein employed notation is core@shell.

are delocalized throughout and thus receive contributions from both the core and the shell [190]. Quasi-Type II CdSe@CdS core-shell quantum dots with thin shells can also be fabricated [189]. Ultimately, the exact charge confinement regime in a core-shell quantum dot determines its potential applications. Due to their spatial proximity, electron-hole recombination times are shorter in Type-I and reverse Type-I core-shells, which therefore are less suitable for photovoltaic applications than Type-II core-shell [38]. Simultaneously, photocatalysis with Type I CdSe@ZnS was shown to be feasible (the ZnS shell was proposed to impede back-electron-transfer once the electron left the quantum dot), but it is only modestly efficient [187]. Moreover, since charge separation is actually enhanced in Type-II materials, these are the natural choice for photovoltaic and photoconductive devices [44, 190]. The dynamics of exciton recombination are highly dependent on the structure of the core/shell interface: defect-free interfaces hinder exciton recombination, whereas defect-ridden interfaces (originated by high lattice mismatches) generate electron trap states that favor non-radiative recombination and reduce photovoltaic efficiency [190]. Minimizing lattice mismatch is therefore a major concern in core-shell quantum dot synthesis, for which atomic layer deposition is a reliable approach [188].

Vegard's law. In the subject of hybrid materials, Vegard's law [196] is now presented as a brief aside. Initially intended for binary solid solutions in mineralogy, Vegard's law states that the final lattice parameter is linearly dependent on the molar fractions of each individual component:

$$a_{MX,NY} = a_{MX} \cdot \chi + a_{NY} \cdot (1 - \chi) \quad (4.1)$$

Where a_{MX} , a_{NY} are the bulk lattice parameters of compound MX (with molar fraction χ) and NY (molar fraction $1 - \chi$). Finally, $a_{MX,NY}$ is the lattice parameter of the resulting solid solution. Impurity-driven changes in each of the surface lattice parameters can be described by Equation 4.1. Also as an extension to Vegard's law for semiconductor bulk materials, the final band gap energy in solid solutions is expected to follow a similar law:

$$E_{g,(MX,NY)} = E_{g,MX} \cdot \chi + E_{g,NY} \cdot (1 - \chi) \quad (4.2)$$

Where $E_{g,MX}$, $E_{g,NY}$ and $E_{g,(MX,NY)}$ are the bulk band gap energies of the corresponding

materials. While not originally intended for low-dimensional materials, Vegard's law could provide an estimate to the lattice parameter of hybrid surface slabs and their band gap energies.

Computational research. Theoretical calculations involving realistically-sized quantum dots, which may involve thousands of atoms, must juggle with the accuracy-to-cost ratio. Adding to the modelling aspects already present for core-only quantum dots (*e.g.* stoichiometry, polarity, facet growth, ligand passivation), lattice mismatch, the core-to-shell ratio and interface morphology are specific to core-shell models. Since the precise structure of core-shell quantum dots is not always experimentally characterized, screening of tentative models is often necessary. Even in spherical core-shell models, there is choice to make on how the interface is dealt with. For instance, in the "pure core" approach the core-shell interface is abrupt and both regions have distinct compositions; meanwhile, in "graded core" models the concentration of core material decreases progressively and only becomes zero at the outermost layers. For instance, Sarma and coworkers [197] developed graded core CdSe@CdS core-shell quantum dots by replacing shell S atoms for core Se atoms, so that the layer concentration of Se decreased from the core (1) to the shell (0) in steps of 0.2 units. Alloyed core models, in which Se atoms were randomly placed throughout the shell, were also developed [197]. Regarding surface defects and reconstruction, capping ligands are commonly employed. It has been suggested that passivation of dangling bonds with pseudohydrogens allows for model-specific changes to be better monitored than with capping ligands [197]. Regardless, defect-sensitive phenomena, such as HOMO-LUMO charge transfer, have been studied in unpassivated core-shell quantum dots [198].

The simulations are most frequently ran at the density functional theory level, with B3LYP and PBE exchange-correlation functionals being a frequent choices [10, 187, 191]. Core-shell quantum dots have also been simulated with LDA functionals (Ceperley-Alder parametrization) and double- ζ basis sets with polarization [197]. For core-shell quantum dots in particular, the band structure of a $(\text{CdSe})_{33} @ (\text{ZnS})_{78}$ was explored after phonon-induced relaxation, showing that the ZnS shell localized a hole-trap state near the valence band (centered on a S atom) whilst not affecting the conduction band [199]. Auger recombination in core-shell quantum dots has been explored with tight-binding wave functions that provide more precise Coulomb matrices, which in turn allow for quantum dots above 11 nm to be considered (involving up to 22.000 atoms and 100.000 atomic

orbitals) [199]. While the literature on *ab initio* core-only quantum dots is extensive and explores a wide range of phenomena (*e.g.* passivation, thermal effects, electronic and phononic dispersion), reports on core-shell quantum dots are comparatively scarce. To the best of our knowledge, a systematic approach to ligand passivation in core-shell systems that also factors in size effects has not been published.

In this Chapter, DFT simulations are used to explore the electronic structure of different CdSe, CdS, ZnSe and ZnS materials, building up from their pristine bulk and surface structures to core-only and core-shell quantum dots. Taking into account the acute toxicity of CdSe, only core-shell quantum dots models in which CdSe is the core are considered. Material and dimensionality-induced changes to the electronic structure are assessed using band gap energies as descriptors. For the quantum dots, the HOMO-LUMO gaps are also calculated. The effect of alkylthiol ligand passivation is similarly considered.

4.2 Computational Details.

Bulk, surface and quantum dot models of the four metal chalcogenides herein considered (CdSe, CdS, ZnSe and ZnS) are explored using DFT calculations. The computational groundwork has already been established in the previous Chapter: suffice it to include a brief account of the specifications and, importantly, the new core-only and core-shell models employed.

Models. The models previously employed for wurtzite and zinc blende CdSe (Chapter 3) have been repurposed for CdS, ZnSe and ZnS, including those of their bulk structures and of pristine WZ(110) and ZB(110) facets (Figure 4.1). The smallest zinc blende slab model, ZB(1x1), is used to study the effect of ligand passivation on the corresponding CdS, ZnSe and ZnS surfaces induced by selected alkylthiols ³.

Different large quantum dot models have been directly cut from bulk wurtzite or generated with the BCN-M code [47]. Different sizes have been considered: (MX)₆, (MX)₃₃, (MX)₆₀, (MX)₆₈, (MX)₁₀₅ and (MX)₁₃₃, where M= Cd, Zn and X = Se, S. These models are shown in Figure 4.2. It should be noted that the (MX)₆₀ and (MX)₁₀₅ (made with BCN-M) are faceted and cylindrical, whereas the other four models are spherical and are cut from bulk wurtzite. Next, following

³Ligand choice was based on the reportedly strong influence thiols have on said semiconductor structures

the modelization scheme proposed in Figure 4.3, a $(\text{CdSe})_6(\text{MX})_{27}$ core-shell model was built by replacing the outermost 27 MX units of $(\text{CdSe})_{33}$ by those of the other three materials (@CdS, @ZnS and @ZnSe).

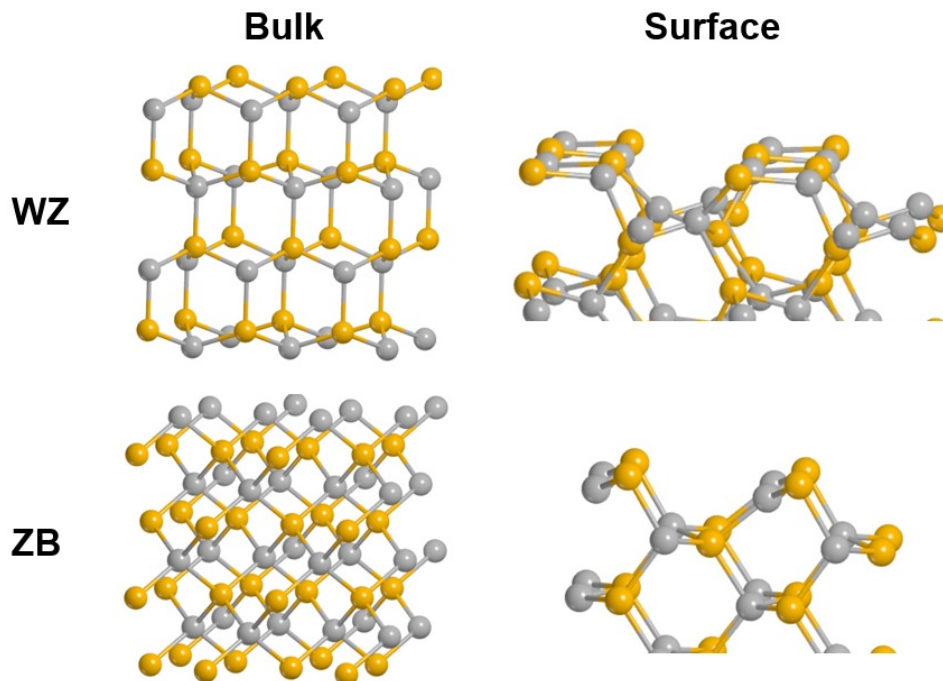


Figure 4.1. *a) Wurtzite and b) zinc blende models corresponding to i) the bulk and ii) the (110) facet structures.*

The last modelization step involves the passivation of the core-shell quantum dots with ligands: ethanethiol or methanethiol, indistinctly.⁴ Based on prior results, thiol adsorption is known to take place at the outermost cation binding sites. As done for the pristine $(\text{MX})_{33}$ core-only quantum dots, 27 ligand molecules were used for the $(\text{CdSe})_6(\text{MX})_{27}$ core-shell structure. Despite being small in experimental terms, the large number of atoms in the passivated $(\text{CdSe})_6(\text{MX})_{27}$ systems (over 300 atoms) already implies significant computational costs.

Level of theory. For each of the four materials, optimization for bulk WZ and ZB, the WZ(110) and ZB(110) surfaces⁵ and each quantum dot model was carried out at DFT level employing the PBE functional [165] under the D2 dispersion correction [166], as implemented in VASP [163, 164]. The atomic ionic cores were represented with projected augmented wave pseudo-potentials [167,

⁴In Chapter 3, band gap energies were shown to be mostly insensitive to alkyl chain length.

⁵Lattice parameter optimization was used.

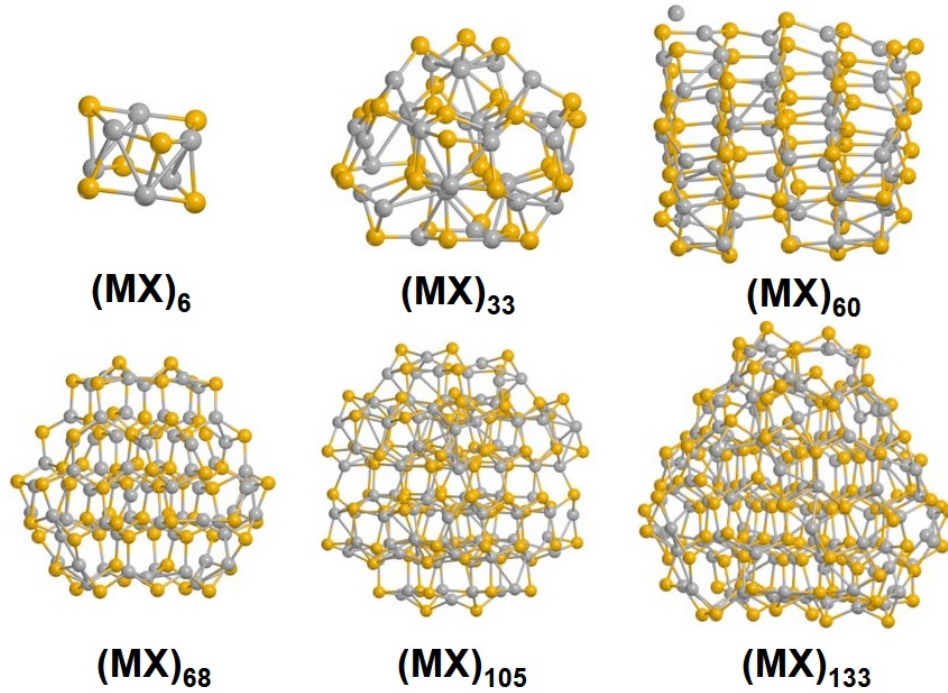


Figure 4.2. Core-only nanoparticle models corresponding to $(CdSe)_6$, $(CdSe)_{33}$, $(CdSe)_{68}$, $(CdSe)_{105}$ and $(CdSe)_{133}$.

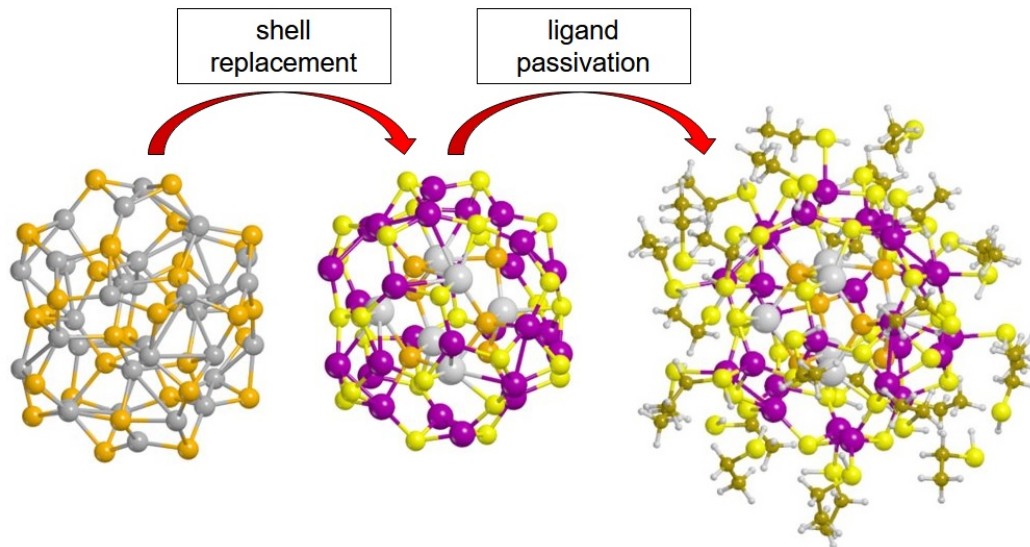


Figure 4.3. Core-shell quantum dot modelization process for $(CdSe)_6@(MX)_{27}$. The outermost atoms on the optimized core-only nanoparticle are replaced, promptly optimized, and finally passivated with ligands to generate the complete model.

168], and 500 eV cutoff for the plane waves of the valence electrons. For bulk ZB and WZ structures, a cubic $8 \times 8 \times 8$ k-point mesh was used for optimization. Band gap energies and DOS profiles were

generated with a denser $32 \times 32 \times 32$ mesh in single-point calculations. For the surface slab models, $8 \times 8 \times 1$ Monkhorst-Pack k -point meshes [169] were employed for ZB(1x1), while for WZ(1x1) coarser ($4 \times 4 \times 1$) meshes were used. Geometry optimizations of core-only and core-shell quantum dots were carried out through Gamma-point calculations, as these systems are non-periodic in nature. Regarding band gap energies, which are poorly reproduced by GGA methods (including PBE), material-specific corrections were determined by means of the hybrid functional PBE0 (reportedly better at reproducing the experimental value of semiconductor materials [137, 151]). This BEV approach has already been tested successfully for CdSe materials in the preceding Chapter. In addition to BEV band gap energies, HOMO-LUMO gaps were calculated at PBE0/def2-SVP level [179, 180] (Gaussian16 package [178]) for core-only and core-shell quantum dots.

4.3 Results and discussion.

In a first Section, structural and electronic changes in bulk and surface solid solutions are explored using hybrid models. Firstly, bulk CdSe-ZnSe solid solutions are explored in terms of lattice compression/expansion and shifts in the band gap energy, which is later extended to surfaces and ligand adsorption on CdS, ZnSe and ZnS (110) surfaces.

4.3.1 Pristine bulk materials.

Wurtzite and zinc blende CdSe have the largest bulk lattice parameters out of the four compounds considered: predictably, as per Vegard's law, progressive replacement of Cd (Se) by Zn (S) should reduce the final lattice parameter. For CdSe-NY solid solutions (NY=CdS, ZnSe or ZnS), lattice mismatch values are reasonably low for CdS (4.27 %) and ZnSe (6.57 %), yet significant for ZnS (11%) as previously reported by Grunwald [11]. Before dealing with solid solutions, it is convenient to characterize the corresponding bulk, single-material WZ and ZB structures. Bulk PBE, PBE0 and best estimate value band gap energies for the structures at hand are presented in Table 4.1.

As expected, PBE band gap energies reported are noticeably underestimated in spite of the dense $32 \times 32 \times 1$ k -point meshes used. Note that the subscript "fine" in Table 4.1 refers to the fineness of the k -point grid ($32 \times 32 \times 1$), compared to the "low" results that employ a coarser $8 \times 8 \times 1$ grid. For CdSe and CdS, theoretical band gap energies are red-shifted by roughly 1 eV, increasing

Table 4.1. *PBE-D2, PBE0-D2, the PBE0 blue-shift (Δ_{PBE0}) and Best Estimated Value band gap energies (in eV) for wurtzite (WZ) and zinc blende (ZB) bulk CdSe, CdS, ZnSe and ZnS. Experimental values added for reference. ^a 32x32x32 k-point mesh. ^b 8x8x8 k-point mesh. ^c Obtained as the difference between PBE_{low} and PBE0 with 8x8x8 k-points used in the optimization. ^d Best Estimated Value.*

Material	Polymorph	PBE_{fine}^a	$PBE0^b$	Δ_{PBE0}^c	BEV^d	EXP
CdSe	WZ	0.68	3.09	1.46	2.24	1.7-1.8
	ZB	0.66	2.49	1.42	2.08	1.7-1.8
CdS	WZ	1.30	3.68	1.65	2.95	2.42
	ZB	1.18	3.11	1.62	2.80	2.42
ZnSe	WZ	1.49	4.08	1.69	3.18	2.70
	ZB	1.39	3.45	1.66	3.05	2.70
ZnS	WZ	2.08	4.67	1.85	3.93	3.91
	ZB	2.22	4.40	1.87	4.09	3.54

1.2 eV in the case of ZnSe and of zinc blende ZnS. The underestimation of the wurtzite ZnS band gap is the most severe. Conversely, PBE0 substantially raises band gap energies due to the inclusion of a significant fraction of exact Hartree-Fock exchange (25%). The PBE0 blue-shift (Δ_{PBE0}) occurs on a composition-specific basis. That is, it depends on the material under consideration: it is the lowest for CdSe (1.46 eV and 1.42 eV for WZ and ZB, respectively), roughly the same for CdS and ZnSe, and up to 0.4 eV higher for ZnS (1.85 - 1.87 eV). There is seemingly no proportionality ratio between the Δ_{PBE0} of the different materials. Interestingly, the difference between band gap energies of the WZ/ZB polymorphs of a material is, at most, 0.2 eV. For each case, best estimate values are obtained by adding the corresponding PBE0 shift. The lowest BEVs correspond to CdSe (1.46 and 1.42 for WZ and ZB, respectively) and the highest for ZnS (3.92 and 4.09 eV for WZ and ZB, respectively). The other two compounds' BEVs fall in between: 2.95 and 2.80 eV for CdS; 3.18 and 3.05 eV for ZnSe. They exceed their respective experimental band gap energies but correctly predicting ZnSe to have the higher value out of the two. The accuracy of the best estimate values, in terms of relative errors, ranges between 31% for wurtzite CdSe to a remarkable 0.5% for wurtzite ZnS, with most BEVs falling in the 10-20% interval. As previously done for CdSe structures, these material-dependent Δ_{PBE0} corrections will be applied to the band gap energies of the new surface and nanoparticle models. This BEV approach is not suitable for core-shell materials, however, as

each component has a different PBE0 blue-shift.

Some final notes on the pristine bulk structures. The projected DOS of bulk CdSe, CdS, ZnSe and ZnS are shown for wurtzite (Figure 4.4 left, a→d) and for zinc blende (Figure 4.4 right, a→d). While the overall shape of the conduction band is similar across materials, the conduction band minimum is increasingly blue-shifted from CdSe to ZnS. In terms of the element-wise contributions to each band, just as with CdSe, it would appear the chalcogenide (Se or S) contributes significantly to the valence band, less so to the conduction band. Conversely, the metal (Cd or Zn) contribute more modestly to either band. It is worth noting that, as discussed for pristine bulk CdSe, none of the bulk materials is expected to exhibit mid-gap states due to the high degree of crystallinity in their lattices.

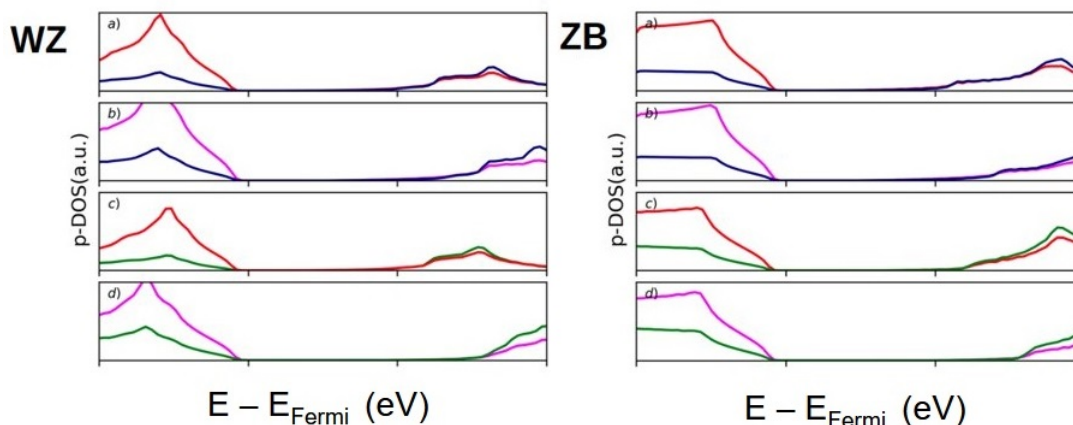


Figure 4.4. *PBE-D2 density of states of pristine wurtzite (left) and zinc blende (right) bulk (a) CdSe, (b) CdS, (c) ZnSe and (d) ZnS. Elemental contributions shown for Cd (blue), Se (red), Zn (green) and S (magenta).*

4.3.2 CdSe-ZnSe solid solutions. Vegard's law.

In spite of their intrinsic differences, solid solutions are expected to provide useful atomistic insight into the core-shell surfaces. Since four materials are being considered, there are six unique binary solid solutions, although only the three involving CdSe are presently considered. As discussed above, Vegard's law has been tested on bulk zinc blende CdSe and ZnSe models, which were built by replacing Cd cations for Zn cations. Both ion and lattice optimization are necessary, since replacement of CdSe units for ZnSe is expected to compress the unit cell due to the latter's shorter

lattice parameter. A systematic substitution pattern has been applied: replaced atoms belong to one layer of the zinc blende supercell bulk model shown in Figure 4.5, although non-systematic substitution fractions below 15 % have also been assayed. Use of supercell is convenient as more atoms can be replaced, that is, a broader range of impurity fractions can be explored. As shown in Figure 4.5, each of the four layers has 8 metal atoms, thus there are a total of 32 Cd atoms. Lattice parameters and band gap energies for the solid solutions are presented in Table 4.2 (note that the latter have not been corrected to the BEV, as it is not clear how to best weigh each material's contribution).

Table 4.2. *Lattice parameters and uncorrected PBE band gap energies in bulk CdSe-ZnSe solid solutions with varying number of ZnSe layers. PBE band gap energies were obtained from a coarser $16 \times 16 \times 16$ k-point mesh.*

System	ZnSe layers	χ	Lattice parameter	E_g
CdSe	-	-	a=12.044	0.66
Cd _{1-x} SeZn _x	1	0.25	a=11.933 b=12.113	0.74
	2	0.50	a=11.688 b=11.911	0.88
	3	0.75	a=11.479 b=11.642	1.09
ZnSe	-	1	a=11.126	1.39

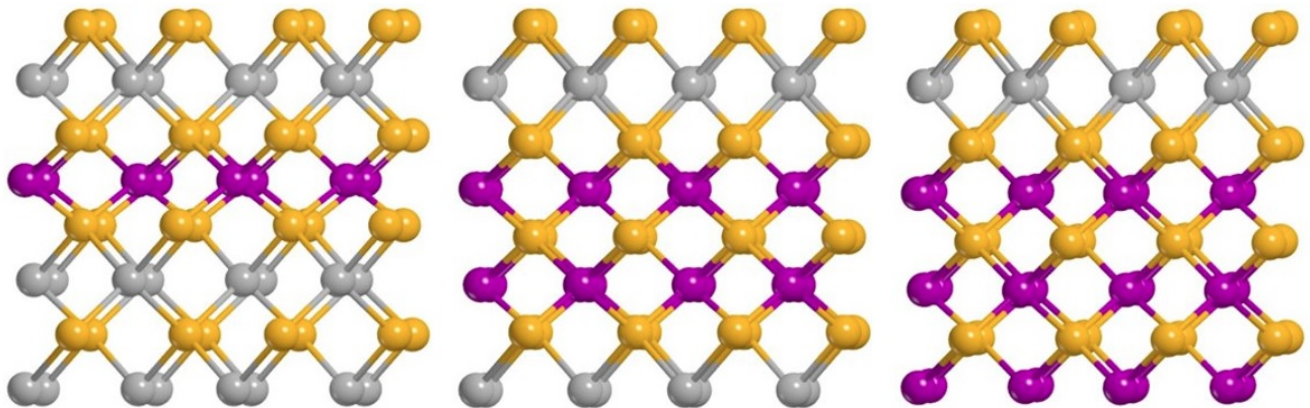


Figure 4.5. *Zinc blende bulk superlattices employed to test Vegard's law in solid solutions. From left to right, one/two/three layers of Cd atoms are replaced by zinc atoms. In gray, Cd; in orange, Se; in purple, Zn.*

Some structural changes are already apparent for substitution fractions below 0.25 (replacement of less than 8 Cd atoms), becoming more important when entire ZnSe layers are added. At this point, cubic symmetry is clearly lost (a and c decrease more than b) and the solid solution's unit cell is progressively compressed. So much is clear from their relative volumes, as the CdSe unit cell is 1.25 times larger than that of ZnSe. Arguably, the fact that the three lattice parameters are not reduced equally is due to lattice vector discrimination: only one substitution direction is selected when replacing layers, even if all three directions are equivalent in practice. Disregarding this as an artifact, the average value of the lattice parameters should be assumed to be equal. Said average parameters have been plotted against the fitting to Vegard's law in the top curve in Figure 4.6.

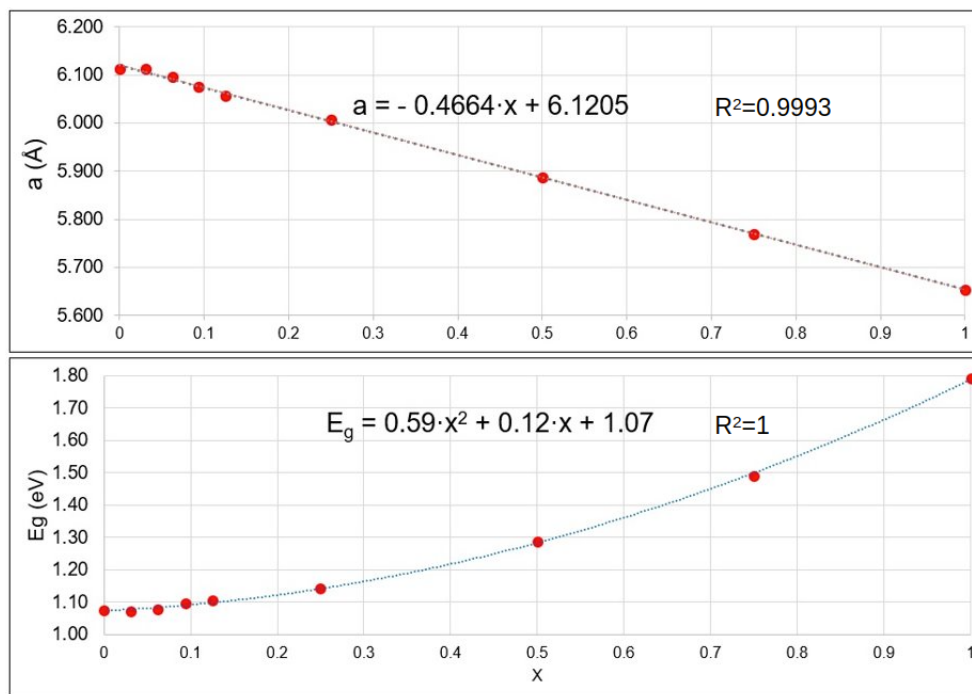


Figure 4.6. *CdSe-ZnSe bulk solid solution PBE lattice parameter (top, in \AA) and band gap energy (bottom, in eV) for increasing atomic fractions of Zn (χ), with their corresponding linear and quadratic fittings.*

Fitting improves as χ is raised above 0.25, although lattice compression when one to five atoms are replaced ($\chi < 15\%$) is not far off. High, positive correlation ($R^2 = 0.9993$) is observed overall, with remarkably accurate fits corresponding to $\chi = 0.25$ (1 layer), $\chi = 0.5$ (2 layers) and $\chi = 0.75$ (3 layers). As presented in the bottom curve in Figure 4.6, the band gap energies are adequately fit by a quadratic polynomial, with a correlation factor of $R^2 = 1$. Just as with the lattice parameters,

fitting improves as more Zn atoms are introduced. Regardless, the results presented in Figure 4.6 prove that Vegard’s law can be used for CdSe-ZnSe solid solutions; similar adequacy is expected for any of the other considered binary combinations of metal chalcogenides. As a step towards core-shell structures, this approach is applied to extended surfaces in the following section.

4.3.3 Pristine extended surface materials.

The optimized, CdSe ZB(110) and WZ(110) surfaces are used as starting points for the atom and cell parameter optimization for CdS, ZnSe and ZnS. As expected from their lower bulk lattice parameters, the surface slab lattice parameters are reduced compared to those of the CdSe slabs (see Table 4.3). Overall, general trends are kept across materials for each polymorph, of which WZ(110) has the highest surface area and number of metal binding sites (twice as many as ZB(110) for any given surface slab unit cell).

Table 4.3. *PBE-D2 optimized lattice parameters of the smallest unit cell of WZ(110) and ZB(110) for CdSe, CdS, ZnSe and ZnS.*

	CdSe	CdS	ZnSe	ZnS
	WZ(110)			
a (Å)	7.047	6.678	6.506	6.200
b (Å)	7.468	7.100	6.852	6.546
	ZB(110)			
a (Å)	4.311	4.119	3.974	3.787
b (Å)	6.097	5.833	5.622	5.362

Once optimized, it is clear that the area of the surface slabs decreases: the CdSe WZ and ZB surface unit cells have the largest area, whereas the ZnS surface slabs are the smallest. Next, their corresponding band gap energies (see Table 4.4) can be calculated. Surface BEV band gap energies in Table 4.4 are consistent with those of their bulk counterparts: energies increase from CdSe (2.70 and 2.66 eV for wurtzite and zinc blende, respectively) up to ZnS (4.48 and 4.31 eV), with CdS (3.40 and 3.19 eV) being above CdSe and below ZnSe (3.68 and 3.47 eV). Moreover, wurtzite consistently exhibits the larger band gap energy out of the two polymorphs (0.21 eV above zinc blende, at most). As expected from the bulk-to-surface reduction in dimensionality, surfaces exhibit larger band gap energies than their corresponding bulk structures. Differences range between 0.22

eV for zinc blende ZnS, up to 0.59 eV for wurtzite CdSe, although no clear trends have been found for this blue-shift. Importantly, the PBE0 corrections of both bulk and surface materials, and for both polymorphs, are almost identical. That is, Δ_{PBE0} depends on the material considered but not on whether it is bulk/surface or wurtzite/zinc blende. Although quantum confinement may alter these trends, it is worth examining the accuracy of best estimate values for the PBE band gap energies of core-only quantum dots, for example, by comparing them to PBE0/def2-SVP band gap energies as was done in Chapter 3.

Table 4.4. *PBE, PBE0 and best estimate value band gap energies (in eV) for bulk WZ, bulk ZB, WZ(110) and ZB(110). For PBE0 and PBE_{low} an 8x8x8 (bulk WZ, bulk ZB), an 8x8x1 (ZB(110)) and an 4x4x1 (WZ(110)) k-point mesh is used. For PBE_{fine} a 32x32x32 (bulk) and a 32x32x1 (surfaces) k-point mesh is used instead.*

System	Level	WZ	ZB	WZ(110)	ZB(110)
CdSe	PBE _{low}	1.63	1.07	1.82	1.54
	PBE _{fine}	0.78	0.68	1.34	1.21
	PBE0	3.09	2.49	3.28	2.99
	Δ_{PBE0}	1.46	1.42	1.46	1.45
	BEV	2.24	2.08	2.79	2.66
CdS	PBE _{low}	2.03	1.49	2.16	1.87
	PBE _{fine}	1.30	1.18	1.75	1.57
	PBE0	3.68	3.11	3.81	3.48
	Δ_{PBE0}	1.65	1.62	1.65	1.61
	BEV	2.95	2.08	3.40	3.19
ZnSe	PBE _{low}	2.39	1.79	2.54	2.23
	PBE _{fine}	1.49	1.39	1.99	1.81
	PBE0	4.08	3.45	4.22	3.87
	Δ_{PBE0}	1.69	1.66	1.68	1.64
	BEV	3.18	3.05	3.68	3.47
ZnS	PBE _{low}	2.82	2.53	3.12	2.79
	PBE _{fine}	2.08	2.22	2.63	2.44
	PBE0	4.67	4.40	4.99	4.62
	Δ_{PBE0}	1.85	1.87	1.87	1.83
	BEV	3.93	4.09	4.48	4.31

Regarding the pDOS in Figure 4.7, it would appear that the overall shape of the valence band is roughly the same regardless of the material considered, and so is the element-wise contribution of its components; changes between polymorphs are certainly more significant. Conversely, each material's conduction band differs significantly in two aspects. Firstly, as deduced from their band

gap energies, the conduction band minima are increasingly blue-shifted from CdSe to ZnS. Secondly, their shape is both material and polymorph-dependent. Importantly, the conduction band of Cd-containing surfaces falls off more slowly towards the band gap region than the Zn-containing, which present a sharp decline. Additionally, both CdSe and CdS present pronounced peaks close to their conduction band minima, while more acute peaks in ZnSe and ZnS appear further away from the band gap.

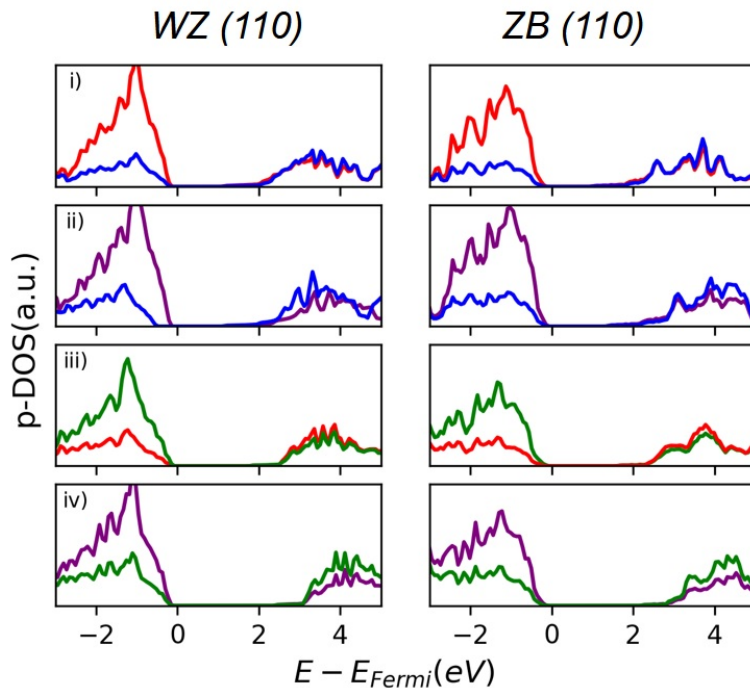


Figure 4.7. Projected DOS of WZ(110) and ZB(110) core-only *i)* CdSe, *ii)* CdS, *iii)* ZnSe and *iv)* ZnS. Blue: Cd, Red: Se, Purple: S, Green: Zn.

4.3.4 Passivated extended surface materials.

The next characterization step involves passivation in ligand-surface systems, and more specifically, its potential impact on the band gap region. In a more qualitative approach, this analysis has been limited to ZB(110) and two thiol ligands, methanethiol and ethanethiol. The corresponding ligand-surface structures are shown in Figure 4.8, while the adsorption energies (ΔE) and BEV band gap energies (E_g) are gathered in Table 4.5.

Table 4.5. Adsorption energies (ΔE , in $\text{kJ}\cdot\text{mol}^{-1}$) and best estimate band gap energies (E_g , in eV) for ZB(110) surfaces passivated with methanethiol (C1-SH) and ethanethiol (C2-SH). BEV pristine (\emptyset) surface band gap energies have been added for reference.

Material	\emptyset	C1-SH		C2-SH	
	E_g	ΔE	E_g	ΔE	E_g
CdSe	2.66	-69.6	3.01	-85.7	2.70
CdS	3.19	-75.2	3.22	-84.0	3.22
ZnSe	3.47	-78.7	3.70	-87.5	3.72
ZnS	4.31	-75.0	4.16	-84.5	4.17

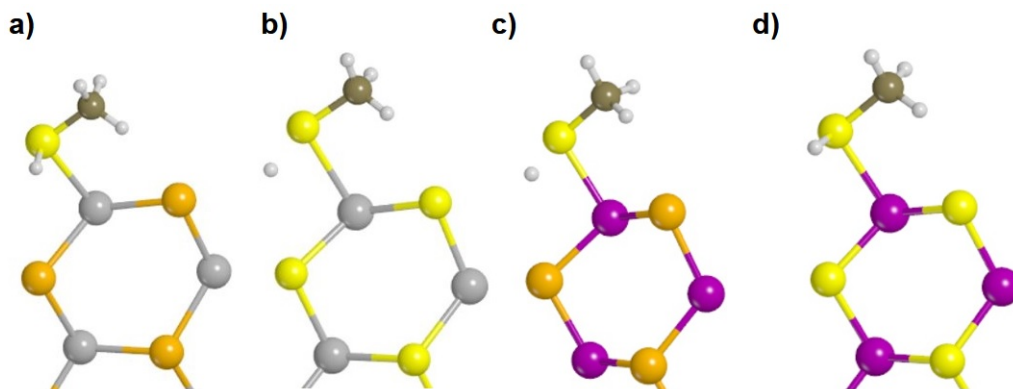


Figure 4.8. Adsorption of methanethiol (C1-SH) on ZB(110), core-only a) CdSe, b) CdS, c) ZnSe and d) ZnS. In gray, Cd; in orange, Se; in purple, Zn; in yellow, S.

It would appear all four surfaces favor the adsorption of either ligand to a similar extent. The importance of dispersion in ligand-surface interactions (which has been examined in detail for alkylthiols in Chapter 3) explains the increased stabilization of C2-SH over C1-SH, considering the former has a larger alkyl chain. For ZnSe, it is worth noting the appearance of moderately strong $\text{Se}\cdots\text{H}$ already seen for CdSe. Relative differences between ligands are lower than $10\text{ kJ}\cdot\text{mol}^{-1}$ for any given material. Moreover, for a given ligand, differences between materials are even lower (roughly $5\text{ kJ}\cdot\text{mol}^{-1}$, at most), which reinforces the idea that the interaction is mostly electrostatic. Band gap energies are consistent with the established trends ($\text{CdSe} < \text{CdS} < \text{ZnSe} < \text{ZnS}$) and are not substantially affected by which ligand is used. The sole exception being the adsorption on CdSe, for which the difference between ligands is $16\text{ kJ}\cdot\text{mol}^{-1}$ and the blue-shift induced by methanethiol is larger than for ethanethiol. The weaker binding of C1-SH on CdSe suggests that

the adsorption could be more dispersion-driven.

As previously seen for the passivated CdSe surfaces in Chapter 3, these extended surfaces do not present mid-gap states. Band gap energies are only slightly shifted after ligand adsorption, being mostly insensitive to which alkylthiol used. Compared to their pristine counterparts, the band gap is blue-shifted for CdSe, CdS and ZnSe, and is red-shifted only for ZnS. In the former group, adsorption of either ligand leads to a minor increase in the band gap energy for the adsorption of C2-SH on CdSe and CdS (between 0.03 and 0.06 eV) and to a larger shift for ZnSe (at most 0.25 eV for C2-SH). Attention is turned to shell-core-shell hybrid surfaces, a logical step towards core-shell quantum dots. While there exist many possible models to work with, the simulations herein discussed involve shell-core-shell slab models of ZB(110) surface unit cells with varying thickness, expressed in terms of their shell-core-shell layer ratio (S-C-S). For example, the 6-layer, ZB(110) CdSe surface can be made into a 1-4-1 or a 2-2-2 MX-CdSe-MX shell-core-shell surface. The selected ZB(110) models shown in Figure 4.9 span the 5 - 10 layer count, and their band gap energies are shown in Table 4.6.

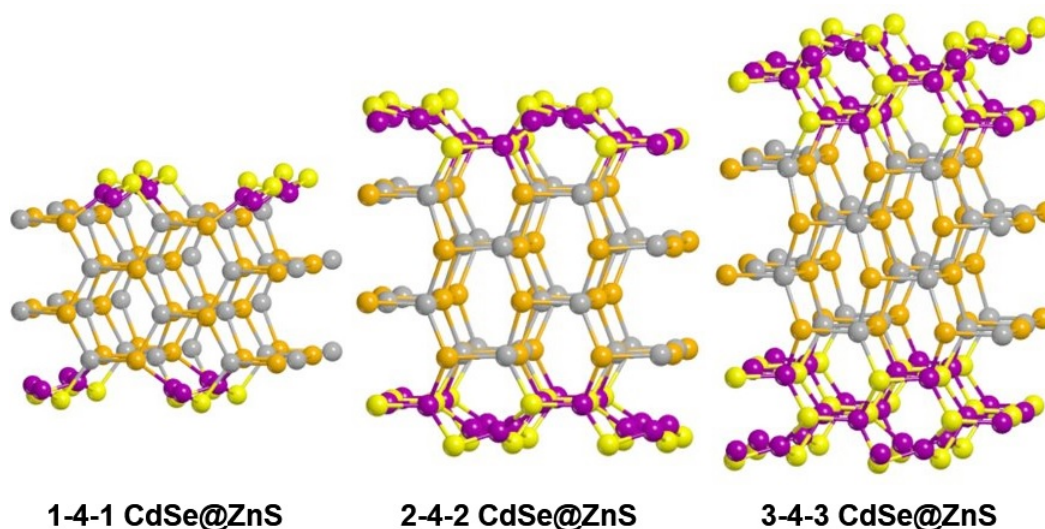


Figure 4.9. Representative CdSe@ZnSe shell-core-shell ZB(110) surface cells with different layer counts (four unit cells are shown for each model for the purposes of representation). In gray, Cd; in orange, Se; in purple, Zn; in yellow, S.

As inferred from Vegard's law, both the lattice parameters and the band gap energies of the hybrid slabs are different from those of the individual materials. The CdSe ZB(110) surface has been shown to have the largest lattice parameter and the smallest band gap energy, therefore

Table 4.6. *PBE-D2 band gap energies (in eV) of ZB(110) surface unit cells with different shell-core-shell ratios (S-C-S). A $4 \times 4 \times 1$ k-point mesh has been used throughout the simulations. Pristine material band gap energies for each slab layer count in parentheses.*

S-C-S	CdSe	@CdS	@ZnSe	@ZnS
131	1.46	1.53	1.69	1.71
212	1.46	2.11 (2.21)	2.38 (2.60)	2.71 (3.16)
141	1.82	1.85	1.97	1.99
222	1.82	1.96 (2.41)	2.18 (2.87)	2.39 (3.42)
161	1.70	1.72	1.78	1.79
242	1.70	1.76	1.90	1.96
323	1.70	1.87 (2.07)	2.14 (2.45)	2.39 (3.07)
181	1.63	1.63	1.68	1.67
262	1.63	1.66	1.76	1.77
343	1.63	1.69 (2.01)	1.90 (2.39)	1.96 (3.04)

progressive replacement with CdS, ZnSe or ZnS should simultaneously reduce the cell size and raise the band gap energy. Indeed, the surface unit cells are compressed as less CdSe is present. However, the extent of the compression does not appear to follow a simple Vegard-like law: the unit cells are rectangular and each parameter (a,b) changes at a different rate. Thus, Vegard's law is herein applied successfully to the surface area instead of the individual lattice parameters, as shown in Figure 4.10. The linear fitting for the CdS-CdSe-CdS core-shell surface slab areas is remarkably good ($R^2=0.992$), closely followed by that of ZnSe-CdSe-ZnSe ($R^2=0.961$) and a less ideal fitting for ZnS-CdSe-ZnS ($R^2=0.897$). Lattice mismatch, which is the highest between CdSe and ZnS, is a likely reason for the observed deviations from linearity.

Regarding the band gap energies changes, the expected correlation is observed: the band gap widens as more layers of CdSe are replaced. In all cases, replacing one layer on each side increases the band gap energy slightly, and more significantly for the thin layers than for the thicker ones.

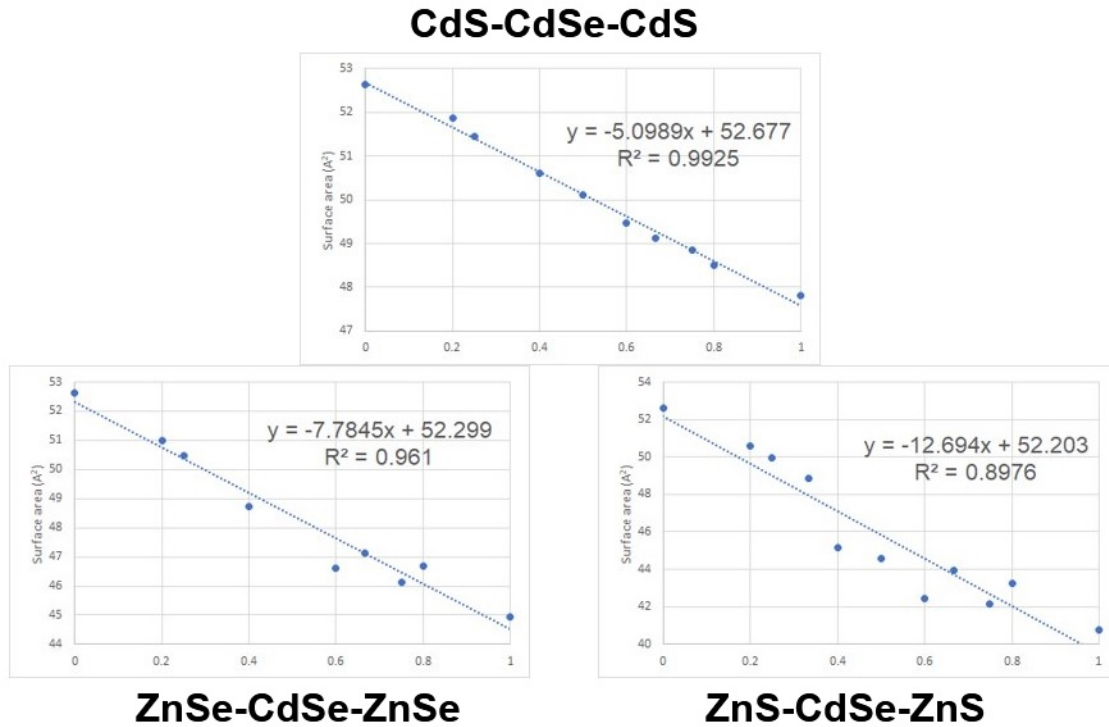


Figure 4.10. Surface slab areas of the shell-core-shell structures as a function of the molar fraction and the corresponding linear fitting.

Note, however, that for the low density k-point grids herein used the band gap energies are more sensitive to thin layer effects; that is, the band gap energies converge as more layers are introduced. Hybrid surfaces in which two layers of CdSe have been replaced on each side should present band gap energies closer to that of the new material. This is quite apparent for the 2-1-2 and 2-2-2 hybrid surfaces, for which the compositional ratio is higher for the new material than it is for CdSe. High ratios are attained in the 3-2-3 surfaces, where the effect on the final band gap energy is consistent with prior results. That is not the case for the 3-4-3 surfaces, where the band gap energies are lower than expected from the higher substitution ratio.

All in all, the inadequacy of PBE band gap energies is apparent, and so is the need to introduce corrections either through a hybrid functional (namely, PBE0) or using the best estimate approximation. For hybrid materials, calculation of best estimate values from bulk band gap energy is straightforward for core-only materials, but not for core-shell surfaces or quantum dots. In those cases, BEV calculations could involve using core-to-shell ratios to determine each material's contribution to the band gap energy. However, this would introduce an important bias, as *a priori*

the exact mechanism of band overlap could be more complex than that (for instance, prior contributions have relied on determining the phonon dispersion relation [190]). Conversely, the energy correction Δ_{PBE0} stemming from the exact Fock exchange applied offer a systematic approach to the determination of any system's band gap energy, whether core-only or core-shell. Thus, PBE0 simulations are proposed to be a more reliable strategy for the core-shell quantum dots explored in the following Section. Moreover, additional ratios could be assayed as well, although it should be noted that the 10-layer surfaces already involve a substantial computational cost. In any case, it has been shown that the high core-to-shell ratios (thin-shell scenario) only induce small shifts in the band gap energies, that is, they remain mostly core-determined. Exploring a wider array of core-to-shell ratios would provide a better picture of the effects of band mixing.

4.4 Core-only and core-shell quantum dots.

Different quantum dot models, varying both in size and shape, have been prepared either by cutting them from bulk wurtzite CdSe or by using the BCN-M code [47]. These models, schematically represented as $(MX)_n$ (where $n = 6, 33, 60, 68, 105, 133$) have been used as starting geometries for the optimizations of the corresponding $(CdSe)_n$, $(CdS)_n$, $(ZnSe)_n$ and $(ZnS)_n$ core-only quantum dots (see Figure 4.2). It should be noted that the $(MX)_{60}$ and $(MX)_{105}$ quantum dots are cylindrical and faceted, whereas the rest are mostly spheroidal in shape. Spherical models are the ones most commonly used in the literature when modeling quantum dots, while the faceted ones aim are reproducing experimentally observed structures. Furthermore, the effect of ligand passivation on these quantum dots has been explored using either methanethiol or ethanethiol, which have been shown to induce comparable band gap energy shifts (see Section 4.3.4). Additionally, HOMO-LUMO gap energies (E_{H-L}) calculated at PBE0/def2-SVP level have also been calculated on the PBE optimized quantum dots up to $n=68$. The representative, optimized core-only quantum dots with ligand passivation are shown in Figure 4.11 (the structure of the ligand passivated $(CdSe)_{33}$ was already shown in Chapter 3). Passivation on $(MX)_{105}$ and $(MX)_{133}$ was not explored due to the computational cost: the models have upwards of 500 atoms, which coupled to the loosely bound alkylthiol ligands makes the optimization highly resource-intensive.

Further below, the $n=33$ model is made into a core-shell quantum dot with a CdSe core and a

one-layer thick shell of the other three materials *i.e.* $(\text{CdSe})_6@(\text{NY})_{27}$, with $\text{MX}=\text{CdS}$, ZnSe and ZnS . The core atoms are all tetraordinated, while the 27 MX shell atoms are undercoordinated.

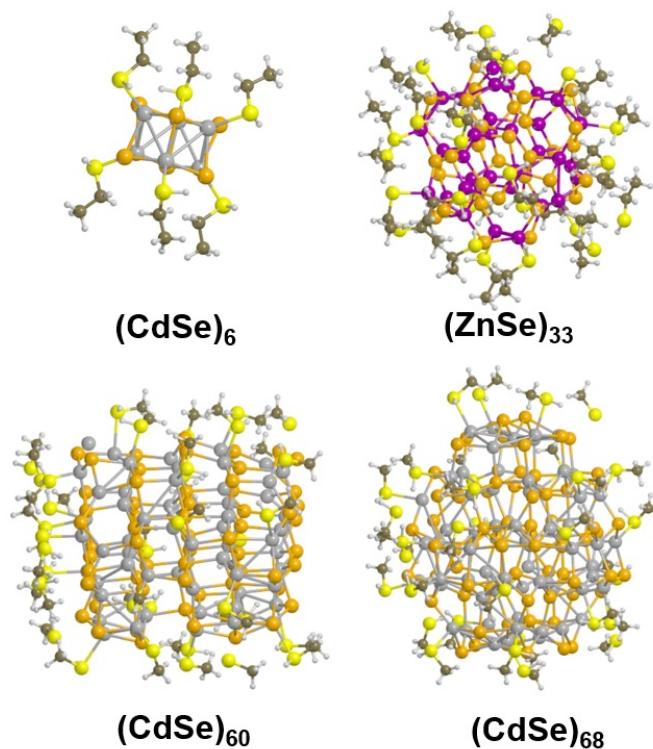


Figure 4.11. Selected, optimized $(\text{MX})_n$ - alkylthiol systems ($M=\text{Cd}$, Zn and $X = \text{Se}$) for $n= 6$, 33 , 60 , 68 .

4.4.1 Core-only quantum dots: effects of size, shape and material composition.

For each material, best estimate PBE band gap energies and PBE0/def2-SVP HOMO-LUMO gap energies are shown in Table 4.7 for sizes $n=6$ to $n=68$, while not all values are available for $n=105,133$. Band gap energies are discussed first, while the HOMO-LUMO gaps are analyzed at the end (complemented with the diagram's of said frontier orbitals).

Structural considerations are worth mentioning promptly. Firstly, it should be noted that M-X distances across materials are consistent with the corresponding bulk trends, and thus for any given $(\text{MX})_n$ quantum dot they are the longest for CdSe and the shortest for ZnS. For example, the average $\text{Cd}\cdots\text{Se}$ distance in $(\text{CdSe})_6$ is 2.574 \AA and decreases to 2.473 \AA in $(\text{ZnS})_6$. Distances

increase in the larger quantum dots, which more closely match the bulk M-X values. This is also consistent with the higher degree of crystallinity in the core region of large quantum dots, which is specially apparent in the faceted $(MX)_{105}$ quantum dots. These same faceted models, however, develop important distortions during optimization: one to three external cations (initially two-coordinated) is expelled from the lattice as a neutral metal atom, drifting away from the quantum dot significantly. This appears to indicate that the metal-terminated (100) polar surface is not stable, and that non-stoichiometric nanoparticles are more favorable.

In general, lattice distortion is present in all the pristine models, although it decreases when ligand passivation is applied. Passivation prevents the excessive lattice relaxation seen in the pristine models, in turn favoring a more bulk-like core. The effect is less obvious on the external layers. However, the metal – chalcogenide, metal – metal and chalcogenide – chalcogenide distances are larger than for the unpassivated models, which also reflects on the wider angles observed. Importantly, cation drift on the faceted quantum dots is prevented entirely through ligand passivation, with only minor M-X distance stretching.

For all models the BEV value and the PBE0 HOMO – LUMO band gap exhibit similar values, with the exception of the pristine $(MX)_{60}$ models, which are unrealistic due to the release of metal atoms from the nanoparticle. Indeed, the mean absolute deviation is 0.2 V, thus indicating that the determination of Δ PBE0 corrections may be a generally interesting strategy to model semiconductor materials and particularly quantum dots, which become highly resource-intensive when using hybrid functionals.

For any given quantum dot size, band gap energies are consistent with the trends observed for the pristine bulk and surfaces materials: $E_g(\text{CdSe})_n < E_g(\text{CdS})_n < E_g(\text{ZnSe})_n < E_g(\text{ZnS})_n$. The magnitude of the energy shifts between materials does not change much with nanoparticle size. For example, the difference between $(\text{CdSe})_6$ (3.47 eV) and $(\text{CdS})_6$ (3.78 eV) is similar to that seen for $(\text{CdSe})_{33}$ (3.05 eV) and $(\text{CdS})_{33}$ (3.36 eV). Furthermore, differences between CdS and ZnSe are generally small, the band gap energy of the ZnSe analogue being between 0.15 and 0.30 eV larger. Finally, ZnS analogues present the largest band gaps for each size and shape, the difference with the values obtained for the related CdSe being between 0.90 and 1.36 eV.

Both band gap energies and HOMO-LUMO gap energies decrease sharply as quantum dot size increases, which is the main trend expected from quantum confinement. For CdSe, band gap

Table 4.7. PBE BEV band gap energies (E_g , in eV) and PBE0/def2-SVP HOMO-LUMO gap energies (E_{H-L} , in eV) of all the core-only quantum dots hereby reported, with (L-) and without (\emptyset) alkylthiol passivation. ^a Inconsistent results, likely due to important surface defects not mended during optimization.

$(MX)_n$	Method	Type	CdSe	CdS	ZnSe	ZnS
$n = 6$	E_g	\emptyset	3.47	3.78	3.93	4.37
		L-	4.10	4.43	4.67	5.12
	E_{H-L}	\emptyset	3.64	3.94	3.95	4.07
		L-	4.18	4.49	4.46	4.54
$n = 33$	E_g	\emptyset	3.05	3.36	3.65	4.00
		L-	3.62	3.82	4.22	4.74
	E_{H-L}	\emptyset	3.20	3.34	3.72	4.11
		L-	3.66	3.86	4.68	5.06
$n = 60$	E_g	\emptyset	NA	-	-	-
		L-	2.50	2.64	3.17	3.70
	E_{H-L}	\emptyset	NA	-	-	-
		L-	2.45	2.60	2.99	4.02
$n = 68$	E_g	\emptyset	2.78	3.12	3.42	3.83
		L-	2.60	2.61	3.43	3.96
	E_{H-L}	\emptyset	2.74	2.83	2.98	3.28
		L-	2.45	2.17	2.99	3.73
$n = 105$	E_g	\emptyset	2.44	2.87	3.03	3.77
		L-	NA ^a	-	-	-
$n = 133$	E_g	\emptyset	1.89	2.21	2.16	3.21
		L-	NA	-	-	-

energies decrease from 3.47 eV in $(\text{CdSe})_6$ to 2.44 eV in $(\text{CdSe})_{133}$, with $(\text{CdSe})_{33}$ and $(\text{CdSe})_{68}$ presenting intermediate values (3.05 eV and 2.78 eV, respectively). Similar results are obtained for the HOMO-LUMO gaps, which decrease from 3.64 eV to 2.74 eV. Another important trend is that of material-dependent energy shifts: for a given size, both E_g and E_{H-L} increase from left to right across Table 4.7. Band gap energies for the pristine $(\text{MX})_{60}$ and $(\text{MX})_{105}$ are unavailable, while those of the passivated $(\text{MX})_{60}$ are mostly comparable to those of $(\text{MX})_{68}$. Trends are observed for the ligand-passivated quantum dots are consistent with those seen for the pristine cases. That is, a) the energy gaps decrease as the quantum dots become larger and b) energy gaps increase from CdSe to ZnS for a fixed quantum dot size. However, trends are less clear for the largest models, which

may be attributed to a higher number of surface defects or the large number of undercoordinated metal centers. Several ligands desorb during the optimization, likely due to the fact that the energy difference between the direct coordination to the metal and the interaction with the quantum dot through van der Waals interactions and hydrogen bonding with other adsorbed capping ligands is limited, as already proposed in the previous Chapter with surface models (around $10 \text{ kJ}\cdot\text{mol}^{-1}$). *Ab initio* molecular dynamics simulations would probably be the computational approach to follow if more stable conformations were to be found. However, their high atom count (210 atoms) make the simulations costly and therefore this strategy is forgone.

It is worth mentioning that, in Chapter 3, implicit solvation was determined to have a similar effect to explicit ligand passivation. It is for this reason that implicit water passivation has been added to the pristine and passivated $(\text{MX})_{33}$ models, as a further correction to ΔPBE0 . The BEV band gap energies and HOMO-LUMO gap energies for the core-only $(\text{MX})_{33}$ materials are reported in Table 4.8. Implicit solvation raises both E_g and E_{H-L} of the non-passivated models compared to the values in Table 4.7, while also reflecting a material-sensitive dependence. For example, the band gap energies of the pristine quantum dots increase between 0.37 eV up to 0.83 eV with the inclusion of solvation. Conversely, the energy shift is less significant for the ligand-passivated quantum dots, being at most of 0.20 eV for $(\text{ZnS})_{33}\text{-L}$ and actually decreasing for $(\text{CdSe})_{33}\text{-L}$. Similarly, the increase in the HOMO-LUMO gaps for the solvated, pristine quantum dots is higher than for the ligand-passivated ones. Based on these results, ligand passivation and inclusion of water solvation on their own have a similar effect on the electronic structure of pristine quantum dots. When combined, the increase in both band gap energy and HOMO-LUMO gap becomes less significant but it is still present. This suggests that the blue-shift of the mid-gap states is enhanced if ligands and implicit solvation are employed cooperatively.

Table 4.8. BEV PBE band gap (E_g , in eV) and PBE0 HOMO-LUMO gap energies (E_{H-L} , in eV) in gas phase (Gp) and implicit water solvation (water) for core-only $(MX)_{33}$ quantum dots, pristine and passivated (L).

Model	Gp		water	
	E_g	E_{H-L}	E_g	E_{H-L}
CdSe	3.06	3.20	3.43	3.71
CdS	3.37	3.34	3.89	3.93
ZnSe	3.66	3.72	4.22	4.81
ZnS	3.99	4.11	4.82	4.98
CdSe-L	3.62	3.66	3.49	3.94
CdS-L	3.83	3.86	3.91	3.86
ZnSe-L	4.23	4.68	4.35	4.93
ZnS-L	4.73	5.06	4.93	5.25

The projected density of states of pristine and passivated $(MX)_{33}$ quantum dot are reported in Figure 4.12. Apart from the expected size and composition trends when compared to the $(MX)_6$ analogues, the same general features are observed. The addition of capping ligands strongly blue-shifts the mid-gap states for all materials, thus highlighting again the importance of adding the ligand passivation in the modeling. Remarkably the valence and conducting band shapes varies significantly with respect to those of $(MX)_6$ because $(MX)_{33}$ has a larger number of electronic states and thus, they are all globally less localized

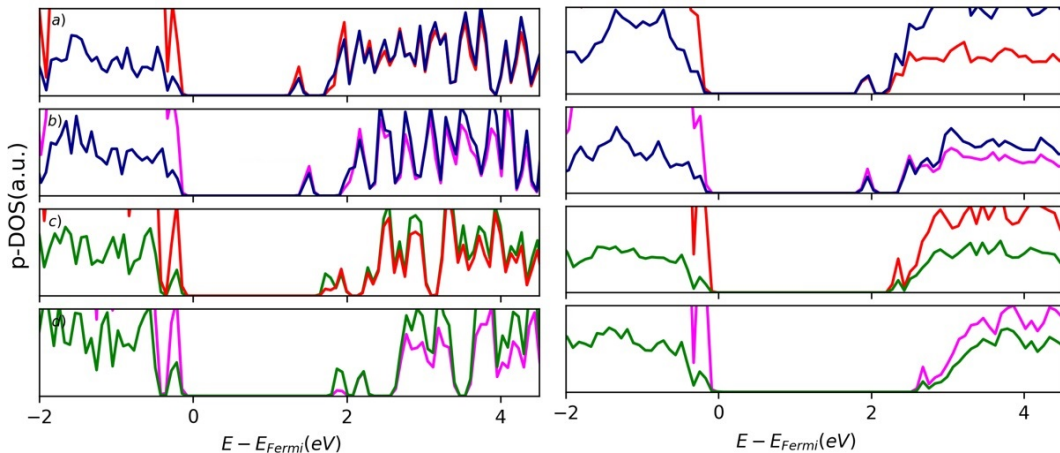


Figure 4.12. Projected DOS of (a) $(CdSe)_{33}$, (b) $(CdS)_{33}$, (c) $(ZnSe)_{33}$ and (d) $(ZnS)_3$, without ligands (left) and with 27 C2-SH ligands (right). Elemental contributions shown for Cd (blue), Se (red), Zn (green) and S (magenta).

The analysis of frontier orbitals gives additional information on the importance of the surface

reconstruction and the role of capping ligands for some selected examples unpassivated (in Figure 4.13) and alkylthiol passivated quantum dot models (in Figure 4.14). Regardless of the material, the unpassivated quantum dot presents the HOMO orbital located at the outermost atoms of a region that it is mainly cation terminated. On the other hand, the LUMO is also located on the outermost atoms of the nanoparticle in a region that it is mainly anion terminated. The addition of the capping ligands, reduce the contributions of the outermost atoms in the HOMO and LUMO orbitals that now become more delocalized toward the core, which may explain the blue-shift observed in the DOS. That is, the ligand passivation effect seems to be mostly material-independent.

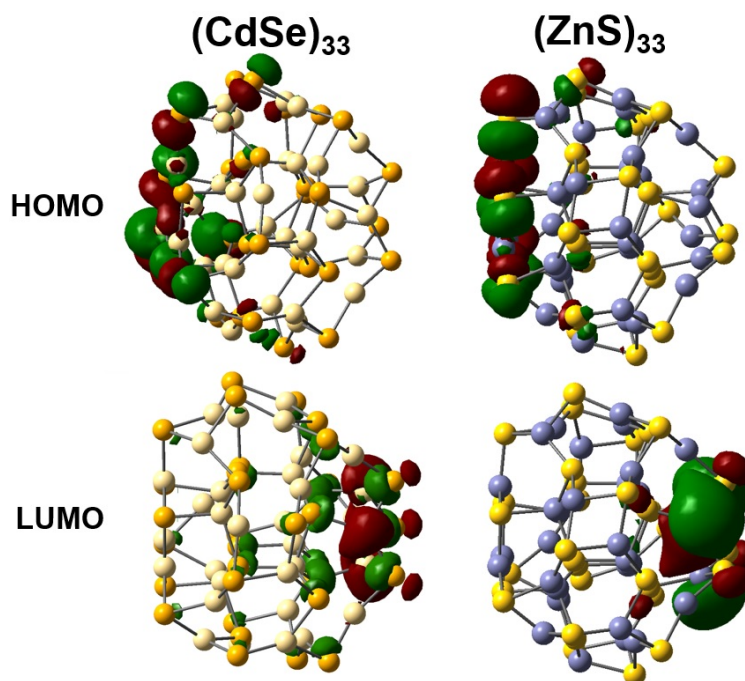


Figure 4.13. Gathered HOMO and LUMO of the unpassivated $(\text{CdSe})_{33}$ and $(\text{ZnS})_{33}$ quantum dot models.

All in all, the band gap energy hierarchy for any given quantum dot size is consistent with bulk behavior and does not appear to depend on which ligand (C1-SH or C2-SH) is being adsorbed. The expected band gap energy decrease with size is observed, but it relies on the use of PBE0-based corrections to be fully consistent. Finally, remarkable agreement is found between the BEV band gap energies and the HOMO-LUMO gaps obtained at PBE-D2/def2-SVP level (see Table 4.8), which suggests that the BEV approach could be a suitable, cost-efficient strategy for future research on modeling semiconductor nanoparticles.

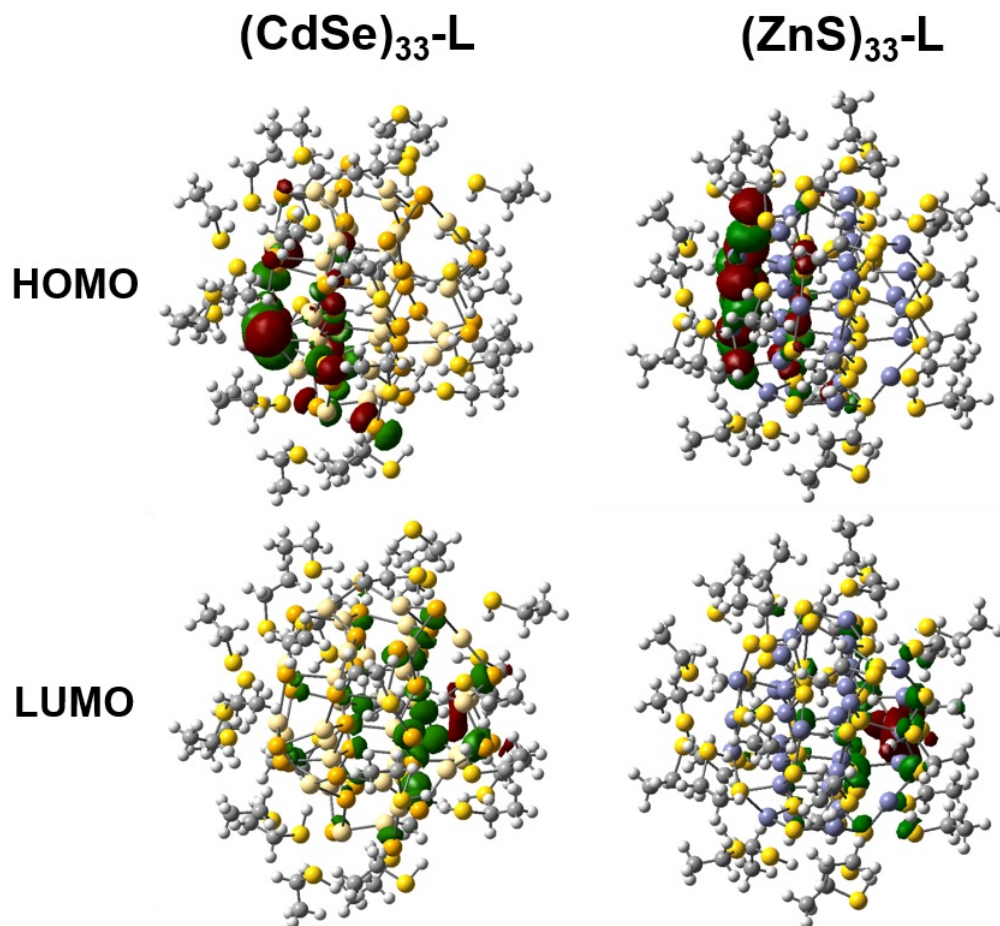


Figure 4.14. Gathered HOMO and LUMO of the unpassivated $(\text{CdSe})_{33}$ and $(\text{ZnS})_{33}$ quantum dot models.

4.4.2 Core-shell $(\text{CdSe})_6@(\text{MX})_{27}$ quantum dots.

While preliminary core-shell quantum dot models have already been built for $n = 33, 60, 68, 105, 133$, only those pertaining to $(\text{CdSe})_6@(\text{MX})_{27}$ are explored in detail in this section. In this context, six new core-shell models have been considered: the unpassivated $(\text{CdSe})_6@(\text{CdS})_{27}$, $(\text{CdSe})_6@(\text{ZnSe})_{27}$ and $(\text{CdSe})_6@(\text{ZnS})_{27}$ and their passivated counterparts $((\text{CdSe})_6@(\text{MX})_{27}\text{-C2-SH})$. Their optical properties are compared to the core-only analogues to elucidate if they are governed by the optical features of the core (Type-I), the shell (reverse type-I) or by a mixture of both (Type-II). Since PBE values are systematically underestimated and the best estimated value approximation cannot be applied for the hybrid materials, the optical properties are determined through single-point PBE0/def2-SVP calculations (Gaussian16) on the PBE optimized structures. Calculations

on larger models with and without ligand passivation are presumably of high interest (since in MX33 the core only represents 18% of the whole material), but they are out of the scope of the present Thesis due to their computational cost. Figure 4.15 shows the optimized structures of the non-passivated and passivated core-shell quantum dots herein considered.

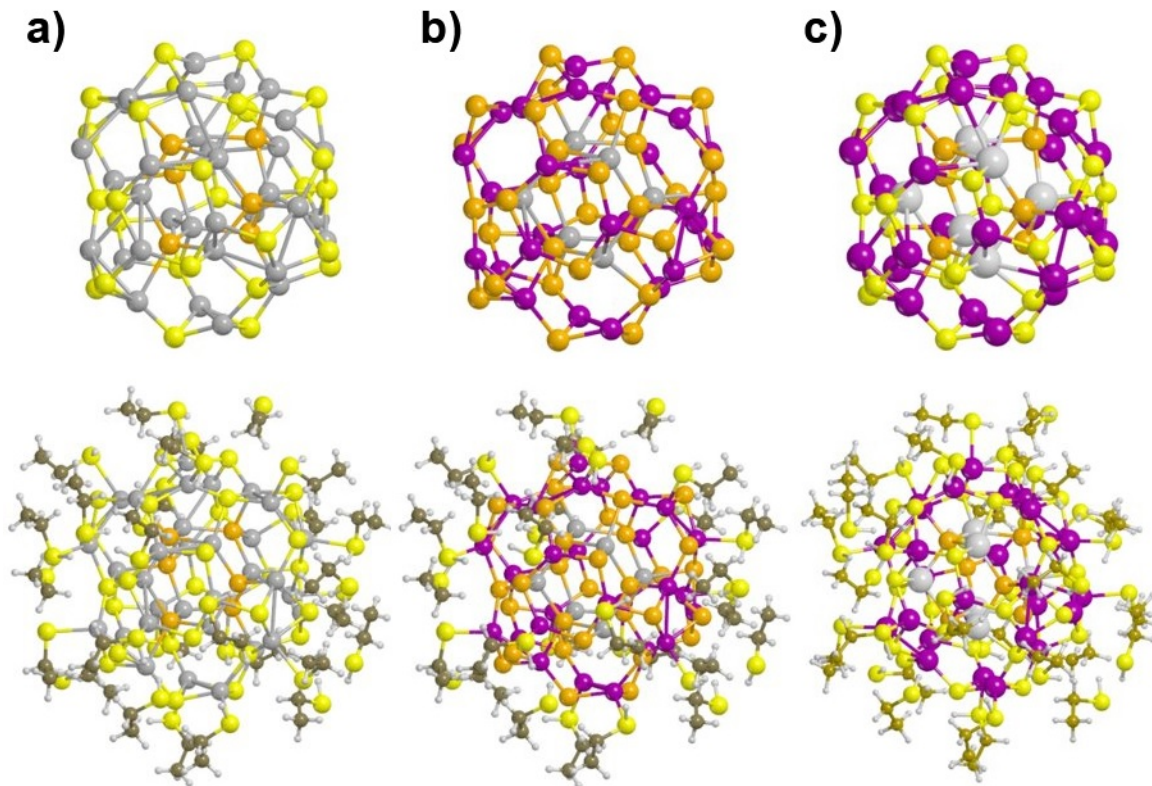


Figure 4.15. *Pristine and passivated models of core-shell a) $(\text{CdSe})_6@(\text{CdS})_{27}$, $(\text{CdSe})_6@(\text{ZnSe})_{27}$ and $(\text{CdSe})_6@(\text{ZnS})_{27}$.*

Optimization starting from the minimum energy structure of $(\text{CdSe})_{33}$, in which the 27 outer undercoordinated units have been replaced by either CdS, ZnSe or ZnS, shows that the shell compresses significantly without affecting the core much. As expected, the compression of the shell is more pronounced in the case of ZnS, but it is also apparent for the other two materials. Addition of the 27 capping ligands reduced the surface compression upon changing the atoms of the shell, suggesting that passivation attenuates all modifications affecting the pristine surface. At this point, it is worth mentioning that some of the 27 ligands desorb from the surface (this was also observed for the core-only nanoparticles). These ligands remain close to the quantum dot through the combination of van der Waals interactions with the surface and hydrogen bonding with the

other coordinated ligands.

The HOMO-LUMO gap energies of the $(\text{CdSe})_6@(\text{MX})_{27}$ core-shell quantum dots with and without implicit water solvation are presented in Table 4.9. The values for the core-only $(\text{MX})_{33}$ have been added for reference.

Table 4.9. *PBE0/def2-SVP HOMO-LUMO gap energies (in eV) in gas phase (Gp) and implicit water solvation (water) for $(\text{CdSe})_6@(\text{MX})_{27}$ core-shell quantum dots, pristine (\emptyset) and passivated (L). Pristine and passivated core-only HOMO-LUMO gaps have been added for reference, including $(\text{CdSe})_{33}$.*

Model	\emptyset		-L	
	Gp	water	Gp	water
CdSe	3.20	3.71	3.66	3.94
CdS	3.34	3.93	3.86	3.86
@CdS	3.37	3.83	3.84	4.04
ZnSe	3.72	4.81	4.68	4.93
@ZnSe	3.78	4.57	4.39	4.72
ZnS	4.11	4.98	5.06	5.25
@ZnS	4.04	4.44	4.51	4.64

For the unpassivated core-shell models, the HOMO-LUMO gap is determined by the shell material. Indeed, the HOMO – LUMO energy differences of the unpassivated core-shell quantum dots are almost identical to the HOMO – LUMO energy differences of the $(\text{MX})_{33}$ unpassivated nanoparticle of the material acting as shell. For example, the gas phase values for $(\text{CdSe})_6@(\text{CdS})_{27}$ (3.37 eV) and $(\text{CdS})_{33}$ (3.34 eV) and for $(\text{CdSe})_6@(\text{ZnSe})_{27}$ (3.78 eV) and $(\text{ZnSe})_{33}$ (3.72 eV) are strikingly close. Meanwhile, the correlation found for passivated core-only and core-shell quantum dots is less optimal. Although the values for $(\text{CdSe})_6@(\text{CdS})_{27}$ -27C2-SH (3.84 eV) and $(\text{CdS})_{33}$ -27C2-SH (3.86 eV) are almost identical, those of $(\text{CdSe})_6@(\text{ZnSe})_{27}$ -27C2-SH (4.39 eV) and $(\text{ZnSe})_{33}$ -27C2-SH (4.68 eV) band gaps are significantly different, more so for $(\text{CdSe})_6@(\text{ZnS})_{27}$ -27C2-SH (4.51 eV) and $(\text{ZnS})_{33}$ -27C2-SH (5.06 eV), with the core-only quantum dots having larger energy gaps than the core-shell ones.

The HOMO and LUMO molecular orbitals of passivated and unpassivated $(\text{CdSe})_6@(\text{CdS})_{27}$ and $(\text{CdSe})_6@(\text{ZnS})_{27}$ nanoparticles are reported in Figure 4.16 and in Figure 4.17 (comparison with the molecular orbitals of the core-only materials can be done by comparing them with Figure 4.13 and Figure 4.14). As seen for the core-only quantum dots, the HOMO of $(\text{CdSe})_6@(\text{CdS})_{27}$ and

$(\text{CdSe})_6@(\text{ZnS})_{27}$ are centered on the shell, in a region rich in metal cations. Their LUMO are also centered on the shell, but in a region rich with anions instead. Based on these similarities, it is suggested that the shell material dominates the core-shell behavior, reinforcing the conclusions drawn above regarding the essentially identical HOMO-LUMO gaps.

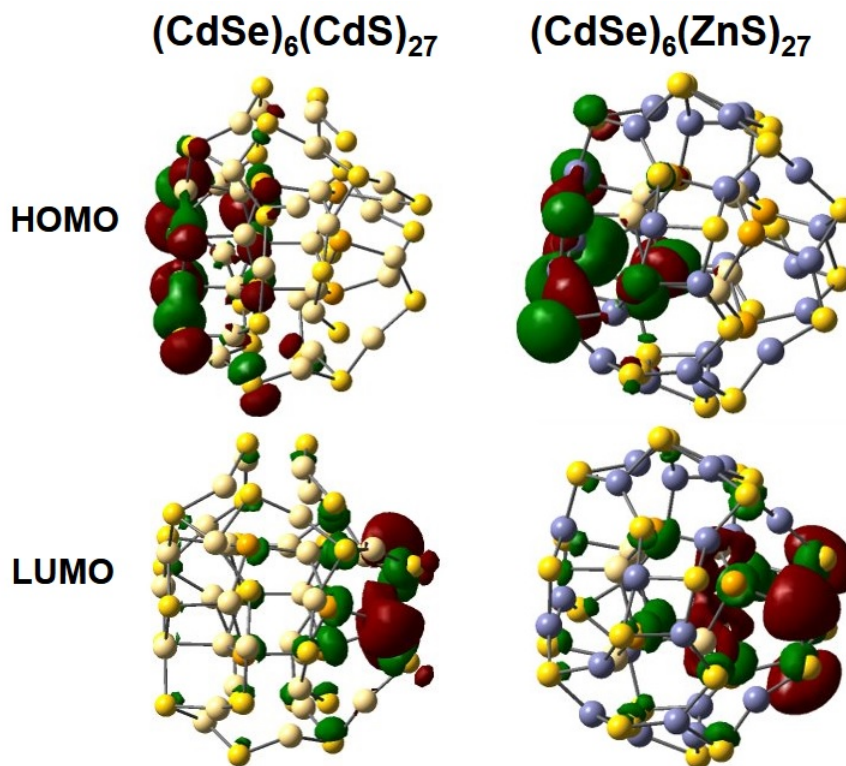


Figure 4.16. Gathered HOMO and LUMO diagrams of the pristine $(\text{CdSe})_6@(\text{CdS})_{27}$ (left) and (right) $(\text{CdSe})_6@(\text{ZnS})_{27}$ quantum dot models.

The behavior of the three passivated materials is remarkably different when compared to each other (see Table 4.9). Firstly, the $(\text{CdSe})_6@(\text{CdS})_{27}$ -27C2-SH HOMO and LUMO orbitals are still mainly located at the shell of the quantum dot, as in the pristine model. Correspondingly, the HOMO-LUMO gap of $(\text{CdSe})_6@(\text{CdS})_{27}$ -27C2-SH is essentially equal to that of (CdS_{33}) -27RSH and is best described as a reverse Type-I quantum dot. The HOMO of $(\text{CdSe})_6@(\text{ZnS})_{27}$ -27C2-SH shows a significant delocalization within the core and the shell of the quantum dot, albeit with major contributions from the shell. However, the LUMO of $(\text{CdSe})_6@(\text{ZnS})_{27}$ -27C2-SH is mainly located at the core. As a consequence, now the HOMO and LUMO are now more localized at the

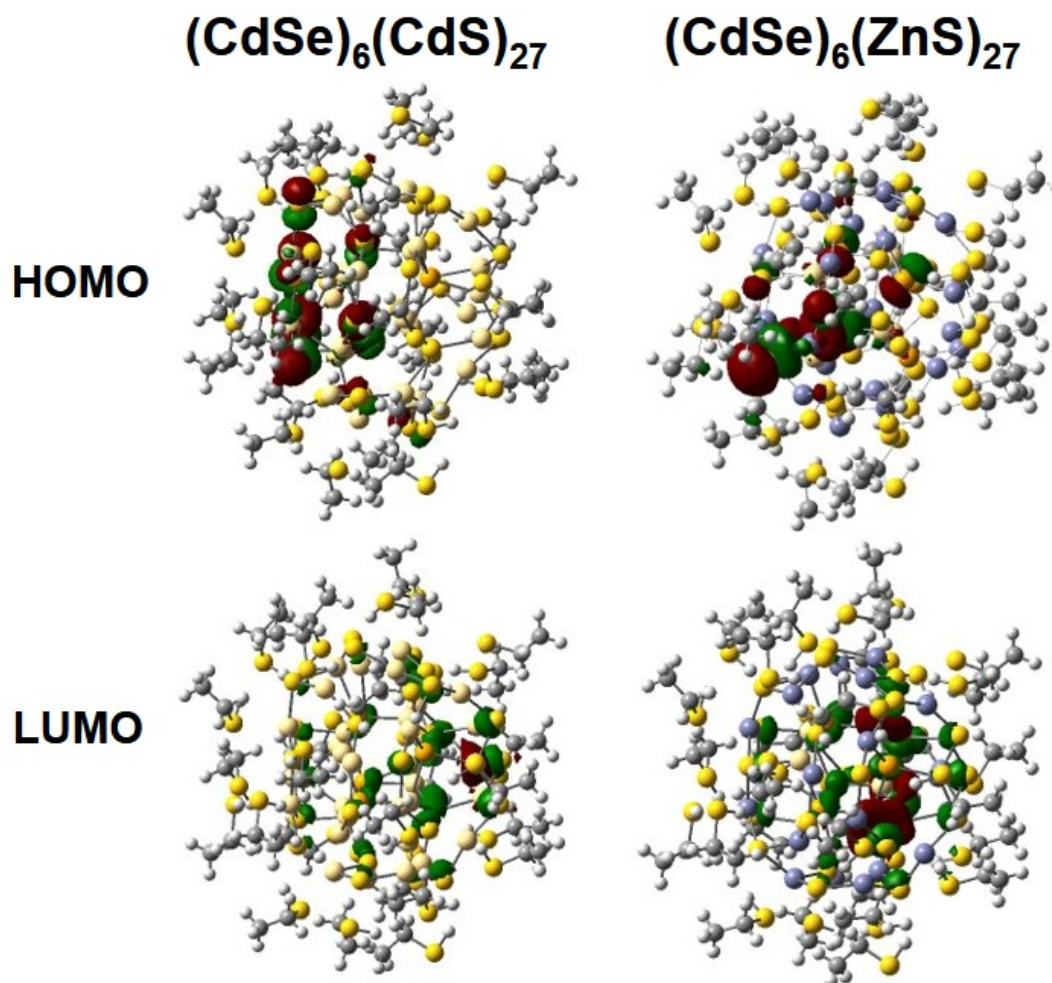


Figure 4.17. Gathered HOMO and LUMO diagrams of the passivated $(\text{CdSe})_6@(\text{CdS})_{27}$ (left) and (right) $(\text{CdSe})_6@(\text{ZnS})_{27}$ quantum dot models.

shell and the HOMO-LUMO gap is smaller to that of the $(\text{ZnSe})_{33}$ core only material. Consequently, it is proposed that $(\text{CdSe})_6@(\text{ZnSe})_{27-27\text{C}2\text{-SH}}$ behaves as a Type-II quantum dot. Finally, the contributions to the HOMO and LUMO orbitals of $(\text{CdSe})_6@(\text{ZnS})_{27-27\text{C}2\text{-SH}}$ are similar to those of $(\text{CdSe})_6@(\text{ZnSe})_{27-27\text{C}2\text{-SH}}$, although contributions of the HOMO are mainly on the core. This being so, the band gap of $(\text{CdSe})_6@(\text{ZnS})_{27-27\text{C}2\text{-SH}}$ is the one differing the most to the core-only analogue. In fact, the computed energy gap is similar to the $(\text{CdS})_6\text{-6C}2\text{-SH}$ quantum dot, which is equivalent to the core, thus reinforcing the idea that in this hybrid quantum dot the optical properties are controlled by the core (Type-I core-shell).

Overall, the inclusion of the ligands not only induces a blue-shift of the HOMO-LUMO energy

differences, but also significantly modifies the optical properties of $(\text{CdSe})_6@(\text{ZnSe})_{27-27\text{C}2\text{-SH}}$ and $(\text{CdSe})_6@(\text{ZnS})_{27-27\text{C}2\text{-SH}}$. Larger cores are expected to have smaller band gaps, so larger core-shell models should be tested. Regardless, the present results clearly show that capping ligands should be added to avoid unrealistic surface relaxation that generates mid-gap states and modifies the final optical properties of the material.

4.5 Conclusions.

Following a top-down approach, pristine and hybrid bulk, surface and quantum dot systems have been simulated for four different materials: CdSe, CdS, ZnSe and ZnS. Firstly, bulk solid solutions and shell-core-shell surfaces have been explored, both serving as successful instances of Vegard-based fitting. Bulk and surface PBE0 corrections (Δ_{PBE0}) have been shown to change only on a material basis. Results from surface slab passivation show that the alkylthiol - surface interaction is electrostatic and equivalent for all four materials.

For core-only $(\text{MX})_n$ quantum dot models, two clear trends have been distinguished: a) energy gaps red-shift as the quantum dot size increases (quantum confinement weakens) and b) for any given model, energy gap widths are consistent with bulk behavior ($\text{CdSe} < \text{CdS} < \text{ZnSe} < \text{ZnS}$). Importantly, using Δ_{PBE0} as an additive correction to PBE band gap energies yields values in close agreement with PBE0/def2-SVP HOMO-LUMO gaps at a fraction of the computational cost. Blue shifts resulting from alkylthiol passivation and implicit solvation are consistent with previous trends. Importantly, passivation enhances surface reconstruction *e.g.* it prevents metal atoms from being expelled in the faceted quantum dots.

Three $(\text{CdSe})_6@(\text{MX})_{27}$ core-shell models have been considered. In their pristine state, a) significant surface reconstruction occurs, akin to ligand passivation, b) their HOMO-LUMO gaps are clearly determined by the shell material and c) their frontier orbitals are equivalent to those in the core-only quantum dots. Ligand passivation and implicit solvation widens the HOMO-LUMO gap following the trends reported for extended surfaces. Interestingly, passivation changes the localization of the frontier orbitals differently for each material, and all three types of core-shell are

reproduced.

Overall, the present work shows that rational ligand passivation offers significant control over the electronic properties of core-only and core-shell quantum dots. For core-only quantum dots, the best estimated value approach provides a work-around for intensive PBE0 calculations, but it has not been extended to their core-shell counterparts. In both instances, explicit ligand passivation is both necessary and computationally demanding. Since $(\text{CdSe})_6@(\text{MX})_{27}$ is decidedly core-skewed, further research into core-shell quantum dots should focus on larger models.

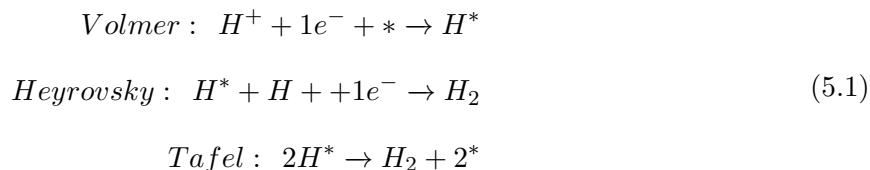
Metal electrocatalysts for hydrogen evolution.

The ever-increasing demand for green hydrogen requires overcoming the up-scaling costs of water electrolysis through intelligent electrocatalyst design. Particularly, the golden standard catalyst for proton reduction half reaction, usually known as hydrogen evolution reaction (HER), is platinum, which is highly expensive. Ruthenium, in the form of small nanoparticles with capped ligands, has been suggested to be a cheaper alternative with similar activities. In this Chapter, the hydrogen evolution capabilities of pristine and defective Pt and Ru surfaces are explored using DFT calculations, with the aim that an atomistic understanding on the catalytic activity of the different sites could pave the way for catalyst design, encompassing the reduction of the amount of costly noble metal without sacrificing catalyst activity. For that we applied the Norskov's approach for material screening, that uses the calculated hydrogen adsorption energies as a descriptor. Results show that at low coverages H^+ are easily reduced on both platinum and ruthenium crystalline and defective surfaces, but the resulting adsorbed hydrides are too strongly adsorbed to undergo HER for any of the considered models. Coverages exceeding the monolayer are significantly more active and usually imply the formation of dihydrogen intermediates. For well-defined crystalline Pt surfaces the adsorption of an additional H atom is very close to the ideal value and thus any defect present on the surface does not significantly improve the catalytic activity. In contrast, pure crystalline ruthenium surfaces show very high overpotentials and only the presence of less coordinated Ru centers ($CN = 6 - 8$) could improve the catalytic performance of ruthenium.

5.1 Introduction.

Water electrolysis triggered by electricity from renewable sources or sunlight conversion (as part of the so-called artificial photosynthesis) has long been considered a highly desirable source of green hydrogen, which can similarly be used as a sustainable energy source [65, 200–207]. Its source (water) is abundant and its by-products (O_2 and H_2) are both non-hazardous and obtained in high purity [204, 206]. Reliable access to cheap, pure H_2 is crucial in the current chemical and in the global energy market, as the so-called “hydrogen economy” [200] is only expected to grow in response to rapid population growth amidst climate change concerns [1]. Hydrogen is a critical feedstock in the equally crucial synthesis of hydrocarbons (Fischer-Tropsch synthesis) and ammonia (Haber-Bosch synthesis), and has found widespread use in fuel cells [96, 207, 208]. Indeed, the energy density of H_2 (140-146 $MJ \cdot kg^{-1}$) greatly surpasses that of liquid fuels (approximately 50 $MJ \cdot kg^{-1}$), explaining its promising use as an energy carrier [201, 206]. Yet mass-scale water electrolysis remains economically unfeasible, with current hydrogen demands being met through steam methane reforming of natural gas and coal gasification despite concerns over their carbon-footprint [200, 206].

As reductive half-reaction in water electrolysis, the hydrogen evolution reaction takes place through the Volmer-Heyrovsky or the Volmer-Tafel mechanisms [1]. Both share the initial Volmer step, and in acidic media there takes place a surface-mediated one-electron transfer to a solvated proton and the formation of an intermediate adsorbed H^* species. It is then followed by the evolution of H_2 either through the Heyrovsky step (binding to a non-adsorbed H) or through the Tafel step (binding to nearby adsorbed H atom), as summarised below ¹:



The HER activity of a catalyst is measured in terms of the exchange current density achieved at a biased (i.e. non-zero overpotential, η , see Section 5.1.1) or at unbiased electrode (i.e. at equilibrium,

¹Both mechanisms are the same in acidic and alkaline conditions except for the source of H - solvated protons or molecular water, respectively

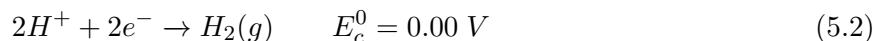
$\eta=0$). Catalysts exhibiting high overpotentials are less cost-efficient, requiring voltages above those predicted by the Nernst equation to operate. Experimental monitoring and computational modeling is essential to the effective design of electrocatalysts, for which vast experimental [65, 208–210] and computational [1, 63, 64, 75, 97, 202, 211] literature is available. Currently, material screening is largely dependent on preexisting data repositories or on the use of computational descriptors. Descriptors like hydrogen adsorption energies or metal d-bands have found widespread use, although structural nuances are oftentimes neglected [212]. Out of the many HER electrocatalysts hitherto designed, platinum is still considered the “golden standard” owing to its high activity stemming from a ideally balanced Pt-H bond strength and for its stability [1, 204–206, 210]. Only minimal overpotentials are needed to achieve high reaction rates in harshly acidic conditions [1]. Conversely, the HER activity of Pt in alkaline conditions is known to be two or three times lower due to the ineffective cleavage of the H-OH bond [202, 204], while stability concerns in these conditions have driven research into molecular and colloidal alternatives [65]. Unfortunately, Pt and other highly HER active late transition metals are remarkably scarce in the Earth’s crust. Their low Earth-abundance makes them expensive, cycling back to the afore-mentioned upscaling limitation [204, 213]. The demand for these so-called “platinum metal group catalysts” (which include palladium, ruthenium, rhodium, and iridium) has so far been met by reducing the noble metal catalyst loading [214] and by looking for alternative materials. From metal chalcogenides, phosphides [203], carbides [208] and nanomaterials alloys [210] to Earth-abundant metals such as Ni or Mo [201, 202, 215], the search for Pt-free HER electrocatalyst remains a high-priority challenge [204, 207]. Advances in material screening and nanofabrication currently allow for atomistic design of catalysts with high surface areas, including single-atom catalysts [62, 89] and nanoparticles [96]. Indeed, the enhanced stability and higher active site density of low-dimensional electrocatalysts (*i.e.* nanostructured catalysts) make them ideal candidates for hydrogen evolution and other catalytic reactions [65]. Their HER activity can be further tuned through rational surface functionalization, inasmuch as capping ligands can either strengthen or weaken hydrogen adsorption [207].

Ruthenium stands out as a promising replacement for Pt, not only being less costly (1/4 of Pt’s cost) [65] but also exhibiting similar Ru-H bond energies (approximately $271 \text{ kJ}\cdot\text{mol}^{-1}$)[206]. Many promising Ru-based homogeneous and heterogeneous catalysts have been characterized thusfar [57, 66, 204]. In theoretical terms, activity-enhancing strategies for Ru-based HER electrocatalysts

include reducing the hydrogen adsorption free energy ($\Delta G_H \approx -0$ eV), as it is higher for Ru (in absolute value) than for other noble metals [206]. It has been proposed that the oxidation state of Ru is particularly important for Ru-based nanomaterials, with oxidized sites presenting lower HER activities than metallic ones [210]. Conversely, water dissociation is favored on high-valence Ru surfaces as the adsorption of H^* and OH^* intermediate species is facilitated by higher oxygen affinities and lower energy barriers [216]. Reportedly, nanoparticle synthesis protocols such as organic precursor condensation yield the best performing Ru systems [65]. For instance, highly stable Ru nanoparticles capped with 4-phenylpyridine exhibit high HER activities ($\eta_{10}=20$ mV, and turnover frequencies of 17 s^{-1} at $\eta=100$ mV), clearly surpassing Ru and even competing with commercial Pt/C catalysts [65]. Similarly, high activities ($\eta_{10} = -29\text{mV}$) comparable to the commercially available 20% Pt/C catalyst have been achieved with ultra-small (1.72 nm), hollow Ru nanoparticles owing to their resistance to oxidation in ambient conditions [210].

5.1.1 Selected elements of electrochemistry.

The reduction solvated protons to dihydrogen taking place at the standard hydrogen electrode (SHE) is given $E_{red}^0 = 0\text{ V}$ by definition.



The E_{cell}^0 of a redox reaction involving any two half-reactions can be calculated from their E_{red}^0 . Under non-standard conditions, the cell potential can be calculated employing the Nernst equation:

$$E_{cell} = E_{cell}^0 - \frac{R \cdot T}{n \cdot F} \ln\left(\frac{a_{Red}}{a_{Ox}}\right) \quad (5.3)$$

Where a_{Red} and a_{Ox} are the activities of the reducing and oxidizing species, respectively. If the spontaneity conditions are met, $E_{cell} > 0$ whether the reaction actually takes place at all or at reasonable velocities is entirely determined by another factor: its kinetics, and the presence or absence of electrocatalysts.

There exists a voltage difference or overpotential between the thermodynamical cell potential determined by Equation (5.3) and the actual potential at which the reaction takes place:

$$\eta = E_{real} - E_{cell} \quad (5.4)$$

Whether caused by insufficient electric contact with the electrodes, slow charge carrier diffusion through or sluggish charge transport, there exists an electrokinetic barrier to the reaction. Reactions with non-zero overpotentials require higher voltages than those predicted by the Nernst equation, which increases the energy requirements of the electrochemical process. Importantly, overpotentials are reported in terms of exchange current density reference values (*e.g.* the overpotential at onset of the reaction, η_0). Therefore low η (in absolute value) are characteristic of reactions with favorable electrokinetics. The exchange current density (*i.e.* the current intensity per unit area) provides an approximate measure of how optimal the electrocatalyst-reactant interaction is: better electrocatalysts offer larger exchange current densities. In non-equilibrium conditions, the current density (i), the cell potential (E_{cell}) and the overpotential are connected through the Butler-Volmer equation. Experimentally, overpotentials are commonly measured employing Tafel plots, derived as a high-overpotential expansion of said equation. When linearized, the following expression is obtained:

$$\log(i) = \log(i_0) + \frac{1}{b} \cdot \eta \quad (5.5)$$

Experimentally, exchange densities are measured for different magnitudes of the overpotential. Direct application of Equation (5.5) results in the so-called Tafel plots, from which the Tafel slopes b can be obtained for any given electrocatalyst. Tafel slopes are a measure of the electrocatalyst's performance and may be used to further elucidate the mechanism, and more specifically, to characterize the rate determining step through consecutive single-electron transfers.

5.2 *In silico* HER on metal surfaces.

As highlighted by Pacchioni *et al* [211], theoretical calculations are crucial to the understanding (and subsequent improvement) of catalytic systems that are scaled down to nearly-isolated atoms, as in the case of single atom catalysts. Since the exhaustive characterization of all potentially active catalysts is impractical, different material screening descriptors have been developed. Sig-

nificantly, the hydrogen adsorption energy descriptor developed by Norskov and coworkers has become essential to in silico material screening for HER electrocatalysis [64]. It has been proposed that other complementary HER descriptors may be needed in alkaline media, in which activity is closely linked to water dissociation rates [205, 217]. In earlier work by Norskov and coworkers [64], catalyst activity was inferred from periodic simulations of surface slab models, on which adsorption energies for one H atom (25% coverage) or four H atoms (corresponding to a full monolayer) were calculated at PBE level. Addition of an explicit water solvation was initially reported to be unnecessary [64], although recent reports highlight the importance of cation concentration [205] or interfacial water [216, 217] on hydrogen evolution kinetics. Setting that aside, the electrochemical model proposed by Norskov is closely linked to the Sabatier principle: based on the mechanisms proposed in Eq. 5.1, the adsorption of an H atom should be neither too weak (the Volmer step becomes rate-determining) nor too strong (the Tafel/Heyrovsky steps become rate-determining). That is, metals that strongly bind atomic hydrogen (e.g. Ni and Mo) or that do not bind it with sufficient strength (e.g. Au) are expected to underperform [201, 207]. Quantitative comparison of catalyst surfaces requires an expression for the H free Gibbs energy of adsorption ΔG_H . Rigorously, the Gibbs free energy of adsorption at a given temperature T is defined as:

$$\Delta G_H = \Delta H_H - T \cdot \Delta S_H \quad (5.6)$$

Where ΔH_H and ΔS_H are the enthalpy and entropy of adsorption, which include crucial zero-point energy and thermal corrections to the H adsorption potential energy *e.g.* vibrational and electronic energies. However, in Norskov's approach only the zero-point energy and the entropic term are explicitly considered:

$$\Delta G_H = E_{ads} + \Delta E_{ZPE} - T \cdot \Delta S_H \quad (5.7)$$

Where E_{ads} is the H adsorption potential energy (without thermal corrections) and ΔE_{ZPE} is the zero-point energy. As an *ansatz*, both corrections are proposed to be constant across all metallic surfaces and equal to +0.24 eV. The ideal H Gibbs free energy of adsorption is that for which $\Delta G_{ads,H} = 0$ (the adsorption is neither too strong, nor too weak), that is $E_{ads} = -\Delta E_{ZPE} + T \cdot \Delta S_H$. Thus a system-independent *ideal value* for the hydrogen adsorption energy is set:

$$E_{ads} = -0.24 \text{ eV} = -23.7 \text{ kJ} \cdot \text{mol}^{-1} \quad (5.8)$$

Partial and full-coverage hydrogen adsorption energies for Pt were determined to be -0.33 eV and -0.27 eV respectively, the former being the closest to the ideal descriptor value. Therefore platinum has a privileged position at the summit of experimental and theoretical HER volcano plots [1]. Metals to the left of Pt in the volcano HER volcano plot (see Figure 1.5, in Chapter 1) bind hydrogen atoms too strongly, thus preventing their desorption. Metals to the right of Pt bind hydrogen too weakly and similarly hinder hydrogen evolution [1]. The effect of increasing hydrogen coverage from 25% to a full monolayer was shown to be beneficial for metals like Pt, Ir, Ni or Rh (E_{ads} became closer to -0.24 eV), but negative for W, Mo or Au [64]. It is proposed that H adsorption energies well above (e.g. Ni, which has $E_{ads} = -0.47$ eV) or well below this descriptor value (e.g. Au (111) and Ag (111) have $E_{ads} > 0$) are unlikely to initiate the onset of HER [64]. However, it is not an infallible criterion as shown for MoS₂ [201]. Huang and coworkers have proposed using kinetic barriers as a more nuanced approach to advanced electrocatalyst design, with hydrogen adsorption energies being better suited for preliminary candidate screening [213]. Periodic surface slab and cluster models were used to estimate kinetic barriers to the Volmer-Heyrovsky mechanism for MoS₂, reportedly in good agreement with experimental results [213]. Computational contributions have been generally focused on the highly active Pt. Particularly, Calle-Vallejo strongly studied Pt as electrocatalyst for several key reactions including the oxygen reduction reaction and the hydrogen evolution reaction (HER) [78, 94, 95, 212]. With the aim of establishing simple structure – activity relationships they proposed the generalized coordination numbers as a simple way to define different active sites. These generalized coordination numbers are computed with equation 1.14 and they take into account not only the coordination of the active center but also those of the first coordination sphere[94]:

$$\bar{CN}(i) = \sum_{j=1}^{n_i} cn(j)n_j/cn_{max} \quad (5.9)$$

Where the coordination number of each neighbor n_j , $cn(j)$, is weighted by their bulk coordination number, cn_{max} . For bulk fcc crystals, the maximum coordination number is twelve. The

surface atoms on the pristine (111) facets have six close neighbors with $cn = 9$, and three other atoms below with full coordination. Thus, the T9 atoms on pristine Pt(111) have the following generalized coordination number:

$$\bar{CN}(T9) = \frac{9 \cdot 6 + 12 \cdot 3}{12} = 7.5 \quad (5.10)$$

The generalized coordination number has been shown to outperform the conventional coordination number, as energy trends better described when differently-sized kinks and terraces can be distinguished (particularly, in small nanoparticles) [94]. For HER, Calle – Vallejo and Bandarenka considered the adsorption of a single H atom on different surface models, and they found that a generalized coordination number of 7.7 is optimal for obtaining the highest catalytic activity [95]. This value corresponds to some atoms of the (311) surface and it is close to the generalized coordination number of surface Pt centers on the most stable (111) surface (7.5).

The HER activity of Ru nanoparticles was explored on a Ru₅₅ model (sliced from bulk hcp Ru at the (001) and (101) planes) employing periodic calculations: the ligand-covered nanoparticle has been placed in differently sized supercells to avoid spurious interactions [65, 96]. While mostly spherical, irregularities were purposely introduced on the surface to mimic the corrugated facets and tips reported in experiments [96]. The surface was saturated with 1.2 hydrides per surface Ru atom, resulting in a Ru₅₅H₅₃ model which was later compared to an alternative Ru₅₅ model capped with eleven 4-phenylpyridine molecules. Both saturation protocols resulted in equivalent changes in the d-band of the surface atoms [65]. It should be noted that generalized coordination numbers can also be calculated for hcp crystal structures, providing different \bar{CN} values for seemingly "equivalent" sites [94].

In this contribution, the hydrogen evolution activity of defective Pt(111) and Ru(100) is explored as a means to reduce noble metal loading and, potentially, to exploit the enhanced activity of sites with lower generalized coordination numbers. Differences in hydrogen adsorption energies across distinct binding sites and for different H coverages are considered, ultimately leading to the formation of a H monolayer at the onset of hydrogen evolution. However, not all computational contributions consider monolayer formation to be essential, focusing instead on partial or single-

H surface coverage [63]. In line with prior contributions by Poteau and coworkers [65, 96], the simulations herein presented explicitly account for the formation of a monolayer with 20-24 hydrogen atoms (the exact number depends on the model under consideration). Despite being considerably more resource-intensive, a more nuanced understanding of hydrogen adsorption is expected to derive from the full-coverage approach.

5.3 Computational details.

Periodic calculations were performed with plane wave-based basis sets as implemented in the VASP 5.4 code [163, 164]. Since three-dimensional periodicity is enforced even for two-dimensional surface slabs, the lattice parameter corresponding to the non-periodic direction was set as a vacuum space of 10 Å to avoid spurious interactions across images.

Level of theory. All theoretical calculations were performed at the density functional theory level, employing the Perdew-Burke-Erzerhof (PBE) exchange-correlation functional [165] with Grimme’s D2 correction [166] to account for dispersive interactions. The herein followed methodology is analogous to that used by Calle-Vallejo and coworkers for water splitting simulations on Pt, as well as in recent contributions from our group [48, 74, 92] [95, 212] and by Pacchioni and coworkers for other transition metals [211]. No significant magnetization has been observed on Ru (100) and Pt (111), thus all calculations are performed closed-shell. Projected augmented wave (PAW) pseudopotentials [168] were used for the atomic ionic cores, while valence electrons were represented by a plane wave basis set with a 500 eV kinetic energy cutoff based on prior calibration [48, 92, 218]. Energy convergence criteria for electronic and geometry optimizations were set to 10^{-5} and 10^{-4} , respectively. The first Brillouin zone was described with a 2x2x1 Monkhorst-Pack reciprocal space k-point grid [169].

In the present contribution, the hydrogen adsorption energy is calculated as proposed by Norskov [1, 64]:

$$E_{ads} = E_{nH-surf} - \frac{E_{surf} + n/2 \cdot E_{H_2}}{n} \quad (5.11)$$

Where E_{ads} , E_{surf} and E_{H_2} are the energies of the surface with n adsorbed hydrogen atoms, of the pristine surface and of the hydrogen molecule, respectively. Descriptor values for surface

coverages above 1 atom per metal center ($\theta > 1$) are computed using the full-coverage surface as a reference:

$$E_{ads} = E_{(N+1)H-surf} - \frac{(E_{NH-surf} + E_{H_2})}{2} \quad (5.12)$$

Where N is the number of available metal centers, which varies between models.

Models. The pristine Pt(111) surface was modelled as $(5 \times 2\sqrt{3}R30)$ supercell of crystalline, 9-layered *fcc* Pt. Meanwhile, the initial Ru (100) 8-layer surface slabs have been cut from bulk *hcp* Ru instead. Owing to crystal structure, the (111) facets have at least four potential binding sites which must be considered: Top (T), octahedral (O_h), tetrahedral (T_d) and Bridge (μ) sites. Based on prior work by Calle-Vallejo and coworkers, each site is herein identified by the site's geometry (T, O_h , T_d , μ) and the generalized coordination number. Notation-wise, adsorptions on Top sites are named TCN, where CN is the conventional coordination number of the adsorbing metal atom; adsorptions on Bridge sites, $\mu(CN_1, CN_2)$; finally, three numbers are needed for the adsorptions on octahedral and tetrahedral sites, $O_h(CN_1, CN_2, CN_3)$ and $T_d(CN_1, CN_2, CN_3)$. For example, there are 20 T9, 20 $O_h(9,9,9)$ and 20 $T_d(9,9,9)$ sites on the pristine surfaces; any bridges between T9 sites would then be named $\mu(9,9)$. Meanwhile, three defective surfaces in Figure 5.1 were built by removing atoms from outermost surface layers (one on each side of the slab to enforce symmetry). Doing so generates new sites with both lower and higher coordination numbers. In doing so, a two-level surface is created: the defect plane, which contains the main defective feature in the model, and the basal plane, which stands below and mostly has T9 sites. The potential adsorption sites on the defective surfaces, henceforth referred to as M_1 , M_7 and M_{10} (M=Pt or Ru), are color-coded in Figure 5.2. These defective surfaces feature quite distinct sites and span site coordination numbers from T3 (the adatom on M_1) to T11 on the basal planes of M_7 and M_{10} . Moreover, since basal T9 sites are predictably different from defective T9 sites, the suffix -b has been added to the former when necessary.

Hereafter, each H adsorption is characterized by the conventional coordination number of the site on which it is being adsorbed for ease of discussion. Furthermore, each particular adsorption is assigned a generalized coordination number, which distinguishes it from inequivalent adsorptions on sites with similar close-neighbor geometries. For example, the hydrogen adsorptions on the T9

sites of pristine Pt(111) and defective Pt₇ are inequivalent, and indeed present different generalized coordination numbers.

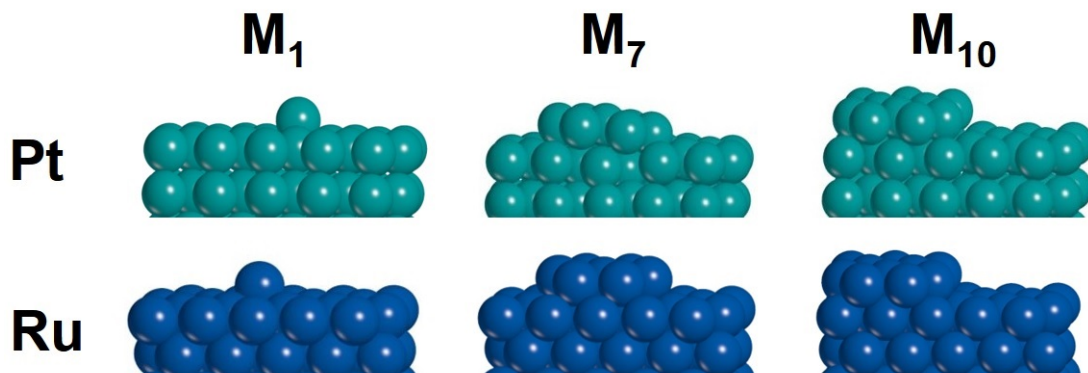


Figure 5.1. Lateral view of the defective Pt(111) (cyan) and Ru(100) (blue) surfaces.

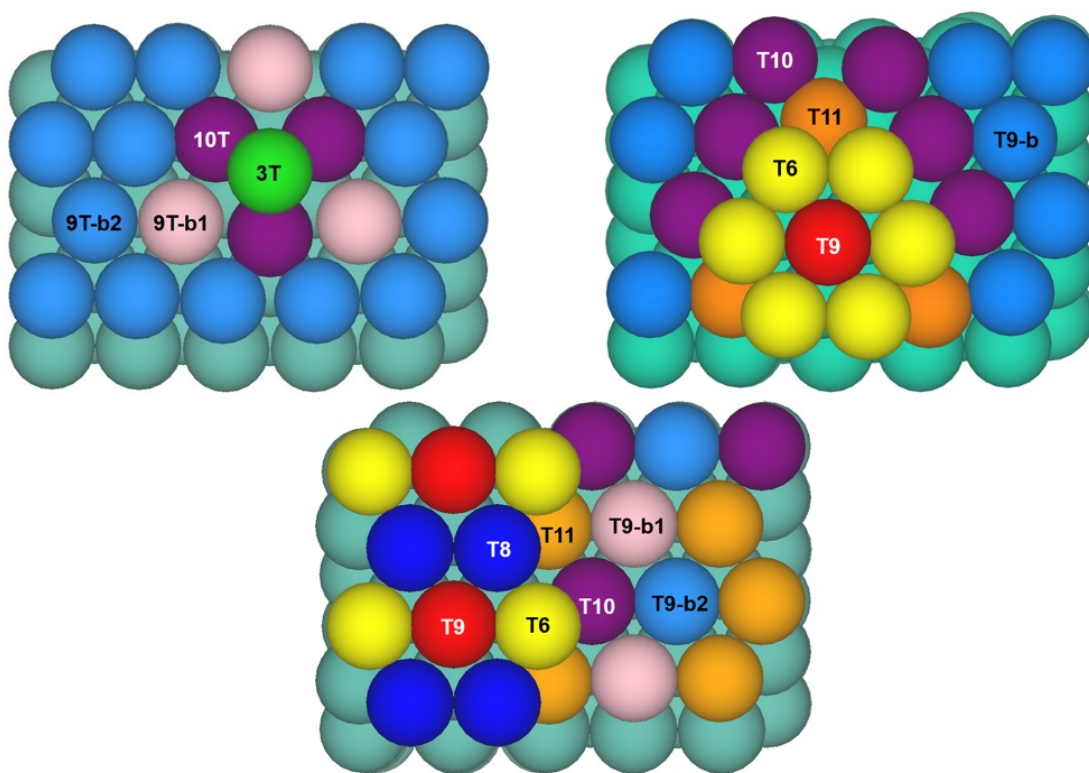


Figure 5.2. Proposed binding sites on defective Pt₁, Pt₇ and Pt₁₀. Sites and their notation are equivalent for the defective Ru(100) surfaces, which are omitted.

5.4 Results and discussion

Firstly, H adsorption energies on the pristine Pt(111) and Ru(100) are discussed. Hydrogen adsorption on the three defective surface models is presented next, focusing not only on the differences between materials but also with their corresponding pristine counterparts.

5.4.1 Hydrogen evolution on pristine Pt(111) and Ru(100) facets.

Single H adsorption has been explored in order to better understand differences between pristine Pt(111) and Ru(100) surfaces. The hydrogen adsorption energies are presented in Table 5.1, while the optimized structures are shown in Figure 5.3. The adsorption energies and M-H bond distances at the full coverage ($\theta = 1$) and at the onset of hydrogen evolution ($\theta = (N + 1)/N$) are presented in Table 5.2, and the corresponding structure are presented in Figure 5.4.

Table 5.1. *Computed PBE-D2 single H adsorption energies and M-H bond distances (in $\text{kJ}\cdot\text{mol}^{-1}$ and \AA , respectively) on the four different sites on the pristine Pt(111) and Ru(100) facets.*

Model	T9	$O_h(9,9,9)$	$T_d(9,9,9)$	$\mu(9,9)$
	E_{ads} d(M-H)	E_{ads} d(M-H)	E_{ads} d(M-H)	E_{ads} d(M-H)
Pt	-57.1 1.558	-61.0 1.861	-55.2 1.861	-56.4 1.760
Ru	-	-70.0 1.906	-62.5 1.896	-

The most apparent difference concerns the T9 sites, for which $C\bar{N} = 7.5$: the strong adsorption on Pt ($-57.1 \text{ kJ}\cdot\text{mol}^{-1}$) could not be optimized for Ru, as any H atoms placed on T9 sites quickly evolve into nearby $O_h(9,9,9)$ or $T_d(9,9,9)$ sites. Adsorption is the strongest on $O_h(9,9,9)$ sites for the two materials, presenting similar values for Pt ($-61.0 \text{ kJ}\cdot\text{mol}^{-1}$) and Ru ($-70.0 \text{ kJ}\cdot\text{mol}^{-1}$). Binding on $T_d(9,9,9)$ sites is most favored by Ru instead ($-62.2 \text{ kJ}\cdot\text{mol}^{-1}$), although the H atom is stabilized to a comparable extent on Pt(111). The $\mu(9,9)$ bridges on Pt (111), which are only $4.6 \text{ kJ}\cdot\text{mol}^{-1}$ below the $O_h(9,9,9)$ sites, are absent on Ru (100) (one of the two $O_h(9,9,9)$ sites below the bridge is occupied instead). Overall, Pt does not present a particular preference for any of the three sites, while Ru shows a clear preference for O_h and T_d positions.

Once the strongest binding sites on each surface are identified, models for the monolayer and the subsequent onset adsorptions are built accordingly, as shown in Figure 5.4). Due to differences

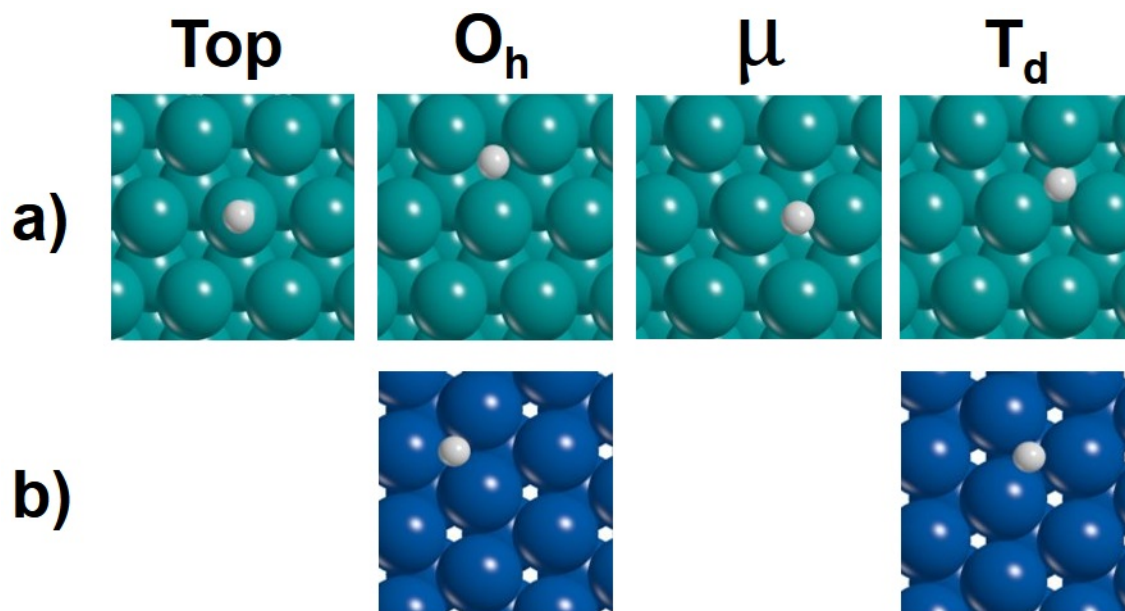


Figure 5.3. Optimized single hydrogen adsorptions on the Top (*T*), octahedral (*O_h*), bridge (*μ*) and tetrahedral sites (*T_d*) of a) Pt(111) and b) Ru(100).

Table 5.2. Computed PBE-D2 H adsorption energies and M-H bond distances (in $\text{kJ}\cdot\text{mol}^{-1}$ and Å , respectively) on the pristine Pt(111) and Ru(100) as a function of hydrogen coverage. Adsorption on ^a T9, ^b on O_h(9,9,9).

Model	$\theta=1$		$\theta=(N+1)/N$		
	E_{ads}	d(M-H)	T9 E_{ads} d(M-H)	O _h (9,9,9) E_{ads} d(M-H)	T _d (9,9,9) E_{ads} d(M-H)
Pt	-49.1 ^a	1.557	-	-33.6 1.843	-26.5 1.843
Ru	-66.0 ^b	1.878	22.9 1.607	-	39.3 1.923

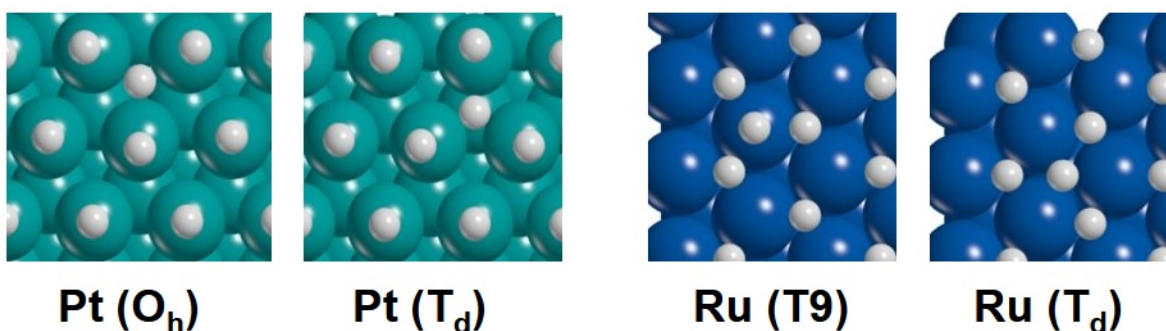


Figure 5.4. Addition of the 21st atom on four different binding sites of the $\theta = 1$ pristine Pt(111) and Ru(100) facets.

in their single hydrogen adsorption energies, the most stable H monolayers on Pt(111) and Ru(100) involve different binding sites. For Pt (111), it is possible for a T9-only monolayer to form without any atoms moving towards an octahedral site, whereas Ru favors a $O_h(9,9,9)$ -only monolayer. The full $T_d(9,9,9)$ monolayer was also assayed, being more weakly bound ($-61.2 \text{ kJ}\cdot\text{mol}^{-1}$ v. $-66.0 \text{ kJ}\cdot\text{mol}^{-1}$) as expected from the weaker binding of its tetrahedral sites. Having occupied the less adsorbing T9 sites, and not the strongly stabilizing O_h sites, the H monolayer on Pt is expected to be more weakly bound. Indeed, adsorption energy per hydrogen atom for $\theta = 1$ is lower for Pt ($-49.1 \text{ kJ}\cdot\text{mol}^{-1}$) than for Ru ($-66.0 \text{ kJ}\cdot\text{mol}^{-1}$).

Adsorption of one additional H atom on Pt can take place on an $O_h(9,9,9)$ ($-33.6 \text{ kJ}\cdot\text{mol}^{-1}$) or on a $T_d(9,9,9)$ site ($-26.5 \text{ kJ}\cdot\text{mol}^{-1}$), with the latter being closer to the $E_{adsa} = -24.7 \text{ kJ}\cdot\text{mol}^{-1}$ and therefore preferred for the hydrogen evolution onset. Meanwhile, adsorptions for $\theta > 1$ on Ru(100) involve the empty $T_h(9,9,9)$ and T9 sites. Based on their $\theta = (N + 1)/N$ descriptor values, pristine Ru(100) cannot compete with Pt(111) as it presents a strongly positive adsorption energy for the 21st atom on both the T9 ($+22.9 \text{ kJ}\cdot\text{mol}^{-1}$) and $T_d(9,9,9)$ sites ($+39.3 \text{ kJ}\cdot\text{mol}^{-1}$). It is worth noting that adsorption on $T_d(9,9,9)$ for $\theta > 1$ is more positive than on the T9 sites, despite the former being preferred in the single-H adsorption scenario: this could be attributed to surface reorganization required to fit the H atom on a $T_d(9,9,9)$ once all nearby $O_h(9,9,9)$ sites are occupied (Figure 5.4).

The results thusfar presented are consistent with experimental evidence and the predictions from volcano plots: pristine Pt (111) clearly outperforms Ru (100). Indeed, assuming that the entropic term is $+24 \text{ kJ}\cdot\text{mol}^{-1}$ for the two materials and assuming that the energy barriers can be neglected, the computed overpotential is lower than 0.1 V for Pt (highest adsorption Gibbs energy of the 21 H on Pt (111)) and around 0.4 V for Ru (adsorption Gibbs energy of the monolayer). Whether the defective surfaces proposed can enhance their HER activity (at any rate, compared to their defective Pt analogues) is a matter of how effectively surface reconstruction can weaken the adsorption of the H monolayer on Ru(100).

5.4.2 Hydrogen evolution on defective metal surfaces.

Starting with single hydrogen adsorption, adsorption energies on defective Pt(111) are presented in Tables 5.3-5.4 (for T sites and O_h/T_d sites, respectively), and in Tables 5.5-5.6 for the defective

Ru(100) models. Inclusion of defects reduces the number of T9 sites whilst giving generating new sites with lower (from 2.5 to 6.05) and higher (from 7.67 to 9.58] coordination numbers.

Table 5.3. *Computed PBE-D2 single H adsorption energies (in $\text{kJ}\cdot\text{mol}^{-1}$) on the T sites of the defective Pt surfaces. ^a At least four T6 sites on the aggregate of Pt₇ are chemically inequivalent in terms of E_{ads} . ^b Basal T9-b adsorptions. ^c Defect-basal bridge. ^d Defect-defect bridge.*

Site	Pt ₁	Pt ₇	Pt ₁₀
T3	-38.9 (2.5)	-	-
T6	-	(-38.9, -48.9) ^a (4.5)	-49.8 (4.8)
T8	-	-	-54.3 (6.0)
T9	(-52.5, -54.3) ^b (7.5-7.6)	-59.6 -48.7 ^b (6/7.6)	-51.0 (-53.8, -54.3) ^b (6.6)
T10	-42.3 ^c (5.5)	-59.1 ^c (6.5)	-66.4 ^c (7.3)
T11	-	-43.6 ^c (6.9)	-59.5 ^d (5.4)

Table 5.4. *Computed PBE-D2 single H adsorption energies, Pt-H bond distances and generalized coordination number for the O_h and T_d sites on the defective Pt surfaces. In some instances, defect-basal bridges have been formed instead. ^a Evolves to T9.*

Site		Pt ₁	Pt ₇	Pt ₁₀
O _h	E_{ads}	-52.3 -48.7	-46.0 -38.2	-47.7 -48.0
	d(Pt-H)	1.855 1.860	1.851 1.856	1.865 1.868
	$\bar{C}\bar{N}$	7.6 7.9	5 7.3	5.6 8
T _d	E_{ads}	-45.5 NA ^a	-73.1 [$\mu(6,6)$] -45.7 [$\mu(9,6)$]	-69.5 [$\mu(8,6)$] -44.2
	d(Pt-H)	1.854 -	(1.734-1.775) (1.724,1.820)	(1.763,1.768) 1.864
	$\bar{C}\bar{N}$	7.5 -	4.5 6.0	5.4 8

Adsorption on the T9 sites present energies in the range of $-51.0 \text{ kJ}\cdot\text{mol}^{-1}$ (on Pt₁₀) to $-59.7 \text{ kJ}\cdot\text{mol}^{-1}$ (on the central aggregate atom on Pt₇). Intermediate values correspond to T9 adsorptions on the basal sites on Pt₁ and Pt₁₀, the exception being a T9 site on Pt₇ presenting weaker binding

(-48.7 kJ·mol⁻¹). The reported range (less than 10.9 kJ·mol⁻¹) is in good agreement with the T9 adsorption on pristine Pt(111) (-57.1 kJ·mol⁻¹), which suggests that the T9 sites remain strongly adsorbing even after surface defects are introduced. Any major changes in HER activity are more likely to stem from the new sites generated, whose generalized coordination numbers are below (from $\bar{C}N = 7.3$ to $\bar{C}N = 2.5$) or roughly the same ($\bar{C}N = 7.6$) as the pristine-like T9 sites. This is so because of how hole and bridge adsorptions are herein used, with their $\bar{C}N$ being averaged over the number of coordinating atoms. The energies are lower for the less-coordinated T3 (-38.9 kJ·mol⁻¹) and the T6 sites on the P₇ aggregate (the adsorption on the uppermost T6 is noticeably stronger). The adsorption on the T8 sites on Pt₁₀ lies in the range of the T9 energies, suggesting $\bar{C}N = 6.0$ and $\bar{C}N = 6.6$ are comparable. Meanwhile, the T10 adsorption on Pt₁ (-42.3 kJ·mol⁻¹) is weaker and closer to the T6 values. This is consistent with the observation that adsorptions on multiple T sites with high coordination numbers evolve into bridges between two atoms instead. Indeed, bridges are formed for T10 on Pt₇ (-59.1 kJ·mol⁻¹) and Pt₁₀ (-66.2 kJ·mol⁻¹) instead of the Top adsorptions seen for lower coordination numbers.

There are at least two types of bridge: those involving a basal-defect atoms (*e.g.* the T10 adsorptions on Pt₇ and Pt₁₀), and those restricted to atoms on either plane (*e.g.* the T11 adsorption on Pt₁₀). On Pt₇ both basal-defect ($\mu(9,6)$, -45.7 kJ·mol⁻¹) and defect-defect ($\mu(6,6)$, -73.1 kJ·mol⁻¹) bridges are formed when the H atoms are placed on the T_d(11109) and T_d(9,6,6) sites, which indicates binding on tetrahedral sites is least favorable adsorption mode. Indeed, only one tetrahedral site has been computed to be minimum of the potential energy surface T_d(9,9,9) and its adsorption energy is within the weakest computed for all sites and models. Although the basal T_d(9,9,9) on Pt₁₀ has been obtained, the T_d sites on the defect plane evolve again into a defect-defect bridge ($\mu(8,6)$, -69.5 kJ·mol⁻¹). Binding on octahedral sites is stronger than on tetrahedral sites, yet less favorable than on the T9 sites. Exceptions include the O_h(9,9,9) site on Pt₁ (-52.3 kJ·mol⁻¹), while already the O_h(10,9,9) is more weakly absorbing (-48.7 kJ·mol⁻¹). Similar adsorptions energies are obtained on the other two defective surfaces.

These results show that although defects generate many binding sites with different generalized coordination numbers, those with $\bar{C}N = [6, 7.5]$ range are predominant for defective Pt(111). Overall, adsorption on T9 and T8 are roughly equivalent, while the latter are closely followed by O_h sites.

Adsorption on sites with $\bar{CN} < 6$ are weaker but remain as Top. Others evolve into weak bridges, and so do the adsorptions on T_d sites (which are, arguably, the weakest herein considered). In line with Calle-Vallejo and coworkers, for Pt(111) the ideal coordination number lies between the pristine-like $\bar{CN} = 7.5$ and the less favorable sites with either higher or lower generalized coordination numbers. Before moving onto Ru(100), the correlation between the Top hydrogen adsorption energies (Table 5.1 and Table 5.3) and generalized coordination numbers described by Calle-Vallejo has been tested (see Figure 5.5) with relative success (correlation factor of $R^2 = 0.3308$). Even after discarding the non-Top adsorptions, there are at least two outliers from the main trends, both on Pt₇: the basal T9 ($-42.3 \text{ kJ}\cdot\text{mol}^{-1}$, with $\bar{CN} = 7.6$) and defect T9 adsorptions ($-59.6 \text{ kJ}\cdot\text{mol}^{-1}$, with $\bar{CN} = 6$). Compared to the other results, the former is too weak for the almost-pristine like \bar{CN} , while the latter is stronger than expected.

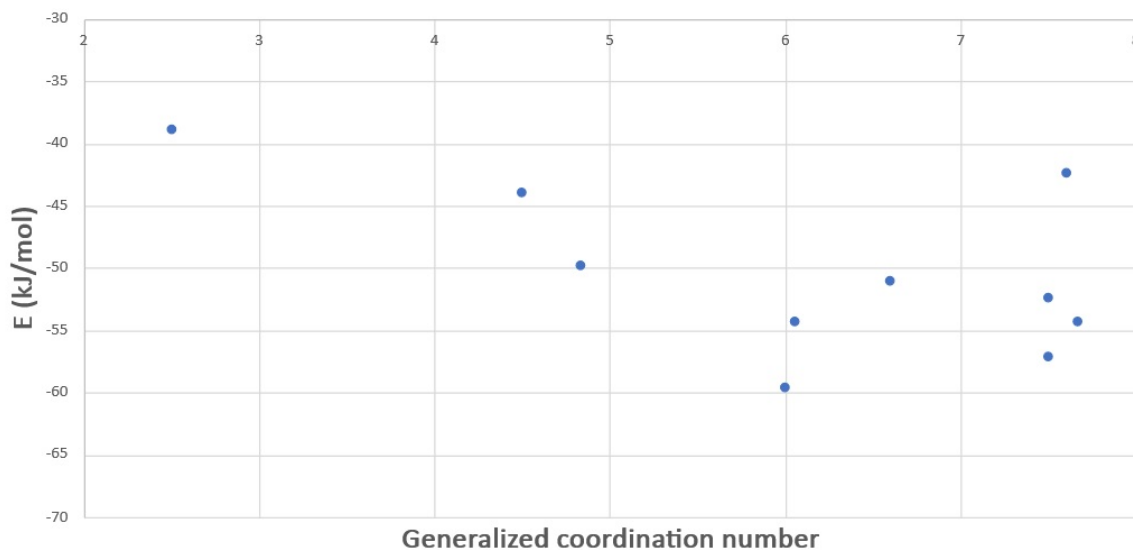


Figure 5.5. *Pristine and defective Pt(111) hydrogen adsorption energies versus the generalized coordination numbers of their T-only binding sites, and tentative linear regression.*

As expected from the absent T9 binding on pristine Ru(100), the T sites on the defective Ru(100) surfaces are unstable and the H atoms are displaced into O_h/T_d holes or μ sites (Table 5.5). For instance, the T6 site on Ru₇ is ultimately replaced by a defect-defect $\mu(6,6)$ bridge ($-69.9 \text{ kJ}\cdot\text{mol}^{-1}$), reinforcing the idea that pure T6 adsorptions would be weak. This is in stark contrast to Pt₆, whose six T6 positions could stabilize hydrogen without needing bridges (even if those were already weaker than the T9 sites). Basal-defect bridges evolve from the T10 sites on Ru₇ ($\mu(10,6)$,

Table 5.5. Computed PBE-D2 single H adsorption energies (in $\text{kJ}\cdot\text{mol}^{-1}$) on the T sites of the defective Ru surfaces. ^a Evolves to T_d . ^b Defect-defect bridge. ^c Defect-basal bridge. ^d Evolves to O_h .

Site	Ru ₁	Ru ₇	Ru ₁₀
T3	-12.9	-	-
T6	-	-69.9 ^b	-70.5 ^d
T8	-	-	-67.9 ^b
T9	-59.7 ^a	-20.8	-52.9 ^a
T10	-44.6 ^c	-65.1 ^c	-67.7 ^c
T11	-	-50.9 ^c	-60.5 ^b

Table 5.6. Computed PBE-D2 single H adsorption energies, Ru-H bond distances and generalized coordination number for the O_h and T_d sites on the defective Ru surfaces.

Site		Ru ₁	Ru ₇	Ru ₁₀
O_h	E_{ads}	-67.4 -57.0	-60.8 -70.8	-70.4 R-csuc
	d(Ru-H)	1.906 1.899	1.918 1.902	1.907
	\bar{CN}	9,9,9 10,9,9	9,6,6 9,9,9	9,8,6
T_d	E_{ads}	-59.8 -47.2	-61.5 -51.3	-53.0 -62.0
	d(Ru-H)	1.906 1.908	1.901 1.889	1.910 1.895
	\bar{CN}	9,9,9 10,9,9	10,9,9 11,9,9	988 9,9,9

-65.1 $\text{kJ}\cdot\text{mol}^{-1}$) and Ru₁₀ ($\mu(10,6)$, -67.7 $\text{kJ}\cdot\text{mol}^{-1}$), as well as from the T11 site on Ru₇ ($\mu(11,6)$, -50.9 $\text{kJ}\cdot\text{mol}^{-1}$). The energies of the first two are comparable to the $\mu(6,6)$ bridges on the Ru₇ aggregate, whereas the $\mu(11,6)$ bridge is noticeably weaker. Meanwhile, the T9b sites on Ru₁ and the T6 on Ru₁₀ are vacated in favor of strong $T_d(9,9,9)$ (-59.8 $\text{kJ}\cdot\text{mol}^{-1}$) and $O_h(9,8,6)$ (-70.4 $\text{kJ}\cdot\text{mol}^{-1}$) adsorptions, respectively. Only two truly Top adsorptions have been found on the defective Ru(100) surfaces: the T3 site on Ru₁ (-12.9 $\text{kJ}\cdot\text{mol}^{-1}$) and the T9 site on Ru₇ (-20.8 $\text{kJ}\cdot\text{mol}^{-1}$), both being below Norksov's ideal descriptor value. While the expected energy-coordination number trend is not inverted (T9 is still more adsorbing than T3), the energy difference is substantially lower than for the platinum surfaces.

Unlike Pt, occupation of octahedral and tetrahedral sites on Ru does not result in bridge formation (Table 5.6). It is apparent that $O_h(9,9,9)$ sites are strongly adsorbing in Ru_1 ($-67.0 \text{ kJ}\cdot\text{mol}^{-1}$) and Ru_7 ($-70.8 \text{ kJ}\cdot\text{mol}^{-1}$), and so is $O_h(9,8,6)$ on Ru_{10} ($-70.4 \text{ kJ}\cdot\text{mol}^{-1}$) despite its lower coordination number. Importantly, for hole sites with the same coordination numbers, the O_h adsorption is higher than that on T_d sites. Moreover, adsorption weakens when coordination is lowered or raised with respect to that of the pristine surface. On T_d sites, this is evidenced on Ru_{10} by the energy difference between $T_d(9,8,8)$ ($-53.0 \text{ kJ}\cdot\text{mol}^{-1}$) and $T_d(9,9,9)$ ($-62.0 \text{ kJ}\cdot\text{mol}^{-1}$). Similarly, binding on the more coordinated $O_h(10,9,9)$ and $T_d(10,9,9)$ sites on Ru_1 ($-57.0 \text{ kJ}\cdot\text{mol}^{-1}$ and $-47.2 \text{ kJ}\cdot\text{mol}^{-1}$, respectively) is less favorable than on the basal sites ($-67.0 \text{ kJ}\cdot\text{mol}^{-1}$ and $-59.8 \text{ kJ}\cdot\text{mol}^{-1}$).

Summing up, it is proposed that on the defective Ru(100) surfaces O_h sites provide the strongest binding, closely followed by T_d sites and certain bridges. Weaker μ sites follow, with Top adsorption being the least favored on Ru(100) (only two could be found - close in energy, despite their different coordination numbers). However, since no Top adsorptions were obtained in the pristine Ru(100) surface, it has been shown that defect inclusion can alter H adsorption trends significantly.

Table 5.7. Computed PBE-D2 H adsorption energies and M-H bond distances (in $\text{kJ}\cdot\text{mol}^{-1}$ and \AA , respectively) on the defective Pt(111) and Ru(100) as a function of hydrogen coverage. ^a T3-T11. ^b T_d . ^c T9. ^d T6. ^e O_h . ^f T3.

Model	$\theta=1$	$\theta=(N+1)/N$
	E_{ads}	E_{ads} d(H-H) (\AA)
Pt ₁	-46.1 ^a	-79.3/-33.5 ^f 1.876/0.853 (2.050)
Pt ₇	-50.5	-23.8 ^c /-45.2 ^d 0.958/0.957
Pt ₁₀	-52.4	-16.6 ^d /+14.0 ^c 0.981/0.945
Ru ₁	-50.4 ^b	-39.8/-56.0 ^f 0.930 /0.940
Ru ₇	-53.5	-47.0 ^d 0.883
Ru ₁₀	-58.0	-3.94 ^c /-15.6 ^d 0.871/0.995

Moving forward onto higher coverages, hydrogen atoms are added until a change in the adsorption energy is measured, which in principle indicates the monolayer is complete (see Figure 5.6).

There are at least 21 H atoms in the hydrogen monolayer of the M_1 surfaces, while the other defective surfaces have been shown to accept higher hydrogen counts. Predictably, only on the defective Pt(111) surfaces can Top coverage be achieved, as the monolayer on Ru(100) is mostly constituted by T_d , O_h and bridge sites instead. Given the complexity of these systems, 20 H atoms were first placed on the 20 sites available on each surface and allowed to optimize. The herein considered Ru_1 surface is constituted by basal $T_d(9,9,9)$ sites and three $\mu(10,3)$ bridges with the adatom, although it could be argued that a full $O_h(9,9,9)$ coverage could be more stable. The presence of steps in M_7 and especially in M_{10} appear to favor the formation of Bridge bonds between the defect and basal planes of the systems once enough atoms are added. Some of the bridges already seen in the single H absorption scenario are present in larger numbers. For instance, as $\mu(8,6)$ bridges along the T8-T6 edges of the step in M_{10} or as $\mu(66)$ T6 atoms in M_7 . For now, suffice it to say that monolayer stabilization on the defective P_7 , Pt_{10} , Ru_1 and Ru_7 surfaces remains mostly comparable to that of their pristine counterparts. Conversely, monolayer stabilization decreases at roughly by $10 \text{ kJ}\cdot\text{mol}^{-1}$ for Ru_1 ($-46.1 \text{ kJ}\cdot\text{mol}^{-1}$), but remains high for Ru_{10} ($-58.0 \text{ kJ}\cdot\text{mol}^{-1}$) if only twenty H atoms are added. Addition of two extra H atoms provides better saturation of the Ru_{10} surface ($-25.6 \text{ kJ}\cdot\text{mol}^{-1}$), and is herein considered to be the $\theta = 1$ structure.

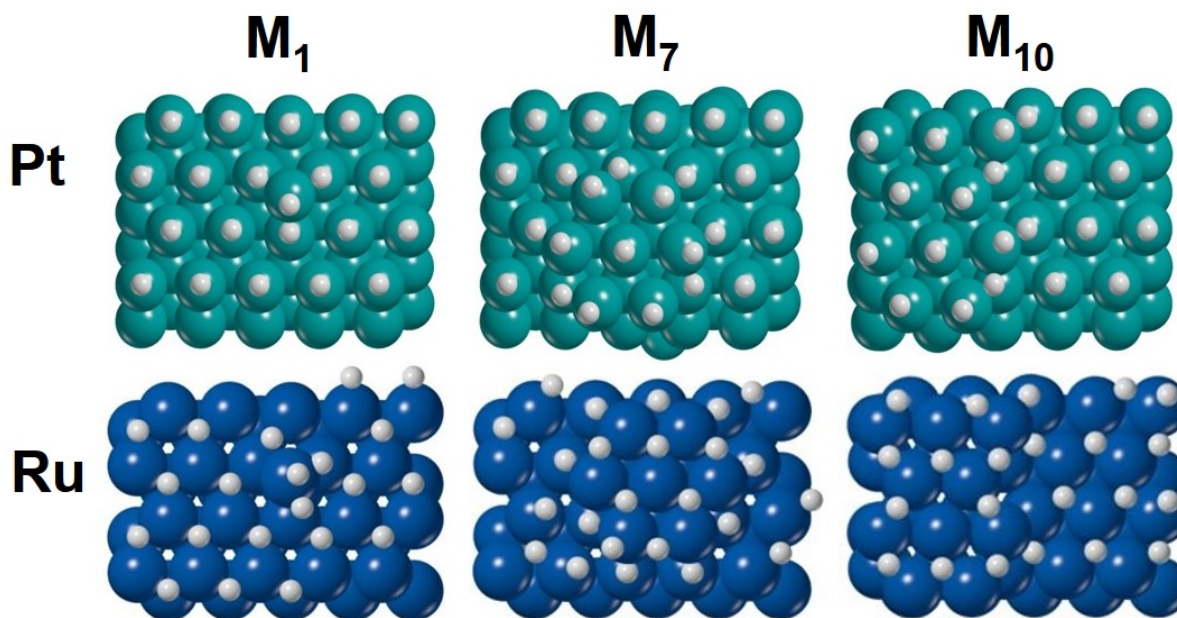
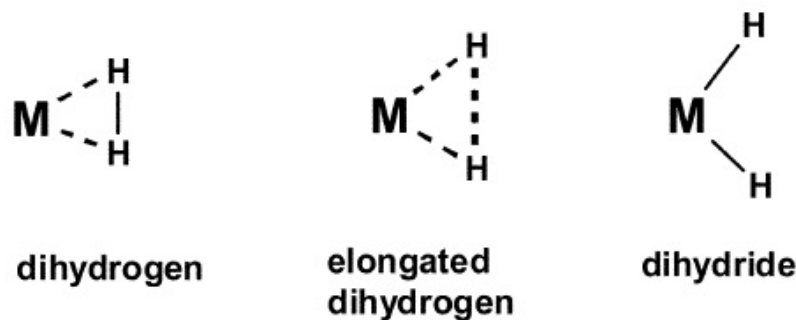


Figure 5.6. Full coverage on defective Pt(111) and Ru(100) surfaces, in correspondence to Table 5.7.

Once the monolayers are formed, which corresponds to the $\theta = 1$ coverage, adsorption of an additional H atom can result in the formation of a dihydride or the evolution of dihydrogen molecule: H \cdot · H distances above 1.5 Å are ascribed to dihydrides, while those below 1.5 Å correspond to elongated dihydrogen molecules [211, 219]. These scenarios are schematically represented in Scheme 5.1. The defective Pt(111) surfaces onto which H₂ is formed for $\theta > 1$ are shown in Figure 5.7. Adsorption of the 21st atom on the T3 site of Pt₁ (-79.3 kJ·mol⁻¹) results in two stable hydride bonds, as indicated by the long H-H distance (1.881 Å) and Pt-H bond length (1.578 Å). Interestingly, addition of two extra hydrogen atoms on the adatom (2T3 in Figure 5.7) does result in the formation of H₂ (0.853 Å) with a promising adsorption energy (-33.5 ·mol⁻¹); said addition also increases the distance between the preexisting hydrides to 2.050 Å. On Pt₇ (Figure 5.7), the T9 adsorption on the aggregate’s central atom (-23.8 kJ·mol⁻¹) almost coincides with Norskov’s ideal value. Furthermore, the measured H-H bond (0.958 Å) is indicative of dihydrogen formation, albeit still strongly bound to the surface. The adsorption on the neighboring T6 site is stronger (-45.2 kJ·mol⁻¹) but equally results in the formation of dihydrogen with a similar bond length (0.957 Å).



Scheme 5.1. Proposed metal-H₂ coordination scenarios, in which the H-H bond elongates from H₂ to a dihydride coordination [219].

On the Pt₁₀ surface (Figure 5.7), adsorption on the T6 site is weaker (-16.6 kJ·mol⁻¹) and lies below Norskov’s ideal value. Still, based on the H-H distance (0.981 Å), H₂ is formed. Elongated dihydrogen (0.945 Å) is also formed from the adsorption on T9 (+14.0 kJ·mol⁻¹) but its positive value suggests hydrogen evolution would not ensure so readily. So far, it would appear defective Pt(111) surfaces do not present any clear advantages over pristine Pt(111): hydrogen evolution

would ensue regardless due to platinum's already excellent activity, and in some instances hydrogen evolution becomes unfavorable. Differences between the computed overpotentials within the present approach are usually less than ± 0.1 V.

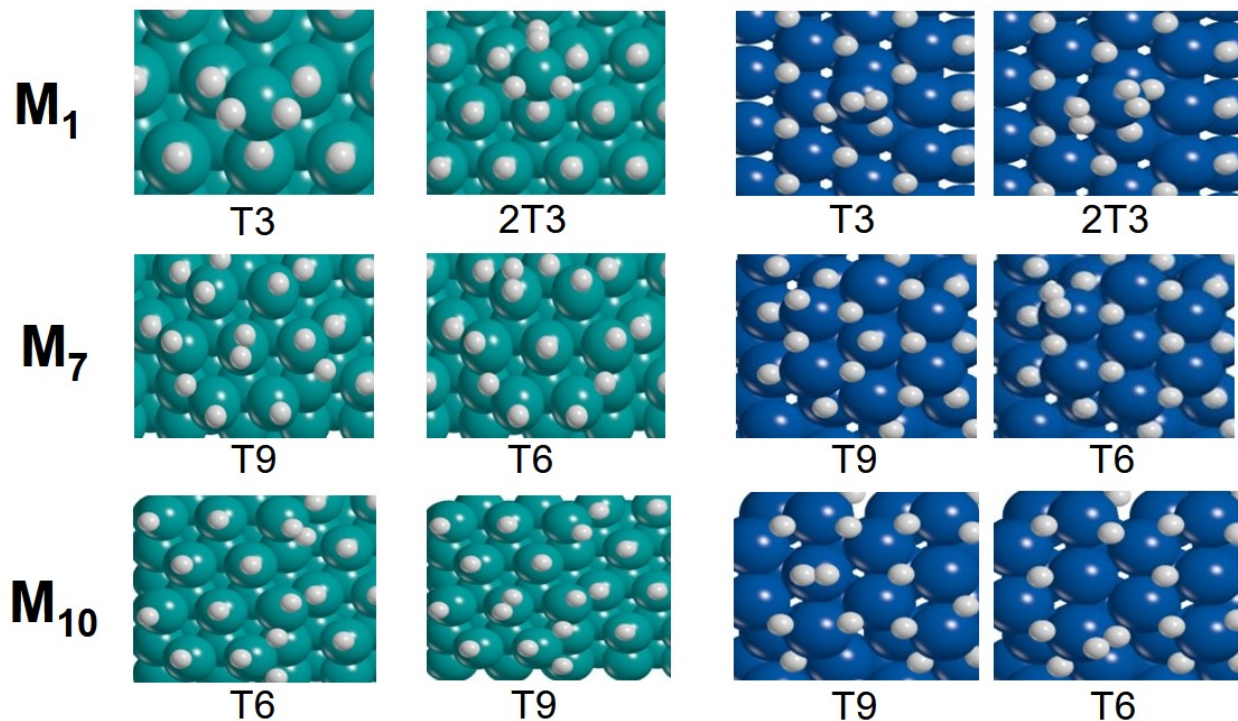


Figure 5.7. Defective Pt (left) and Ru (right) surfaces at the onset of hydrogen evolution for different ulterior H atom adsorption sites, in correspondence to Table 5.7.

The HER-enhancing effect is more apparent for the defective Ru surfaces. Dihydrogen molecules are formed when two H atoms are bound to the T3 site of Ru₁ (Ru₁₀ in Figure 5.7), unlike Pt₁, in which a hydride was formed instead. Formation of the first dihydrogen molecule (0.930 Å) is strongly favored (-39.8 kJ·mol⁻¹), and so is the formation of a second H₂ molecule (-56.0 kJ·mol⁻¹, 0.930 Å and 0.940 Å) when two more H atoms are adsorbed. By the same logic both molecules remain strongly bound to the surface. The T9 adsorption on Ru₇ (Ru₇ in Figure 5.7) is roughly equivalent to that on non-defective Ru and does not result in H₂ formation (H₂ was formed in the equivalent adsorption on Pt₇). Meanwhile, the adsorption on the neighboring T6 sites (-47.0 kJ·mol⁻¹) does result in H₂ being formed. Importantly, this H₂ molecule has a shorter bond length than those in Ru₁ (0.883 Å), although its strong binding to the surface suggests desorption would be hindered. Different $\theta > 1$ H coverage scenarios have been screened for Ru₁₀, seeing as there

are many available sites, with dihydrogen being formed in two instances (Ru_{10} in Figure 5.7). Adsorption on the defect T9 site is considerably weak ($-3.94 \text{ kJ}\cdot\text{mol}^{-1}$) and results in H_2 formation with the shortest bond length measured (0.871 \AA). Adsorption on the edge T6 sites ($-15.6 \text{ kJ}\cdot\text{mol}^{-1}$) also results in H_2 being formed, this time with a longer H-H bond (0.995 \AA). Both values are below Norskov’s ideal descriptor value, but closer to it than the overly absorbed H_2 molecules seen for Ru_1 and Ru_7 . On these grounds, desorption of H_2 on Ru_{10} seems to be most favored out of the three defective Ru(100) surfaces. More importantly, these changes in HER activity seen for the defective surfaces Ru(100) shows that surface defects can be used to favor hydrogen evolution compared to pristine. This observation is consistent with the enhanced HER activity demonstrated by Ru nanoparticles, whose multiple facets and edges contain multiple atoms with $\bar{CN} < 9$ that are HER-active. Indeed, the present computational approach predicts that the required overpotentials decrease from around 0.4 V for crystalline Ru to about 0.15 - 0.25 V for the defective models.

5.5 Conclusions.

In this Chapter, pristine and defective Pt(111) and Ru(100) surfaces have been studied for their potential use as hydrogen evolution catalysts, using hydrogen adsorption energies and generalized coordination numbers as a screening strategy. On a general note, it has been shown that single hydrogen adsorption on any of the surfaces considered, whether pristine or defective, is too strong for dihydrogen to evolve. It is not until full coverage has been achieved or even surpassed that dihydrogen can be formed, which is in agreement with experimental reports. Even at full coverage, hydrogen evolution is restricted to certain surfaces and adsorption sites, with dihydrides being formed in other instances.

More specifically, the high HER activity of pristine Pt(111) herein reported is consistent with prior experimental and computational reports. The measured adsorption energy at the onset of hydrogen evolution is close to the ideal value proposed by Norskov, with an overpotential estimate of 0.1 V. Conversely, less ideal hydrogen adsorption energies were obtained for pristine Ru(100), which is expected to require higher overpotentials of roughly 0.4 V and is therefore a worse candidate for hydrogen evolution than Pt(111).

Overall, and strictly within the limits of descriptor-based material screening, the use of defective

surfaces does not particularly enhance the activity of already-active Pt. Favorable onset sites have been detected on the full coverage Pt defective surfaces, but their proximity to the ideal descriptor value is roughly the same. More significantly, the hydrogen evolution activity of defective Ru is enhanced compared to the rather inactive pristine surfaces. The extensive defects introduced with Ru₇ and Ru₁₀ significantly enhance the adsorption of hydrogen atoms once a monolayer has been formed. Dihydrogen is also formed on the T3 sites of Ru₁, but as expected from $\bar{CN} < 6$, actual evolution of H₂ is likely hindered. It is proposed that defective surface are behind two HER-enhancing phenomena: a) the strongly adsorbing O_h has been shown to consistently decrease on the defective surfaces, which would explain the decreased H monolayer stabilization. b) Surface reconstruction leads to the appearance of more binding sites with generalized coordination numbers below the 7.5 on pristine Pt(111), which have been proposed to be more HER active. The combination of these two effects (weaker binding on O_h sites and more sites with coordination numbers closer to 7) would favor the onset of the HER, from which H₂ evolution would ensue when not strongly bound to the surface.

Hybrid materials for hydrogen evolution.

In this Chapter, DFT periodic calculations on surface slab models of metal - metal oxide species representing RuO₂@Ru core-shell nanoparticles are used to rationalize the experimental evidences for related systems. This work stems from a collaboration with Dr. Xavier Sala and co-workers at UAB. Firstly, a short specific introduction on the role of Ru nanoparticles for HER will be presented. This is followed by a summary of the main experimental results. Finally, an in-depth discussion of the results obtained from the simulations is presented. Results show that the enhanced catalytic activity of RuO₂@Ru nanoparticles when compared to pure Ru species arise mainly from the combination of two factors: i) the partial oxidation of the exposed metallic Ru atoms due to the presence of RuO₂, which decreases (in absolute value) the H adsorption energy and ii) surface amorphization, which increases the number of accessible adsorption sites, most of them with adsorption energies close to the Norskov ideal value.

6.1 Introduction.

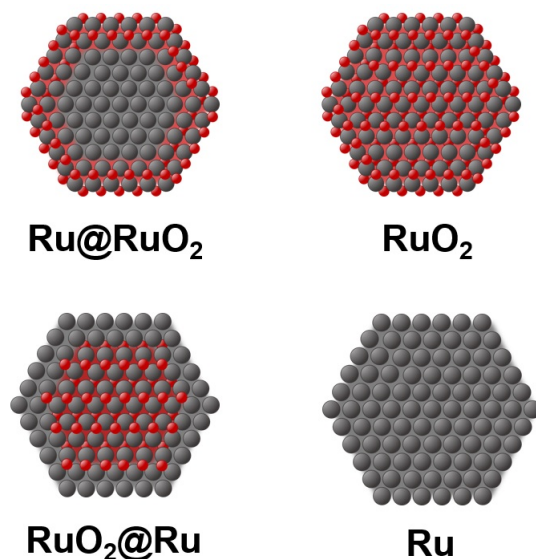
Research into renewable energy technologies has been driven forwards by the need to replace fossil fuels and reduce the effects of climate change [220–222]. Production of hydrogen through water electrolysis is a promising strategy, as it can be achieved with green electricity or sunlight conversion [223]. Thus, designing cheap, stable and active electrocatalysts to accelerate both water electrolysis half-reactions is essential. Metal-based nanoparticles with high surface-to-volume ratios and good stability are known to be efficient and selective electrocatalytic materials for the hydrogen

evolution reaction [83, 84], among other transformations [82]. Although Pt remains the state-of-the-art HER electrocatalyst in acidic media, emerging Ru-based nanomaterials can rival Pt [79] owing to their wide-range pH stability and competitive kinetics (*i.e.* adequate Gibbs free energy of the M-H bond [224]) when adequately designed [85]. However, compared to their Pt counterparts, Ru nanoparticles exhibit larger cohesive energies [225], making them prone to aggregation. Consequently, dispersion and immobilization of nanoparticles onto a conductive support is a key strategy to achieve electrocatalysts with adequate long-term performance, both preventing aggregation and improving the electronic contact between the catalyst and the electrode [83–85]. Among other conductive supports, carbon-based nanomaterials are commonly employed in electrocatalysis due to their robustness, inertness and availability in a wide range of well-defined morphologies [226]. Carbon nanotubes (CNTs) are of particular interest for electrocatalysis in aqueous media [227], given their high surface areas, metal-like conductivity, chemical stability and optimal hydrophilicity [228]. In this regard, CNTs have been shown to effectively stabilize Ru nanoparticles on hybrid electrodes for the HER [86–88, 229–233]. Globally, the effect of i) functionalizing the CNT surface by oxidative methods [87, 88], ii) doping the CNT support with one or more elements (*e.g.* N, B, Co/N [231, 233]), and iii) combining Ru with other elements to modulate the nanoparticle’s electronic properties (*e.g.* RuP₂ or B-doped Ru), on the overall electrocatalytic performance has been reported [230, 232]. It should be noted that despite having identified the as-synthesized mixtures of Ru and RuO₂ phases as the best-performing Ru-CNT electrocatalysts [87, 229], their interconversion under reductive turnover conditions and synergistic role in HER performance have not been studied in detail. Similarly, the effect of the structure properties (*i.e.* amorphization) of the CNT-supported Ru/RuO₂ electrocatalysts on HER activity has not been discussed yet.

6.1.1 Summary of experimental results.

The experimental evidence reported by Sala and coworkers must be reviewed before discussing the computational models derived thereof. The initial Ru-based nanoparticles were prepared in a CNT-THF dispersion under a H₂ atmosphere employing [Ru(COD)(COT)] as an organometallic precursor (COD: 1,5-cyclooctadiene, COT: cyclooctatetraene); their surfaces were promptly oxidized to RuO₂ through air exposure, while their cores remained as Ru(0). These Ru@RuO₂ nanoparticles were completely oxidized through thermal annealing at 300°C, either during 10 minutes or during 120

minutes. Finally, a 20 minute chronopotentiometry ($-10 \text{ mA}\cdot\text{cm}^{-2}$) was used to individually reduce the Ru@RuO₂ and RuO₂ nanoparticles: the former could be fully reduced to Ru(0) nanoparticles, while in the latter only a thin layer of Ru(0) was formed (RuO₂@Ru). In conclusion, four types of CNT supported Ru-based structures were prepared: two core-only (RuO₂ and metallic Ru) and two core-shell nanoparticles (RuO₂@Ru and Ru@RuO₂), whose suggested structures are shown in Scheme 6.1.



Scheme 6.1. Proposed Ru-based nanoparticle structures. In gray, Ru; in red, O. Adapted from [234].

Characterization with TEM confirmed the presence of optimally dispersed, as-synthesized Ru nanoparticles in the range size of $(2 \pm 0.8) \text{ nm}$, while X-ray photoelectron spectroscopy further confirmed the presence of metallic Ru and RuO₂. Nanoparticle crystallinity and post-synthesis growth (up to $5.3 \pm 0.9 \text{ nm}$) were assessed with HRTEM.

Linear sweep voltammetry was carried out in order to determine the polarization curves of CNT-supported Ru, RuO₂@Ru and RuO₂ deposited on glassy carbon rotating disk electrodes, shown in Figure 6.1. Their corresponding onset overpotentials and Tafel slopes are presented in Table 6.1. Firstly, the CNT themselves are shown not be responsible for the HER onset, seeing as they do not generate any exchange current on their own regardless of the applied potential (black curve in Figure 6.1). The exchange current induced by the fully oxidized RuO₂ nanoparticles does not go above $-10 \text{ mA}\cdot\text{cm}^{-2}$, which suggests they are not suitable for HER catalysis either. Conversely, both

the Ru-only and the RuO₂@Ru nanoparticles induce significant exchange current densities, albeit requiring different applied potentials to achieve the same current. Taking the $j=-10 \text{ mA}\cdot\text{cm}^{-2}$ as a reference, it is apparent that RuO₂@Ru needs a lower overpotential than the Ru-only nanoparticles. Thus, the CNT-supported RuO₂@Ru nanoparticles are the most promising of the materials hereby considered, a fact consistent with their electrochemical data ($\eta_{10}=115 \text{ mV}$ and $b=77 \text{ mV}\cdot\text{dec}^{-1}$). This must be rationalized through the crucial DFT analysis in terms of hydrogen adsorption energies (as per Norskov's approach), potential charge transfer or surface reconstruction.

Table 6.1. Overpotentials and Tafel slopes corresponding to the Ru-based HER electrocatalysts herein discussed.

System	η_0 (mV)	η_{10} (mV)	b (mV $\cdot\text{dec}^{-1}$)
RuO ₂	125	-	251
Ru (0)	150	222	115
Ru@RuO ₂	200	272	116
RuO ₂ @Ru	50	115	77

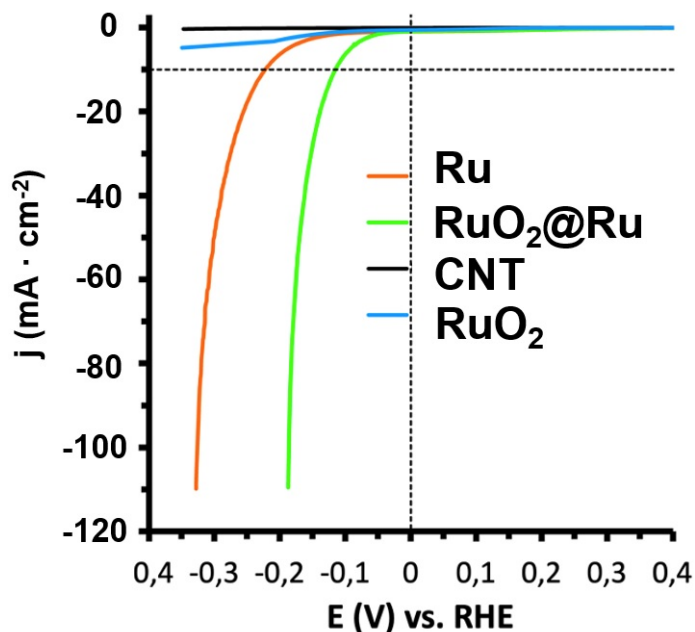


Figure 6.1. Linear sweep voltammetry polarization curves (in 1M H₂SO₄) of Ru (orange), RuO₂@Ru (green) and RuO₂ (blue) CNT-supported nanoparticles. In black, polarization curve of a CNT-only sample. Adapted from [234].

6.2 Computational details.

Models. DFT calculations were performed to rationalize the difference observed for the nanoparticles present in r-Ru@RuO₂/CNT/GC and Ru-RuO₂-10'/CNT/GC. The latter were modelled with three non-polar slab models differing in the Ru content above and below the RuO₂ slab (see Figure 6.2): the RuO₂@Ru₇ model (henceforth: Ru₇) model is formed by a seven Ru atom aggregate with a close-packed plane structure, the RuO₂@Ru₁₀ model (Ru₁₀) consists of a small nanoparticle model with two close-packed planes with 7 and 3 atoms, respectively, and the RuO₂@Ru₂₀ model (Ru₂₀) implies a full Ru shell with a close-packed structure over the RuO₂ core. Additionally, a model consisting of a Ru₂₀ with twice the thickness of the RuO₂ core, (RuO₂)₈@Ru₂₀, was also constructed, as well as a model with two full Ru layers over RuO₂ (Ru₄₀).

The RuO₂ rutile-like structure in these three models was represented by a (3x2) supercell, four-layer slab model of the most stable (110) surface to give enough space to fit the Ru₇ and Ru₁₀ models and to avoid a large mismatch (less than 6%) with the Ru monolayer on the Ru₂₀ model. The Ru monolayer of Ru₂₀ corresponds to a (5x2√3R30) supercell of crystalline (100) Ru. The final cell parameters are $a = 9.4609\text{\AA}$, $b = 13.6556\text{\AA}$ and $C = 35\text{\AA}$. Finally, a (5x2√3R30) supercell of a crystalline 9-layer cubic close-packed (111) slab of platinum was also considered as a reference system.

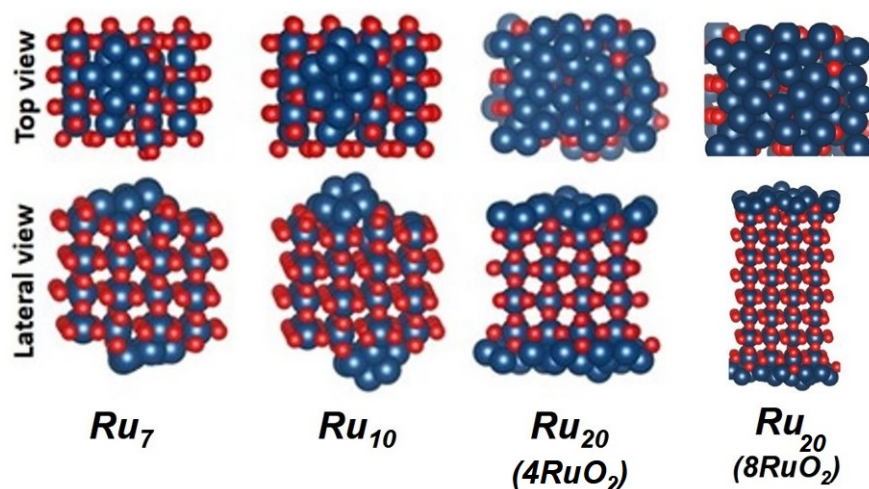


Figure 6.2. Optimized RuO₂@Ru structures herein, including two defective surfaces (Ru₇ and Ru₁₀) and two pristine slabs with different layer count (Ru₂₀ and Ru₄₀). In blue, Ru; in red, O.

Level of theory. All calculations were performed with the PBE [165] density functional as implemented in VASP [163, 164]. The dispersion forces were considered by adding Grimme’s D2 empirical correction [166]. Atomic cores are described with PAW pseudopotentials [167, 168] and their valence electrons are represented with a plane-wave basis set with an energy cutoff of 500 eV. The first Brillouin zone is described with a (4,4,1) Monkhorst-Pack k -point mesh [169]. The energy convergence criteria are fixed to 10^{-5} and 10^{-4} eV for electronic and geometry relaxations, respectively. This methodology is analogous to that used in prior contributions involving RuO₂ and IrO₂ surfaces and their electrocatalytic activity [74, 92]. Bader charge analysis [170, 171] was performed to analyze the influence of the Ru charge on the H adsorption energies. H adsorption energies reported along the contribution are mean values computed as proposed by Norskov and coworkers [1]:

$$E_{ads} = E_{nH-surf} - \frac{E_{surf} + n/2 \cdot E_{H_2}}{n} \quad (6.1)$$

Where $E_{nH-surf}$, E_{surf} and E_{H_2} are the energies of the surface with adsorbed hydrogen atoms, of the clean surface and of the H₂ molecule, respectively; n is the number of hydrogen atoms. For coverages (θ) higher than 1 hydrogen atom per unsaturated metal center, the adsorption energies were computed with respect to the 1 hydrogen per Ru center coverage, that is:

$$E_{ads} = E_{(N+1)H-surf} - \frac{(E_{NH-surf} + E_{H_2})}{2} \quad (6.2)$$

Where N is the number of accessible ruthenium centers. Norskov and coworkers have proposed that the ideal value for this descriptor is $-23.0 \text{ kJ}\cdot\text{mol}^{-1}$, corresponding to a rightly balanced adsorption on the surface.

6.3 Results and discussion.

6.3.1 Hydrogen adsorption energies on RuO₂@Ru surface slabs.

According to Norskov and co-workers, the H adsorption energy can be used as a descriptor of the electrocatalytic activity in the HER [1, 64, 97]. Therefore, the adsorption energy of H was computed for the five models at three different hydrogen coverages, namely, 1 hydrogen on the

surface ($\theta = 1/N$), 1 hydrogen per Ru surface atom ($\theta = 1$), and one additional hydrogen atom over said H monolayer ($\theta = (N + 1)/N$). As shown in previous Chapter, coverages above 1 may likely be needed to correctly represent the surface at reaction conditions. Moreover, different sites were considered in each case. For Ru and Pt surfaces with ordered close-packed planes, three different sites were analyzed: 1) above the tetrahedral (T_d) hole (3_{T_d}); 2) above an octahedral (O_h) hole (3_{O_h}) and 3) over a metal atom of the surface (1_{top}). Alternatively, for Ru₇, Ru₁₀ and Ru₂₀ other sites covering the most representative environments were explored, such as the interaction of H with 1, 2 and 3 Ru centers. Table 6.2 reports the highest adsorption energies of the first H atom, the mean value of the adsorption energy of one H per Ru surface site ($\theta = 1$) and the adsorption energy range of additional H atoms after full coverage is achieved ($\theta > 1$). In this last case, since there are several potential sites available, only a selected representative set has been considered.

Table 6.2. *PBE-D2 H adsorption energies ($\text{kJ} \cdot \text{mol}^{-1}$) for the surface models discussed at different hydrogen coverages (Θ). ^a Highest adsorption energy at this H coverage. ^b Range of adsorption energies. ^c H adsorption energies computed with a RuO₂@Ru₂₀ model containing an 8 RuO₂ layer-thick core (Figure 6.2).*

Model	$\Theta = 1/N$	$\Theta = 1$	$\Theta = (N + 1)/N$
Pt	-58.0 ^a	-50.3	-32.0 to -34.9
Ru	-71.1 ^a	-66.8	+14.1 to +33.8
RuO ₂ @Ru ₇	-76.6 to -49.7 ^b	-66.3	-23.5 to -31.2
RuO ₂ @Ru ₁₀	-76.1 to -31.4 ^b	-59.7	-27.5 to -32.2
RuO ₂ @Ru ₂₀	-70.7 to -30.5 ^b -70.3 to -38.5 ^c	-57.9 -56.6 ^c	-31.9 to -51.3 -20.5 to -55.3 ^c

As already discussed in the previous Chapter, adsorption of the first H on Ru is strong ($-71.1 \text{ kJ} \cdot \text{mol}^{-1}$) and has a clear preference for the octahedral 3_{O_h} sites, while that occurring on Pt is weaker ($-58.0 \text{ kJ} \cdot \text{mol}^{-1}$) and does not exhibit preference for any of the three sites. At full coverage ($\theta = 1$, Figure 6.4), the same trends are observed: the adsorption of H on Ru is stronger than on Pt ($-66.8 \text{ vs. } -50.3 \text{ kJ} \cdot \text{mol}^{-1}$), with the latter lacking a clear preferred site. However, in both cases, adsorption energies are significantly higher (in absolute value) than those corresponding to an optimal catalyst as defined by the Norskov descriptor ($E_{ads}(H) = -23 \text{ kJ} \cdot \text{mol}^{-1}$) [64]. Remarkably,

the adsorption of additional H atoms on the monolayer is unfavorable on Ru, but remains favorable on Pt (with adsorption energies close to $-32.0 \text{ kJ}\cdot\text{mol}^{-1}$). This suggests that H adsorbs too strongly on Ru at low coverages, ultimately preventing H_2 evolution. Furthermore, at higher H coverages, H_2 evolution on crystalline Ru is hindered by the unfavorable H adsorption. Conversely, while at low coverages H_2 evolution on Pt is also unfavorable owing to strong H adsorption, at higher coverages it weakens and becomes closer to the ideal value [64], so that H_2 evolution is favored on Pt.

The outermost Ru centers of Ru_7 , Ru_{10} and Ru_{20} present a high degree of amorphization. This is attributed to the roughness of the (110) RuO_2 surface, which prevents the formation of Ru close-packed planes. Thus, the exposed atoms present lower coordination and the surface does not have well-defined O_h , T_d and Top sites. The adsorption energy of H on said three models at low coverage ranges from -76.7 to $-30.5 \text{ kJ}\cdot\text{mol}^{-1}$, depending on the number of Ru centers interacting with the adsorbed hydrogen and their charges (see below).

Taking Ru_7 as paradigmatic case, the adsorption modes and their energetics to all potential sites were analyzed. Single H adsorption descriptor values in Table 6.3 offer a closer look into the effect of amorphization on the diversity of binding sites on Ru_7 , Figure 6.3. Based on the adsorption energies in Table 6.3, highly favorable adsorptions of at least $-60 \text{ kJ}\cdot\text{mol}^{-1}$ take place on sites 2, 3 and 4, which are the furthest from the RuO_2 core. Adsorption on 5 is slightly less favorable, at most $17 \text{ kJ}\cdot\text{mol}^{-1}$ above that on site 2. Meanwhile, adsorption on site 1, which consists of a mostly burrowed Ru, does not appear to take place: any H placed on top of 1 are rapidly displaced to site 2. This is consistent with the large positive charge on 1 induced by the RuO_2 and the subsequent hindering of H adsorption. Regarding hydride bridge formation, site 2, being the highest above the surface, allows for stable bridges to form with sites 2, 3 and 4; bridges to 1 are not formed, and 5 is not close enough. Only another, slightly less strong bridge is formed between sites 4 and 5. Meanwhile, simultaneous formation of multiple H adsorption leads to a complex scenario: whether 6, 7 or 8 H atoms are added to Ru_7 , only 2 or 3 hydride bridges are formed, yet adding more than 6 atoms completely rearranges the aggregate. On these grounds, it is suggested that at the onset of the HER Ru_7 is not fully covered.

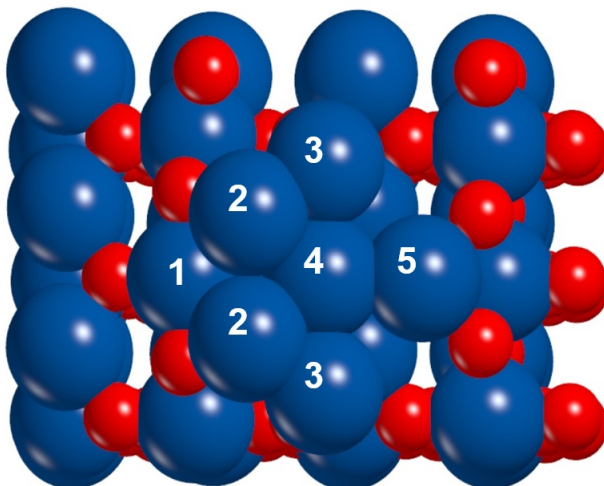


Figure 6.3. Apical view of the Ru₇ surface slab, in which the seven Ru atoms have been numbered to better examine their chemical inequivalency.

Table 6.3. Single on-site and bridge H interactions on Ru₇, as described in Figure 6.3. The Ru atom pairs involved in a bridge are indicated in parenthesis.

Site	2	3	4	5
On-site	-67.8	-60.1	-63.5	-49.7
Bridge	-76.7 (2-2) -68.9 (2-3) -71.0 (2-4)	-	-66.3 (4-5)	-

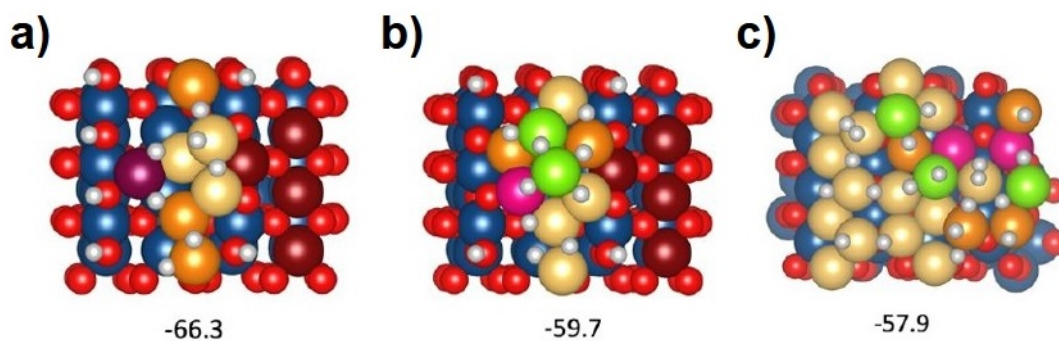


Figure 6.4. Full coverage structures and H adsorption energies corresponding to a) Ru₇, b) Ru₁₀ c) and Ru₂₀. Bader charges on Ru atoms are color coded from green (no net charge), to yellow (low charge build-up) to dark red (significant charge build-up).

For Ru₁₀ and Ru₂₀, no systematic study has been performed due to the larger number of sites and

adsorption possibilities. Alternatively, some selected sites were analyzed and the following trends obtained. The adsorption energy of the sites presenting the strongest interaction with H of each model is comparable to the values computed for Ru, although there are also several sites on which H adsorbs more weakly. The H adsorption energy tends to increase upon increasing the number of metal centers the adsorbed H is interacting with, and on decreasing the positive charge of the interacting Ru centers. The final adsorption energies are probably a compromise of three factors: a) reduced metal coordination in the amorphous shells enhances H adsorption, b) the strongly-binding O_h sites become less accessible due to surface amorphization and c) oxidation of the outermost Ru atoms by the RuO_2 core. By virtue of (a), adsorption on the already strongly binding octahedral sites should be made all the more favorable than in pristine Ru; yet, as per (b), these sites are not available to the same extent. Based on the overall observed weakening of the Ru-H interactions, it would appear that the RuO_2 -induced oxidation makes up for the incomplete coordination of the shell. Thus, the RuO_2 core generates partially oxidized Ru binding sites (c) which weakly bind hydrogen. Importantly, the concomitant surface amorphization weakens subsequent adsorptions on the hydrogen monolayer, thus facilitating H_2 formation and its release.

The average adsorption energies of one H atom per exposed Ru center at full coverage are quite similar for Ru_7 , Ru_{10} and Ru_{20} (-66.3, -59.7 and -57.9 $\text{kJ}\cdot\text{mol}^{-1}$, respectively) and close to the value on crystalline Ru (-66.8 $\text{kJ}\cdot\text{mol}^{-1}$). This suggests that H_2 evolution only occurs at coverages above unity. However, in contrast to crystalline Ru, adsorption of one additional H atom on the three models of r- RuO_2 -10'/CNT/GC is favorable and usually weak, with values ranging from -23.5 to -51.3 $\text{kJ}\cdot\text{mol}^{-1}$. While there are still some sites exhibiting strong adsorption energies, most of the explored sites present values similar to those of Pt or even close to the ideal value. Remarkably, increasing the width of the RuO_2 core (see Figure 6.2) does not alter the H adsorption energies (in Table 6.2), which suggests that the thickness of the RuO_2 core has little influence on the material's catalytic activity. Moreover, results obtained when considering a two-layer thick shell of metallic Ru over RuO_2 (the Ru_{40} model) show that the addition of the second layer is sufficient to obtain a material that behaves similarly to metallic Ru. This is associated to the fact that Ru_{40} presents an almost crystalline outermost Ru metallic surface and that the charges of this external surface are similar to those of full Ru.

Important information regarding surface atom oxidation in the two amorphous Ru_7 and Ru_{10}

systems shown in Figure 6.4 can be obtained by comparing to crystalline Ru₂₀. Indeed, significant surface rearrangement in Ru₇ and Ru₁₀ results in differently charged binding sites. Large positive charges appear on exposed core atoms of Ru₇ and Ru₁₀, which is consistent with their expected oxidation state as RuO₂; furthermore, proximity to the RuO₂ should raise the oxidation state of the shell atoms. Indeed, in Ru₇ the burrowed Ru accumulates the largest positive charge in the aggregate, with the other atoms still exhibiting charges in the +0.2 - +0.4 range as distance to the core increases. This is more apparent in Ru₁₀, where the uppermost two Ru atoms are almost neutral, while those below appear to be significantly oxidized by the core. Arguably, the addition of extra Ru atoms on the shell reduces the positive charge on the already present shell atoms.

In summary, calculations are in agreement with the higher HER catalytic activity of RuO₂@Ru when compared to Ru@RuO₂, which has been attributed to two factors based on theoretical calculations: a) amorphization of the external Ru atoms increases the number of H atoms that can be adsorbed and b) partial oxidation of the surface Ru centers by RuO₂ globally weakens the H adsorption.

6.4 Conclusions.

As part of a collaboration with Dr. Xavier Sala (UAB), simulations were carried out to understand the enhanced catalytic activity of a newly synthesized HER hybrid electrocatalyst. Core-shell periodic slab models were used to mimic CNT-supported RuO₂@Ru nanoparticles, which were then compared to pure Ru and Pt surfaces at different H coverages. Use of hydrogen adsorption energies as HER descriptors is commonplace, but reports on coverages of more than one hydrogen atom are more scarce in the existing literature. Calculated data of H adsorption energies reproduce the experimental catalytic activity trends and reinforce their use as descriptors in material screening.

Simulations with different Ru thicknesses indicate that catalytic activity is highly dependent on said thicknesses. When the Ru shell is only one layer thick, surface amorphization prevents the adsorption of H at the octahedral sites. This weakens the overall Ru-H interaction, and as part of the reconstruction, additional sites are generated with adsorption energies close to those of Pt. However, HER activity in two-layer shells (which exhibit a greater degree of crystallinity) is

lower and resembles that of pristine Ru, which further evidences the importance of amorphization. Defective surfaces with less than one layer exhibit a greater degree of surface reconstruction and are highly HER active. The latter observation is crucial, as experimental reports do suggest that an incomplete shell could be formed around the RuO₂@Ru nanoparticles. Moreover, the presence of a RuO₂ core induces the oxidation of the Ru shell, through which charge transport properties are enhanced. It is worth noting that the thickness of the RuO₂ core is proposed to be less impacting than that of the Ru shell.

Amorphization may also explain the high HER activity exhibited by very small Ru nanoparticles, which also present numerous surface sites and defects [85, 224]. Overall, theoretical calculations suggest that the reported catalytic enhancement arises from the structure of the partially oxidized, highly amorphous Ru shell.

General conclusions

The theoretical calculations presented throughout this thesis are intended to contribute to the better understanding of hybrid nanomaterials, particularly, regarding low-dimensional semiconductors for photonic applications and metal surfaces for hydrogen evolution. To that end, atomistic DFT simulations have been carried out for a wide variety of rationally-designed models varying in dimensionality, composition, and morphology.

Regarding semiconductor materials for applications in photonics, this Thesis provides a comparative description of the electronic structure of (MX) binary metal chalcogenides (MX = CdSe, CdS, ZnSe and ZnS) and core-shell CdSe@MX (MX = CdS, ZnSe or ZnS) models, from bulk and surfaces to quantum dots. Results presented for surface slabs reveal that interactions with the ligands are mostly electrostatic in nature, with little to no surface charge transfer. Ligand-surface dispersive interactions have been shown to strongly influence adsorption at low surface coverages, while at high coverages, steric effects become significant for the bulkier ligands and the energy balance may favor parallel adsorptions over the stacked conformations. Important energy gap shifts are reported when ligand passivation is coupled to implicit solvation and AIMD thermal effects. From a methodological standpoint, the underestimated PBE band gap energies have been successfully corrected in a cost-effective, material-specific approach known as best estimated value. For the (CdSe₆@(MX)₂₇) model, simulations suggest that Type-I, reverse Type-I and Type-II core-shell behavior can be achieved by changing the material on the shell. Solvent and thermal effects should be considered for the full understanding of ligand passivation.

On the topic of hydrogen evolution electrocatalysts, the activity of three defective Pt(111) and Ru(100)-based surfaces has been tested. Unlike their pristine counterparts, which have also been explored, the defective surfaces present an increasing amorphization degree and metal centers with varying coordination numbers. Based on hydrogen adsorption energy material screening, it is proposed that the activity of platinum is mostly unchanged when defects are introduced. Conversely, promising descriptor values reported for the defective Ru(100) slabs suggest that the HER activity could be higher than for their pristine counterparts. Future surface and nanoparticle-based studies are best aimed at tuning the activity of defective Ru or assaying Earth-abundant metals.

Finally, hybrid RuO₂@Ru core-shell nanoparticles have been simulated as periodic surfaces, shedding light on their reportedly higher HER activity. Different shell models were built as new evidence suggested that the high degree of surface amorphization could lie behind said enhancement. The strong Ru-H interactions on octahedral sites are suggested to be weaker as a result of amorphization, which is also evidenced by the presence of undercoordinated H atoms. The surface itself becomes more oxidized, and charge transport properties are enhanced. Further material screening would benefit from the use of nanoparticle models in which facet-specific reconstruction and hydrogen adsorption could be assayed.

Despite the computational challenges encountered, the wide-scope results herein presented open new lines of research while remaining consistent with previous theoretical and experimental reports on semiconductor materials and metallic electrocatalysts. As an added challenge to the already-complex systems herein considered, the high atom counts commonly involved have made access to high-performance computing facilities an absolute necessity.

Acknowledgements

Firstly, I would like to thank those who have helped me throughout these four years. To my family and friends, for their endless patience and unwavering support. To my thesis directors, Prof. Dr. Mariona Sodupe and Dr. Xavier Solans-Monfort, for their constant help, valuable advice and wise supervision. Last but not least, I would like to thank the many people at the Chemistry Department I have had the pleasure to work with during my PhD research. I extend my gratitude to the Spanish Ministerio de Universidades for the FPU Grant provided. Similarly, the opportunity provided by the *Red Española de Supercomputación* (RES) and the *Consorti de Serveis Universitaris de Catalunya* (CSIC) to use their computational facilities has been essential.

Dídac Armand Fenoll Silvestre, Manresa, 2023

CURRICULUM VITAE

Education

- 2019-2023 PhD, Theoretical Chemistry (UAB)
- 2018-2019 Msc, Advanced Nanoscience and Nanotechnology (UAB)
- 2013-2018 Bsc, Chemistry Degree, Mention in Material Science (UAB)
- 2013-2018 Bsc, Physics Degree (UAB)

Recent publications

- X. Sala *et al.*, *Inorg. Chem. Front.* **2023**, 10, 20, 5885-5896.
- D.A. Fenoll, M. Sodupe, X. Solans-Monfort, *ACS Omega* **2023**, 8, 12, 11467-11478.

Other publications

- G. Tejada, D.S. Belov, D.A. Fenoll, K.L. Rue, Ch. Tsay, X. Solans-Monfort, K. Bukhryakov, *Organometallics* **2022**, 41, 4, 361-354.
- D.S. Belov, D.A. Fenoll, I. Chakraborty, X. Solans-Monfort, K. Bukhryakov, *Organometallics* **2021**, 40, 17, 2939-2944.

Workshops and training

- Training School "Computational Materials Modeling" at Technion-Israel Institute of Technology (COST Action 18234).

Teaching and outreach activities

- Extended tuition activities during PhD programme
- Currently an S18 Substitute Teacher at UAB (Chemistry Department)
- *Jornades de Química Interactiva* 2020-2023

references

Bibliography

- [1] Z.W. Seh et al. “Combining Theory and Experiment in Electrocatalysis: Insights into Materials Design”. In: *Science* 355, eaad4998 (2017).
- [2] E. Pomerantseva et al. “Energy storage: the Future Enabled by Nanomaterials”. In: *Science* 2019, 366, 6468 (2019).
- [3] A.P. Alivisatos. “Semiconductor Clusters, Nanocrystals and Quantum Dots.” In: *Science* 271, 933-937 (1996).
- [4] M.A. Boles et al. “The Surface Science of Nanocrystals”. In: *Nat. Mater.* 15, 141-153 (2016).
- [5] G. Cao. *Nanostructures and Nanomaterials: Synthesis, Properties, and Applications (1st edition)*. Imperial College Press, United Kingdom. ISBN: 9781860944802, 2004.
- [6] H. Gao et al. “Three-Dimensional Hierarchical g-C₃N₄ Architectures Assembled by Ultrathin Self-Doped Nanosheets: Extremely Facile Hexamethylenetetramine Actiation and Superior Photocatalytic Hydrogen Evolution”. In: *ACS Appl. Mater. Interfaces* 2019, 11, 2, 2050-2059 (2019).
- [7] P. Gomez-Romero and C. Sanchez. *Functional Hybrid Materials*. Ed. by Wiley-VCH. 2004.
- [8] A. Puzder et al. “Self-Healing of CdSe Nanocrystals”. In: *Phys. Rev. Lett.* 92, 217401 (2004).
- [9] S. Kilina, S. Ivanov, and S. Tretiak. “Effect of Surface Ligands on Optical and Electronic Spectra of Semiconductor Nanoclusters”. In: *J. Am. Chem. Soc.* 131, 7717-7726 (2009).

- [10] D. Ghosh, S.A. Ivanov, and S. Tretiak. "Structural Dynamics and Electronic Properties of Semiconductor Quantum Dots: Computational Insights". In: *Chem. Mater.* 33, 7848-7857 (2021).
- [11] M. Grunwald et al. "Metastability in Pressure-Induced Structural Transformations of CdSe/ZnSe Core/Shell Nanocrystals". In: *Nano Lett* 13, 4, pp. 1367-1372 (2012).
- [12] H.J. Hou et al. "Structural, Elastic and Thermodynamic Properties of Rock-salt structure CdSe at High Temperature and High Pressure". In: *Chalcogenide Letters* 11, 121-128 (2014).
- [13] C.B. Murray, D.J. Norris, and M.G. Bawendi. "Synthesis and Characterization of Nearly Monodisperse CdE (E=S, Se, Te) Semiconductor Nanocrystallites". In: *J. Am. Chem. Soc.* 115, 19, 8706-8715 (1993).
- [14] Z. Peng and X. Peng. "Formation of High-quality CdTe, CdSe and CdS Nanocrystals using CdO as precursor". In: *J. Am. Chem. Soc.* 123, 1, 183-184 (2001).
- [15] T. Kippeny, L. Swafford, and S. Rosenthal. "Semiconductor Nanocrystals: a powerful visual aid for introducing the Particle in a Box". In: *Journal of Chemical Education* 79, 1094-1100 (2002).
- [16] I. Mir et al. "Hot Injection versus room Temperature Synthesis of CdSe Quantum Dots: A differential Spectroscopic and Bioanalyte sensing efficacy Evaluation". In: *Colloids and Surfaces A: Physicochem. Eng. Aspects* 494, 162-169 (2016).
- [17] H. Mattousi et al. "Self-Assembly of CdSe-ZnS Quantum Dot Bioconjugates Using an Engineered Recombinant Protein". In: *J. Am. Chem. Soc.* 2000, 122, 12142-12510 (2000).
- [18] Y. Zholudov, A.S. Aljebur, and A. Kukoba. "Top-down Synthesized CdSe Nanoparticles for Electroanalytical and Labeling Applications". In: *IEEE 39th International Conference on Electronics and Nanotechnology* (2019).
- [19] H.S. Han et al. "Quantum Dot/Antibody Conjugates for in vivo Cytometric imaging in Mice". In: *PNAS* 112, 5, 1350-1355 (2015).
- [20] P. Kong et al. "Identification of Surface-Passivating Ligands and Core-size-dependent CdSe/CdZnS with Highly Emitting for Cell Labeling". In: *Physica E* 112, 142-148 (2019).

- [21] B.O. Dabbousi et al. “(CdSe)ZnS Core-Shell Quantum Dots: Synthesis and Characterization of a Size Series of Highly Luminescent Nanocrystallites”. In: *J. Phys. Chem. B* 1997, 101, 9463-9475 (1997).
- [22] T. Takagahara and K. Takeda. “Theory of the Quantum Confinement effect on excitons in Quantum Dots of indirect-gap Materials”. In: *Phys. Rev. B* 46, 15578-15581 (2014).
- [23] S. Alnemrat, Y.H. Park, and I. Vasiliev. “Ab initio study of ZnSe and CdTe semiconductor quantum dots”. In: *Physica E* 57, 96-102 (2014).
- [24] M. Rafipoor et al. “Strain Engineering in InP/(Zn,Se)Se core/shell Quantum Dots,” in: *Chem. Mater.* 30, 13, 4393-4400 (2018).
- [25] G. Pilania, T. Sadowski, and R. Ramprasad. “Oxygen Adsorption on CdSe Surfaces: Case of Study of Asymmetric Anisotropic Growth through ab initio Computations”. In: *J. Phys. Chem. C* 113, 1863-1871 (2009).
- [26] E. Krishnan Vishnu, A. Ajaya Kumar Nair, and K. George Thomas. “Core-Size-Dependent Trapping and Detrapping Dynamics in CdSe/CdS/ZnS Quantum Dots”. In: *J. Phys. Chem. C* 2021, 125, 25706-25716 (2021).
- [27] J. Rodriguez-Viejo et al. “Cathodoluminescence and Photoluminescence of Highly Luminescent CdSe/ZnSe Quantum Dot Composites”. In: *Appl. Phys. Lett* 70, 16, 2132-2134 (1997).
- [28] L. Hartmann et al. “Quenching dynamics in CdSe Nanoparticles: Surface-Induced Defects upon Dilution”. In: *ACS Nano* 6, 9033-9041. (2012).
- [29] M.A. Hines and P. Guyot-Sionnest. “Synthesis and Characterization of strongly Luminescent ZnS-capped CdSe Nanocrystals”. In: *J. Phys. Chem.* 100, 2, 468-471 (1997).
- [30] T. Inerbaev et al. “Quantum Chemistry of Quantum Dots: Effects of Ligands and Oxidation”. In: *Journal of Chemical Physics* 131, 044106 (2009).
- [31] Q. Zhou et al. “Large Band Edge Tunability in Colloidal Nanoplatelets”. In: *Nano Lett* 19, 7124-7129 (2019).
- [32] W. Cho et al. “Synthesis of Six-Monolayer (1.9 Nm) Thick Zinc-Blende CdSe Nanoplatelets Emitting at 585 Nm”. In: *Chem. Mater.* 30, 6957-6960 (2018).

- [33] S. Yang, D. Prendergast, and J.B. Neaton. "Tuning Semiconductor Band Edge Energies for Solar Photocatalysis via Surface Ligand Passivation". In: *Nano Lett.* *12*, 383-388 (2012).
- [34] O. Elimelech et al. "A Tale of Tails: Thermodynamics of CdSe Nanocrystal Surface Ligand Exchange". In: *Nano Lett.* *20*, 6396-6403 (2020).
- [35] S.V. Kilina, P.K. Tamukong, and D.S. Kilin. "Surface Chemistry of Semiconducting Quantum Dots: Theoretical Perspectives". In: *Acc. Chem. Res.* *2016*, *49*, 2127-2135 (2016).
- [36] E. Scalise et al. "Surface chemistry and buried interfaces in all-inorganic nanocrystalline solids". In: *Nature Nanotechnology* *13*, 841-848 (2018).
- [37] A. Shafiee et al. "Core-Shell Nanophotocatalysts: Review of Materials and Applications". In: *ACS Appl. Nano Mater.* *2022*, *5*, 55-86 (2022).
- [38] R.G. Chaudhuri and S. Paria. "Core/Shell Nanoparticles: Classes, Properties, Synthesis Mechanisms, Characterization, and Applications". In: *Chem. Rev.* *2012*, *112*, 2373-2433 (2012).
- [39] N. Xu et al. "Imaging of Water Soluble CdTe/CdS Core-shell Quantum Dots in Inhibiting Multidrug Resistance of Cancer Cells". In: *Talanta* *201*, 309-316 (2019).
- [40] H. Zhu, N. Song, and T. Lian. "Controlling Charge Separation and Recombination Rates in CdSe/ZnS Type I Core-Shell Quantum Dots by Shell Thickness". In: *J. Am. Chem. Soc.* *2010*, *132*, 15038-15045. DOI: 10.1021/ja106710m ().
- [41] A. Szemjonov et al. "Combined Computational and Experimental study of CdSeS/ZnS Nanoplatelets: Structural, Vibrational and Electronic Aspects of Core-shell Interface Formation". In: *ACS Langmuir* *34*, *46*, 13828-13836 (2018).
- [42] X. Wang et al. "Core-shell Interaction and its Impact on the Optical Absorption of Pure and Doped Core-shell CdSe/ZnSe Nanoclusters". In: *J. Chem. Phys.* *144*, 134307 (2016).
- [43] H. Eshet, M. Grünwald, and E. Rabani. "The Electronic Structure of CdSe/CdS core/shell Seeded Nanorods: type-I or quasi-type-II?" In: *Nano Letters* *13*, *12*, 5880-5885 (2013).
- [44] S. Kim et al. "Type-II Quantum Dots: CdTe/CdSe (core/shell) and CdSe/ZnTe (core/shell) Heterostructures". In: *J. Am. Chem. Soc.* *129*, *38*, 11708-11719 (2003).

- [45] J.M. Azpiroz and F. de Angelis. “Ligand Induced Spectral Changes in CdSe Quantum Dots”. In: *ACS Appl. Mater. Interfaces* 7, 19736-19745 (2015).
- [46] C. Noguera. “Polar Oxide Surfaces”. In: *J.Phys.: Condens. Matter* 12, 367-410 (2000).
- [47] D. González et al. “BCN-M: A free computational tool for Generating Wulff-like Nanoparticle Models with Controlled Stoichiometry”. In: *J. Phys. Chem. C* 124, 1, 1227-1237 (2020).
- [48] D. González et al. “Metal coordination determines the catalytic activity of IrO₂ nanoparticles for the oxygen evolution reaction”. In: *Journal of Catalysis* 412, 78-86. (2022).
- [49] C.M. Isborn et al. “Generation of Multiple Excitons in PbSe and CdSe Quantum Dots by Direct Photoexcitation: First-Principles Calculations on Small PbSe and CdSe Clusters.” In: *Phys. Chem. C* 2008, 112, 47, 18291-19284. (2008).
- [50] A. Puzder et al. “The Effect of Organic Ligand Binding on the Growth of CdSe Nanoparticles Probed by ab initio Calculations”. In: *Nano Lett.* 4, 2361-2365 (2004).
- [51] S.U. Rehman, H.M. Li, and Z.J. Ding. “Structural and Electronic Characterization of CdSe/ZnS and ZnS/CdSe Core/shell Nanowires via First Principles Study”. In: *Journal of Physics and Chemistry of Solids* 116, 37-52 (2018).
- [52] G.E. Scuseria J. Heyd J.E. Peralta. “Energy Band Gaps and Lattice Parameters Evaluated with the Heyd-Scuseria-Ernzerhof Screened Hybrid Functional”. In: *J. Chem. Phys.* 123, 17, 174101 (2005).
- [53] A. Walsh, A.A. Sokol, and C.R.A. Catlow. *Computational Approaches to Energy Materials*. Wiley, United Kingdom, 2013. ISBN: 9781119950936, 2013.
- [54] K. Ko et al. “Performance of a Modified Hybrid Functional in the Simultaneous Description of Stoichiometric and Reduced TiO₂ Polymorphs”. In: *Phys. Chem. Chem. Phys.* 18, 12357-12367 (2016).
- [55] S.V. Kilina, P.K. Tamukong, and D.S. Kilin. “Surface chemistry of semiconducting quantum dots: theoretical perspectives”. In: *Acc. Chem. Res.* 49, 2127-2135. (2016).
- [56] S. Kilina, D. Kilin, and D. Prezhdov. “Breaking the phonon bottleneck in PbSe and CdSe quantum dots: Time-domain density functional theory of charge carrier relaxation”. In: *ACS NANO* 3, 93-99 (2009).

- [57] X. Sala et al. "Molecular Water Oxidation Mechanisms Followed by Transition Metals: State of the Art". In: *Acc. Chem. Res.* 47, 2, 504-516. (2014).
- [58] I. Ledezma-Yanez et al. "Electrocatalysis under Cover: Enhanced Hydrogen Evolution via Defective Graphene-Covered Pt(111)". In: *Nature Energy* 2017, 2, 17031 (2017).
- [59] J. Yu et al. "Recent Advances and Prospective in Ruthenium-Based Materials for Electrochemical Water Splitting". In: *ACS Catal.* 9, 9973-10011 (2019).
- [60] A.J. Shih, N. Arulmozhi, and M.T.M. Koper. "Electrocatalysis under Cover: Enhanced Hydrogen Evolution via Defective Graphene-Covered Pt(111)". In: *ACS Catal* 2021, 11, 10892-10901 (2021).
- [61] M. Schwarze A. Ghaffar Rana et al. "Influence of Cocatalysts (Ni, Co and Cu) and Synthesis Method on the Photocatalytic Activity of Exfoliated Graphitic Carbon Nitride for Hydrogen Production". In: *Nanomaterials* 12, 4006. (2022).
- [62] Z. Ma et al. "Recent Advances of Single-Atom Electrocatalysts for Hydrogen Evolution Reaction". In: *J.Phys.Mater.* 4, 2021, 04002 (2021).
- [63] J.K. Norskov et al. "Origin of the Overpotential for Oxygen Reduction at a Fuel-Cell Cathode". In: *J. Phys. Chem. B* 2004, 108, 17886-17892 (2004).
- [64] J.K. Norskov et al. "Trends in The Exchange Current for Hydrogen Evolution". In: *J. Electrochem. Soc.* 152, J23 (2005).
- [65] J. Creus et al. "Ligand-Capped Ru Nanoparticles as Efficient Electrocatalyst for the Hydrogen Evolution Reaction". In: *ACS Catal.* 2018, 8, 12, 11094-11102 (2018).
- [66] N. Romero et al. "Light-Driven Hydrogen Evolution Assisted by Covalent Organic Frameworks". In: *Catalysts* 11, 754 (2021).
- [67] B. Jiang et al. "Unravelling the Mechanistic Pathway of the Hydrogen Evolution Reaction Driven by a Cobalt Catalyst". In: *Angew. Chem. Int. Ed.* 61, e202209075 (2022).
- [68] D.G. Nocera. "Chemistry of Personalized Solar Energy". In: *Inorg.Chem.* 2009, 48, 10001-10017 (2009).
- [69] M.A. Abdelkareem et al. "Environmental Aspects of Fuel Cells: A review." In: *Science of the Total Environment* 752, 141803 (2021).

- [70] *Fuel Cells - Department of Energy*. <http://https://www.energy.gov/eere/fuelcells/fuel-cells>. Accessed: 2023-05-23.
- [71] D. Lebedev et al. "Atomically Dispersed Iridium on Indium Tin Oxide Efficiently Catalyzed Water Oxidation". In: *ACS Cent. Sci.* **6**, 1189-1198. (2020).
- [72] C. Sealy. "The Problem with Platinum". In: *Materials Today* **11**, 12, 2008 (2008).
- [73] H.N. Nong, T. Reier, and H.S. Oh et al. "A Unique Oxygen Ligand Environment Facilitates Water Oxidation in Hole-Doped IrNiOx Core-Shell Electrocatalysts". In: *Nature Catalysis* **1**, 841-851, 2018. (2018).
- [74] D. González et al. "Water Adsorption on MO₂ (M= Ti, Ru, and Ir) surfaces. Importance of Octahedral Distortion and Cooperative effects". In: *ACS Omega* **4**, 2989-2999 (2019).
- [75] E. Skúlason et al. "Modelling the Electrochemical Hydrogen Oxidation and Evolution Reactions on the Basis of Density Functional Theory Calculations". In: *J. Phys. Chem. C* **114**, 18182-18197 (2010).
- [76] C. Li and J.B. Baek. "Recent Advances in Noble Metal (Pt, Ru and Ir)-Based Electrocatalysts for Efficient Hydrogen Evolution Reaction". In: *ACS Omega* **5**, 31-40. (2020).
- [77] V. Vij et al. "Nickel-Based Electrocatalysts for Energy-Related Applications: Oxygen Reduction, Oxygen Evolution and Hydrogen Evolution Reactions". In: *ACS Catal.* **2017**, **7**, 7196-7225 (2017).
- [78] M.J. Kolb et al. "Density Functional Theory Study of Adsorption of H₂O, H, O and OH on stepped platinum surfaces". In: *The Journal of Chemical Physics* **140**, 134708, 2014 (2014).
- [79] Q. Hu et al. "Subnanometric Ru Clusters with upshifted D Band Center Improve Performance for Alkaline Hydrogen Evolution Reaction". In: *Nat. Commun.* **13**, 3958 (2012).
- [80] M.D. Hossain et al. "Rational Design of Graphene-Supported Single Atom Catalysts for Hydrogen Evolution Reaction". In: *Adv. Energy Mater.* **9**, 1803689 (2019).
- [81] M.A. Holmes, T.K. Townsend, and F.E. Osterloh. "Quantum Confinement Controlled Photocatalytic Water Splitting by Suspended CdSe Nanocrystals". In: *Chem. Commun.*, 2012, **48**, 371-373 (2012).

- [82] D. Astruc, F. Lu, and J.R. Aranzaes. “Nanoparticles as Recyclable Catalysts: the Frontier between Homogeneous and Heterogeneous Catalysis”. In: *Angew. Chem. Int. Ed.* *44*, 7852-7872 (2005).
- [83] J. Zhu et al. “Recent Advances in Electrocatalytic Hydrogen Evolution Using Nanoparticles”. In: *Chem. Rev.* *120*, 851-918 (2020).
- [84] S. Fukuzumi and Y. Yamada. “Catalytic Activity of Metal-Based Nanoparticles for Photocatalytic Water Oxidation and Reduction”. In: *J. Mater. Chem.* *22*, 24284-24296 (2012).
- [85] J. Creus et al. “Ruthenium Nanoparticles for Catalytic Water Splitting”. In: *ChemSusChem* *12*, 2493-2514 (2019).
- [86] B. Santosh et al. “Ruthenium Decorated Carbon Nanoink as Highly Active Electrocatalyst in Hydrogen Evolution Reaction”. In: *Int. J. Hydrogen Energy* *41*, 23007-23014 (2016).
- [87] D.H. Kweon et al. “Ruthenium Anchored on Carbon Nanotube Electrocatalyst for Hydrogen Production with Enhanced Faradaic Efficiency”. In: *Nat. Commun.* *11*, 1278 (2020).
- [88] R. Ding et al. “Hierarchical Architectures Based on Ru Nanoparticles/Oxygen-Rich-Carbon Nanotubes for Efficient Hydrogen Evolution”. In: *Chem. - Eur. J.* *27*, 11150-11157 (2021).
- [89] N. Cheng et al. “Platinum Single-Atom and Cluster Catalysis of the Hydrogen Evolution Reaction”. In: *Nature Communications* *2016*, *7*, 13638 (2016).
- [90] Mark T.M. Koper. “Thermodynamic Theory of Multi-electron Transfer Reaction: Implications for Electrocatalysis.” In: *Journal of Electroanalytical Chemistry* *660*, 254-260 (2011).
- [91] “The Reversible Hydrogen Electrode: Potential-Dependent Activation Energies over Platinum from Quantum Theory”. In: *J. Phys. Chem. B* *108*, 9829-9833 (2004).
- [92] J. Heras-Domingo, M. Sodupe, and X. Solans-Monfort. “Interaction Between Ruthenium Oxide Surface and Water Molecules. Effect of Surface Morphology and Water Coverage”. In: *J. Phys. Chem. C* *123*, 7786-7798 (2019).
- [93] Y. Liu et al. “Modulating Hydrogen Adsorption via Charge Transfer at the Semiconductor-Metal Heterointerface for Highly Efficient Hydrogen Evolution Catalysis”. In: *Adv. Mater.* *2023*, *35*, 2207114 (2023).

- [94] F. Callejo-Vallejo et al. "Fast Prediction of Adsorption Properties for Platinum Nanocatalysts with Generalized Coordination Numbers". In: *Angew. Chem. Int. Ed.* 2014, 53, 8316-8319 (2014).
- [95] M.D. Pohl et al. "Nature of Highly Active Electrocatalytic Sites for the Hydrogen Evolution Reaction at Pt Electrodes in Acidic Media". In: *ACS Omega* 2017, 2, 8141-8147 (2017).
- [96] L. Cusinato et al. "Theoretical Characterization of the Surface Composition of Ruthenium Nanoparticles in Equilibrium with Syngas". In: *Nanoscale*, 2016, 8, 10974 (2016).
- [97] J. Greely et al. "Computational high-throughput screening of electrocatalytical materials for hydrogen evolution". In: *Nature Mater* 5, 909-913. (2006).
- [98] Christopher J. Cramer. *Essentials of Computational Chemistry. Theories and Models. 2nd Edition*. Wiley, 2006.
- [99] Frank Jensen. *Introduction to Computational Chemistry*. Wiley, 1999.
- [100] J.P. Perdew et al. "Prescription for the Design and Selection of Density Functional Approximations: more Constraint Satisfaction with fewer Fits". In: *J. Chem. Phys.* 123, 6, 062201 (2005).
- [101] A. Polman et al. "Photovoltaic Materials: Present Efficiencies and Future Challenges". In: *Science* 352, no. aad4424 (2016).
- [102] Y. Yang et al. "High-Efficiency Light Emitting Devices Based on Quantum Dots with Tailored Nanostructures". In: *Nat. Photonics* 9, 259-265 (2015).
- [103] G.H. Carey et al. "Colloidal Quantum Dot Solar Cells". In: *Chem. Rev.* 115, 12732-12763 (2015).
- [104] P.V. Kaamt. "Quantum Dot Solar cells. The next Big Thing in Photovoltaics". In: *J. Phys. Chem. Lett.* 4, 908-918 (2013).
- [105] I. Mora-Seró et al. "Recombination in Quantum Dot Sensitized Solar Cells". In: *Acc. Chem. Res.* 42, 1848-1857 (2009).
- [106] J. Jia et al. "Solar Water Splitting by Photovoltaic-Electrolysis with a Solar-to-Hydrogen Efficiency over 30%". In: *Nat. Commun.* 7, 13237 (2016).

- [107] D. Kand et al. “Electrochemical Synthesis of Photoelectrodes and Catalysts for Use in Solar Water Splitting”. In: *Chem. Rev.* 115, 12839-12887 (2015).
- [108] A. Das et al. “Photogeneration of Hydrogen from Water using CdSe Nanocrystals Demonstrating the importance of Surface Exchange”. In: *PNAS* 110, 16716-16723 (2013).
- [109] I.L. Medint et al. “Quantum Dot Bioconjugates for Imaging, Labelling and Sensing”. In: *Nat. Mater.* 4, 435-446 (2005).
- [110] O.S. Wolfbeis. “An Overview of Nanoparticles Commonly Used in Fluorescent Bioimaging”. In: *Chem. Soc. Rev.* 44, 4743-4768 (2015).
- [111] K.D. Wegner and N. Hildebrandt. “Quantum Dots: Bright and Versatile in Vitro and in Vivo Fluorescent Imagin Biosensors”. In: *Chem. Soc. Rev.* 44, 4792-4834 (2015).
- [112] X. Michaelt et al. “Quantum Dots for Live cells, in Vivo Imagin and Diagnostics”. In: *Science* 307, 538-544 (2005).
- [113] C.L. Hartley, M.L. Kessler, and J.L. Dempsey. “Molecular-Level Insight into Semiconductor Nanocrystal Surfaces”. In: *J. Am. Chem. Soc.* 143, 1251-1266 (2021).
- [114] J. Jasieniak, M. Califano, and S.E. Watkins. “Size-Dependent Valence and Conduction Band-Edge Energies of Semiconductor Nanocrystals”. In: *ACS Nano* 5, 5888-5902 (2011).
- [115] D.A. Hines and P.V. Kamat. “Recent Advances in Quantum Dot Surface Chemistry”. In: *ACS Appl. Mater. Interfaces* 6, 3041-3057 (2014).
- [116] Z. Hens and J. de Roo. “Atomically Precise Nanocrystals”. In: *J. Am. Chem. Soc.* 142, 15627-15637 (2020).
- [117] D.M. Kroupa et al. “Tuning Colloidal Quantum Dot Band Edge Positions through Solution-Phase Surface Chemistry Modification”. In: *Nat. Commun.* 8, 15257 (2017).
- [118] S. Asokan et al. “Shape-Controlled Synthesis of CdSe Tetrapods Using Cationic Surfactant Ligands”. In: *Small* 3, 7, 1164-1169 (2007).
- [119] M. Meyns et al. “Shape Evolution of CdSe Nanoparticles Controlled by Halogen Compounds”. In: *Chem. Mater.* 26, 1813-1821 (2014).
- [120] X. Peng et al. “Shape Control of CdSe Nanocrystals”. In: *Nature* 404, 59-61. (2000).

- [121] L. Liu et al. "Shape Control of CdSe Nanocrystals with Zinc Blende Structure". In: *J. Am. Chem. Soc.* *131*, 16423-16429 (2009).
- [122] W. Shan et al. "Determination of the Fundamental and Split-off Band Gaps in Zinc-Blende CdSe by Photomodulation Spectroscopy". In: *Phys. Rev. B.* *50*, 8012-8015 (1994).
- [123] U. Lunz et al. "Temperature Dependence of the Energy Gap of Zinc-Blende CdSe and Cd_{1-x}Zn_xSe Epitaxial Layers". In: *J. Appl. Phys.* *80*, 6871-6863 (1996).
- [124] L. Hartmann et al. "Quenching dynamics in CdSe Nanoparticles: Surface-Induced Defects upon Dilution". In: *ACS Nano* *6*, *10*, 9033-9041. (2012).
- [125] Q. Lin et al. "Phase-Transfer Ligand Exchange of Lead Chalcogenide Quantum Dots for Direct Deposition of Thick, Highly Conductive Films". In: *J. Am. Chem. Soc.* *139*, 6644-6653 (2017).
- [126] N.C. Anderson et al. "Ligand Exchange and the Stoichiometry of Metal Chalcogenide Nanocrystals: Spectroscopic Observation of Facile Metal-Carboxylate Displacement and Binding". In: *J. Am. Chem. Soc.* *135*, 18536-18548 (2013).
- [127] Y. Ben-Shahar et al. "Effect of Surface Coating on the Photocatalytic Function of Hybrid CdS-Au Nanorods". In: *Small* *11*, 462-471 (2015).
- [128] R.J. Capek et al. "Synthesis of Extremely Small CdSe and Bright Blue Luminescent CdSe/ZnS Nanoparticles by a Prefocused Hot-Injection Approach". In: *Chem. Mater.* *21*, 1743-1749 (2009).
- [129] J. Cho et al. "Highly-Efficient Blue-Emitting CdSe-Derived Core/Shell Gradient Alloy Quantum Dots with Improved Photoluminescent Quantum Yield and Enhanced Photostability". In: *Langmuir* *33*, 3711-3719 (2017).
- [130] I. Moreels et al. "Band-Edge Exciton Fine Structure of Small, Nearly Spherical Colloidal CdSe/ZnS Quantum Dots". In: *ACS Nano* *5*, 8033-8039 (2011).
- [131] K. Boldt et al. "Synthesis of Highly Luminescent and Photo-stable, Graded Shell CdSe/CdXZn_{1-X}S Nanoparticles by in situ Alloying". In: *Chem. Mater.* *25*, 4731-4738 (2013).

- [132] X. Peng et al. "Epitaxial Growth of Highly Luminescent CdSe/CdS Core/Shell Nanocrystals with Photostability and Electronic Accessibility". In: *J. Am. Chem. Soc.* *119*, 7019-7029 (1997).
- [133] O. Elimelech et al. "Entropy of Branching Out: Linear versus Branched Alkylthiol Ligands on CdSe Nanocrystals". In: *ACS Nano* *16*, 4308-4321 (2022).
- [134] R. Gomes et al. "Binding of Phosphonic Acids to CdSe Quantum Dots: A Solution NMR Study". In: *J. Phys. Chem. Lett.* *2*, 145-152 (2011).
- [135] R. Jose et al. "Structure-Property Correlation of CdSe Clusters Using Experimental Results and First-Principles DFT Calculatons". In: *J. Am. Chem. Soc.* *128*, 629-636 (2006).
- [136] S. Singh et al. "Ligand Adsorption Energy and the Postpurification Surface Chemistry of Colloidal Metal Chalcogenide Nanocrystals". In: *Chem. Mater.* *33*, 2796-2803 (2021).
- [137] K.A. Nguyen, R. Pacter, and P.N. Day. "Computational Prediction of Structures and Optical Excitations for Nanoscale Ultrasmall ZnS and CdSe Clusters". In: *J. Chem. Theory Comput.* *9*, 3581-3596 (2013).
- [138] M. del Ben et al. "Functional Study on the Morphology and Photoadsorption of CdSe Nanoclusters". In: *J. Phys. Chem. C* *115*, 16782-16796 (2011).
- [139] V.V. Albert et al. "Electronic Structure of Ligated CdSe Clusters: Dependence on DFT Methodology". In: *J. Phys. Chem. C* *115*, 15793-15800 (2011).
- [140] S.A. Fischer et al. "Passivating Ligand and Solvent Contributions to the Electronic Properties of Semiconductor Nanocrystals". In: *Nanoscale* *4*, 904-914 (2012).
- [141] C. Giansante and I. Infante. "Surface Traps in Colloidal Quantum Dots: A Combined Experimental and Theoretical Perspective". In: *J. Phys. Chem. Lett.* *8*, 5209-5215 (2017).
- [142] I. du Fosse et al. "Dynamic Formaton of Metal-Based Traps in Photoexcited Colloidal Quantum Dots and Their Relevance for Photoluminescence". In: *Chem. Mater.* *33*, 3349-3358 (2021).
- [143] A.J. Houtepen et al. "On the Origin of Surface Traps in Colloidal II-VI Semiconductor Nanocrystals". In: *Chem. Mater.* *29*, 752-761 (2017).

- [144] E. Drijvers et al. "Ligand Displacement Exposes Binding Site Heterogeneity on CdSe Nanocrystal Surfaces". In: *Chem. Mater.* *30*, 1178-1186 (2018).
- [145] I. du Fosse et al. "Effect of Ligands and Solvents on the Stability of Electron Charged CdSe Colloidal Quantum Dots". In: *J. Phys. Chem. C* *125*, 23968-23975 (2021).
- [146] A.E. Kuznetsov and D.N. Beratan. "Structural and Electronic Properties of Bare and Capped Cd₃₃Se₃₃ and Cd₃₃Te₃₃ Quantum Dots". In: *J. Phys. Chem. C* *118*, 7094-7109 (2014).
- [147] I. Csik, S.P. Russo, and O. Mulvaney. "Density Functional Study of Surface Passivation of Nonpolar Wurtzite CdSe Surfaces". In: *J. Phys. Chem. C* *112*, 20413-20417 (2008).
- [148] T. Virgili et al. "Hybridized Electronic States between CdSe Nanoparticles and Conjugated Organic Ligands: A Theoretical and Ultrafast Photo-excited carrier Dynamics Study". In: *Nano Res.* *11*, 142-150 (2018).
- [149] T. Virgili et al. "Charge Separation in the Hybrid CdSe Nanocrystal-Organic Interface: Role of the Ligands Studied in the Hybrid Ultrafast Spectroscopy and Density Functional Theory". In: *J. Phys. Chem. C* *117*, 5969-5974 (2013).
- [150] L. Manna et al. "First-Principles Modeling of Unpassivated and Surfactant-Passivated Bulk Facets of Wurtzite CdSe: A Model System for Studying the Anisotropic Growth of CdSe Nanocrystals". In: *J. Phys. Chem. B* *109*, 6183-6192 (2005).
- [151] J.M. Azpirov et al. "Benchmark Assessment of Density Functional Methods on Group II-VI MX (M=Zn, Cd; X = S, Se, Te) Quantum Dots". In: *J. Chem. Theory Comp.* *10*, 76-89 (2014).
- [152] Y. Gao et al. "Effect of Ligands on the Characteristics of (CdSe)₁₃ Quantum Dots". In: *RSC Adv* *4*, 27146-27151 (2014).
- [153] N.K. Swenson, M.A. Ratner, and E.A. Weiss. "Computational Study of the Influence of the Binding Geometries of Organic Ligands on the Photoluminescence Quantum Yield of CdSe Clusters". In: *J. Phys. Chem. C* *120*, 6859-6868 (2016).
- [154] L. Tan et al. "Structures of CdSe and CdS Nanoclusters from ab initio Random Structure Searching". In: *J. Phys. Chem. C* *123*, 29370-29378 (2019).

- [155] P. Sarkar and M. Springborg. “Density-Functional Study of Size-Dependent Properties of Cd₁₀Se₁₀ Clusters”. In: *Phys. Rev. B*. 68, no. 235409 (2003).
- [156] J.M. Azpiroz et al. “A DFT/TDDFT Study on the Optoelectronic Properties of the amine-Capped Magic (CdSe)₁₃ Nanocluster”. In: *Phys. Chem. Chem. Phys* 15, 10996-11005 (2013).
- [157] Y. Cui et al. “Theoretical Characterization on the Size-Dependent Electron and Hole Trapping Activity of Chloride-Passivated CdSe Nanoclusters”. In: *J. Chem. Phys.* 148, 134308 (2018).
- [158] Y. Cui et al. “A Study of Optical Adsorption of Cysteine-Capped CdSe Nanoclusters Using First-Principles Calculations”. In: *Phys. Chem. Chem. Phys.* 17, 9222-9230 (2015).
- [159] J. Sun et al. “Theoretical Study of Ligand and Solvent Effects on Optical Properties and Stabilities of CdSe Nanoclusters”. In: *J. Mol. Struct.* 1114, 123-131 (2016).
- [160] O. Voznyy et al. “Computational Study of Magic-Size CdSe Clusters with Complementary Passivation by Carboxylic and Amine Ligands”. In: *J. Phys. Chem. C* 120, 10015-10019 (2016).
- [161] H. Liu. “Tuning the Binding Energy of Surfactant to CdSe Nanocrystal: A Theoretical Study”. In: *J. Phys. Chem. C* 113, 3116-3119 (2009).
- [162] A. Kasuya, R. Sivamohan, and Y.A. Barnakov et al. “Ultra-Stable Nanoparticles of CdSe Revealed from Mass Spectrometry”. In: *Nat. Mater.* 3, 99-102 (2004).
- [163] G. Kresse and J. Furthmüller. “Efficient Iterative Schemes for ab initio Total-Energy Calculations Using a Plane-Wave Basis Set”. In: *Phys. Rev. B*. 54, 99-102 (1996).
- [164] G. Kresse and J. Hafner. “Ab initio Molecular Dynamics for Liquid Metals”. In: *Phys. Rev. B*. 47, 558-561 (1993).
- [165] J.P. Perdew, K. Burke, and M. Ernzerhof. “Generalized Gradient Approximation Made Simple”. In: *Phys. Rev. Lett.* 77, 3865-3868 (1996).
- [166] S. Grimme. “Accurate Description of van Der Waals Complexes by Density Functional Theory Including Empirical Corrections”. In: *J. Comput. Chem.* 25, 1463-1473 (2004).

- [167] P.E. Blöchl, C.J. Först, and J. Schimpl. “Projector Augmented-Wave Method: ab initio Molecular Dynamics with Full Wave Functions”. In: *Bull. Mater. Sci.* 2003, 26, 33-41 (2003).
- [168] G. Kresse and D. Joubert. “From Ultrasoft Pseudopotentials to the Projector Augmented Wave Method”. In: *Phys. Rev. B: Condens. Matter Mater. Phys.*, vol. 59, pp. 1758-1775 (1999).
- [169] H. Monkhorst and J. Pack. “Special Points for Brillouin Zone Integration”. In: *Phys. Rev. B* 13, 5188-5192 (1976).
- [170] R.F.W. Bader. “A Quantum Theory of Molecular Structure and Its Applications”. In: *Chem. Rev.* 1991, 91, 893-928 (1991).
- [171] G. Henkelman, A. Arnaldson, and H.A. Jonsson. “A Fast and Robust Algorithm for Bader Decomposition of Charge Density”. In: *Comput. Mater. Sci* 2006, 36, 354-360 (2006).
- [172] K.A. Romanova and Y.G. Galyametdinov. “Quantum Chemical Study of CdSe/CdS Core/Shell and CdSe/CdS/ZnS Core/Shell/Shell Quantum Dots with Different Layers Ratio”. In: *In AIP Conference Proceedings; AIP Publishing, 2021, 2380, 060001* (2021).
- [173] S.L. Dudarev and G.A. Botton et al. “Electron-Energy-Loss Spectra and the Structural Stability of Nickel Oxide: An LSDA+U Study”. In: *Phys. Rev. B.* 1998, 57, 1505-1509 (1998).
- [174] S.A. Nosé. “A Unified Formulation of the Constant Temperature Molecular Dynamics Methods”. In: *J. Chem. Phys.* 1984, 81, 511-519 (1984).
- [175] W.G. Hoover. “Canonical Dynamics: Equilibrium Phase-Space Distributions”. In: *Phys. Rev. A.* 1985, 31, 1695-1697 (1985).
- [176] E.F. Pettersen et al. “UCSF Chimera - A Visualization System for Exploratory Research and Analysis”. In: *J. Comput. Chem.* 2004, 25, 1605-1612 (2004).
- [177] K. Mathew et al. “Implicit Solvation Model for Density Functional Study of Nanocrystal Surfaces and Reaction Pathways”. In: *J. Chem. Phys.* 2014, 140, 084106 (2014).
- [178] M. J. Frisch et al. “Gaussian 09 Revision C.01”. In: (2009). Gaussian Inc. Wallingford CT.

- [179] F. Weigend and R. Ahlrichs. “Balanced Basis Sets of Split Valence, Triple Zeta Valence and Quadruple Zeta Valence Quality for H to Rn: Design and Assessment of Accuracy”. In: *Phys. Chem. Chem. Phys.* 2005, 7, 3297 (2005).
- [180] B.P. Pritchard et al. “A New Basis Set Exchange: An Open, Up-to-date Resource for the Molecular Sciences Community”. In: *J. Chem. Inf. Model.* 2019, 59(11), 4814-4820 (2019).
- [181] D. Andrae et al. “Energy-Adjusted ab initio pseudopotentials for the Second and Third Row Transition Elements”. In: *Theor. Chim. Acta* 1990, 77, 123-141 (1990).
- [182] V. Barone and M. Cossi. “Quantum Calculations of Molecular Energies and Energy Gradients in Solution by a Conductor Solvent Model”. In: *J. Phys. Chem. A.* 1998, 102, 1995-2001 (1998).
- [183] M. Cossi et al. “Energies, Structures and Electronic Properties of Molecules in Solution with the C-PCM Solvation Model”. In: *J. Comput. Chem.* 2003, 24, 669-681 (2003).
- [184] A. Kaneta and S. Adachi. “Photoreflectance Study of Hexagonal CdSe”. In: *J. Phys. D: Appl. Phys.* 1999, 32, 2337-2341 (1999).
- [185] C. Janowitz et al. “Dielectric Function and Critical Points of Cubic and Hexagonal CdSe”. In: *Phys. Rev. B.* 1994, 50, 2181-2187 (1994).
- [186] S. Ninomiya and S. Adachi. “Optical Properties of Cubic and Hexagonal CdSe”. In: *J. Appl. Phys.* 1995, 78, 4681-4689 (1995).
- [187] T. Chauviré et al. “Redox Photocatalysis with Water-Soluble Core-Shell CdSe-ZnS Quantum Dots”. In: *J. Phys. Chem. C* 2015, 119, 17857-17866 (2015).
- [188] D. Ma et al. “Rational Design of CdS@ZnO Core-Shell Structure via Atomic Layer Deposition for Drastically Enhanced Photocatalytic H₂ Evolution with Excellent Photostability”. In: *Nano Energy* 39, 2017, 183-191 (2017).
- [189] L. Wang et al. “Quasi-Type II Carrier Distribution in CdSe/CdS Core/Shell Quantum Dots with Type I Band Alignment”. In: *J. Phys. Chem. C* 2018, 122, 12038-12046 (2018).
- [190] L. Lystrom et al. “Phonon-Driven Energy Relaxation in PbS/CdS and PbSe/CdSe Core/Shell Quantum Dots”. In: *J. Phys. Chem. Lett.* 2020, 11, 4269-4278 (2020).

- [191] D.A. Fenoll, M. Sodupe, and X. Solans-Monfort. "Influence of Capping Ligands, Solvent and Thermal Effects on CdSe Quantum Dot Optical Properties by DFT calculations". In: *ACS Omega* 8, 12, 11467-11478. (2023).
- [192] K. Gong and D.F. Kelley. "A Predictive Model of Shell Morphology in CdSe/CdS Core/Shell Quantum Dots". In: *J. Chem. Phys.* 141, 194704 (2014) (2014).
- [193] G. Genchi et al. "The Effects of Cadmium Toxicity". In: *Int. J. Environ. Res. Public Health* 2020, 17, 3782 (2020).
- [194] M.P. Rayman. "Selenium Intake, Status, and Health: a Complex Relationship". In: *Hormones* 2020, 19, 9-14 (2020).
- [195] S. Kim et al. "Near-Infrared Fluorescent Type II Quantum Dots for Sentinel Lymph Node Mapping". In: *Nature Biotechnology* 22, 1, 2004 (2004).
- [196] L. Vegard. "Die Konstitution der Mischkristalle un die Raumfüllung der Atome," in: *Zeitschrift fur Physik* 5 (1921).
- [197] V. Kocovski et al. "First-Principles Study of the influence of different interfaces and core types on the properties of CdSe/CdS core-shell nanocrystals". In: *Scientific Reports* 5, 10865 (2015).
- [198] P. Sarkar, M. Springborg, and G. Seifert. "A Theoretical Study of the structural and electronic properties of CdSe/CdS and CdS/CdSe core/shell nanoparticles". In: *Chemical Physics Letters* 405, 103-107 (2005).
- [199] A. Jain et al. "Atomistic Design of CdSe/CdS Core-Shell Quantum Dots with Supressed Auger Recombination". In: *Nano Lett.* 2016, 16, 6491-6496 (2016).
- [200] J.A. Turner. "Sustainable Hydrogen production". In: *Science* 305, 5686, 972-974 (2004).
- [201] B. Hinnemann et al. "Biomimetic Hydrogen Evolution: MoS₂ Nanoparticles as Catalyst for Hydrogen Evolution". In: *Journal of the American Chemical Society* 127, 15, 5308-5309 (2005).
- [202] P. Wang et al. "Precise Tuning in Platinum-Nickel/Nickel Sulfide Interface Nanowires for Synergistic Hydrogen Evolution Catalysis". In: *Nature Communications* 8, 14580, 2017 (2017).

- [203] X.L. Ho et al. "Visible Light Driven Hydrogen Evolution by Molecular Nickel Catalysts with Time-Resolved Spectroscopic and DFT insights". In: *Inorg. Chem.* 2019, 58, 2, 1469-1480 (2019).
- [204] Sh. Zhang, J. Li, and E. Wang. "Recent Progress of Ruthenium-based Nanomaterials for Electrochemical Hydrogen Evolution". In: *ChemElectroChem* 2020, 7, 4526-4534 (2020).
- [205] M.C.O. Monteiro et al. "Understanding Cation Trends for Hydrogen Evolution on Platinum and Gold Electrodes in Alkaline Media". In: *ACS Catal.* 2021, 11, 14328-14335 (2021).
- [206] Y. Yang et al. "Engineering Ruthenium-Based Electrocatalysts for Effective Hydrogen Evolution Reaction". In: *Nano-Micro Lett.* 2021, 13:160 (2021).
- [207] G. Marti et al. "Surface-Functionalized Nanoparticles as Catalysts for Artificial Photosynthesis". In: *Adv. Energy Mater.* 2023, 13, 2300282 (2023).
- [208] R. Michalsky, Y.-J. Zhang, and A.A. Peterson. "Trends in the Hydrogen Evolution Activity of Metal Carbide Catalysts". In: *ACS Catal.* 2014, 4, 1274-1278 (2014).
- [209] B.A. Nail et al. "Nickel Oxide Particles Catalyze Photochemical Hydrogen Evolution from Water-Nanoscaling Promotes p-Type Character and Minority Carrier Extraction". In: *ACS Nano* 2015, 9, 5, 5135-5142 (2015).
- [210] C. Zhang and F. Han. "Hollow Ru Nanoparticles for Electrocatalytic Hydrogen Evolution". In: *ACS Appl. Nano Mater* 2021, 4, 8530-8538 (2021).
- [211] I. Barlocco, G. Di Liberto, and G. Pacchioni. "Hydrogen Complexes on Single Atom Alloys: Classical Chemisorption versus Coordination Chemistry". In: *Catal. Sci. Technol.* 13, 5301-5312 (2023).
- [212] F. Calle-Vallejo and A.S. Bandarenka. "Enabling Generalized Coordination Numbers to Describe Strain Effects". In: *ChemSusChem* 11, 1824-1828 (2018).
- [213] Y. Huang et al. "The Reaction Mechanism with Free Energy Barriers for Electrochemical Dihydrogen Evolution on MoS₂". In: *Journal of American Chemical Society* 137, 20, 6692-6698 (2015).
- [214] S.Chu and A. Majmudar. "Opportunities and Challenges for a Sustainable Energy Future". In: *Nature* 488, 7411, 294-303 (2012).

- [215] X. Li et al. "Sequential Electrodeposition of Bifunctional Catalytically Active Structures in MoO₃/Ni-NiO Composite Electrocatalysts for Selective Hydrogen and Oxygen Evolution". In: *Adv. Mater.* 2020, 32, 2003414 (2020).
- [216] J.-F. Li et al. "Revealing the role of Interfacial Water and Key Intermediate at Ruthenium Surfaces in the Alkaline Hydrogen Evolution Reaction". In: *Nature Communications* 2023, 14:5289 (2023).
- [217] I. Ledezma-Yanez W.D.Z. Wallace et al. "Interfacial Water Reorganization as a pH-Dependent Descriptor of the Hydrogen Evolution rate of Platinum Electrodes". In: *Nature Energy* 2, 17031, 2017 (2017).
- [218] D. González et al. "Importance of the Oxy Character on the IrO₂ Surface Dependent Catalytic Activity for the Oxygen Evolution Reaction". In: *Journal of Catalysis* 396, 192-201 (2021).
- [219] D.M. Heinekey, A. Lledos, and J.M. Lluch. "Elongated Dihydrogen Complexes: what remains of the H-H Bond?" In: *Chem. Soc. Rev.* 33, 175-182 (2004).
- [220] X. Li et al. "Amorphous NiFe Oxide-based Nanoreactors for Efficient Electrocatalytic Water Oxidation". In: *Angew. Chem. Int. Ed.* 62, e202300478 (2023).
- [221] Q. Hu et al. "A Unique Space Confined Strategy to Construct Defective Metal Oxides within Porous Nanofibers for Electrocatalysis". In: *Energy Environ. Sci.* 13, 5097-5103 (2020).
- [222] Q. Hu et al. "Facile Synthesis of Sub-Nanometric Copper Clusters by Double Confinement Enables Selective Reduction of Carbon Dioxide to Methane," in: *Angew. Chem. Int. Ed.* 59, 19054-19059 (2020).
- [223] N.S. Lewis. "Research Opportunities to Advance Solar Energy Utilization". In: *Science* 351, aad1920 (2016).
- [224] J. Creus et al. "Ligand-Capped Ru Nanoparticles as Efficient Electrocatalyst for The Hydrogen Evolution Reactions". In: *ACS Catal.* 8, 11094-11102 (2018).
- [225] Q. Wang et al. "Scalable Solid-State Synthesis of Highly Dispersed Uncapped Metal (Rh, Ru, Ir) Nanoparticles for Efficient Hydrogen Evolution". In: *Adv. Energy Mater.* 8, 1801698 (2018).

- [226] N. Karousis, N. Tagmatarchis, and D. Tasis. “Current Progress on the Chemical Modification of Carbon Nanotubes”. In: *Chem. Rev.* *110*, 5366-5397 (2010).
- [227] X. Zhang et al. “Deposition of Platinum-Ruthenium Nano-particles on Multi-walled carbon Nano-tubes Studied by Gamma-Irradiation”. In: *Radiat. Phys. Chem.* *79*, 1058-1062 (2010).
- [228] J. Sheng and Y. Li. “Applications of Carbon Nanotubes in Oxygen Electrocatalytic Reactions”. In: *ACS Appl. Mater. Interfaces* *14*, 20455-20462 (2022).
- [229] M. Zhang et al. “RuO₂/CNT Hybrids as High-Activity pH-universal Electrocatalysts for Water Splitting within 0.73 V in and Asymmetric-Electrolyte Electrolyzer”. In: *Nano Energy* *61*, 576-583 (2019).
- [230] M. Cheng et al. “Optimization of the Hydrogen-Adsorption Free Energy of Ru-Based Catalysts towards High-Efficiency Hydrogen Evolution Reaction at all pH”. In: *Chem. - Eur. J.* *25*, 8579-8584 (2019).
- [231] M. Fan et al. “Highly Dispersed Ru Nanoclusters Anchored on B, N co-doped Carbon Nanotubes for Water Splitting”. In: *Inorg. Chem. Front.* *9*, 968-976 (2022).
- [232] X. Sun et al. “Boron-induced Activation of Ru Nanoparticles Anchored on Carbon Nanotubes for the Enhanced pH-independent Hydrogen Evolution Reaction”. In: *J. Colloid Interface Sci.* *616*, 338-356 (2022).
- [233] Z. Liu et al. “Ru Nanoclusters Coupled on Co/N-Doped Carbon Nanotubes Efficiently Catalyzed the Hydrogen Evolution Reaction”. In: *ACS Sustainable Chem. Eng.* *8*, 9136-9144 (2022).
- [234] N. Romero et al. “Ru-based Nanoparticles Supported in Carbon Nanotubes for Electrocatalytic Hydrogen Evolution: Structural and Electronic Effects”. In: *Inorg. Chem. Front.* *10*, 5885-5896 (2023).